2010

Scanning acoustic microscopy for GDL water distribution characterization

Christopher McDade

SCANNING ACOUSTIC MICROSCOPY FOR GDL WATER DISTRIBUTION CHARACTERIZATION

by

C. Lee McDade

A Thesis Submitted in Partial Fulfillment of the Requirements for the degree of

Master of Science in Mechanical Engineering

Approved By:

Dr. Satish G. Kandlikar Professor of Mechanical Engineering	_____ (Thesis Advisor)
Dr. Navalgund Rao Associate Professor of Imaging Science	_____
Dr. Maria Helguera Assistant Professor of Imaging Science	_____
Dr. Tuhin Das Assistant Professor of Mechanical Engineering	_____
Dr. Edward C. Hensel / Dr. Alan H. Nye Department Head of Mechanical Engineering	_____ (Department Representative)

Rochester Institute of Technology

2010

Permission to Reproduce

Title: Scanning Acoustic Microscopy for GDL Water Distribution Characterization

I, Christopher Lee McDade, hereby grant permission to the Wallace Memorial Library of Rochester Institute of Technology to reproduce my thesis in the whole part. Any reproduction will not be for commercial use or profit.

Date: _____ Signature of Author: _____

Abstract

The objective of this research was to identify and apply possible acoustic imaging techniques for water transport studies in PEM fuel cell diffusion mediums. To accomplish this, a scanning acoustic microscope (SAM) was designed and built along with dedicated control and analysis software to implement all investigative tests and scans. The results of the study were in two parts, acoustic response characterization of the fibrous material and implementation of the developed imaging technique for water saturation distribution characterization.

Having used a focused $30MHz$ centered wide band transducer with focal point FWHM beam diameter of $90\mu m$ the target material ensured a ka number approximately equal to one given the average fiber diameter around $8\mu m$. The result was a diffractive acoustic response subject to phase sensitive interference. Traditional ultrasonic techniques for material characterization or imaging were inapplicable so a signal correlation ratio method was developed which relies on the variations in acoustic responses between two scans. Results from different GDL samples at varying levels of saturation were compared to characterize their individual spatial distribution patterns.

Table of Contents

List of Figures

List of Tables

Introduction

Fuel cells show promise in the future of alternative energy sources. Among the most capable is the Proton Exchange Membrane (PEM) fuel cell. PEMFCs are currently being developed for transportation, portable and stationary power sources given their relatively high energy conversion efficiency, zero emissions, and low operating temperatures and pressures. Even with their relative success, issues still need to be resolved. One of the primary areas of research is water management and its effect on the overall cell performance and durability.

A key component to water management and control is the gas diffusion layer (GDL), commonly constructed of carbon paper. Its role within the cell is to ensure even distribution of reactant gasses and removal of excess product water while not inhibiting the flow of electrons between cells. Two common problems of poor water management are flooding and membrane dehydration. Excess water can inhibit reactant gas transport while improper membrane hydration reduces proton conductivity. To solve these problems, knowledge of the propagation characteristics of gas and water within the GDL is required. With varying levels of success, neutron and x-ray imaging techniques have been used to study water distribution within the GDL. While both methods can resolve high resolution 2D maps of water in-plane, neither can produce three dimensional distributions. In an effort to overcome this deficiency ultrasonic imaging was proposed.

Ultrasound imaging is a well established technology that has many applications for three dimensional reconstruction. The most common use is for medical applications, where ultrasound has been successfully utilized to image most parts of the human anatomy. Equally successful is the use of ultrasound to scan for internal fractures or anomalies within performance critical parts. However the use of ultrasound to image a GDL, a highly inhomogeneous material with micron size features, presents a new challenge. With the use of high frequency transducers and tuned signal processing, this objective is being pursued. Ultimately, extracting meaningful information and new insights to the water distribution characteristics of various GDLs.

Chapter 1: Ultrasound Theory

1.1-Applying Ultrasound

Ultrasound is defined as sound waves having frequencies higher than $20kHz$, the typical upper limit for human hearing. It is used for a variety of purposes, medical imaging, flaw detection, short range distance measurements, acoustic cleaning, etcetera. Operating frequencies can range from $100kHz$ to $100MHz$ depending on the application [1].

Unlike light, ultrasound waves need an elastic medium to propagate, relying on the particles connective forces to translate the wave. These waves are subject to typical macroscopic effects of all waves, namely reflection, refraction, and diffraction [1].

When applying ultrasound to a target sample a short pulse of some primary frequency is introduced to the object via an ultrasound transducer. This pulse then travels through the material at approximately constant speed. When an echo generating object or scatterer is encountered by the high frequency pulse some of its energy is reflected back to the transducer. This echo pulse is then converted into a time varying voltage, typically called the A-line signal, which is then analyzed [2]. While the time of travel is converted into scatterer depth, relative echo signal amplitude and phase can be used in material property characterization [3].

The process of pulse/echo imaging can be approximated as a linear system. It is common to model the series of events as a series of time convolved modifiers or effectively a frequency domain series of filters.

$$\begin{aligned} p_i(r_i, z, t) = a_T(t) *_t a_D(r_i, z, t) *_t \delta(t - t_i) *_t a_a(t) \\ *_t a_s(t) *_t a_a(t) *_t \delta(t - t_i) \\ *_t a_D(r_i, z, t) *_t a_T(t) \end{aligned} \qquad (1.1\text{-}1)$$

$$\begin{aligned} P_i(r_i, z, f) = A_T^2(t) \times A_D^2(r_i, z, f)\, exp(-2\alpha z f) \\ \times (\sim df^n) \times exp(-i4\pi t_i f) \end{aligned} \qquad (1.1\text{-}2)$$

These functions include the transducers effect, $a_T(t)$, on the pulse as well as the functions that describe the attenuation, $a_a(t)$, diffraction, $a_D(r_i, z, t)$, and scattering physics, $a_s(t)$. Note the use of two transducer, diffraction and attenuation functions to account for the two way travel of the pulse and both transmit and receive events.

1.2-Wave Propagation

The governing equation for wave motion and propagation is given in equation *1.2-1*,

$$\frac{\partial \sigma_{ij}}{\partial x_j} + f_i = \rho \frac{\partial^2 \vec{u}}{\partial^2 t^2} \qquad (1.2\text{-}1)$$

Where f and ρ are the body forces and material density respectively. The connection between stress and strain are listed in equation *1.2-2* assuming a linear relation where λ and μ are the first and second Lame's constants.

$$\sigma_{ij} = 2\mu\varepsilon_{ij} + \lambda\delta_{ij}\varepsilon_{ij} \qquad (1.2\text{-}2)$$

$$(\lambda + \mu)\nabla(\nabla.\vec{u}) + \mu\nabla^2\vec{u} = \rho \frac{\partial^2 \vec{u}}{\partial^2 t^2} \qquad (1.2\text{-}3)$$

Time harmonic solutions to these equations come in the form where *w* is the angular velocity of the wave and k is the wave number.

$$u = u_0 exp\big(i(wt - kz)\big) \qquad (1.2\text{-}4)$$

The two are related by the material property phase velocity which is not only dependent on the material properties but also the type of wave motion, distortional or dilatational.

$$c = {}^{w}/_{k} \qquad (1.2\text{-}5)$$

For distortional waves where shear and rotation of particles define their motion, the propagation speed is defined by equation *1.2-6* below.

$$c_r = \sqrt{\frac{\mu}{\rho}} \tag{1.2-6}$$

For dilatational waves, dominant form in liquids, where the particle motion is in-line with the wave propagation the phase velocity becomes,

$$c_l = \sqrt{\frac{\lambda + 2\mu}{\rho}} \tag{1.2-7}$$

or in engineering constants where E is the Young's modulus and ν is the Poisson's ratio of the material.

$$c_l = \sqrt{\frac{E(1-\nu)}{\rho(1-2\nu)(\nu+1)}} \tag{1.2-8}$$

For fluids where the Poisson's ratio approaches one half, zero viscosity, the propagation speed is then expressed in terms of the fluids bulk modulus.

$$c_l = \sqrt{\frac{K}{\rho}} \tag{1.2-9}$$

There are many vibratory modes in which ultrasound can propagate but longitudinal waves are the most common in imaging applications [1]. This can be attributed to liquids inability to support shear waves and the relatively straight forward implementation of compressional wave imaging.

1.3- Backscatter Effects and Attenuation

The ability of an object to produce an echo signal is dependent on its reflection/scattering characteristics. In order for ultrasound waves to be reflected or scattered there needs to be an interface at which there is a change in acoustic impedance, Z [1]. Z is a material property which quantifies the resistance of its particles motion induced by a sound wave [4]. Acoustic impedance is defined by the following formula where ρ is the material density and c is the propagation speed for the material.

$$Z = \rho c \qquad (1.3\text{-}1)$$

For example, water has an average propagation speed of $1{,}481 ms^{-1}$ and an acoustic impedance of $1.48x10^{6} kg/m^{2}s$ at standard temperature and pressure [1]. If a propagating wave encounters a material with a different acoustic impedance than the coupling medium vibratory energy will be scattered in a manner dependent on the materials size and shape [2].

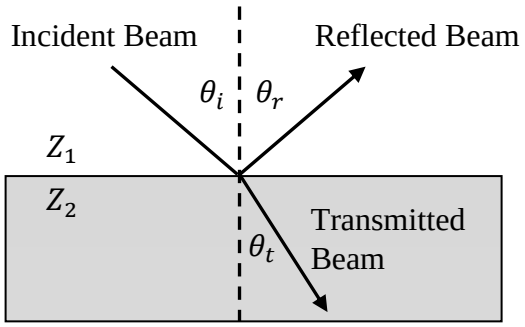

Figure 1.3-1: Specular beam reflection rays.

There are three general categories in which a scattering boundary can fall, specular, diffractive, and diffusive. The first being a scatterer with a length scale much larger than the sound wavelength. In this case the pulse wave reflection and refraction will be specular, allowing the waves to be approximated as rays following Snells's law for reflection and refraction.

$$\frac{sin\theta_i}{sin\theta_t} = \frac{c_1}{c_2} \qquad (1.3\text{-}2)$$

The strength of the reflected and transmitted waves can be approximated by the relation between the materials acoustic impedances [2].

$$RF = \frac{Z_2 cos\theta_i - Z_1 cos\theta_t}{Z_2 cos\theta_i + Z_1 cos\theta_t} \qquad (1.3\text{-}3)$$

$$TF = \frac{2Z_2 cos\theta_i}{Z_2 cos\theta_i + Z_1 cos\theta_t} \qquad (1.3\text{-}4)$$

Where θ_i and θ_t are the incident and transmitted ray angles respectively. The echo signal strength for this category of reflector is relatively strong and independent of frequency [1].

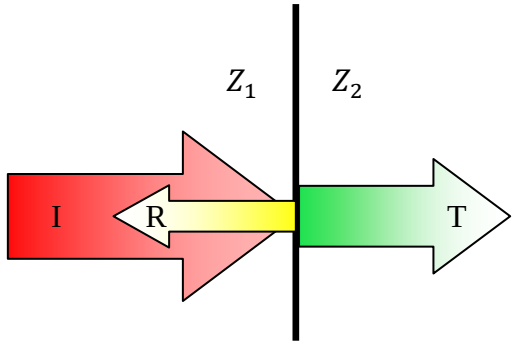

Figure 1.3-2: Impedance boundary pulse energy division.

The second and most complicated category, diffractive, is for objects with sizes comparable to the ultrasound wavelength. Generally the echo signal strength from this category of scatterer is $10\ to\ 30dB$ lower than that of specular boundaries and are dependent on the pulse frequency [1]. For this size scale the scattering pattern is generally modeled by taking the scatterer surface as the source of the reflected waves. The result of diffractive interference from all infinitesimal point sources on the surface construct the scattering pattern. Modeling the backscatter for this regime is difficult and exact solutions for only some simple geometries have been solved analytically [5].

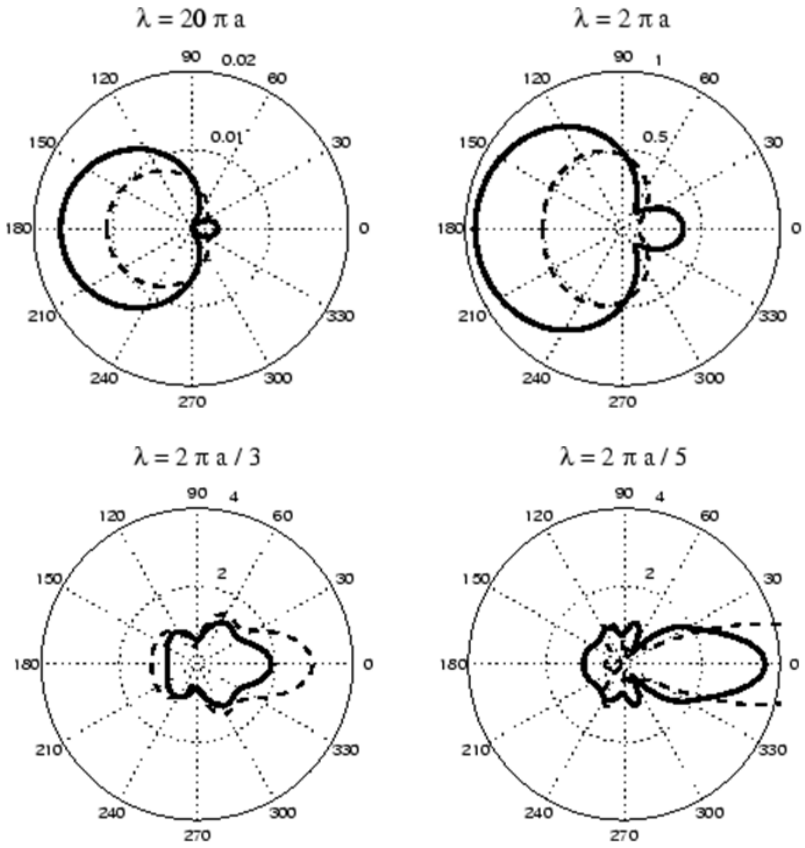

Figure 1.3-3: Diffractive scattering polar plots. [5]

In this scattering regime, where the ka number is approximately equal to one, a relative small change in the relation between the wavenumber, k, to the scatterer size, a, can result in a large change in the scattering pattern. This effect makes ultrasonic signals difficult to interpret and is illustrated in figure *1.3-3*.

$$k = \frac{2\pi}{\lambda} \qquad (1.3\text{-}5)$$

An additional phenomenon that is relevant for this scatterer size regime is speckle. Given that the feature sizes of the reflectors are on the order of the pulse wavelength multiple scatterers can be present in the transducers resolution cell. Constructive and destructive interference between all echoes results in a semi-random but deterministic echo signal at the

transducer. This produces a texture in the resulting image known as speckle. Statistical analysis of the speckle pattern can be used to extract useful tissue characteristics and can enhance image contrast [2].

The third category is for scatterers that have dimensions much smaller than the ultrasound wavelength, $ka \ll 1$. Scatterers possessing this size scale produce very weak reflections but whose amplitude is highly dependent on the pulse frequency, $I \sim f^4$ [1]. It is also noted that individual echoes from surface roughness features of this size regime exhibit insignificant interference with each other. This given the small phase difference between reflections from high and low points of the surface [5].

Derived from an exact solution, Lord Rayleigh developed an expression for the radiating intensity from an elastic sphere much smaller than the irradiating ultrasound wavelength.

$$\frac{I_s}{I_i} = \frac{k^4 a^6}{9r^2}\left[\frac{3\left(1-{\rho_2}/{\rho_1}\right)cos\vartheta}{1+2\,{\rho_2}/{\rho_1}} + \left(1-\frac{\kappa_1}{\kappa_2}\right)\right]^2 \qquad \textit{(1.3-6)}$$

Subscript 2 in equation *1.3-6* indicates the spheres density, ρ_2, and compressibility , k_2 [5]. Note the scattered intensities fourth power dependence on frequency and the sixth power dependence on the scatter radius.

A major obstacle to overcome in any ultrasound imaging system when depth penetration and resolution is of concern is attenuation. During a wave's propagation its amplitude drops with distance exponentially [2]. Reduction in the wave's energy or intensity can be attributed to absorption and scattering losses. The combined effect of these two losses defines attenuation and is approximately linearly dependant on frequency for most tissues. This loss is accounted for with the material transfer function (MTF) in the frequency domain and the material impulse response function (*mirf*) in the time domain for modeling purposes.

The resulting pulse, $p(t,z)$, after a given distance traveled is calculated by convolving the initial pulse with the *mirf*.

$$p(t,z) = p_0(t) *_t mirf(t,z) \qquad \textit{(1.3-7)}$$

This is equivalent to multiplying the Fourier transformed pulse with the MTF [6] where α is the attenuation factor and β_E is an excess dispersion term to account for causality [7].

$$MTF(f,z) = exp(\gamma(f)z) \tag{1.3-8}$$

$$\gamma(f) = -\alpha(f) - i[k_0(f) + \beta_E(f)] \tag{1.3-9}$$

$$\alpha(f) = \alpha_0 + \alpha_1|f|^y \tag{1.3-10}$$

The effect is an exponential decay in the pulse amplitude with distance. Generally, lossy materials act as a lowpass filter, causing a shift towards zero in the center frequency.

$$f_{peak} = f_c - \frac{\alpha_1 z}{2b} \tag{1.3-11}$$

This model also accounts for phase velocities dependence on frequency, known as dispersion, this effect is where propagation speed increases with frequency.

$$c(\omega) - c_0 = -\frac{c_0^2 \beta_E}{\omega} \tag{1.3-12}$$

When the non-linear response of a medium is taken into account the phase velocity then depends on the displacement gradient $\partial u/\partial z$ where $u(z,t)$ is the particle displacement [1].

$$\frac{\partial u^2}{\partial t^2} = \frac{c_0^2}{\left(1 + \frac{\partial u}{\partial z}\right)^{(B/A)+2}} \frac{\partial u^2}{\partial z^2} \tag{1.3-13}$$

Where B/A is the non-linear parameter of the material. The consequence is that the higher pressure or higher frequency regions of the wave will travel faster than the lower pressure regions, resulting in a distortion of the original pulse.

1.4-Sound Field

The sound field of a transducer can be divided into two regions, the near field and the far field, or the Fresnel and Fraunhofer regions respectively. The near field is defined as the beam section in front of the transducer element where the sound field undergoes a series of maxima and minima, ending with the last maxima [1].

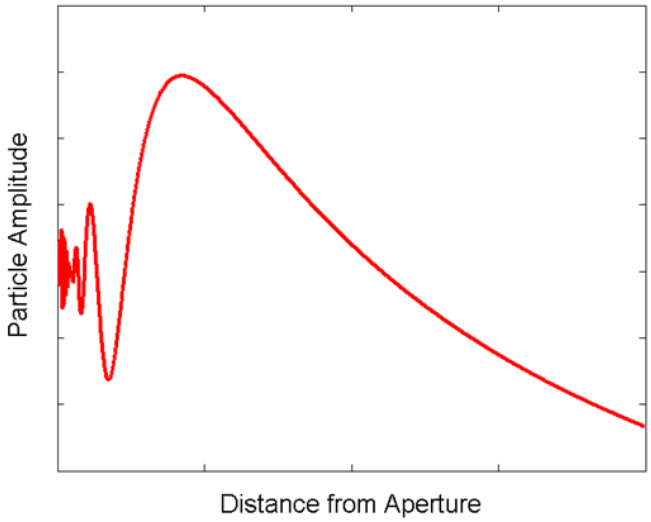

Figure 1.4-1: Beam intensity profile as a function of aperture distance.

The region after this last maximum in known as the far field where the waveform intensity gradually decays. The size and shape of the near field, N, is governed by diffraction but its length can be approximated with knowledge of the transducer frequency, element diameter, and material sound velocity [8].

$$N = \frac{D^2 f}{4c} = \frac{D^2}{4\lambda} \qquad (1.4\text{-}1)$$

Due to the near fields variation in waveform intensity it is difficult to perform any amplitude based imaging in this region.

The sound field pattern was explained by Christian Huygens as the interference pattern from many infinitesimally small wave radiators that make up the transducer face. To solve for the pattern, each location in space was the result of summing the contributions from all point sources making up the face of the transducer. The Rayleigh-Sommerfeld integral for a piston type transducer describes the sound field pattern and is given by equation *1.4-2* where $\bar{\rho}$ and $\bar{\rho}_0$ are the cylindrical coordinate radii for the source and field point.

$$p(\bar{\rho},z,\lambda) = \frac{i2\pi p_0}{\lambda z} exp\left(\frac{-i\pi\bar{\rho}^2}{\lambda z}\right) \times \int_0^\infty A(\bar{\rho}_0) \times exp\left(\frac{-i\pi\bar{\rho}_0^2}{\lambda z}\right) J_0\left(\frac{2\pi\overline{\rho\rho_0}}{\lambda z}\right)\bar{\rho}_0 d\bar{\rho}_0 \qquad (1.4\text{-}2)$$

Additionally, J_0 is a zero-order Bessel function and the $A(\bar{\rho}_0)$ term accounts for the transducer face apodization [6]. As distance from the transducer increases the $\overline{\rho_0}/z$ terms go to zero, reducing the above expression and stating that the beam pattern is simply the Hankel transform of the aperture function.

$$p(\bar{\rho},z,\lambda) \approx \frac{i2\pi p_0}{\lambda z}\int_0^\infty A(\bar{\rho}_0) J_0\left(\frac{2\pi\overline{\rho\rho_0}}{\lambda z}\right)\bar{\rho}_0 d\bar{\rho}_0 \qquad (1.4\text{-}3)$$

Assuming a constant normal velocity on an aperture of radius a, the equation is further reduced,

$$A(\bar{\rho}_0) = \prod\left(\frac{\overline{\rho_0}/2}{a}\right) \qquad (1.4\text{-}4)$$

$$p(\bar{\rho},z,\lambda) \approx \frac{i2\pi p_0}{\lambda z} H\left[\prod\left(\frac{\overline{\rho_0}/2}{a}\right)\right] \qquad (1.4\text{-}5)$$

$$p(\bar{\rho},z,\lambda) \approx \frac{ip_0\pi a^2}{\lambda z}\frac{2J_1\left(2\pi\bar{\rho}a/\lambda z\right)}{2\pi\bar{\rho}a/\lambda z} = ip_0\left(\frac{\pi a^2}{\lambda z}\right) jinc\left(\frac{\bar{\rho}a}{\lambda z}\right) \qquad (1.4\text{-}6)$$

$$jinc(x) = \frac{2J_1(2\pi\bar{x})}{2\pi\bar{x}} \qquad (1.4\text{-}7)$$

The result shows that a jinc function approximates the shape of the far-field beam for a circular transducer [6].

$$z_{max} = {a^2}/{\lambda} \qquad (1.4\text{-}8)$$

After the last maxima in beam intensity its full width half maximum (FWHM) dimension can be approximated by the following [6].

$$FWHM = 0.7047\,{\lambda z}/{a} \qquad (1.4\text{-}9)$$

1.5-PSF and Resolution

The lateral and axial resolution of the system is quantified by the point-spread function (PSF) of the system. The PSF is defined as the resulting image of a scanned point object, mathematically a two dimensional delta function [1]. Scanning a point object over two dimensions will generate a three dimensional PSF whose projection dimensions define the system resolution [1]. As the beam profile and pulse vary with time and depth the PSF does as well. Diffraction accounts for most of the PSF's lateral variation with depth. The PSF determines some imaging limits of the system. If two objects to be imaged are separated by a distance smaller than the lateral resolution of the system, which is determined by the PSF, they will not be resolved as two independent entities.

It is common for an ultrasound system's resolution to be quantified by scanning a thin wire target, acting as a line of delta function inputs, mutually perpendicular to the wires length axis and the beam axis. The resulting image defines the one-dimensional line-spread function (LSF). The LSF is mathematically the integration of the PSF over the lines objects axis. This can be thought of as the projection of the PSF along the integration axis [1].

$$LSF(y) = \int PSF(x, y)dx \qquad (1.5\text{-}1)$$

The image produced from the scan described above will show a singular blob, representing the PSF for the system at that particular depth. The system resolution is commonly defined by the $-6dB$, or half amplitude, full width and length of the imaged line-target. The FWHM along the scan axis will define the lateral resolution while the axial resolution will be defined by the temporal FWHM of the envelope signal.

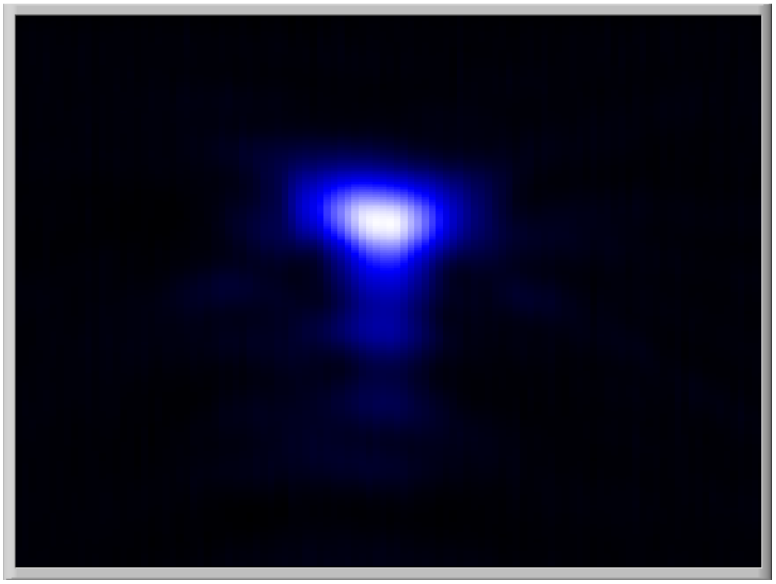

Figure 1.5-1: B-scan image of 12.7μm diameter tungsten wire at transducer focal depth.

The PSF is spatially variant, meaning its size and shape are dependent on the distance from the pulse source. While the lateral resolution is governed by the beam width the temporal resolution is governed by frequency dependent attenuation. This is explained by the inverse relation between pulse duration and bandwidth. As the pulse propagates through the medium its frequency content is altered, changing the pulse duration and consequently the temporal resolution [4]. Typical resolutions to be expected depend on the size, shape, and frequency of the transducer as well as the propagating medium. Frequencies in the megahertz range will see resolutions on the order of a few millimeters while frequencies exceeding 10 megahertz can see sub millimeter resolutions [1].

1.6-Focusing

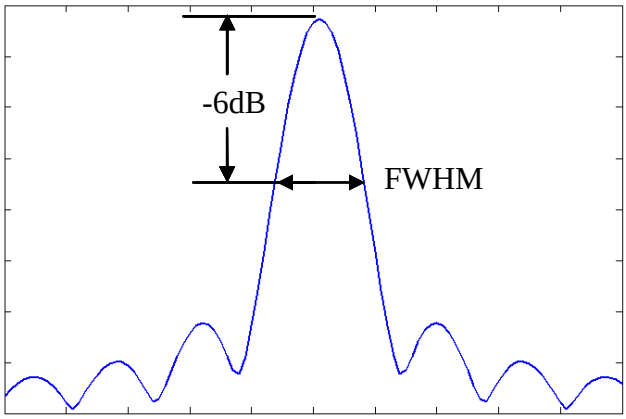

Figure 1.6-1: Beam profile plot illustrating full width half maximum.

Focusing is used to increase the lateral resolution and sensitivity of a transducer. This is accomplished by either using a curved lens to focus the acoustic beam or to curve the element face itself. The result is a focal point which is defined by the mutual delay time of propagation for each location on the element. Electronic focusing is also implemented with multi-element array transducers where delays are applied to the transmit and receive signals appropriately to achieve the same effect. Not only will the beam intensity increase but the width and side lobes of the beam are reduced, increasing image resolution and contrast consequently. The benefits are significant but localized to the focal zone. The trade off is that the diffraction driven widening of the beam is accelerated after the focal point.

It's interesting to note that unfocused transducers exhibit a natural focusing effect where the peak acoustic intensity is located at the near-field far-field transition. When focused this transition point is simply shifted closer to the transducer. All the same diffraction effects are present in a focused beam but are expedited along the beam axis.

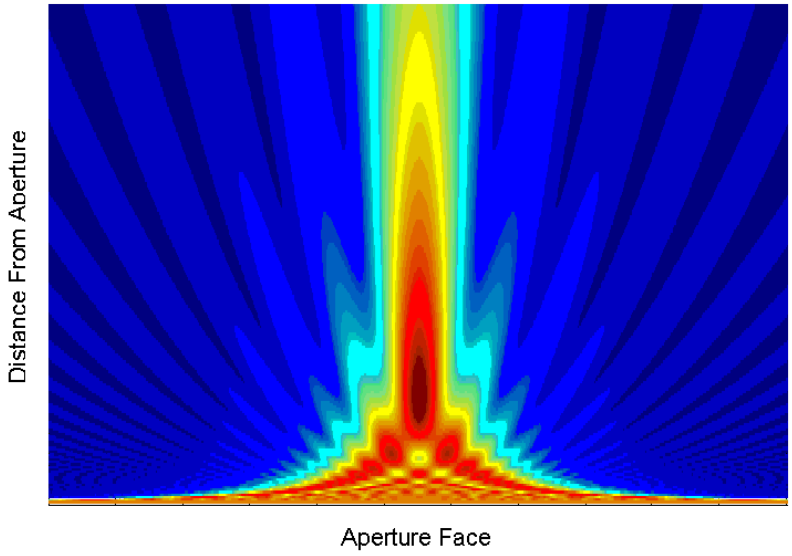

Figure 1.6-2: Beam intensity profile map for an unfocused rectangular aperture.

One might expect the point of maximum acoustic intensity to be at the geometric focal length, F, but this turns out to be untrue. The combined effects of natural focusing from diffraction and geometrical focusing results in a reciprocal relation to the focused peak amplitude depth, z_{fp} [6].

$$z_{fp} = \frac{z_{ufp}F}{(z_{ufp} + F)} = \frac{a^2F}{(a^2 + \lambda F)} \qquad (1.6\text{-}1)$$

To quantify the improvements obtained by focusing a gain factor can be derived from the Rayleigh-Sommerfeld integral for a unapodized circular aperture. An approximate solution for the on-axis beam amplitude is listed below.

$$p(0,z,\lambda) \approx \frac{i2p_0 exp(-ikz) exp\left(-i\pi a^2 / 2\lambda z_e\right)}{(z/z_e)} sin\left(\frac{\pi a^2}{2\lambda z_e}\right) \qquad (1.6\text{-}2)$$

The above equation was derived using the Fresnel approximation, $z^2 \gg a^2$, and an account for focusing by replacing z with an effective z_e term.

$$z_e = \frac{z}{(1 - z/F)} \tag{1.6-3}$$

Defining a gain factor as the ratio of the pulse amplitude at the focal distance over the pulse amplitude at the transducer face it is found to be proportional to the aperture area, wave length and focal distance.

$$G = \frac{\pi a^2}{\lambda F} \tag{1.6-4}$$

Another focusing effectiveness quantification is the reduction in beam width. In this case the formula for an unfocused circular aperture holds for the focused case but since the focal distance is now shorter a reduction in beam width is predicted.

The final focusing quality factor is the depth of field (DOF). It defines the working range for a transducer where reasonable acoustic energy and resolution are maintained. Called the focal Fraunhofer zone, it is defined as the depth range encompassed by the fore and aft $-6dB$ beam amplitude points relative to the peak amplitude focal depth. Due to the complex formulations for spherically focused transducers calculating this DOF can be computationally intensive. G. Kossoff addressed this by developing a method that approximates the DOF on the idea that the intensity beamwidth squared product remains constant for any depth.

$$I^2 w_{-6db}^2 = I_F^2 w_{-6db}^2 \tag{1.6-5}$$

Since the FWHM at the focal point can be calculated with equation *1.4-9* and the beam intensity estimated with equation *1.6-2*, the $-6dB$ beamwidths can be solved for with the equation *1.6-5* [9].

1.7-Processing the Echo Signal

Given that the transducer is driven by a 100 to 600 volt pulse and the received echo signal generates voltages in the millivolt range a lot of signal conditioning/processing is needed. The A-line signal in medical applications can typically see a dynamic range of $70\ to\ 80dB$, attenuation accounting for $30\ to\ 50dB$ while differences in backscatter are responsible for the rest [1]. To correct for the attenuation loss a time dependent amplification or time-gain correction is applied to the signal. This still leaves a dynamic range to large for useful display. A non linear amplifier biases more amplification to weaker signals than the stronger. At this point the signals dynamic range is reduced to around $20\ to\ 30dB$ [1].

In addition to signal amplification the signal is generally demodulated for display purposes. The objective is to remove the high frequency oscillations in the signal and simply display the effective amplitude trend. There are various methods to do this but the most common is to calculate the envelope of the RF signal. The envelope is defined as the magnitude of the signal considering the real and imaginary parts.

$$E(t) = \sqrt{R(t)^2 + I(t)^2} \qquad (1.7\text{-}1)$$

The real part of the RF signal is obtained through measurement while the imaginary portion is calculated from the measured through the Hilbert transform.

$$X_a(t) = X(t) + \frac{i}{\pi}\int_{-\infty}^{+\infty}\frac{X(\tau)}{t-\tau}\,d\tau \qquad (1.7\text{-}2)$$

The result is an outline of the A-Line signal which is typically used to define echoes and image intensity images.

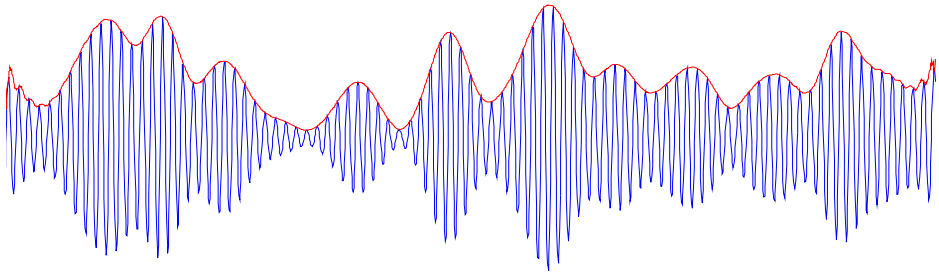

Figure 1.7-1: Example A-line envelope. [10]

1.8-Transducer Operation

Given that the transducer is responsible for generating and receiving the acoustic waves and that its construction and design define the characteristics of those waves it is important to understand the transducer. The following will overview the fundamental components of the transducer and typical modeling methods.

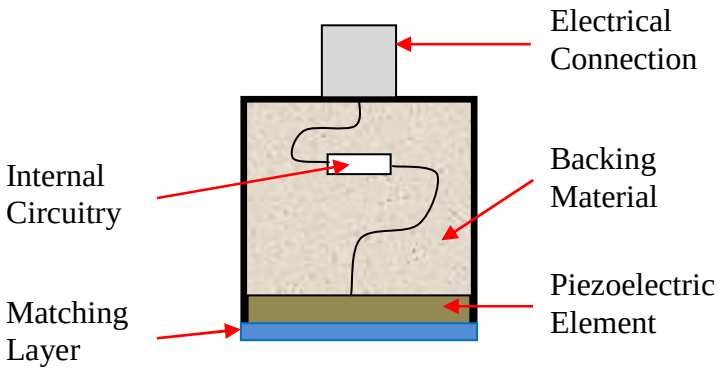

Figure 1.8-1: Typical transducer construction.

The active element is generally a piezoelectric material, most commonly lead zirconate titanate (PZT) [1]. Piezoelectric materials have the unique characteristic of being a dielectric, meaning its dipoles shift and align with applied electric fields. The effect is that the piezoelectric will alter its shape in the presence of and electric field. This can be modeled

by a modification to the Hooke's law shown in equation *1.8-1* where C^D is the elastic stiffness for longitudinal compression and D is the dielectric displacement.

$$\sigma = C^D \varepsilon - hD \qquad (1.8\text{-}1)$$

This displacement is defined by the clamped dielectric constant (ς^s), area (A), and applied electric field (E).

$$C_0 = \frac{\varsigma^s A}{d} \qquad (1.8\text{-}2)$$

$$D = \varsigma^s E = \frac{C_0 V}{A} \qquad (1.8\text{-}3)$$

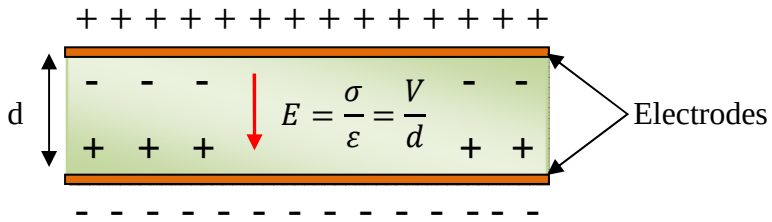

Figure 1.8-2: Piezoelectric cartoon.

When a voltage is applied across the area of the piezoelectric the electric field then induces an internal stress which forces a change in the elements thickness. The interesting thing is when a voltage impulse is applied to the element. Since the Fourier transform of a delta function is a function whose magnitude is one, or signifying a flat frequency response, the transducers natural frequency, f_0, is then exited. The response is to oscillate at this frequency until damped.

$$f_0 = \frac{\sqrt{\frac{C^D}{\rho}}}{2d} \qquad (1.8\text{-}4)$$

The Fourier transform of the force formulation multiplied by a delta function impulse reveals an odd harmonic maxima pattern of the fundamental frequency, assuming no interaction with its surroundings [11].

$$F(f) = -i(hC_0V)exp\left(\frac{-i\pi fd}{c}\right)sin\left[\frac{\pi(2n+1)f}{2f_0}\right] \qquad (1.8\text{-}5)$$

To better understand the operation of the transducer a model of its interactions between various elements is needed. The Krimholtz-Leedom-Matthaei (KLM) model is a common method used to represent the system. It is based on the ABCD matrix relations from electrical design where a circuit is defined by a 2 by 2 matrix that relates the output voltage and current to its input. By relating pressure to voltage, particle velocity to current, and particle displacement to charge an equivalent matrix based on an elements impedance, wave number, and thickness can be defined.

$$\begin{bmatrix} V_1 \\ I_1 \end{bmatrix} = \begin{bmatrix} A_e & B_e \\ C_e & D_e \end{bmatrix} \begin{bmatrix} V_2 \\ I_2 \end{bmatrix} \qquad (1.8\text{-}6)$$

$$\begin{bmatrix} p_1 \\ v_1 \end{bmatrix} = \begin{bmatrix} A_a & B_a \\ C_a & D_a \end{bmatrix} \begin{bmatrix} p_2 \\ v_2 \end{bmatrix} \qquad (1.8\text{-}7)$$

The model is laid out so that the piezoelectric element is split down the middle, where there are three ports for connections to the surroundings. Port one couples the dielectric to the coupling layers of the transducer while port two couples the backing layers. The third port makes the electrical connection to the external electric circuit.

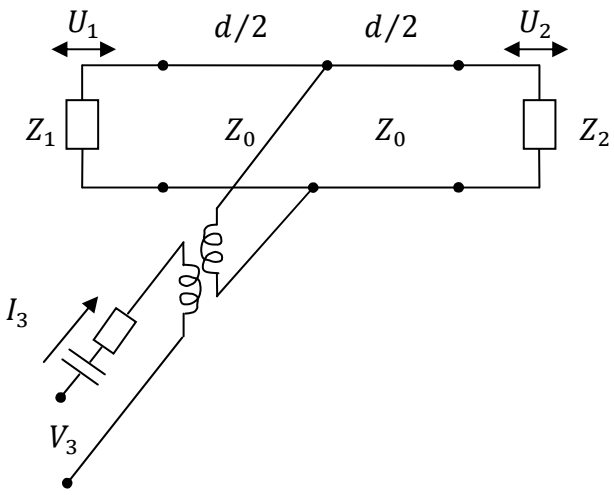

Figure 1.8-3: KLM Transducer electrical equivalency model.

The relation between the electric input to port one or two is made by the product of the corresponding ABCD matrices. Additional elements of the transducer can be added to the model through the same process, a product series of individual ABCD impedance matrices to define the overall system relation between input and output.

$$\begin{bmatrix} V_3 \\ I_3 \end{bmatrix} = \begin{bmatrix} A & B \\ C & D \end{bmatrix} \begin{bmatrix} F_2 \\ U_2 \end{bmatrix} \tag{1.8-8}$$

This method allows for quick evaluations of individual parts of the transducer for easy design optimization. It's also open to the use of complex terms for material losses which are very significant for inorganic polymer piezoelectrics. Given their nature, polymers will have large dispersion in their mechanical and electrical constants which are temperature and frequency dependent [12].

To quantify the efficiency of a transducer design some defining quantities need to be established. The first is the insertion loss which is a measure of the round-trip efficiency of a transmit/receive system. The insertion loss is defined as the ratio between the power received over the power supplied. So it is a measure of the total energy loss for each step in the pulse echo process, electrical/mechanical conversion losses, matching layer coupling losses, and medium coupling losses for transmission and reception [11].

$$IL(f) = \frac{P_r}{P_s} = \left[\left|\frac{V_r}{V_s}\right|^2 \left(\frac{R_r + R_s}{R_r}\right)\right] \quad (1.8\text{-}9)$$

Equation *1.8-9* defines the insertion loss where s and r subscripts denote source and recive qunatites respectively and P and V are for power and voltage respectively. R_s is the real part of the pulser impedance and R_r similarly is the receiver resistance. Note that maximum efficiency is obtained if $R_r = R_s$.

The efficiency of the transducers electrical response can be optimized through the use of an electrical matching network just as the acoustic efficiency is optimized through material selection and dimensioning. The electrical loss (EL) is defined as the total converted acoustic energy at the active element over the power supplied by the source.

$$EL = \frac{P_{ra}}{P_s} = \frac{I^2 R_a/2}{V_s^2 8 R_s} \quad (1.8\text{-}10)$$

From the model depicted in figure *1.8-4* the ratio of the voltage over the transducer to the voltage of the source is defined by equation *1.8-11* where Z_T is the dielectrics impedance consisting of real, R_a, and imaginary, X_a, parts.

$$\frac{V_T}{V_s} = \frac{Z_T}{AZ_T + B} \quad (1.8\text{-}11)$$

$$Z_T = R_a(f) + i\left[X_a(f) - \frac{1}{\omega C_o}\right] \quad (1.8\text{-}12)$$

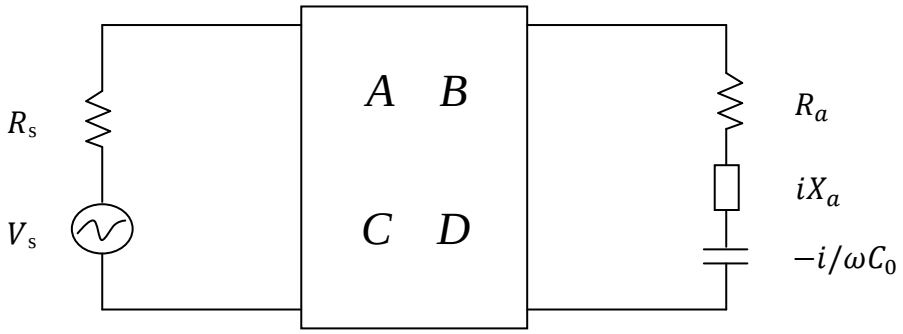

Figure 1.8-4: Transducer electrical model

The result is the following formula for the electrical loss in terms of the source's resistance, R_s, and both the matching circuit's and dielectric's impedance.

$$EL = \frac{4R_a R_s}{|AZ_T + B|^2} \tag{1.8-13}$$

The final quantification of the transducers efficiency is the acoustical loss. This loss is defined as the total power converted to acoustical energy over that finally transmitted into the coupling medium.

$$AL = \frac{P_{out}}{P_{ra}} \tag{1.8-14}$$

$$P_{ra} = P_{BL} + P_{ML} \tag{1.8-15}$$

The acoustic energy generated in the active element is split between propagating through the backing layers and the matching layers to the coupling medium. The ratio of divided energy is governed by either directions impedance to propagation.

$$P_{BL} = \frac{1}{2}\left|\frac{F_c}{Z_{BL}}\right|^2 Re(Z_{BL}) \tag{1.8-16}$$

$$P_{ML} = \frac{1}{2}\left|\frac{F_c}{Z_{ML}}\right|^2 Re(Z_{ML}) \tag{1.8-17}$$

Similarly the amount of energy transferred to the coupling medium, equation *1.8-19*, is governed by its effective impedance, Z_{CM} where $F_{CM}$is the force on the transducer face and U_1 would be the particle velocity on the face. The resulting acoustic loss is defined by equation *1.8-20*.

$$U_1 = \frac{F_{CM}}{Z_{CM}} \tag{1.8-18}$$

$$P_{CM} = \frac{1}{2}\left|\frac{F_{CM}}{Z_{CM}}\right|^2 Re(Z_{CM}) \qquad (1.8\text{-}19)$$

$$AL = \frac{P_{CM}}{P_{BL} + P_{BL}} \qquad (1.8\text{-}20)$$

One metric which characterizes the frequency response of the transducer is measured by the quality factor Q, defined as the ratio of the resonate frequency over the $-6dB$ bandwidth as defined in equation *1.8-21* [1].

$$Q = \frac{f_0}{\Delta f} \qquad (1.8\text{-}21)$$

1.9-Scanning Modes

To put to use ultrasound waves for imaging there are a few methods of doing so that provide different advantages between them. The objective is to extract meaningful information about the scanned object.

The simplest mode is referred to as an M-scan. This requires the transducer to be held at a fixed location while acoustic pulses are repetitively triggered. The echo signals are received for review and termed A-Lines. The results are displayed by stacking the A-line envelope or brightness values as a function of time and depth. This type of scanning is used to capture movement within the acoustic beam. A common example is to measure the movement of heart valves.

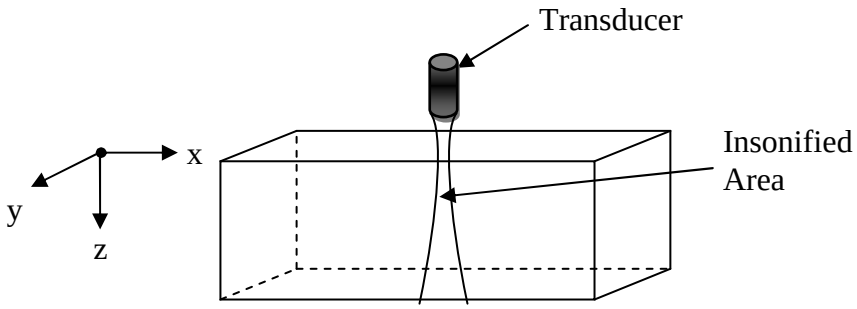

Figure 1.9-1: M-scan orientation.

The next scanning mode is the B-scan or brightness scan. In this mode the transducer is moved perpendicular to its transmission axis which will be refered to as the z axis. Generally displays will present the data in a grayscale fashion where brighter regions depict locations of high acoustic reflectivity. This image represents a two dimensional cross-section of the scanned object in the x-z plan but since the beam is of finite thickness so too does the image represent. This thickness is defined by the systems PSF for the given depth.

Some applications require a quick refresh rate on the generated image so temporal changes in the scanned area can be captured. The refresh rate on single transducer systems are limited by their translational speed but most medical devices use phased array transducer probes. These probes provide the advantage of electronic steering and focusing, allowing rapid refresh rates on B-scan images.

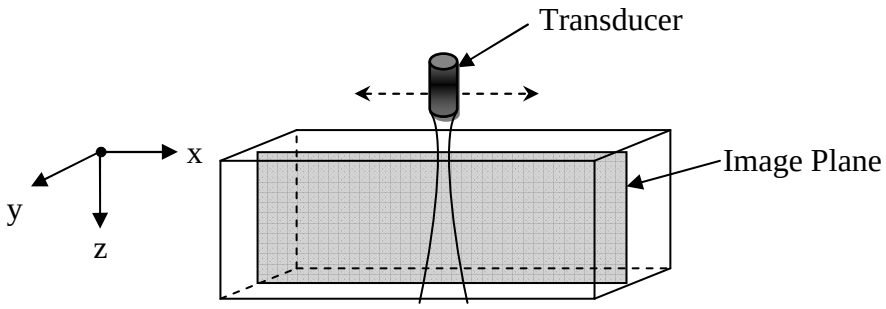

Figure 1.9-2: B-scan orientation.

The final scanning mode used commonly is the C-scan or constant depth scan. This mode produces a two dimensional constant depth slice of the target by translating the transducer in line with the x-y plane. The depth of interest is chosen by time-gating the A-line signal to a specified delay which corresponds to the desired depth. The image can be constructed of the envelope value at a single time point or of the cumulative effect of all envelope values in a specified time-gate.

One of the benefits of a C-scan over a B-scan is that the PSF is spatially invariant. This means that the transducer can be focused to the desired depth, optimizing the resolution or acoustic sensitivity for the scan. The primary disadvantage of the C-scan is it dependence on two scanning axes. This requires a relatively long time to cover the entire scan area. In the same way 1D phased array transducer probes increased the refresh rates for B-scans, 2D transducer arrays have been constructed to expedite C-scans. This is similar to optical CCD technology but at the moment they remain impractical. Due to the long scan times and two scanning axes C-scans are more common in non-destructive evaluations than medical applications [1].

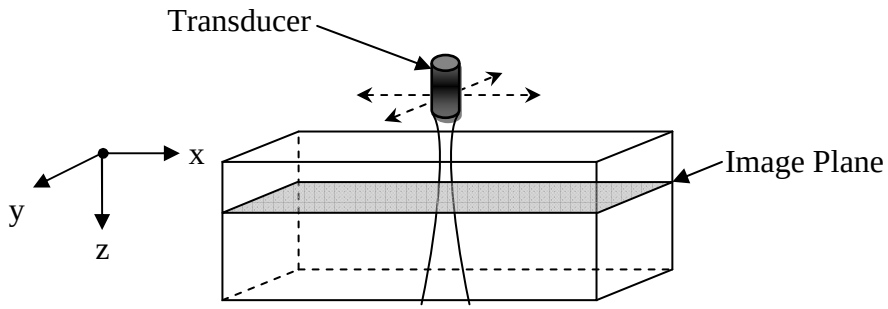

Figure 1.9-3: C-scan orientation.

Chapter 2: Literature Review

Before developing a solid research question, knowledge of recent advances in ultrasound and GDL saturation studies needs to be completed. The following literature review will discuss general trends in ultrasound research as well as a review of other GDL saturation studies and their methodology. The objective is to learn of the existing research surrounding acoustic imaging and GDL studies and to identify their short comings. From there a focus for this research can be stated with confidence of uniqueness and merit.

2.1-Ultrasound

This literature review will cover the broad spectrum of ultrasound applications, leading to a more focused look at publications on scanning acoustic microscopy. Medical and non-destructive evaluation (NDE) are the most broad categories for ultrasound applications. It was clear that the bulk of ultrasound research was devoted to medical applications, given the favorable nature of acoustic tissue properties, but the level of innovation in non-medical applications is notable. The papers that would be classified under medical ultrasound applications deal mostly with imaging characteristics of various modalities. Key papers and their contribution to furthering the ultrasound communities' collective knowledge will be presented. Given that the proposed research is more in line with NDE, papers on this subject will be presented on an application basis.

2.1.1-Medical

2.1.1.1-

" Advances in Ultrasound Biomicroscopy"

F. Stuart Foster, Charles J. Pavlin, Kasia A. Harasiewicz, Donald A. Christopher, and Daniel H. Turnbull

Characteristics of ultrasound propagation in tissue lend itself to medical applications, notably low attenuation coefficients and support of one wave type. With considerable interest in this field great advancements have been made in our understanding. This development was discussed in "Advances in Ultrasound Biomicroscopy" written by F. Stuart Foster, Charles J. Pavlin, Kasia A. Harasiewicz, Donald A. Christopher, and Daniel H. Turnbull [3]. Progress of ultrasound biomicroscopy, aspects of transducer development, system design, and tissue properties are presented in this paper. The section on tissue properties presents the results of studies on frequency dependent attenuation coefficients for various tissue types. The studies show a strong dependence of tissue type on attenuation. Skin, arterial walls, sclera, and other structural tissues have the largest attenuation coefficients while the iris and cornea have coefficients approaching that of water. It was also noted that the concentration and organization of structural proteins like collagen are key to acoustic properties. This section of the paper continues with a discussion of bloods attenuation coefficient being dependent on both shear rate and pulse frequency. An important speculation presented was that red blood cells begin to act like Rayleigh reflectors at frequencies greater than $60MHz$, explaining the reduction in shear rate dependence on attenuation. Further explanation on this subject was not explored. Additional problems and phenomenon were presented but were left unanswered.

2.1.1.2-

"Measurement of Spatial Time-of-Flight Fluctuations of Ultrasound Pulses Passing Through Inhomogeneous Layers"

P. Krammer and D. Hassler

A more specific element of tissue properties was investigated by P. Krammer and D. Hassler. They had performed in-vitro tests of the human abdominal wall and liver to gain data on fluctuations of time-of-flight for computer simulations and imaging experiments. The results were presented in "Measurement of Spatial Time-of-Flight Fluctuations of Ultrasound Pulses Passing Through Inhomogeneous Layers" [13].

The basis for the research was that inhomogeneities introduce spatial distortions in the wave front. The experiment used a $10mm$ diameter $5MHz$ damped piezoelectric plane transducer as the transmitter and a PVDF hydrophone with 1mm diameter aperture as the receiver. The tissue to be tested was placed in a saline solution, in the 140mm space between the transmitter and receiver, perpendicular to their faces, being as close as possible to the receiver. The tissue was sectioned into a $0.5mm$ spaced grid and at each location a measurement of pulse travel time was taken. This was essentially a C-scan of the tissue. 16 samples of abdominal wall and 3 samples of liver tissue were scanned. The results were presented in tabular form, showing the sample number, thickness, scan size, maximum time-of-flight difference, and standard deviation. The occurrence distribution of time-of-flight differences was also calculated and graphed.

For ultrasound pulses passing through abdominal tissue a strong dependence on individual samples was shown. Max time-of-flight values ranged from $200ns$ to $989ns$ while their standard deviations ranged from $50ns$ to $200ns$. The liver samples on the other hand had relatively little effect on propagation speed.

2.1.1.3-

"75 MHz Ultrasound Biomicroscopy of Anterior Segment of Eye"

Ronald H. Silverman, Jonathan Cannata, K. Kirk Shung, Omer Gal, Monica Patel, Harriet O. Lloyd, Ernest J. Feleppa, and D. Jackson Coleman

While most medical applications use frequencies in the range of 2 to $20MHz$ for a good compromise between imaging depth and resolution, modern research is geared toward higher resolution scanning. To achieve these higher resolutions, the fundamental transducer frequency has been increased. An example of this movement toward higher frequencies is the work described in "75 MHz Ultrasound Biomicroscopy of Anterior Segment of Eye" written by Ronald H. Silverman, Jonathan Cannata, K. Kirk Shung, Omer Gal, Monica Patel, Harriet O. Lloyd, Ernest J. Feleppa, and D. Jackson Coleman [14]. Until recently imaging of the anterior segment of the eye was limited to a frequency band of 30 to $50MHz$. The authors wanted to show that higher frequencies can be used to increase resolution with minimal loss in backscatter sensitivity. To achieve this, a $75MHz$ lithium niobate transducer with an F number of 3 was used to scan the ciliary body and cornea of a human eye. The outcome was then compared to results produced using a similar $35MHz$ lithium niobate transducer.

Their experimental setup used a 28 year old female that had LASIK surgery six years prior. The transducers were scanned across the eyes surface, using a warm saline water bath as coupling fluid. The resulting B-mode images were shown in close to real time, 2 frames per second, using a midband fit spectral parameter post processing scheme. The corneal and LASIK interfaces and faint backscatter from the stroma were visible in the images. It was reported that the $75MHz$ transducer produced relatively higher amplitudes of backscatter compared to the $35MHz$ transducer. This allowed sufficient sensitivity to visualize the ciliary body and iris as well as noticeable improvements in resolution and texture.

2.1.1.4-

"A 100-200 MHz Ultrasound Biomicroscope"

Donald A. Knapik, Brian Starkoski, Charles J. Pavlin, and F. Stuart Foster

Use of very high frequency biomicroscopy has found applications in dermatology, intravascular imaging, ocular imaging, and invasive imaging with needle based probes. Donald A. Knapik, Brian Starkoski, Charles J. Pavlin, and F. Stuart Foster have documented the development of a $200MHz$ ultrasound imaging system, "A 100-200 MHz Ultrasound Biomicroscope" [15]. Reported in this paper is the transducer fabrication, the imaging system hardware and characteristics, imaging examples, and final thoughts and discussions.

The piezoelectric material used to fabricate their transducer was made of lithium niobate ($LiNbO_3$) given its good electromechanical coupling, single crystal structure, and high sound wave propagation speed. The fabrication of the transducer started with electrodes made of gold and chromium evaporated onto the $LiNbO_3$ crystal. From there an electrically conductive epoxy was applied to the metalized surface and circular disks were cutout. These disks were then mounted into SMA electrical connectors. The final step was forming the spherical face of the transducer. For this the structure was heated to $70°C$ and a ball bearing was pressed into the $LiNbO_3$ surface. The electrical impedance of the transducer, magnitude and phase, were presented along with a resolution phantom image to verify good electrical contact and beam focus.

The article continues with a description of the imaging system. A list of hardware manufactures accompanied by a schematic diagram of the motion control and signal processing describe the basic layout. System characteristics such as impedance, insertion loss, transducer pulse echo response, and lateral resolution were quantified and compared to a theoretical model. It was found that the measured values were close to the theoretical estimates. The axial resolution was measured to be $12\mu m$ while the theoretical value was $14\mu m$.

After the system characteristics were quantified example images of an eye, skin, and coronary arteries were discussed. The key to their success in image production for these extreme frequencies was a zone-focused technique. Due to the high attenuation of these

frequencies a standard B-scan would result in inadequate signal strength at depths away from the focal zone. To overcome this, the zone-focus technique combines 10 successive B-scans with different focal region depths, separated by $100\mu m$. The result is improved signal intensity and focus over the entire image with lateral and axial resolutions of 14 and 12 microns respectively.

It was concluded from these results that this technique and transducer design has possible applications in dermatology, intravascular imaging, ocular imaging, and invasive probe imaging. Despite the quality results it was also noted that a flexible piezo-composite material would be more adapt for high-frequency transducer manufacture given the reduced risk of micro-fractures during focusing.

2.1.1.5-

"A 120-MHz Ultrasound Probe for Tissue Imaging"

Koichi Yokosawa, Ryuichi Shinomura, Shyuzo Sano, Yukio Ito, Shizuo Ishikawa, and Yutaka Sato

Continuing on the idea of improving signal intensity for high frequency imaging is the use of needle based transducer probes. Clinical tests of $40MHz$ probes have shown lateral resolutions of $200\mu m$ while experimental in-vivo or in-vitro skin and eye tissue scans have been reported to see 11 micron lateral resolution [16]. One of the more successful reports on probe based scans is "A 120-MHz Ultrasound Probe for Tissue Imaging" written by Koichi Yokosawa, Ryuichi Shinomura, Shyuzo Sano, Yukio Ito, Shizuo Ishikawa, and Yutaka Sato [16]. In this paper a $120MHz$ transducer made from ZnO piezoelectric film on a sapphire substrate was fabricated. The functionality of this high frequency probe based transducer was demonstrated with images of in-vitro bovine kidney.

The transducer was approximately $550\mu m$ thick having a diameter of $1mm$. The piezoelectric material was a $12.5\mu m$ thick ZnO film with a $0.5mm$ thick sapphire substrate and silicon dioxide matching layer of $14\mu m$ thickness. The formed lens for focusing had a radius of $500\mu m$ with an F number, ratio of lens diameter to curvature radius, of one. This resulted in a transducer whose electrical impedance reached a minimum at $120MHz$, an

insertion loss of $-45dB$, a $-6dB$ bandwidth of $40MHz$, and a calculated lateral resolution of $13\mu m$.

The transducer was then mounted into a rod shaped probe of $3mm$ outer diameter. An imaging window was cut into a spacing tube which allowed for coupling gel to connect the transducer face with the tissue. This design positions the focal point $130\mu m$ into the tissue from the probe surface and allows for a cylindrical C-scan. It also allows for focal depth adjustment by changing the spacing tube thickness.

The received RF signal was high pass filtered and amplified before being digitized and time gated by a $500MHz$ sampling rate oscilloscope. Each pixel location was scanned four times and averaged to reduce noise, taking approximately 1.8 seconds for each position. Even though the transducer resolution was 13 microns the total system resolution was reduced to $26\mu m$ due to limitations with motion control; however axial resolution was maintained at $18\mu m$.

To confirm resolution numbers a thin copper sheet with $30\mu m$ square holes was imaged. The copper sheet was positioned in the focal zone of the transducer, having the assembly submerged in ultrasound conductivity gel. The resulting 450 x $340\mu m$ image showed good contrast between the copper and holes, clearly showing the structure. Also imaged were layers of onion. A 730 x $730\mu m$ scan revealed cell walls as small as 10 to $20\mu m$, confirming the estimated resolution values. All images were compared to optical microscope photographs for comparison.

To test the validity of their probe design for tissue imaging a sample of fresh bovine kidney was scanned. Before the probe was inserted into the sample it was coated with conductivity gel to fill the gap in the spacing tube window. The images were 70 x 99 pixels which translate to an 890 x $1280\mu m$ area with a time gated $15\mu m$ thickness ($20ns$ gate). Unlike the test samples of the copper sheet and onion layers, each pixel was the average of four scans and the gray scale was linearly converted to prevent the image from becoming indistinct. After scanning, the sample was cut into histologic sections and compared to the ultrasound images. Similar string-like structures found in the sample showed up in the ultrasound images, demonstrating the ability of the probe to image microstructures within tissue.

2.1.1.6-

"Finite Amplitude Distortion-Based Inhomogeneous Pulse Echo Ultrasonic Imaging"

Ted Christopher

Up until now increased system resolution was achieved by using higher frequency pulses and/or focusing the transducer beam. An alternative approach to improved image quality is to address the defocusing effects of inhomogeneities within the propagation medium. This phenomenon is responsible for widening of the main beam and increases in side-lobe amplitudes, resulting in lower resolution and weaker image contrast respectively. Ted Christopher has conducted a study of these effects and proposed a novel imaging scheme to form images using the finite amplitude distortion portions of the received waveforms. His efforts and results are reported in "Finite Amplitude Distortion-Based Inhomogeneous Pulse Echo Ultrasonic Imaging" [17]. This paper discusses the finite amplitude production of higher harmonics, requisite field amplitudes, and the associated governing mathematics for homogeneous and inhomogeneous propagation through a liver like medium.

The first models discussed were for a continuous wave source of homogeneous non-linear propagation. Linear propagation results for a $2MHz$ Gaussian transducer were compared to that of the models results for first and second harmonics. The source plane, on-axis, and focal plane beam profiles were presented along with comparisons between linear and non-linear outcomes. An interesting note from the results was that the non-linear waveform curve at the focal point was 1% lower than that of the linear curve. This difference in pulse energy at $2MHz$ was accounted for by the formation of higher harmonics. Comparison between the linear and non-linear propagation beam profiles showed little difference in shape between the two. The stated conclusion from this section was that the second harmonic profile of a focused apodized transducer could provide improved contrast resolution over the corresponding or same frequency transducer field at the expense of reduced lateral resolution.

The author then performed the same calculations for pulsed propagation of a $2MHz$ Gaussian source. It was found that the focal pulse waveform had marginally smaller peak pressures than the corresponding continuous wave case but was less distorted. Unlike the

continuous case, characteristics of the harmonic patterns were not displayed for the pulsed propagation but were described as being identical in both the radial and axial directions to those produced in the continuous propagation case.

After an extensive study of linear and non-linear wave propagation through homogeneous and inhomogeneous liver like medium it was clear that the two-way propagation profile of the second harmonic contained lower side lobe levels and a narrower main beam diameter compared to the fundamental beam from which it was created. This shows that significant improvements can be made to the contrast and lateral resolution of an imaging system through use of harmonic content to produce the image. Another resolution improving scheme was brought up which takes advantage of the fact that higher intensity waves produce harmonic energy at a faster rate. By replacing a single pulse scheme with one that sends a smaller amplitude pulse after the main its received echo will have relatively less harmonic content, and could then be used to remove the linear components of the main pulse. The advantage here is to eliminate lingering linear content present in the high-pass filtered signal which substantially reduces the axial contrast.

2.1.1.7-

"Estimation of Ultrasound Attenuation from Broadband Echo-Signals Using Bandpass Filtering"

Hyungsuk Kim, James A. Zagzebski, and Tomy Varghese

Another area in medical ultrasound is the characterization of various tissue parameters like backscatter and attenuation coefficients and frequency dependence. With better understandings of these phenomenons more accurate models can be developed, leading to improved systems and signal processing. An example of recent work in this area is Hyungsuk Kim, James A. Zagzebski, and Tomy Varghese's paper, "Estimation of Ultrasound Attenuation from Broadband Echo-Signals Using Bandpass Filtering" [18]. They describe their work in attenuation coefficient estimation through signal intensity comparisons between measured values of a known tissue and a sample.

Various methods for medium attenuation characterizing are split between either frequency or time domain analysis. In the frequency domain most methods use either a spectral shift or spectral difference measurement of the echo spectrum centroid [18]. The time domain methods include measurement of the RF echo signals zero density crossing and entropy differences between two adjacent segments of the RF echo signal [18]. Kim *et al*. uses a video signal analysis (VSA) method which uses the ratio of echo signal intensity between a sample medium with an unknown attenuation and a reference medium with known attenuation. Estimated attenuation coefficient versus imaging depth using the VSA method were obtained and presented using mathematical simulation and experimentally measured values.

The VSA method is based on a linear frequency dependence of the attenuation, like most methods using the pulse-echo signals. Other assumptions made are uniform backscatter, a constant propagation speed, and the Born approximation which ignores contributions from multiple scatterings. These assumptions define the RF signal in the frequency domain as the product of the pulse, diffraction, attenuation, and backscatter transfer functions. By taking the ratio of the frequency domain RF signal from a sample and that from a reference medium the transducer dependant terms, transmit pulse and diffraction, drop out leaving the attenuation and backscatter terms. To normalize the backscatter terms this ratio is computed for a frequency that yields the same backscatter and attenuation in the sample as the B-mode signal, leaving relative echogenicity as a function of depth and the difference in attenuation coefficients of the sample and reference medium.

To simulate this method the echo signals for both the reference and sample medias were calculated using an 80% bandwidth $5MHz$ Gaussian-shaped pulse and various attenuation coefficient values. The sample and reference phantoms were simulated by assuming a random distribution of glass beads in a medium having a wave propagation speed of $1540m/s$ and a bead density of 9.7 per cubic millimeter. With a $25\mu m$ bead diameter Rayleigh statistics criterion were satisfied. The simulated echo signal envelopes were computed by first taking the inverse Fourier transform of calculated backscatter, leaving the real part of the echo signal. To find the envelope the imaginary part is also required, being calculated from the real part by the Hilbert transform. Plots of the relative echogenicity on a log scale versus depth for various pulse bandwidths were presented. It was found that the

higher bandwidth pulses deviate from a straight line due to varying frequency dependant attenuation in the reference and sample.

Since many ultrasound systems use pulse widths greater than 60%, improved results were sought using band pass filtering. A $5MHz$ center frequency pulse was used for simulation and band pass filters were applied to the resulting signal for VSA. The filters used had center frequencies at 3, 4, 5, 6 and $7MHz$ with a bandwidth of $1MHz$. The results showed that filtered signals at or below the center frequency of the transmitted pulse provide the best results for attenuation estimation. It was found that the higher center frequency filters produce estimations below the actual attenuation value of the sample medium. It was also found that the VSA method using filtering produces underestimates of the attenuation coefficient when the reference medium has a lower attenuation than the sample. Conversely, when the reference medium has a higher attenuation than the medium the VSA method produces overestimated values for the sample attenuation coefficient.

After simulating the results of the VSA method an experiment was performed to confirm these findings. Two phantoms were used, one with an attenuation coefficient of $0.5dB/cm/MHz$ and another with $0.7dB/cm/MHz$. The lower attenuating medium was taken as the reference. These two medias were scanned using a Siemens Antares ultrasound system with a linear array transducer (VFX 9-5) having a center frequency of $5MHz$ and a bandwidth of 80%. Like the simulations the VSA method was applied to the broadband signal and to various narrow bandwidth filtered signals. The results showed similar findings to the simulation tests. The VSA method applied to the broadband signal estimated attenuation below the actual values where as those found using VSA applied to narrow bandwidth filtered signals showed accurate attenuation values independent of depth.

The conclusion of the paper stated that the use of VSA and narrowband filtering provides unbiased attenuation estimates comparably to other existing estimation methods while remaining computationally efficient. It was also concluded that improved results are obtained with smaller attenuation differences between the reference and sample medium. Additionally, signals from lower frequency filters contain more useful information from the backscattered echo signal since higher frequencies attenuate faster.

2.1.2-NDE

Moving away from medical applications of ultrasound, brings forward acoustic imaging for internal defect detection. This modality of ultrasound is becoming more prevalent in quality control as the available systems become more sophisticated. This form of ultrasound has found applications in the electronics, automotive, aerospace, and thin films manufacturing industries. Being able to test products or raw material without destroying the specimen is very desirable and cost effective, especially in costly materials.

Unlike medical applications where almost all propagation medias are tissue, ultrasonic non-destructive evaluation (NDE) deals mostly with solid medias. The primary difference between the two is the presence of many different wave types in solids. Most liquids can only support longitudinal waves where as solids support many, including surface, shear, and transverse waves in addition to longitudinal. Various benefits and hindrances come with this spectrum of wave types. The following will present various papers on ultrasonic NDE, giving examples of different applications in this field of ultrasound.

2.1.2.1-

"Acoustic Images Reveal Flaws"

Tom Adams

A good overview of ultrasonic NDE in electronic applications is Tom Adams's article "Acoustic Images Reveal Flaws" [19]. Adams describes the basic theory behind acoustic imaging of various electronic devices. He outlines how acoustic imaging can identify defects in complex ceramic and flip chips.

It is stated that the three most frequent internal defects of electronic elements are cracks, delamination, and voids, all containing a gas. The first example given is of a ceramic chip capacitor with an internal void that shows up clearly on a scanned image. Given the high acoustic impedance difference between the solid and gas this void provides a large contrast between the well adhered surface and the gap. Additionally, the chip was sectioned and imaged optically to verify the findings of the acoustic scan.

A more complex example was discussed where the use of time gating the received signal was used to evaluate various sections of a multi layer device. The presented images were produced from an acoustic scan of a multi-layer device with the A-line signal time gated to encompass the mating surface between the die attach material and the silicon chip. From the resulting image a clear delamination is discovered. Although the delamination is wide it is very thin. A cross-section optical image barely detects the gap. It is common for these acoustic NDE systems to be able to detect defects as thin as $0.01\mu m$. Due to the high reflection coefficients of these gaps almost all of the pulse energy is reflected back to the transducer, producing large echo signals for the first defect inline but leaving very little energy for the next deeper defect. The result is an acoustic shadow hiding other flaws below.

To end with the paper discusses the use of acoustic NDE for "acoustically guided destructive physical analysis (DPA)". The idea here is that the images produced using ultrasound will not only reveal information about a defect but will determine the depth and location to section a specimen to be analyzed further. The example given is of a flip chip whose silicon chip is connected to a substrate by small solider bumps measure in microns. It is common for cracks to form in the bump itself or between the bump and chip or between the bump and substrate. The acoustic image will not only distinguish good and bad solider connections but will reveal where the cracks have formed relative to the bump. The vertical plane to section the flip chip was located exactly through the use of DPA, saving valuable resources that would have been spent trying to find the defects.

2.1.2.2-

"Acoustic Micro Imaging of Cracks"

Ray Thomas

Another article written by Ray Thomas is similar to the article just discussed by Tom Adams. The article by Thomas, "Acoustic Micro Imaging of Cracks" [20], is another light over view of acoustic NDE. Thomas adds to Adams discussion with examples of displaying scanned solids in three dimensions and use of surface waves to evaluate surface defects.

The article discusses the application of surface waves in flaw detection by first describing how they are produced. It was stated that surface waves result when the pulse of the transducer impinges the surface of the material at an angle, converting the longitudinal waves to surface waves. This is common for transducers with small F numbers (focal distance over aperture diameter). Theses surface waves will travel sideways along the surface of the material, with a penetration depth of around one wavelength. If no defect is encountered by these waves the pulse will be picked up by the transducer some time later. Conversely, if the pulse encounters a defect within this depth range the pulse will be reflected and only a small pulse if any will be detected by the transducer. With this in mind an image of the surface can be produced showing the location of surface flaws on the material being imaged.

2.1.2.3-

"Acoustic Microscopy of Internal Structure of Resistance Spot Welds"

A. M. Chertov, Roman Gr. Maev, and F. M. Severin

An application that lends itself very well to acoustic NDE is the evaluation of resistance spot welds. This form of welding is used predominantly in automotive manufacture for its relatively cheap and reliable process. Even so, quality control requires inspections of these welds for strength verification and repeatability. A. M. Chertov, Roman Gr. Maev, and F. M. Severin have authored "Acoustic Microscopy of Internal Structure of Resistance Spot Welds" [21], an article detailing the methods and capabilities of scanning acoustic microscopy (S.A.M.) for the evaluation of internal structure of resistance spot welds. The article first describes the process of resistance spot welds then details the nature of applying S.A.M. in the following categories, data collection, experimental results, anisotropy, and non-linear effects.

In the section on resistance spot welds a brief overview of the process is presented with various facts. It is stated that the metal sheets to be welded are squeezed between two electrodes with a force ranging from 500 to 1500 pounds. To weld the sheets an electric current of approximately 5 to $15kA$ is sent through the electrodes for around 100 to $500ms$.

The contact resistance between the sheets allows conversion of the electrical energy into thermal energy, melting and merging the two sheets. This process leaves thermal stresses in the material which are generally relived through material plasticity but for brittle materials the cooling process tears the weld nugget from the base material, forming micro cracks. These cracks reduce the integrity of the weld, ultimately reducing the effective size and strength of the weld.

The standard testing practice of weld size and strength has been the destructive peel test. This test uses the force required to tear the weld apart to back out the size of the weld. Despite its simplicity this test has many drawbacks, for one the joint is destroyed. It is common for the weld nugget to break along micro cracks which act as stress risers, reducing the force required to tear the joint apart, reducing the calculated weld size. This problem is amplified for brittle materials.

In the next section the article describes the systems used to apply SAM to various spot welds. Two models were used, a Sonix HS1000 and a Tessonics AM1103. The HS1000 is a high speed high resolution scanner designed to inspect JEDEC trays, strips, and individual parts. It is capable of a 10 to $260MHz$ transducer operating range with $1\mu m$ spatial translation resolution.

While the HS1000 is a large machine the AM1103 is a desktop design intended for individual sample scanning with three dimensional analyses. The scanner can image a volume as large as 100 x 150 x $50mm$ compared to the HS1000's 381 x $305mm$ scan area. Additionally the AM1103 has a transducer operating range of 5 to $200MHz$ with spatial repeatability of $2\mu m$ laterally and $0.2\mu m$ vertically. It is uncommon for a system to support multiple scanning modes like the AM1103, but the ability to save the entire volume data on the desktop allows post processing with separate software to be as intensive as necessary.

Before B and C-scan images are analyzed wave mode conversion and its effects on the resulting images are discussed. As previously stated solids can support a number of wave types other than longitudinal. It is common for a mode conversion to take place at an interface. The examples discussed in this article show such a conversion on the metal to metal interface where some longitudinal waves are converted to shear waves. The result is a pulse in the A-line data that does not correlate to any defect in the specimen. Given the slower propagation speed of shear waves their echo or reflection from the same surface will

arrive at the transducer delayed, appearing to be from a deeper reflector. The amount of mode conversion is dependent on the material and incident angle of the pulse.

The objective of acoustically scanning the spot welds is to determine the welds physical size and to discover any cracks or internal defects within or around the weld. The article presents a number of B and C-scan images that are then described and analyzed. To interpret the resulting images it must be understood that a good weld will not reflect the transmitted pulse. The effect is a B-scan image showing interfaces for the top and bottom plates and for the metal to metal interface except for the weld location. A C-scan image will appear dark where the weld is good. These scans are then used to compare the weld bead size, defined as the average of the largest vertical and horizontal measurements, to that obtained by a peel test. The systems used are able to scan at 1-5 micron steps but $100\mu m$ steps are adequate to measure bead diameters.

To compare the bead diameter estimate accuracy between a peel test and SAM multiple samples were tested. The samples consisted of 2, 4, and $6mm$ diameter beads in $1.2mm$ thick mild galvanneal steel. It was found that the smaller bead sizes resulted in larger relative error, defined as the difference in measured values over the SAM measurement, but rarely exceeded $0.25mm$. The two methods agree within a 10% error and a mean of around 4% overestimate for SAM.

A common problem with the peel test is that without extensive post analysis defects like stick welds cause huge errors in bead size estimates. With SAM the nature and condition of a weld can be studied without costly procedures. Stick welds occur when the material temperature did not reach the desired level to ensure a thorough merging. The result is a bead that is weakly welded on its perimeter, leaving a metal to metal interface in the center. This interface will be well defined in an acoustic scan but visual inspection reveals a solid weld. The properties of this half merged volume allow for alternative imaging methods that help in their identification. The final discussions in the article talk about anisotropy of spot welds and the non-linear effects on the ultrasound pulse.

Stick welds are common in zinc coated plates given the intensive melting and spreading of zinc during the welding process. The result is a ring of material around the weld that has a random crystalline microstructure. This ring provides a relatively inhomogeneous material for the ultrasound pulse to propagate through, the production of higher harmonic

energy results. SAM systems can use this to their advantage by filtering the fundamental frequency and listen for these harmonics. Since these higher frequencies are a result of inhomogeneous material, the ring of poor weld will show up highlighted in the C-scan. The experiments in the article state that the second harmonic amplitudes in those regions reached as much as ten times that of the surrounding areas.

The conclusion of the article stated that scanning acoustic microscopy provides superior diagnostic capabilities over destructive forms of weld quantification but yields similar results for actual bead size estimates. Application of SAM for resistance spot weld inspection is a reliable and effective means of weld examination and quality control.

2.1.2.4-

"Application of pulse acoustic microscopy technique for 3D imaging bulk microstructure of carbon fiber-reinforced composites"

Songping Liu, Enming Guo, V.M. Levin, Feifei Liu, Yu.S. Petronyuk, and Qianlin Zhang

Given the inhomogeneous nature of carbon fiber composites, the application of ultrasound imaging for microstructure characterization is a complex task. This challenge was attempted by Songping Liu, Enming Guo, V.M. Levin, Feifei Liu, Yu.S. Petronyuk, and Qianlin Zhang, documented in their article "Application of pulse acoustic microscopy technique for 3D imaging bulk microstructure of carbon fiber-reinforced composites" [22]. Their attempt was to use acoustic microscopy to characterize and image carbon fiber-reinforced composites (CFRC) as an alternative to the traditional destructive methods currently in use. These would include optical, electron, and atomic force microscopy. The problem with these techniques, besides being destructive to the sample, is that only surface information can be extracted and any information about mechanical properties is left wanting. Conversely, acoustic microscopy data has a direct relation to the materials elastic properties.

These properties can be extracted through knowledge of sonic velocity, scattering, and time-resolved echoes. With all these benefits of acoustic imaging for CFRC there is a compromise, penetration depth. Given the very inhomogeneous makeup of CFRC's

ultrasound pulses attenuate quickly, allowing for only shallow subsurface imaging. The penetration depth can be optimized with careful selection of operating frequency and focusing or if appropriate a probe type system can be used.

The 3D acoustic imaging system employed here uses a low aperture transducer operating at $50MHz$. The focal distance is $27mm$ in water with a focal zone of $3mm$. The ultrasound beam provides an approximate $60\mu m$ lateral resolution while the pulse duration of 20 to $40ns$ translates to an approximate $80\mu m$ temporal resolution. Given this short pulse duration the 120 to $150\mu m$ thick structural layers of the CFRC can be resolved.

Both B-scan and C-scan methods were used to image the CFRC samples. Successive C-scans were time gated based on boundary reflections that correspond to the different layers that make up the composite. The compilation of these scans would constitute a T-scan. When combined with multiple B-scans cross-sectional images of the bulk microstructure were available for multiple directions.

The CFRC for this test is constructed of 16 plies and one inter-laminar adhesive film. The ply orientations are organized in a $-45/45/0$ degree relation with the adhesive layer in the middle for a total thickness of $2.14mm$. A B-scan image of the samples cross-section was first to be discussed. The top and bottom surfaces were easily identified as well as 7 ply-ply interfaces and numerous defects. The lower ply-ply interfaces were clearly defined but those located closer to the top surface, being out of the focal zone, were blurred. Flaws in the adhesive layer produced large bright spots in the B-scan image. Given the high reflection of these flaws acoustic shadows are seen on the lower surface of the sample. The B-scan results were then cross checked against the findings of the T-scan.

The CFRC sample was broken into 90 to $100ns$ time gated segments which translate to approximately $0.1mm$ thick layers, the objective being to obtain cross-sectional images of each layer in the stack. These scans were able to reveal the ply's orientation with a clear grain direction in the image. Given that the plies are not always parallel it is difficult to get an image of just one layer. The effect is multiple visible grain directions in one time gated segment given the presence of adjacent plies. The C-scan image contrast of the fiber-bundle directions was found to be directly related to the fiber uniformity and density, the more non-uniform the fiber the greater the image contrast. Similarly, the echo signals from the inter-ply interfaces would weaken and blur with increasing fiber tightness.

In addition to the plies fiber orientation, the C-scan images revealed flaws within the sample. In the upper layers of the stack random white lines appeared in the C-scan images. They are believed to be natural defects in the composite material. These flaws show up as white lines in the time gates that correspond to their ply location but are also visible in the succeeding layers as dark shadows. The lower layers were not free of flaws, a lot of small strong reflectors, small voids in the adhesive film showed up in the C-scans as well. Results from the B and C-scans where confirmed by optical images of these defects.

Stated conclusion of the article: Given the data collected and the confirmation of results by optical imaging it is concluded that acoustic microscopy of CFRC materials is possible. Plies, fiber bundles, and micro flaws as reflectors provide the contrast needed to construct microstructure images of CFRC laminates. This imaging technique provides a promising alternative for microstructure imaging and defect detection of different types of fiber packing.

2.1.2.5-

"Detection and Localization of Subsurface Defects in DLC Films by Acoustic Microscopy"

Pave1 V. Zinin, Sofia Berezina, Dong Fei, Douglas A. Rebinsky, Robert M. Lemor, Eike C. Weiss, Caron Arnoud, Walter Arnold, and Bernd Koehler

The final article to be discussed deals with ultra high frequency scanning of protective films. Pave1 V. Zinin, Sofia Berezina, Dong Fei, Douglas A. Rebinsky, Robert M. Lemor, Eike C. Weiss, Caron Arnoud, Walter Arnold, and Bernd Koehler collaborated in the investigation of subsurface defects in diamond-like carbon (DLC) films using GHz acoustic scanning. The resulting paper was "Detection and Localization of Subsurface Defects in DLC Films by Acoustic Microscopy" [23].

SAM operating at 0.2 to $1.3GHz$ was used to image wear resistant coatings of chromium containing DLC films. These films provide significant wear and abrasion resistance for coated parts without changing the bulk mechanical properties. With the increasing performance of today's products the demand for these protective films follows. Interest in imaging these films steams from the relation between their wear resistance

performance and the condition of their microstructure, most importantly defect density, size, and location. Even in the GHz frequency range the 2 to $3\mu m$ thickness of the film is comparable to the pulse wavelength, making echo signal interpretation difficult. To assist in this interpretation a multitude of imaging modalities was used. On top of SAM, atomic force microscopy, focused ion beam, surface Brillouin spectroscopy, and optical microscopy were used.

For acoustic waves operating in the GHz range for films as thin as $1\mu m$ the primary contributor to image contrast are Rayleigh surface waves. These waves penetrate the material deeper than the respective longitudinal and shear waves. At the time of this research a detailed analysis of image formation for micron sized defects under these conditions had not been documented. The authors used a recently developed theory for three dimensional imaging [24] to facilitate the image processing necessary to extract meaningful results.

The article discusses the use of simulations to develop the ideal imaging technique, concluding that defocused transverse to transverse waves produce the greatest echo contrast. What this means is that transverse waves scattered by a cavity or defect as a transverse wave will produce the largest received echo signal compared to any other form of pulse wave mode conversion.

The result of scanning a 240 x $240\mu m$ area of the DLC film was a surface image with better contrast than the comparative optical microscope image. The various defects and cavities of the film were much more visible and defined in the acoustic image than the optical image. A careful comparison between the two showed that 90% of the defects found in the acoustic image were present in the optical image.

The effect of defocus distance on the resulting image was tested. It was found that for positions on focus and below the surface the defects became brighter and wider. In combination with the fact that anomalies smaller than the pulse wavelength should not be detected unless they are gas bubbles, researchers concluded that the defects were most likely subsurface cavities. The operating frequency was also varied to test its effect. When the pulse frequency was dropped from $1GHz$ to $0.2GHz$ an increase in defect size and number was observed, adding to the idea that they are subsurface voids.

A flaw detected by both acoustic imaging and optical imaging was a $200nm$ high bump on the surface. Acoustic microscopes cannot detect such an anomaly give the feature

size is much less than the wavelength of the pulse. The only logical reason for this acoustic detection was if this bump was a subsurface bubble formed during the deposition process. To confirm this hypothesis, an ion sputtering process was used to mill the bump down. It was found that a small void did exist under the bump, confirming the original hypothesis.

The article was wrapped up with a list of three conclusions reached at the completion of their experiments and analysis. One, S.A.M. operating at $1GHz$ can detect subsurface defects in films as thin as $3\mu m$. Two, S.A.M. provides superior image contrast than optical microscopes for these DLC film coatings. Third, the increased defect contrast at the lower operating frequency of $0.2GHz$ suggests that there are a lot of subsurface scatterers in the coating.

2.1.3-Paper Saturation

In an extensive search for papers that discuss the application of ultrasound to gas diffusion layers no such research was found. Although this leaves an opening for new and innovative research it also means there is no solid foundation to advance upon. The closest match to GDL saturation studies with ultrasound is its use for saturation characterization of paper. With ultrasound being the obvious link between the two, the fact that paper is quite similar to a GDL makes this connection very solid. Both having fibrous microstructures, various levels of hydrophobicity, and comparably sized features.

The following will discuss the various techniques used to characterize papers wettability, thickness, surface roughness, and water content.

2.1.3.1-

"Measurement of Paper-wetting Processes by Ultrasound Transmission"

Jyrki Stor-Pellinen, Edward Hæggstrom, and Mauri Luukkala

The first paper to be discussed is by Jyrki Stor-Pellinen, Edward Hæggstrom, and Mauri Luukkala from the physics department of the University of Helsinki in Finland. Their

paper, “Measurement of Paper-wetting Processes by Ultrasound Transmission”, was published in 2000 in Measurement Science and Technology [25]. The objective was to capture transient wetting characteristics for various sizing content and water/isopropanol ratios. This was accomplished by correlating transient acoustic transmission amplitudes to different wetting modalities.

Their setup used a stationary transmit/receive water bath that used a $12.5mm$ diameter transducer capable of 0.5 *to* $14MHz$ monochromatic continuous signals. The paper samples where affixed to either a metal frame, allowing contact with the wetting fluid on both sides, or a polystyrene frame which only allowed wetting of one side. These frames where used to control the samples descent into the water bath at a controlled rate, approximately $0.47m/s$, for consistent submersion time. An optical trigger sampled at $1kHz$ was used to initiate acoustic sampling upon full insertion. Each specimen was sampled at $600Hz$ for a duration 4000 samples. It was stated that the measurement system had an estimated 3% error derived experimentally.

Their conclusions were based on three factors that affect the transmission coefficient for the samples, acoustic impedance, surface roughness, and microstructure stiffness. All three affect the ultrasonic propagation and all three are varied by saturation levels of the samples.

Acoustic impedance is dependent on the materials propagation speed and density and determines the ratio of reflected to transmitted energy across a mismatch boundary. The authors define the transmission and reflection coefficients from the following assuming orthogonal incident to the boundary and no vibrational mode conversion.

$$A_2 = T_2 A_1 \qquad A_1 = T_1 A_0 \tag{2.1-1}$$

$$A_2 * T_1 A_0 = (1 - R_1)^2 A_0 \tag{2.1-2}$$

$$\frac{A_2}{A_0} = \left(\frac{2Z_2}{Z_1 + Z_1}\right)^2 \qquad Z_2 < Z_1 \tag{2.1-3}$$

$$\frac{A_2}{A_0} = \left(\frac{2Z_1}{Z_1 + Z_1}\right)^2 \qquad Z_2 > Z_1 \tag{2.1-4}$$

Where T is the transmission coefficient, R is the reflection coefficient, and A_0, A_1, and A_2 are the incident amplitude, first boundary transmission, and second boundary transmission amplitudes respectively. Considering that the impedance of water is approximately $1.5MRayl$ and the paper samples can have impedances that range from 0.0005 to $2.6MRayl$ the change in transmitted amplitude was found to change significantly.

The second cause of attenuation is the surface roughness which is defined by the vertical standard variation in the sample thickness per unit area. The irregularities on the surface which are on the order of the acoustic wave length cause diffusive backscatter, dispersing the wave energy in directions other than through the sample. During the wetting process it is expected that the individual fibers will absorb water, inducing swelling and altering the roughness of the samples surface. The authors model this as a simple additional term to the reflection coefficient.

$$\frac{A_2(\lambda, R_q)}{A_0} = exp\left[-\left(\frac{4\pi R_q}{\lambda}\right)^2\right] \tag{2.1-5}$$

Where λ is the acoustic wave length and R_q is the surface roughness. To illustrate the effects of surface roughness on the transmission amplitude for two different frequencies, 0.5 and $10MHz$, with a roughness range of 10 to $50\mu m$.

The third cause of signal attenuations are the effects of microstructure stiffness on the propagating wave. Unlike the previous two phenomena which define the amount of energy passing through the surfaces of the paper, this defines the attenuation within the sample in terms of energy absorption. It is typical to model the attenuation of an acoustic pulse with and exponential decay. The authors relate the attenuation coefficient to the wave frequency f, effective sample viscosity η, its density ρ, and the effective bulk modulus K.

$$\alpha = \frac{8\pi^2 f^2 \eta}{3\rho c^3} = \frac{8\pi^2 f^2 \eta\sqrt{\rho}}{3K^{1.5}} \tag{2.1-6}$$

$$\frac{A_1}{A_0} = exp(-\alpha z) \qquad (2.1\text{-}7)$$

The justification being that when the sample becomes overly saturated the bounds holding the individual fibers together break down, weakening the structure and leaving fibers floating in a solution. The beginning of the process where the structure is weakening and reducing its stiffness the attenuation rate increases until the trend reverses and starts to decrease. This inversion point signifies the transition from intact microstructure to a continuous liquid solution with fibers suspended throughout.

The authors also discuss the effects of acoustic frequency on backscatter for different size objects. Depending on the relation between the ultrasonic wave length and the scattering objects size the backscatter and attenuation characteristics change. When comparing the scatter size range to the practical wave length range it is apparent that ka values from much greater than one to much less than one can be achieved. For example, large air pockets of a few millimeters being insonifed by an acoustic pulse with a wavelength of a few hundred microns will exhibit specular reflections. Conversely the fibers of the sample having diameters of a few microns can be insonified by an acoustic pulse having a wavelength of a few millimeters, follows a Rayleigh scattering pattern with interference losses. The point is that the dominant attenuating feature is dependent on the wavelength of the acoustic pulse so the object size of interest to be observed can be selected by the ultrasonic frequency.

The authors tested paper samples that varied only in their sizing content which affects the surface energy. The contact angles for testing where 40°, 70°, and 110°. The saturating liquid was also varied by its concentration of isopropanol. The ratios of water to isopropanol tested were 0%, 10%, 25%, 50%, 80%, and 100%. The isopropanol in contrast to water does not saturate the individual fibers and does not break the interfiber bounds.

For each test four values were noted, coefficient of inclination, coefficient of declination, and the instant and amplitude of peak transmission. The transient response of the transmission amplitude was plotted versus the immersion time. The coefficient of inclination is defined as the slope of the initial increase in transmission where as the declination coefficient is the slope of the curve after the peak transmission instant.

The samples were also tested at various ultrasonic frequencies. The results for identical wetting schemes and samples were compared at different frequencies. Since the only difference is the insonifying wavelength the variations in the transmission trends can be attributed to the various frequencies sensitivity to different wetting aspects. Transmission trends for $1MHz$ and $4MHz$ waves through a sample with $110°$ contact angle were presented.

It was found that the range of frequencies used provided ample variation in the ka number to identify different wetting processes on a range of spatial resolutions. The fastest wetting process was stated to be capillary wetting where air within the paper was displaced by the wetting fluid, driven by capillary forces. The authors report that this wetting process was detectable at only the highest frequencies, above $8MHz$.

The second wetting process describes the diffusion of the wetting fluid into the fibers. This diffusion process breaks down the molecular bonds in the fibers and also contributes to degradation of the interfiber bounds. This process was identified at approximately $120ms$ after insertion where the attenuation of the signal began to increase after the initial decrease. This trend was most prominent with high concentrations of isopropanol, 4 *to* $9MHz$ frequencies, and papers with high contact angles.

The objective of the paper was to prove that their method can identify different wetting processes and provide distinct differences between paper samples. The supplied graphs show these differences but the explanations as to their trends were left invalidated. Furthermore it was stated that the measured values had an experimentally derived 3% error associated with them but no mention as to the repeatability of the individual tests. The paper did however provide insight into the temporal response of paper wetting and its effects on the transmitted wave.

2.1.3.2-

"The Use of Air-Coupled Ultrasound to Test Paper"

Craig S. McIntyre, David A. Hutchins, Duncan R. Billson, and Jyrki Stor-Pellinen

In 2001 a group of researchers published a paper titled "The Use of Air-Coupled Ultrasound to Test Paper" in IEEE Transaction on Ultrasonics, Ferroelectrics, and Frequency Control [26]. The work was similar to the previous paper in that characteristics of the sample were correlated to an acoustic measurement for comparison but the experimental methods are quite different.

To accomplish this task the authors devised a setup which utilizes two high-frequency, broadband, air-coupled capacitance transducers, one acting as the transmitter and the other as the receiver. For their experiments the samples were placed equidistant between the transducers which were separated by $90mm$. For each sample to be tested an acoustic pulse is sent at normal incident to the sample where the transmitted pulse is received on the other side. Each result was the average of a 1000 transmit/receive operations, reducing the noise in the signal and showing good reproducibility. In addition, three samples were cut from each sheet of paper and tested individually.

The first series of experiments where to identify the through thickness resonant frequency for various samples and determine if there is a correlation between any of the papers characteristics. This resonant frequency is defined as the frequency of greatest magnitude in the response of the transmitted pulse when normalized by a reference spectrum. This reference spectrum is obtained by taking a sample response with no paper between the transducers. The benefit is that the systems spectral response is divided out, highlighting the modification of the pulse due the presence of a paper sample.

The significance of this resonant frequency can be seen in the following equation.

$$f_{resonant} = \frac{V_1}{\lambda} = \frac{V_1}{2d} \qquad (2.1\text{-}8)$$

Where λ is the wavelength for the resonant frequency, V_1 is the phase velocity of the pulse through the paper, and d is the thickness of the paper. The authors put forth an equation for this phase velocity which was derived in [27].

$$V_1 = \sqrt{\frac{E_1}{\rho(1 - \nu_{12}\nu_{21})}} \qquad (2.1\text{-}9)$$

Where ρ is the density of the paper, E_1 is the Young's modulus of the paper in the machine direction, and ν_{12} and ν_{21} are the Poisson ratios of the paper in the directions parallel and perpendicular to the machine direction respectively.

The significance of this equation is that the phase velocity through the paper is dependent on its stiffness. Any modification to the paper which alters it elasticity will change the resonant frequency. And as one might expect the thickness of the paper, d, is also a primary variable in the determination of resonant frequency.

To validate their setup, the first test was to identify the resonant frequency of two paper samples, identical except in their thickness, 278 and $226\mu m$.

The paper provided plots of the acoustic response from both samples along with their spectral content. The reduced pulse amplitude and reduced resonant frequency for the thicker paper was noted. This is to be expected as the thicker paper allows for increased attenuation given the greater propagation distance and the half wavelength definition for resonance requires a lower frequency to fit in the thicker paper.

The next series of test that were performed had been designed to capture the effect matrix stiffness has on resonant frequency in terms of two paper quality parameters, V_p and H_p, and glue content.

V_p and H_p are standardized parameters used to quantify the water penetration time for either side of a paper. The significance of these wetting parameters is that the matrix characteristics of paper will alter the capillary and diffusive transport properties as well as the stiffness of the structure. A correlation between these parameters and the resonant frequency is expected. As for glue, the addition of an adhesive will also alter the stiffness of the paper matrix and again a correlation with resonant frequency is expected.

The results show a strong correlation for both parameters. It was found that the wetting parameter H_p had an inverse relation to the resonant frequency with the data having an R^2 value of 0.8505 for a best-fit straight line. The relation between glue content and resonant frequency had an even stronger fit with an R^2value of 0.8969.

The next section of the paper deals with a topic more closely related to this thesis, paper moisture content. The water content of paper has a large effect on its mechanical properties. Its properties determine the feed rate and other physical parameters used to design printers, presses, and any other products which use paper. When water is introduced to paper the fibers that make up its structure absorbs the water and expands in size. This affects the surface roughness of the paper and the individual fibers mechanical strength. In addition the bonds that connect the fibers to each other are weakened and break, reducing the stiffness of the paper. This change in material property will alter its response to an acoustic wave.

To test this, the authors took paper samples and sprayed water on to its surface. From their periodic acoustic measurements were taken in the same fashion as the previous tests while the paper dried. To quantify the saturation level of the paper its weight was measured for each acoustic reading and compared to a dry reference weight. The water content was reported in grams of water per unit area. The balance used to measure the mass was reported to have a $10\mu g$ accuracy but the size of the wetted area was not reported nor was an estimate on the accuracy of the water content measurements. In addition, the transducer sizes were neglected, leaving to speculation the insonified area.

From the data collected it was clear that the added water increased the attenuation of the signal. The authors state that this is due in part to the increased surface roughness and acoustic impedance mismatch with air. Increasing the surface roughness produced more diffuse scattering at the paper surfaces, reducing the amount of energy transmitted through the sample. While the pulse propagates within the sample, the reduction in matrix stiffness will increase the papers acoustic attenuation, further reducing the amplitude. Additionally, the increased acoustic impedance due to the addition of water resulted in more reflected energy at the surfaces, again, reducing the transmitted energy.

The analyses of the results were well founded but the authors failed to address the peak in received amplitude around 5% water content. It was not mentioned as to whether this trend was typical for other samples but it does merit speculation as to its cause. From what

was presented, conjecture as the reason for this peak is difficult given the complex nature of elastic wave propagation in a fibrous matrix. However it seems likely that an optimal combination of impedance mismatch, low acoustic attenuation in water, and matrix stiffness was reached.

As for the frequency content of the received signal, a significant drop in resonant frequency was noted for increasing water content. This is also attributed to the samples reduced matrix stiffness. Upon review of the change in acoustic pulses with water content it was apparent that the resonant frequency diminished in both amplitude and value. The received pulses for high water content values showed similar shapes to that of the reference pulse but with reduced peak-to-peak amplitude, showing no resonance. As the paper sample dried the resonance reappeared in the received signals. The authors justify this disappearance in acoustic resonance by pointing to the limited bandwidth of the system. The wetted paper resonance frequency was simply lower than the detectible response of the system.

The final experiments performed where to acquire C-scan images of paper and cardboard samples. From the previous tests it's clear that their ultrasonic air-coupled techniques can identify various parameters of the paper. To implement this for image generation, the two transducers where affixed to a motorized stage with two degrees of freedom, allowing for samples to be acquired at various locations on the paper.

A drop of water was placed on a sample paper and then scanned. The result was a 40 by $40mm$ grayscale image whose pixel values correspond to the received pulse peak-to-peak amplitude. The presented image clearly shows a region of low acoustic transmission in the shape of a circle, as would be expected from the previous results and the description of the setup.

In addition to the paper sample being scanned, a cardboard sample was as well. The objective of this test was to demonstrate the ability of the system to detect delaminations in the cardboard. The theory states that when a layer of the cardboard is disassociated from the other layers the overall structure is weakened, reducing the stiffness in that region and reducing the resonant frequency. More definitively is the effect on the transmitted amplitude. In the region of delamination the acoustic pulse will be severely attenuated given the breakup in the acoustic path. This was illustrated by presenting two plots of the through-thickness

pulses, one for no delamination and the other through a delaminated region. They clearly showed a reduced transmission through the intact cardboard section.

To test the imaging technique for delaminations the sample cardboard was cut open and a layer was delaminated at which point the sample was glued together and scanned. The presented image shows two clear semi-circular regions opposite from each other that would indicate the delaminated sections. The line between the two is where the sample was cut and glue back together.

The authors put forth a solid defense as to the applicability of their non-contact air-coupled acoustic transmission technique for identifying both mechanical parameters of the paper and variations in water content. The significance of this research is for commercial applications where such knowledge of the paper is desired but coupling fluids or contact with the material is restricted.

2.2-PEMFC Water Distribution Imaging

The next section in the literature review switches gears from ultrasonic applications to PEM fuel cell water management studies. The following papers will be discussing the recent developments in neutron radiography and x-ray scanning techniques for quantifying water content and distribution within the fuel cell.

2.2.1-Neutron Radiography

2.2.1.1-

"Quantification of Liquid Water Accumulation and Distribution in a Polymer Electrolyte Fuel Cell Using Neutron Imaging"

A. Turhan, K. Heller, J.S. Brenizer, and M.M. Mench

A group of researchers from Pennsylvania state university released a paper in 2006, "Quantification of Liquid Water Accumulation and Distribution in a Polymer Electrolyte Fuel Cell Using Neutron Imaging" [28]. The topic, as the title suggests, is the application of

neutron radiography to characterize the water distribution and quantity for given operating conditions. Improper management of water within the cell can lead to membrane dehydration, flooding, and other parasitic losses that affect the overall performance of the cell.

The cell to be tested had an active area of $14.5cm^2$ with a $200\mu m$, 75% porous media GDL and a $40\mu m$ thick Nafion® membrane. The flow fields consisted of $1mm$ wide by $0.5mm$ tall channels which run parallel with their cathode or anode side counterpart. The test conditions for the cell where varied by three parameters, inlet relative humidity, cell pressure, and gas flow rate. For each steady-state cell condition 60 neutron images where acquired at a rate of $5fps$ and averaged together to reduce noise and pixel variations.

The neutron imaging setup is rated at $30fps$ temporal resolution and $129\mu m$ spatial resolution. The images are loaded into in-house developed processing software which performs image enhancement techniques and assigns water thickness values to the corresponding pixel luminance. This correlation between water thickness and pixel luminance was calibrated using an aluminum wedge filled with water. For any scanned location of the wedge both water thickness and transmitted neutron intensity where known, thus producing a correlation table. The calibration tests did reveal a minimum $10\mu m$ water thickness which can be detected by the system.

The first set of tests were performed to investigate the effect that gas flow rate has on the water distribution within the cell. Out of the 23 different test conditions performed this section deals with three to illustrate the effect. Two fully humidified conditions, one with low flow rate, condition 2, and other with a high gas flow rate, condition 4. The third used dry inlet gases at a high flow rate, condition 8. All tests were run at constant current density, $0.35Acm^{-2}$.

The resulting images showed that increased flow rate reduced the amount of water within the cell. It was calculated that condition 2 had a total of $155mg$ of stored water where as the higher flow rate condition 4 showed a reduction to $106mg$. It was also noted that the reduction in inlet humidity reduced the amount of retained water within the cell as well. Test condition 8 showed a total of $93mg$ of stored water.

The distribution of the retained water was also of interest to the researchers. Digital masks were applied the neutron images to isolate water under the lands or water in the

channels. When comparing the distributions for conditions 2 and 4 it is apparent that water is accumulating under the lands and is difficult to remove with high gas flow rates in the channels. The difference between water content in the channels for conditions 2 and 4 was $12mg$. Comparing that to the change in water under the lands, $5mg$, it's clear that high flow rates preferentially affect channel water.

The cell performance was simultaneously monitored during these experiments. The authors define two operation regions. The first identifies low flow rate conditions where cell water holdup is at a peak, low cell voltage is also associated with this region. The second is for higher flow rate conditions obtaining increased cell voltage. This correlation was justified by reduced channel water with increased flow rate and an increased average oxygen concentration, both allowing more reactant to reach the catalyst sites.

The following section investigates the effect of cell pressure on water retention and distribution. Test conditions 1, 9, and 10 were all supplied with over humidified inlet gasses, identical flow rates, and a cell temperature of $80°C$. Test case 1, 9, and 12 had cell pressures of 0.2, 0.15, and $0.1MPa$ respectively. Like the previous tests both neutron images and cell voltage was recorded at steady-state condition.

The results showed an increase in cell water retention with decreasing pressure. The authors thought this was a bit counter intuitive since the mole fraction of water vapor in air reduces with increasing pressure. To explain this, a calculation of the inlet molar flow rate of water was presented.

$$\dot{\eta}_{H_2O} = \frac{\gamma_{H_2O}^{in}\left(\dot{\eta}_{H_2}^{dry} + \dot{\eta}_{air}^{dry}\right)}{1 - \gamma_{H_2O}^{sat}} \qquad (2.2\text{-}1)$$

For each case the inlet and exit molar water flow rates were given. Since the inlet gasses were over humidified there would be some level of condensation in the cell. The exit value was calculated by the difference in the inlet water flow rate and the condensed water rate which was derived using the saturation pressure at the given cell temperature. With the relative humidities at the inlet and outlet of the cell it was found that greater amounts of condensation occur at lower cell pressures.

Again the cell voltage was monitored for this series of tests. It was found that increasing cell pressure improved the voltage of the cell given the higher oxygen partial

pressure on the cathode side. Additionally, it was noted that increasing the cathode flow rate also improved the cell performance in the same way by reducing the overall water content and improving the average molar concentration of oxygen. Since both anode and cathode inlets are overly humidified any increase in excess water removal reduces the chances of flooding and helps keep gas diffusion paths free.

The final operating parameter to be investigated was the effect inlet humidity has on the cells performance holding everything else constant. Nine tests were performed with three different humidity levels, 25%, 41%, and 66%. As usual each steady-state condition is recorded with neutron images, cell voltage measurements, and all operating parameters.

It was found that there were insignificant variations in the cell water content between the three humidity levels. Most of the water was found to be accumulated under the lands of the channel.

Even though there was very little variation in the neutron images there was a large change in the performance of the cell. At lower humidity levels and increased flow rates the voltage dropped off quickly. The hypothesis was that this was due to membrane dehydration. For flooding conditions it requires a large change in water volume to induce significant performance issues. When membrane hydration is near its critical value very little change in water volume is needed to see changes in the cell performance. The authors supported their theory by calculating the total water capacitance of the membrane used. It was found that the membrane had a capacity of $2.42 mg/cm^3$, which translates to roughly $8\mu m$ of water thickness. Given that this water thickness is below the rated sensitivity of the neutron imager it seems reasonable that the drop in cell voltage observed was due to membrane dehydration.

The authors demonstrated the ability of neutron radiography to capture the changes in cell water content. With the use of digital masks and parallel channels they were also able to differentiate between water in or under the channels from water under the lands. The major limitation for this method is its inability to quantify water content variations in the through-plane direction. It is however, able to capture transient motion with it's close to real time image refresh rate. This did assist in distinguishing between anode and cathode water given the cross flow design of the cell.

2.2.1.2-

"In Situ Observation of the Water Distribution Across a PEMFC using High Resolution Neutron Radiography"

P. Boillat, D. Kramer, B.C. Seyfang, G. Frei, E. Lehmann, G.G. Scherer, A. Wokaun, Y. Ichikawa, Y. Tasaki, and K. Shinohara

The last paper to discuss neutron radiography is "In Situ Observation of the Water Distribution Across a PEMFC using High Resolution Neutron Radiography" [29]. In this paper the authors test a new neutron imaging technique that reaches new levels of spatial resolution. An active fuel cell is then used to demonstrate its ability to quantify the water distribution for both in-plane and through-plane perspectives.

The motivation for this work was to address a recent criticism of neutron imaging that it is incapable of differentiating anode side water from cathode side water. This is true for in-plane setups but the system can be used for through-plane quantification as well. The primary difficulty with that is the lack of spatial resolution associated with most neutron imaging systems. Typical resolution values cannot adequately capture the slight variations in water content over the relatively thin membrane electrode assembly thickness which ranges from 400 to $600\mu m$, including both GDLs. The authors proposed a unique solution to the diffraction limited resolution problems which decreased resolution to $2.5\mu m$ per pixel, more than enough to quantify through-plane water distribution.

This method addresses the limiting factor of beam divergence for neutron imagers and is typically defined by the L/D ratio. This ratio measures the ratio between the neutron sources aperture diameter, D, and the length between it and the targets plane, L. The selection of the L/D ratio during the design process will determine the characteristics of the imaging system. A balance between image clarity and temporal resolution is to be considered. For small L/D ratios the image capture rate is high given the large neutron flux but the image becomes blurred. In the opposite case for large L/D ratios the image clarity returns but exposure times then increase, reducing temporal resolution.

To help reduce this compromise the authors allowed a reduction in resolution of one axis for an increase in the other. This is justified since the distribution in water content in the

through-plane direction is of concern while the perpendicular axis is not. By making the aperture rectangular instead of circular the L/D ratio can be tailored for both horizontal and vertical directions. The neutron flux is proportional to the aperture area so it scales inversely with the square of the L/D ratio.

$$\emptyset \sim \left(L/D\right)^{-2} \qquad (2.2\text{-}2)$$

With a rectangular aperture the L/D ratio can be varied with one dimension so the scaling between the neutron flux and the L/D ratio will scale linearly. It was stated that a traditional $2cm$ diameter circular aperture would have an L/D ratio of 350 while the slit aperture design was able to use an L/D ratio up to 3000 and still maintain a reasonable exposure time, approximately 2 to 5 minutes.

$$\emptyset \sim \left(L/D_x\right)^{-1} \qquad (2.2\text{-}3)$$

Another modification was used to improve system resolution, again only applicable to one axis. The neutron detector was tilted to achieve a magnifying effect.

The resolution improvements where measured by comparing results from three different setups for a scanned $150\mu m$ wide slit. The amplitude of the transmitted beam is plotted versus the spatial location of the transmitter. As the resolution of the system improves the trace will better match the actual profile of the slit. The FWHM is calculated by taking the derivative of the trace over the edge of the slit and measuring the full width of the plot between both points of half its peak value. It was found that the system incorporating both resolution enhancement methods had a FWHM of approximately $20\mu m$ while the base systems FWHM was approximately $100\mu m$.

To further illustrate the improvements in the imaging resolution the paper presents example images for a dry cell using all three imaging setups. They clearly show the progression in blurring reduction.

After validation of the system resolution improvement techniques an active fuel cell was used to test it ability to differentiate water content in the through-thickness direction. The cell was set to operate at a constant $1A/cm^2$ current density, ambient pressure, and

$70°C$. Images were taken at four different inlet humidity levels and the cell voltage was also noted. The results show a correlation between cathode water content and cell performance. It was revealed that the cell voltage dropped with increasing water volume at the cathode.

The distribution of the cathode water was also of interest. The authors noted that for low cathode inlet humidities the water was mostly located under the channel lands. It was put forth that for low gas humidity the dominant water removal phase in vapor, so the water removal under the lands was low given the longer diffusion path. The opposite was observed at higher inlet humidity which supports the transport assumption.

This paper provided a quick overview of the steps taken to improve the neutron imager's resolution. The results of the new methods were shown clearly in the provided example images. The section involving the testing of the active fuel cell acted only as a proof of concept for the new method. Given the limited test data and little information as to the experimental setup the conclusions presented are supported adequately.

2.2.2-X-Ray

In this next section, a discussion on the recent developments in x-ray technology that have been utilized to capture water transport mechanisms in operating fuel cells. It has been noted that neutron radiography's increase in spatial resolution has risen the exposure times to levels inadequate for capturing temporal transport phenomena. This gap is addressed with x-ray imaging techniques that allow for high resolutions in both time and space. The following papers provide examples of recent x-ray imaging techniques applied to an operating fuel cell and an isolated component, the GDL.

2.2.2.1-

"High-resolution in-plane investigation of the water evolution and transport in PEM fuel cells"

Christoph Hartniga, Ingo Mankeb, Robert Kuhna, Sebastian Kleinaua, Jürgen Goebbels, and John Banhart

The first paper to be discussed studies the water saturation distribution and transport mechanism for an operating fuel cell. The authors, Christoph Hartniga, Ingo Mankeb, Robert Kuhna, Sebastian Kleinaua, Jürgen Goebbels, and John Banhart, published their work in 2009 under the title "High-resolution in-plane investigation of the water evolution and transport in PEM fuel cells" [30].

The cell used for the investigation had and active area $12cm^2$ using a serpentine flow field machined in graphite composite. The diffusion media used in all experiments was SGL Sigracet 10BB with a 5% PTFE content. Theses GDLs then sandwich a $40\mu m$ thick GORE 5621 MEA. Operating parameters held fixed for all tests where a 25% cathodic utilization rate and 90% utilization rate at the anode. These values define the fraction of supplied reactants to that which was consumed in the cell. Additionally, the cell temperature was held constant at $60°C$ and the cathode inlet humidity was set for a dew point of $25°C$ while the anode gas stream was left um humidified.

The source of the x-ray radiation was the tomography facility in Berlin. A monochromatic beam with an energy level tuned for maximum sensitivity for water was capture by a Princeton CCD camera with 2048 pixels by 2048 pixels, translating to an approximate 3 to $7\mu m$ resolution. The image refresh rate was stated to be 3 to 5 seconds.

To differentiate the attenuation of water from the surrounding cell structure all images were referenced to a dry cell image. The results were then presented as wet image divided by the dry reference. An example image was displayed showing marks to indicate the boundaries for the GDL and MEA. Those boundaries were magnified to show the different granular structure in the image for different elements of the cell.

The first set of tests where designed to study the effect current density has on the spatial distribution of water in the cell. For each current density of interest the cell was

allowed 20 minutes to reach steady state, at which point the image was taken. The results showed clearly that the higher the current density the greater the retained water content in the cell. This is not suppressing since the water production rate is defined by the current density. For low current densities hardly any liquid water is present, suggesting that the majority of water transport is maintained in the gaseous phase. It was found that liquid water starts to manifest around $420 mA cm^{-2}$ in the cathode GDL. As the current density rises to approximately $500 mA cm^{-2}$ the anode GDL starts to show liquid water. Given the unhumidified reactant supply for the anode, the source of this water was due to the back diffusion through the membrane given the large concentration gradient.

The authors noted two main positions for water agglomerations, in the GDL close to the MPL and another close to the channels. Given the very small pore size and extreme hydrophobicity of the MPL, water produced from the electrochemical reaction remains in a gaseous phase and diffuses to the GDL. Once inside the GDL the vapor pressure of water is achieved and condensation occurs on hydrophilic locations. From there the transport of water to the channels can take place in both the gaseous phase and the liquid phase.

To quantify these trends the authors summed up 100 rows in the region of interest for each axial position along the cell thickness. The water thickness was calculated based on the known attenuation of the x-ray through water.

Two distinct locations for water formation were clearly seen in the water thickness plots. While the first formation of liquid water near the MPL becomes apparent even at low current densities the second peak does not form until greater cell activity is reached. The authors attribute this second agglomerate to the cooler temperatures near the channels and under the lands, causing an increased rate of condensation. In addition to that the cathode humidified air restricts the transport of water in the vapor phase, causing a transport limitation. This hypothesis is supported by the delay in the second peak forming on the anode side. Given the non-humidified reactant gas flow of the anode this transport limitation on vapor is less prominent.

Water distribution was also investigated in the in-plane orientation. From these images it was noted that the majority of liquid water was formed under the lands of the channels. The authors proposed that this is due to the higher electrical conductivity and reduced pore sizes of the GDL due to compression. No further investigation was presented.

Transient operations were also explored in addition to the static states. The method used held the cell at a constant current density until steady-state was reached. At this point the current density was jumped up and x-ray images were taken consecutively to capture the dynamic response. This experiment is similar to the operating conditions a fuel cell would see in an automotive application. The currents chosen were $500 mA cm^{-2}$ to $600 mA cm^{-2}$, given the formation of a second peck in the anode GDL between these two currents.

After the switch in current, steady-state was reach within *15* minutes. On the cathode side, water content reached steady-state quickly and proceeded to transport water into the channels. The response on the anode side was much slower. Even though the peak in water content near the anode MPL reached its peak quickly the second agglomerate near the channels was much slower compared to the cathode side. This is not surprising given the source of water for the cathode is from the humidified reactant supply and the electrochemical production of water, which is much faster than back diffusion through the membrane to the anode channels.

The final topic covered in this paper was the dynamic transport mechanism for localized regions. Different porous media models predict various transport processes but experimental verification is limited. The authors present two images separated by five seconds. In that time period a water droplet has formed in a cathode gas channel. A third image is generated from the difference between the other two, showing regions of water accumulation and reduction.

Small water clusters in the hydrophobic GDL grow and form large clustering's which eventually destabilize and move into the gas channels. The driving forces behind these sudden bursts of movement are the high capillary pressures in filed pores relative to low pressure regions in neighboring pores. When the jump is made the water is dragged to the next location, leaving an empty pore until refilled, at which point the process starts again. It has been noted that these eruptive processes tend of occur in repeated location, showing a preferred transport path. The authors illustrate this by plotting the water content at a specific location versus time. From the plot a clear cyclic trend with a steady period is observed. A more in-depth investigation of these localized dynamic transport mechanisms using the same synchrotron x-ray imaging technique can be found in Ref. [31].

The work presented above describes recent advances in the achievable resolution levels for synchrotron x-ray imaging. Given the $3\mu m$ lateral resolution their system was able to capture the spatial distribution of water accumulation in the through-plane direction, noting two distinct preferable locations. Even though the two dimensional quantification of liquid water hindered the ability to discern water transport in three dimensional terms they were able to acquire images showing the liquid water distribution patterns in the in-plane perspective.

2.2.2.2-

"Quantification of Liquid Water Saturation in a PEM Fuel Cell Diffusion Medium Using X-Ray Microtomography"

Puneet K. Sinha, Philip Halleck, and Chao- Yang Wang

The final paper to be reviewed, "Quantification of Liquid Water Saturation in a PEM Fuel Cell Diffusion Medium Using X-Ray Microtomography" [32], utilizes x-ray computer tomography in an attempt to visualize water distribution in three dimensions. Unlike the previous imaging techniques which rely on 2D images captured from one perspective, computer tomography constructs 3D images from the results of many scans taken at different perspectives. This method avoids the limitations of traditional x-ray and neutron imaging techniques which cannot discern the location of attenuating water within the beams path. In this paper the authors study a single GDL housed in a custom enclosure. The objective was more a proof of concept for applying x-ray tomography on a GDL than to study its water transport properties.

To start the authors describe the basic theory used to quantify water saturation. It is based on the Beer-Lambert's attenuation law for monochromatic beams.

$$\frac{I}{I_0} = exp(-\mu x) \qquad (2.2\text{-}4)$$

This states that the original beam intensity, I_0, is attenuated as it passes through a material with a linear attenuation coefficient, μ, and is reduced to I after propagating a distance x. A more common way to express a material absorption rate is by the CT number.

$$CT = A\left(\frac{\mu_{material} - \mu_{air}}{\mu_{ref} - \mu_{air}}\right) - B \qquad (2.2\text{-}5)$$

Where $\mu_{material}$, μ_{air}, and μ_{ref} are the linear attenuation coefficients for the scanned material, air, and a reference material, respectively. A and B are said to be chosen arbitrarily and are given values of 100 and 2048 for this work.

To extract the saturation value of a given GDL scan it is correlated to the average CT value of the scan and its porosity through the following proportionality.

$$CT = CT_{air}\varepsilon(1 - s) + CT_w\varepsilon s + CT_s(1 - s) \qquad (2.2\text{-}6)$$

Where ε and s are the porosity and saturation for the scanned area and CT_{air}, CT_w, and CT_s are the CT numbers for air, water, and the solid substrate respectively. From this the authors define the CT numbers for a completely dry and wet GDL as follows.

$$CT_{dry} = CT_{air}\varepsilon + CT_s(1 - \varepsilon) \qquad (2.2\text{-}7)$$

$$CT_{wet} = CT_w\varepsilon + CT_s(1 - \varepsilon) \qquad (2.2\text{-}8)$$

To eliminate the effect of the solid substrate the authors subtract the dry reference scan from a scan of a completely saturated GDL.

$$CT_{wet} - CT_{dry} = (CT_w - CT_{air})\varepsilon \qquad (2.2\text{-}9)$$

And the variation from a scan to the saturated condition is,

$$CT - CT_{wet} = (CT_w - CT_{air})\varepsilon(1 - s) \qquad (2.2\text{-}10)$$

So the saturation at a particular pixel location is defined by the ratio of the difference in the CT value from the current state to its value in the dry state over the total difference between the CT values at the dry and wet states.

$$s = \frac{CT - CT_{dry}}{CT_{wet} - CT_{dry}} \qquad (2.2\text{-}11)$$

A $200\mu m$ thick Toray carbon paper was held in a custom fixture designed to rotate 360 degrees on an axis perpendicular to the x-ray source. The attenuated beam was then captured by a 2D array of detectors. This setup allows the images to be separated into 15 slices along the thickness of the GDL. The resulting 3D voxels have a 10 by 10 by $13.4\mu m$ dimensional resolution.

The GDL fixture houses the GDL between a water chamber and a series of 1 by $1mm$ parallel channels. These channels allow nitrogen to be used in purge simulating fashion after the GDL is saturated by first applying a vacuum to the channels, forcing water through the GDL from the chamber above.

A scan of the dry GDL is taken before the GDL is saturated, at which point the wet reference scan is taken. The purge process was then initiated, flowing nitrogen at room temperature through the channels at a rate of $5L/min$. Scans of the GDL where taken periodically to capture the progress of the purging process.

Displayed were the middle slice images of the GDL at times 2, 6, 12, and 25 minutes after the purge was started. Both reference scan middle slices were also displayed. These images represent the raw CT values obtained from the scan. The next set of images presented are the result of image normalization to the reference scans. The first image showed the locations of water at full saturation by subtracting the reference wet scan from the reference dry scan. The following images depicted the change in water location from on time to the next by presenting the difference between the two scans normalized to the saturated case. The results show a large change in water content from full saturation to 6 minutes after the start of purge. After 6 minutes the changes in the images was minimal.

The change in water content was quantified by displaying the saturation of each slice for all time steps. Only the middle seven slices were used since large ring artifacts were present in the results for scans on the edges of the GDL. The authors reported that this is primarily due to abrupt changes in the material density and atomic number between the GDL and its fixture. However the trend is captured with the middle seven slices, showing the same fast initial change in saturation then a slow decrease after 6 minutes of purge.

The reason for this abrupt change in transport speed is better understood after viewing a 3D rendering of those 7 slices. The authors used an image processing software called ImageJ to construct three dimensional renderings of the capture scans. The paper displayed two images, a three dimensional view of the fully saturated scan and another at the 2 minutes of purge time. The fully saturated image shows large clusters of water connected through the thickness of the GDL. The second image showed smaller clustering's of water which are separated from each other. The authors speculate that the large decrease in water removal is due to the division of the large water clusters. Water stationary in individual pores can only be removed via evaporation. Since the nitrogen purge gas was held at the same temperature as the liquid water in the GDL, evaporative water removal is very slow.

Assuming the dry and wet reference scans are truly that, this method provides a high resolution technique for defining the location of water within the GDL. Those main assumption are of concern, it was said the water camber which is used as a supply for the vacuum pulls provides some head at the GDL interface. Even for hydrophobic PTFE coated Toray some water is expected to enter the GDL. Secondly, the level of vacuum used to saturate the GDL was not stated and it is likely that the fully saturated reference scan is not. If these concerns are minimal the method holds firm but an estimation of the uncertainty was not provided.

Chapter 3: Research Question

3.1-PEM Fuel Cells

Proton Exchange Membrane (PEM) fuel cells are an electrical power source fueled by the chemical reaction between hydrogen and oxygen. They were originally designed by General Electric in the 1960's for NASA's first manned space vehicles [33]. Typical power densities for automotive PEM fuel cell systems exceed 500 watts per liter with efficiencies around 50% [34]. Given their low operating temperature and pressures and relatively high power density PEMFC's show promise in a wide range of applications like Auxiliary, stationary, automotive, and consumer electronics power. All problems associated, however, are not resolved. Water management, durability and system life, manufacturing cost, and dynamic power response all have issues in which limit the marketability.

3.1.1-Opreation

The operation of a PEM fuel cell begins with the overall chemical reaction between hydrogen and oxygen.

$$2H_2 + O_2 \rightarrow 2\,H_2O \qquad (3.1\text{-}1)$$

The reactant gasses are supplied to the membrane electrode assembly (MEA) via channels in the bi-polar plates. The shape and pattern of these channels affect the performance of the cell to distribute gasses effectively. Similarly, the bi-polar plate can have channels dedicated to coolant flow. Given that the electrochemical reaction is not 100% efficient, some energy is released in the form of thermal energy, mandating cell temperature control via excess reactant flow and/or coolant flow. These plates makes up about 80% of

the fuel cell stacks mass [33] and so provide the structural support for the weak soft goods, namely the diffusion media and MEA.

The MEA consists of anode and cathode electrodes sandwiching the electrolyte membrane and is where all the chemical activity proceeds. These electrodes consists of a slurry of catalyst, support carbon particles, PTFE, and a small fraction of ionomer to support proton conduction to the electrolyte [34]. The catalyst serves to reduce the activation energy required to initiate the reaction. It is typically platinum nano particles around $10nm$ applied to the carbon substrate particles which range from 45 to $90nm$ in diameter [34]. The cost and manufacturability of the cell is directly influenced by the electrode design. Through the use of creative manufacturing techniques, the amount of platinum required in a fuel cell has dropped significantly, roughly $28mgcm^{-1}$ to $0.2mgcm^{-1}$ [33].

For both anode and cathode electrodes a triple phase boundary (TPB) must exist for the reaction to proceed. This boundary is where the catalysts, reactant, and electrolyte meet to contribute their respective roles in the half cell reactions.

Hydrogen is supplied to the anode side of the fuel cell where it makes its way to the electrode. When a TPB forms by the contact between hydrogen, electrolyte, and catalyst, the hydrogen molecule is stripped of its two electrons. This TPB allows the liberated electrons to transport through the electrically conductive electrode substrate while the hydrogen proton is transported to the cathode electrode via the proton conductive electrolyte.

$$H_2 \rightarrow 2e^- + 2H^+ \qquad (3.1\text{-}2)$$

On the cathode side the conducted proton is reacted with an electron that has passed through the external circuit and an oxygen molecule supplied via the cathode gas channels. The reaction product is water and heat.

$$O_2 + 4e^- + 4H^+ \rightarrow 2\,H_2O + Heat \qquad (3.1\text{-}3)$$

The amount of heat produced is based on the thermal efficiency of the reaction. The total energy released from the reaction is defined by the difference in molar enthalpy of formation, $\bar{h}_f$, between the products and reactants.

$$\Delta\bar{h}_f = \left(\bar{h}_f\right)_{H_2O} - \left(\bar{h}_f\right)_{H_2} - \frac{1}{2}\left(\bar{h}_f\right)_{O_2} \quad (3.1\text{-}4)$$

The available amount of this energy for use is governed by how much is lost to entropy per mole, $\bar{s}_f$, and is called the molar specific Gibb's energy of formation at constant temperature.

$$\Delta\bar{g}_f = \Delta\bar{h}_f - T\Delta\bar{s} \quad (3.1\text{-}5)$$

Where $\Delta\bar{s}$ similarly is defined by the difference in molar entropy, $\bar{s}$, between the products and reactants.

$$\Delta\bar{s} = (\bar{s})_{H_2O} - (\bar{s})_{H_2} - \frac{1}{2}(\bar{s})_{O_2} \quad (3.1\text{-}6)$$

The efficiency of the reaction is defined by the ratio of available energy over the total chemical energy released or the change in molar Gibb's free energy over the change in molar enthalpy.

$$\eta_{th} = \frac{\Delta\bar{g}_f}{\Delta\bar{h}_f} = 1 - \frac{T\Delta\bar{s}}{\Delta\bar{h}_f} \quad (3.1\text{-}7)$$

Both $\bar{h}_f$ and $\bar{s}$ are dependent on temperature and state so the total available energy per mole, $\Delta\bar{g}_f$, and the thermal efficiency, η_{th}, are conditional. It is common to express the thermal efficiency based either on the higher heating value (HHV) or the lower heating value (LHV). The HHV corresponds to the change in enthalpy of formation when the product water is in liquid phase and the LHV, conversely is for the product water in the gaseous phase. The difference between the two is related to the latent heat of vaporization.

The maximum theoretical cell voltage is also defined using the change in Gibb's free energy. Given that ever hydrogen molecule relinquishes two electrons, the total charge released per mole of hydrogen is twice Avogadro's number, N, times the charge on each electron, e, where F is Faraday's constant.

$$-2Ne = -2F \tag{3.1-8}$$

The product of voltage and charge define the amount of electrical work done and since the total available energy is governed by the change in Gibb's free energy the maximum cell voltage is defined by the following.

$$E = \frac{-\Delta \bar{g}_f}{2F} \tag{3.1-9}$$

This voltage is however a theoretical maximum. Various losses and operational conditions affecting the Gibb's free energy will play a significant role in the operational voltage of the cell.

The Nernst equation demonstrates the relation between operational conditions and the cell voltage. It shows the variation in $\Delta \bar{g}_f$ dependent on the cell temperature and activation energies of the reactants and products. For a general reaction the Nernst equation is as follows.

$$aA + bB = cC \tag{3.1-10}$$

$$\Delta \bar{g}_f = \Delta \bar{g}_f^0(T) - RTln\left(\frac{a_A^a a_B^b}{a_C^c}\right) \tag{3.1-11}$$

Where $\Delta \bar{g}_f^0$ is the change in molar Gibb's free energy of formation at standard pressure and a_j^i are the activation energies for the elements in the chemical reaction. By approximating the reactant gasses as ideal the activation energies are simply the ratio of the elements partial pressures over the reference pressure, P^0, used for $\Delta \bar{g}_f^0$, typically 1atm [35]. Taking this and applying it to a hydrogen PEM fuel cell reaction, the relation between reactant concentration and cell potential becomes clear.

$$\Delta\bar{g}_f = \Delta\bar{g}_f^0(T) - RTln\left(\frac{\left(\frac{P_{H_2}}{P^0}\right)\left(\frac{P_{O_2}}{P^0}\right)^{1/2}}{\left(\frac{P_{H_2O}}{P^0}\right)}\right) \quad (3.1\text{-}12)$$

$$E = E^0(T) + \frac{RT}{2F}\left[ln\left(\frac{P_{H_2}{P_{O_2}}^{1/2}}{P_{H_2O}}\right) - \frac{1}{2}ln(P^0)\right] \quad (3.1\text{-}13)$$

Again this voltage represents a lossless case, not taking into account the various losses that are present in a real system. The majority of these losses can be grouped into four main categories, activation, fuel crossover, ohmic, and mass transport losses.

The activation losses of a cell are dependent on the overall reaction rate and overvoltage potential resisting the net forward motion [36]. The reduction in the cell voltage, ΔV_{act}, due to the activation losses is typically modeled as a logarithmic relation to the current density, i.

$$\Delta V_{act} = \frac{RT}{2\alpha F}ln\left(\frac{i}{i_0}\right) \quad (3.1\text{-}14)$$

Where α is the charge transfer coefficient and i_0 is the exchange current density. Both α and i_0 are dependent on the reaction occurring and the material of the catalyst.

In addition to the activation overvoltage loss fuel cells are susceptible to fuel cross over and internal current losses. Even thought the electrolyte is designed to be electrically resistant and impermeable to reactant gasses both can occur in small amounts. It is common to combine the two effects into a single phenomenon even though they are two separate issues but the result on cell performance are essentially equivalent.

For fuel cross-over hydrogen diffuses through the electrolyte and reacts with cathode oxygen. For every molecule of hydrogen crossing over there are two electrons not used to power the external device. If those two electrons pass through the electrolyte the same effect is achieved. This reduction in cell voltage can be modeled in with the activation losses by adding the internal current, i_n, caused by cross-over with the observed current density i. With this the cell voltage is predicted with following equation where E is the theoretical reversible voltage.

$$V = E - \frac{RT}{2\alpha F} ln\left(\frac{i + i_n}{i_0}\right) \quad (3.1\text{-}15)$$

Another area of concern for fuel cell designers is the ohmic voltage drops associated with the transport of electrons through the cell. The harvested electrons on the anode reaction sites need to pass through both electrodes and diffusion medias along with the bi-polar plate to get to the cathode reaction sites. All elements have a certain level of resistivity that contributes to the overall voltage loss. The modeling of this irreversible drop is straight forward with ohms law.

$$V = IR \quad (3.1\text{-}16)$$

Any loss in cell performance due to the lack of reactant supply is categorized as a mass transport loss. It was discussed previously that the theoretical open circuit voltage (OCV) is dependent, in part, on the reactant gasses partial pressures. During the operation of the cell oxygen is consumed from the supplied gas stream, reducing the partial pressure of oxygen. For the anode condition, hydrogen pressure decreases along the channel length given the fluid resistance to flow. Both reductions in partial pressures depend on the rate of reactant consumption or cell current. At some point the reactant supply system will not be able to meet the rate of consumption demanded by the operating cell. The output at this point is known as the limiting current density, i_l.

The most straight forward method to model the voltage drop from mass transport losses is with the Nernst equation. Assuming that the partial pressure of a reactant falls linearly to zero at the limiting current the Nernst equation produces the following voltage differential from OCV [36].

$$\Delta V_{MT} = \frac{RT}{\eta F} ln\left(1 - \frac{i}{i_l}\right) \quad (3.1\text{-}17)$$

Where η is the number of electrons associated with one reactant molecule of interest. η would be 2 if concerned with the drop in hydrogen partial pressure and 4 for oxygen partial pressure loss.

This model, though theoretically founded, does not perfectly fit experimental data [37]. It is common practice to use an exponential decay model to predict mass transport losses given its superior fit even though it has no connection to theory.

$$\Delta V_{MT} = mexp(ni) \tag{3.1-18}$$

Where m and n are constants used to fit measured data.

The combined effect of all these losses can be combined to model any given PEM fuel cell assuming the relevant constants are known.

$$V = E - \frac{RT}{2\alpha F} ln\left(\frac{i + i_n}{i_0}\right) - ir - mexp(ni) \tag{3.1-19}$$

Mass transport losses are of particular interest to this thesis as the resistance to reactant flow and the restrictions on circulation play a huge role in the localized partial pressures. The gas channels and diffusion media are designed to reduce these restrictions and ensure even distribution. Equally important is the handling of water within the cell. Excessive liquid water can cause flooding and block the transport of reactants. Conversely the dependence of proper membrane hydration must be considered. The following section will discuss the diffusion media's role in managing water within the cell.

3.1.2-DiffusionMedia

The primary functional requirement of the GDL is to distribute reactant gasses evenly over the electrode faces. Similarly, it is responsible for assisting in the removal of product water away from the reaction sites and out of the cell. The channels in the bi-polar plates allow access to the area of the electrodes directly under the channels but reactant gasses depend on the GDL to reach the areas of the electrodes covered by the channel lands.

Like the bi-polar plates the GDL needs to be electrically conductive, providing the connection between the bi-polar plates and the electrodes. Any resistance to electrical flow

will result in lower operating voltages through ohmic losses. Another functional requirement of the GDL is to provide structural strength to the membrane electrode assembly.

A PEM fuel cell requires the presence of hydrogen and oxygen to fuel the electrochemical reaction that produces electrical power. The goal is to supply the reaction sites in the catalyst layer with ample concentrations of these two gases, hydrogen to the anode and oxygen to the cathode. As the reaction consumes these reactants the local concentration is reduced, causing a need for more hydrogen or oxygen to be supplied. As the reaction rate increases the required flow of new gas is increased as well. If there is impedance to this flow, as the GDL, a concentration gradient arises. This gradient is dependent on the resistance to flow and the required flow rate. The GDL is made up of a very inhomogeneous and porous carbon paper which provides these reactant gases a tortuous path of varying pore sizes from the channels to the reaction sites in the catalyst layer. The mentioned impedance of gas flow is directly proportional to these two quantities. With greater porosity and reduced torosity of the medium the lower the resistance to flow and consequently greater current densities can be achieve for a given cell. An ideal diffusion medium would have no resistance to the flow of gases in any direction, in-plane or through-plane travel. With this all reaction sites would be perfectly supplied.

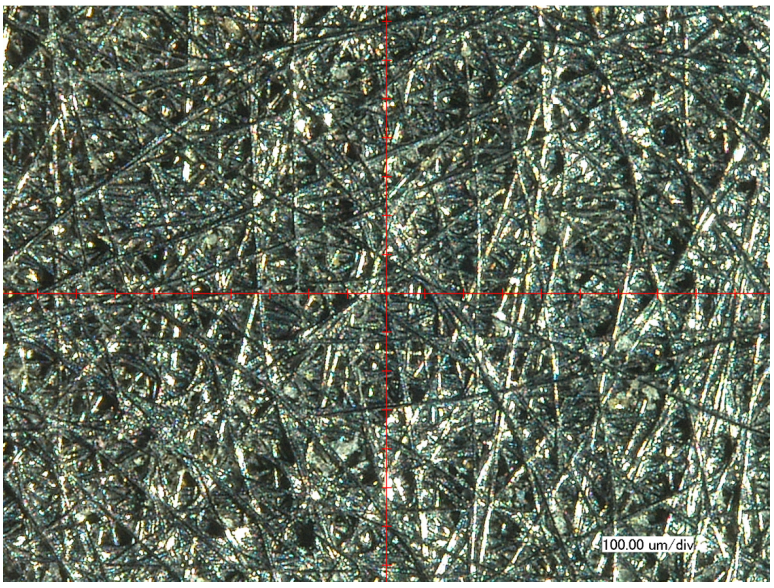

Figure 3.1-1: Optical image of Toray-120 GDL with 20% PTFE loading (2x2mm).

Gas diffusion is not the only concern for a PEMFC GDL, water transport is just as important to the overall performance of a cell. On the cathode side oxygen is being consumed as water is being produced. The bulk motion of oxygen and water oppose each other's motion. The local saturation of the diffusion medium affects the number of available pores oxygen has to travel through. So saturation affects the effective porosity seen by the diffusing gas. Similarly, the anode GDL can be affected by the presence of water. The source for the anode side GDL being back diffusion of water through the membrane and inlet water vapor from humidified hydrogen. It is clear that the GDL needs to deal with water transport in a manner that effectively removes product water while minimizing the impedance of gas diffusion.

In porous medias water transport is driven by a number of effects. These include capillary forces, which is pressure differences between phases and is the dominate driving force in a GDL [38], convectional forces, and evaporating and condensation effects. Interfacial effects also play a major role in the behavior of water within the GDL.

For a porous system where two or more fluids interact there are interfaces between the elements that produce imbalances in molecular forces. The pressure differences at these boundaries are the resulting capillary pressures. These capillary pressures are dependent on pore size and variations in fluid surface tension and energies. Many have modeled the GDL as a series of capillary tubes in which the driving force for water transport is the capillary pressures. As pore size is reduced this force is increased. The problem with this is that at the microscopic level the GDL structure is very complicated. All pores are not connected, resulting in isolated pockets that cannot exploit these pressure differences to drive their motion. As the local saturation within the GDL increases these isolated pockets will begin to connect, allowing for capillary effects to exist. This brings in the effects of localized flooding within the GDL.

In porous medias like the GDL, liquids and gases need to share the available pores. Increasing the saturation level within the pore network reduces the effective pathways for gas diffusion. For those areas were reactant gas is being displaced for water transport they are still being utilized for product removal. What needs to be minimized are irreducible liquid saturation areas. These locations hold water in isolated pores, as mention above, that cannot

be removed by either capillary forces or by drag effects but can only be removed via evaporation. The effect of these areas is a net reduction in available diffusion paths for both gas and liquid. This increases resistance to both flows and results in higher mass transport losses. Not only does this affect the performance of the cell but in practical use it promotes freezing concerns. The presence of water within the cell allows for ice to form which can cause irreparable damage to the GDL as well as the membrane electrode assembly.

To improve on the two-phase flow within the diffusion medium pore size distribution and surface energies are optimized to achieve the desired characteristics. A key parameter here is the surface energies of the GDL. The carbon material which makes up the structure of the GDL is naturally hydrophilic. Hydrophilic meaning that the interfacial contact angle between water and solid is less than 90° at the three phase contact point. With this contact angle the water will be considered the wetting fluid. The degree of wettability dictates the rate at which the fluid spreads across the surface. For a porous material the wetting fluid will tend to be absorbed into the medium while displacing the non-wetting fluid. This effect is directly related to the interfacial forces at the solid interface and has a pronounced effect on capillary pressures within the pores.

Since the objective of the GDL is not to absorb water but to displace it, a highly hydrophobic material, PTFE, is added to the diffusion medium. For the surfaces coated with PTFE the water contact angle is increased beyond the 90° mark and is now the non-wetting fluid, tending to be displaced. It is a production fact that not all fibers of the GDL are coated with this hydrophobic material, a few papers have looked into its effects on water distribution [39, 40]. This results in an inhomogeneous network of hydrophobic and hydrophilic pores. The result is a branching of paths that lend themselves to water transport and others to gas transport. As discussed one of the goals is to reduce the negative effects of opposing phase diffusion. It can also be speculated that these varying surface energies aids in the motion of water translation from pore to pore [41]. Additionally on the channel scale the presence of PTFE results in improved water transport within the channels. Having higher contact angles on the surface of the GDL reduces the stiction of water to the GDL.

In addition to the diffusion properties of the GDL it is also equally responsible for transporting electrons to and from the catalyst layer. Any resistance to the flow of electricity will result in ohmic losses, reducing the power output of the cell. The ideal GDL will have no

resistance, resulting in no power loss. With this the goal of GDL design is to minimize these losses by improving the electrical conductivity within. Unlike gas and liquid transport the electrons flow though the fibers, each being connected by their mechanical connection.

The source of electrical resistance within the GDL is a combination of the solid body resistance of the carbon and contact resistance on two scales [42]. Macro scale being the interface between the GDL and bi-polar plates and the interface between the GDL and the catalyst layer. This being the primary source of electrical resistance associated with the GDL. On the Micro scale there are contact resistances between individual fibers that transmit electrons between them. Given that the fibers are usually aligned in the in-plane orientation there is much less boundaries between fibers, hence much fewer instances of contact resistance in the in-plane direction. Conversely, electrons flowing in the through-plane direction encounter a greater density of inter fiber boundaries resulting in a greater number of contact resistance occurrences. The ideal GDL, in terms of electrical conductivity, would be a single solid body with very little electrical resistance associated with it, this would yield the minimum number of interfacial contact resistance. However a solid body would result in effectively zero diffusion of gas and liquid.

Clearly the ideal GDL is one that offers no resistance to gas and liquid transport while supplying a super conductor like electron transport characteristic. In addition this ideal material or structure would need to be a thin as possible to insure minimal size of the overall system. While this list of required properties seems mutually exclusive, existing GDL's provide a remarkable balance of all the aforementioned properties. With that said there is still much to be improved in terms of GDL performance, most notably water management and uniform reactant gas diffusion.

3.2-Ultrasound Application

3.2.1-Hypothisis

Having reviewed the operation and scope of PEM fuel cells and discussing its dependence on the GDL for proper water management and gas diffusion the final step is to make the connection to non-destructive ultrasonic evaluation.

The purpose of this research can be broken into two sections. The first objective was to observe the basic acoustic response from the GDL as there is no prior work for a basis. After a clear understanding of GDL-acoustic coupling a research objective was defined.

After familiarization of the developed system, initial scans of the GDL revealed echo signals with seemingly random shape. The echo signals also showed large variations in shape and magnitude with scanned position. Continued investigation demonstrated that the saturation level of the GDL had a huge effect on the apparent attenuation of the signal. Initial B-scans showed no back reflection of the GDL support until high levels of saturation. It was determined that the primary acoustic reflector was encapsulated air within the GDL, substantiated with theoretical validation.

From quantification tests that define the system resolution it was found that the microstructure of the GDL falls into diffractive scattering. This is between specular and diffuse scattering where backscatter theories are well defined. The result is an acoustic resolution that cannot resolve individual fibers within the GDL, producing a response which is the phase sensitive summation of all reflections within the resolution cell. Figure *3.2-1* illustrates this with an optical image of a Toray-120 GDL sample shown with a $90\mu m$ diameter dot representing the acoustic beam diameter.

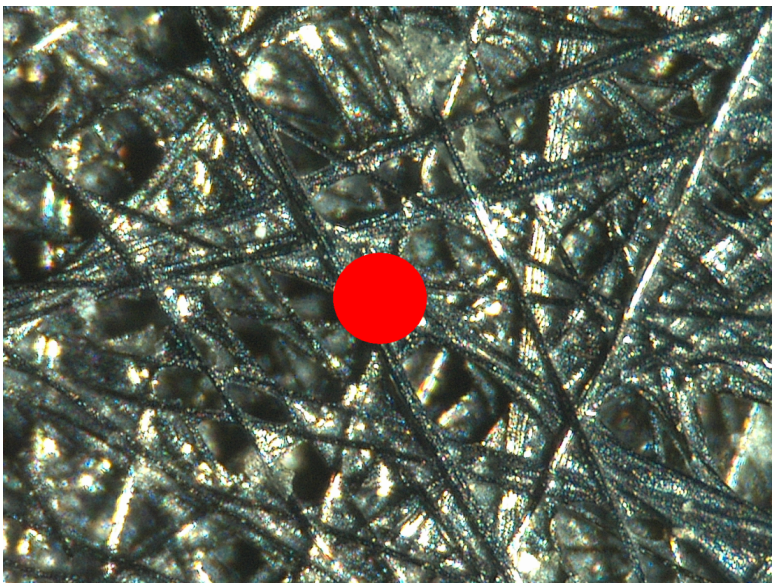

Figure 3.2-1: Optical image of Toray-120 GDL with 90 micron diameter dot (0.8x0.8mm).

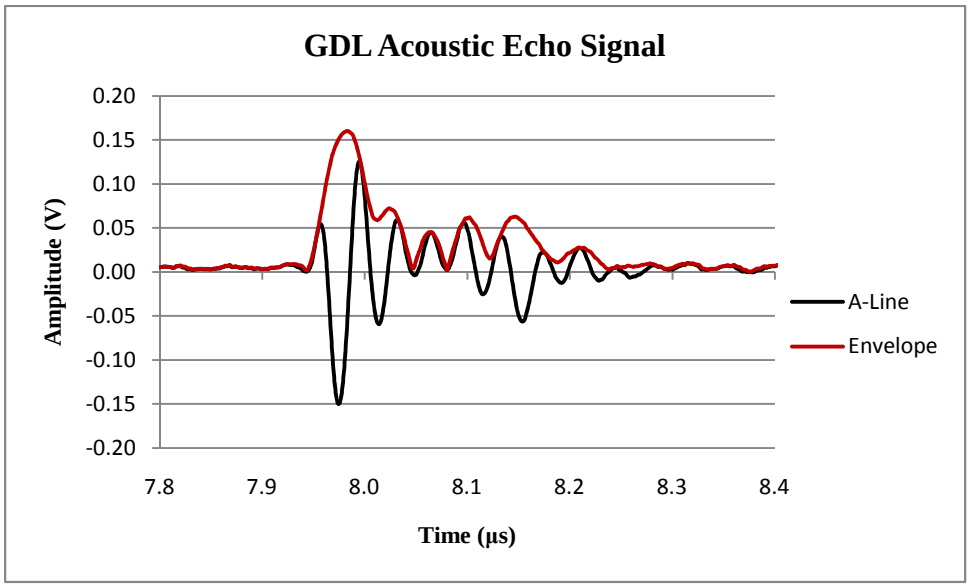

Figure 3.2-2: Plot illustrating random nature of received echo signals.

The signal, however, is deterministic. For any one location there is a distinct and consistent echo pattern. If enough information is known about the insonified region of the GDL the received echo signal can be reproduced. The difficulty lies in the reverse problem, trying to extract information about the structure from the semi-random signal. This phenomenon is known as speckle, the result of constructive and destructive interference showing no inherent relation to the physical structure imaged.

The first set of investigations attempted to quantify the change in acoustic attenuation with saturation. Given the variation in acoustic response, a large data set was needed to define the average echo amplitude with depth. This was accomplished by identifying all peaks in the received A-line signals and plotting their amplitude versus the time of arrival. For a standard $2x2mm$ scanned area and a pixel size of $20\mu m$, approximately thirty thousand echoes where identified for any given scan. With that the recorded time-gate was split into 50 equal sections where the corresponding echo amplitudes in that time frame where averaged. The trend in average echo amplitude was then fit to an exponential decay with scaling constant a and a dampening constant b.

$$A(t) = ae^{-bt} \qquad (3.2\text{-}1)$$

Figure *3.2-3* illustrates a typical result for a sample C-scan of $4mm^2$, showing decreased amplitude with depth. This characterization was then applied to a series of scanned GDLs which had increasing levels of saturation.

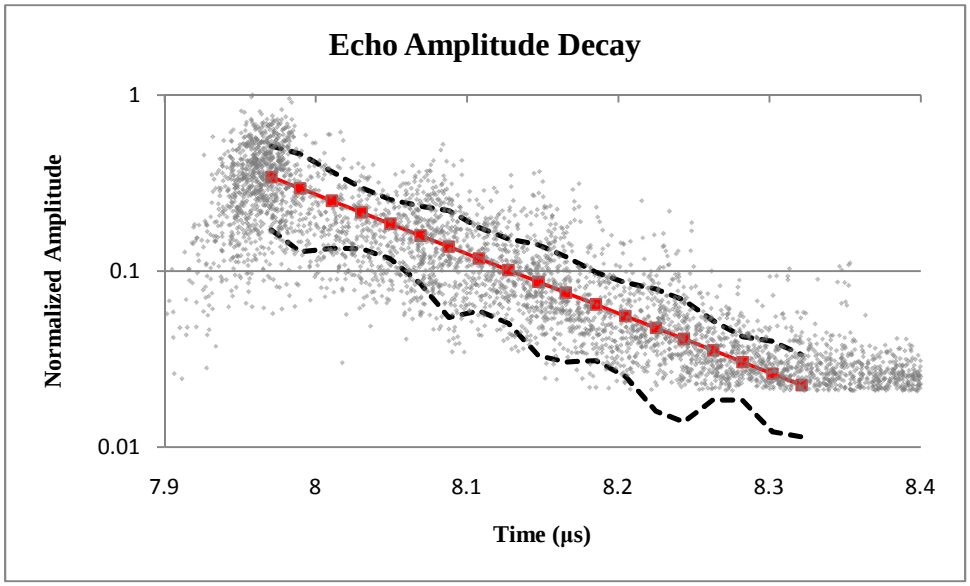

Figure 3.2-3: Plot of detected peaks with exponential fit trend line and one standard deviation boundaries.

To control the water content in the GDL a specific pressure differential was applied across its face. More detail on the methodology used is discussed in the results section. Duplicate scans were performed before and after each application of differential pressure, providing reference points for comparison.

Figure *3.2-4* illustrates the acoustic response of Toray-120 plain after varying levels of applied differential pressure.

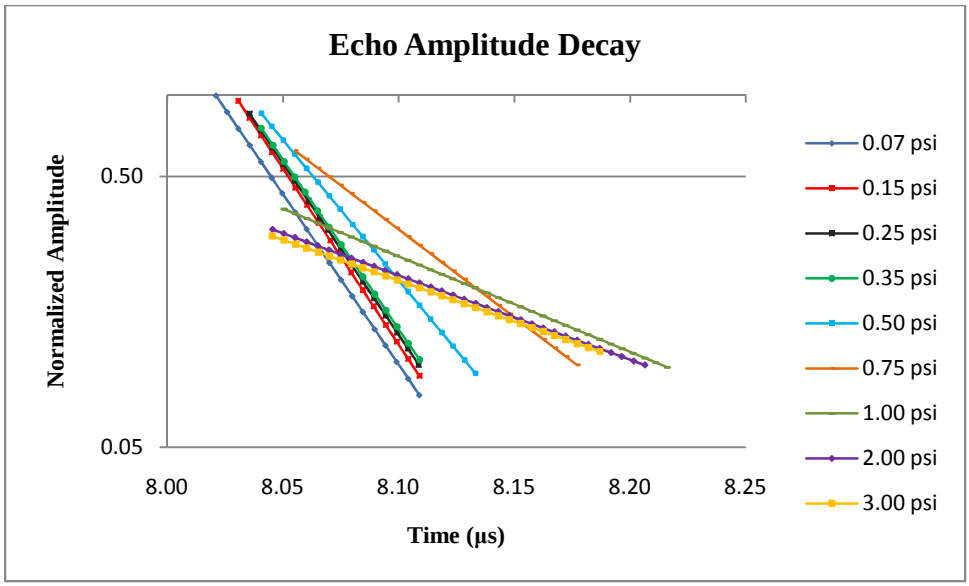

Figure 3.2-4: Plot illustrating the decrease in acoustic attenuation with increasing saturation.

Scan	*ΔP Applied kPa (psi)*	*Amplitude (V)*	*Dampening Constant (μs^{-1})*
GDL-C-Scan_263	*0.50 (0.07)*	*1.452E+104*	*30.058*
GDL-C-Scan_264	*1.03 (0.15)*	*4.613E+103*	*29.903*
GDL-C-Scan_265	*1.72 (0.25)*	*2.678E+101*	*29.258*
GDL-C-Scan_266	*2.41 (0.35)*	*6.435E+99*	*28.791*
GDL-C-Scan_267	*3.45 (0.50)*	*6.894E+82*	*23.916*
GDL-C-Scan_268	*5.17 (0.75)*	*3.461E+51*	*14.965*
GDL-C-Scan_269	*6.89 (1.00)*	*2.399E+27*	*8.126*
GDL-C-Scan_270	*13.79 (2.00)*	*8.911E+23*	*7.171*
GDL-C-Scan_271	*20.68 (3.00)*	*1.459E+23*	*6.953*

Table 3.2-1: Listing of applied differential pressures used for the corresponding scans with their respective exponential decay fit constants.

The trends show a clear decrease in attenuation with an increase in applied pressure. The shapes of the trends are also consistent with theory as the effects of acoustic shadowing are clear. GDLs with higher saturation levels show increased acoustic energy deeper in the

sample compared to the dryer samples. Logically this makes sense given the reduced reflected energy earlier in the sample, leaving more energy to be transmitted into and reflected from deeper sections.

To gain further insight into the variations seen from one scan to the next, plots of the acoustic backscatter were generated. These 2D images of the $4mm^2$ scanned areas reveal coherent regions of high and low ultrasonic reflectivity. Backscatter being defined by the sum of all data point values squared at each pixel location, ij, where N is the number of data points recorded at each location. This quantity considers the cumulative effect of all backscattered energy within the GDL.

$$B_{ij} = \sum_{k=0}^{N-1} A(k)_{ij}^2 \qquad (3.2\text{-}2)$$

Intuitively the regions of high acoustic backscatter correspond to pockets of air while lower value areas reveal saturated sections of the GDL. However, since there is no secondary validation to the speculation confidence in signal interpretation is low given the constructive and destructive interference of the received signal.

Figure *3.2-5* below depict sample C-scan images of the backscatter received for a dry reference scan and vacuum saturated scan after an application of $0.5psi$ pressure differential across the GDL face.

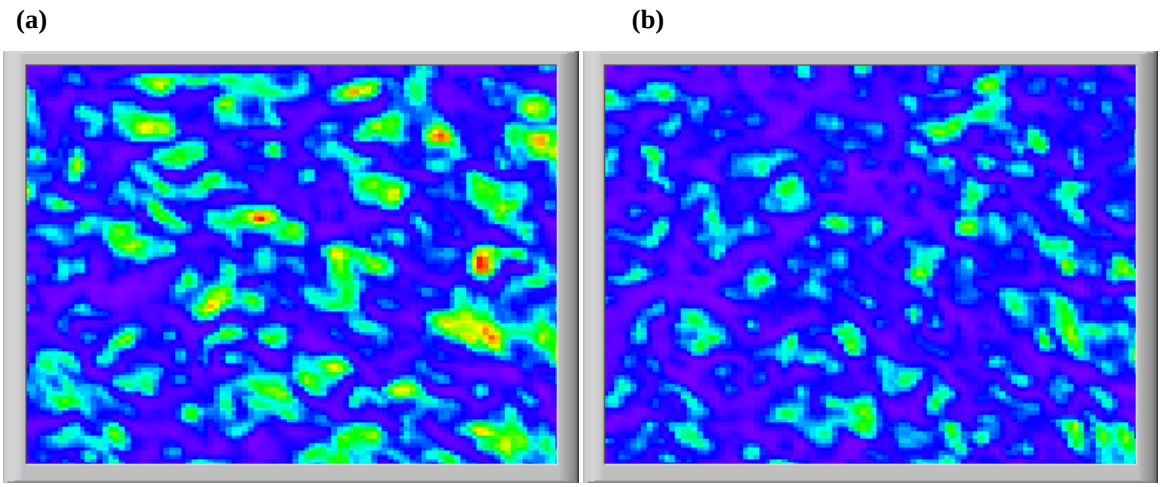

Figure 3.2-5: Typical C-scan images illustrating change after differential pressure application. (a) C-Scan_263 Dry Reference Image, (b) C-Scan_268 image from 0.5psi ∆p.

It can be seen that the regions of high acoustic reflectivity suffer reduced area and backscatter after a pressure differential is applied across the GDL face. To visualize the change between scans simple image subtraction was used, identifying areas of altered backscatter. The problem with this method is the inconsideration of distorted A-line shape with consistent backscatter, meaning different A-lines with vastly different shapes can produce the same acoustic backscatter value. For a sample location where interference defines the shape and reflected energy a simple reduction or change in the position of air within the insonified region results in a major change in A-line shape but little change in backscatter energy. The consequence is a missed alteration from the dry condition to a now saturated condition.

This phenomenon can be illustrated with a simple example. Figure *3.2-6* show the results of two different methodologies used to quantify the changes in GDL saturation. Figure *3.2-6a* is the result of image subtraction between a dry reference scan and a scan after a $0.07psi$ pressure differential is applied across the sample. Figure *3.2-6b* shows the variation in saturation by quantifying the change in the A-line signal at each pixel location from the dry reference scan.

(a) **(b)**

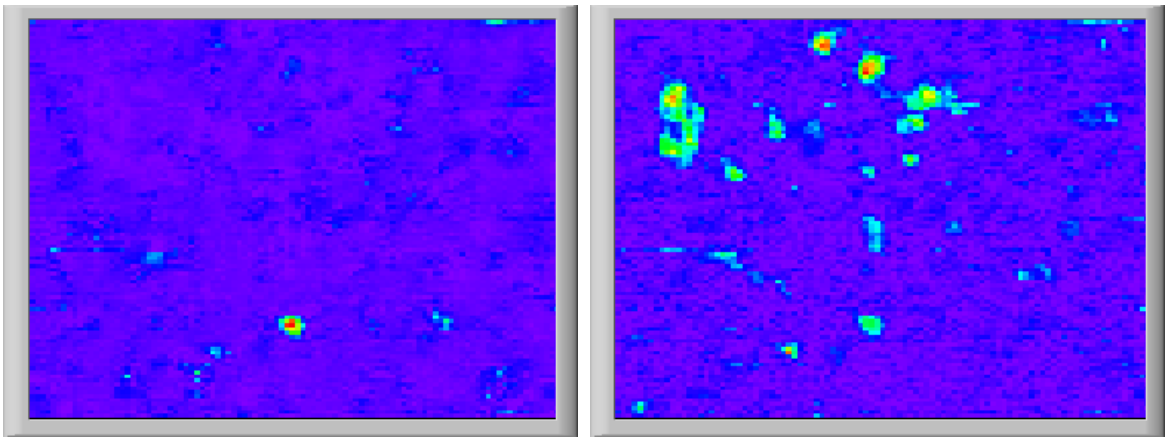

Figure 3.2-6: Two method for identifying regions of water intrusion. Sample is of Toray 120 plain after 0.07psi ⊿p . (a) C-Scan_128-131 image difference, (b) C-Scan_128-131 scan correlation.

Clearly the simple image subtraction method misses areas of altered A-line signal whereas the correlation method captures all locations of altered acoustic reflection. The following defines the values used to quantify the variation in A-line signals at each pixel location, as used in figure *3.2-6b*.

$$S_{ij} = \left| \frac{\left[\sqrt{H(CC_{ijt})^2 + CC_{ijt}^2}\right]_{max}}{\sqrt{H(AC_{ijt})^2 + AC_{ijt}^2}} - 1 \right| \times 100 \qquad (3.2\text{-}3)$$

$$CC_{ijt} = \frac{\Delta t}{2} \sum_{\tau=1}^{N-1} X_{ij\tau}^{*} \cdot Y_{ij(t+\tau)} \qquad (3.2\text{-}4)$$

$$AC_{ijt} = \frac{\Delta t}{2} \sum_{\tau=1}^{N-1} X_{ij\tau}^{*} \cdot X_{ij(t+\tau)} \qquad (3.2\text{-}5)$$

$$H(x_t) = \frac{\Delta t}{2\pi} \sum_{i=1}^{N-1} \frac{x_i}{t - \tau_i} + \frac{x_{i+1}}{t - \tau_{i+1}} \qquad (3.2\text{-}6)$$

It is based on the cross-correlation between two scans A-lines. Each scan is compared to the dry reference and a correlation ratio is defined for each pixel location. The advantage of this method is the independence from A-line interpretation to define the physical

scattering media. Assuming that the dry scan is void of water within the GDL any change to the A-line signal must be due to the occupation of water within the insonified region. This is also dependent on the stationary fixture of the samples microstructure as any change in its position between scans would also be a source of altered A-line signals.

Using this method of quantifying changes in the A-line signals and the methodology for acquiring scans for varying saturation levels, images of water intrusion upon the GDL can be acquired for different levels of pressure application. The spatial distribution of water intrusion is characterized and quantified using algorithms developed for this research. The ultimate objective is to compare the results of various diffusion medias and identify differences between their spatial saturation characteristics.

Chapter 4: Methodological Design

4.1-Hardware

The experimental setup can be broken down into two categories, hardware and software. A large investment in time was devoted to the development of both. This section will focus on the design and functionality of the experimental hardware.

Figure *4.1-1* below depicts the basic connectivity of the equipment used. A standard Dell desktop computer connects to a PXI chassis via a PCIe card. The chassis houses three modules, a PXI-5152 high speed digitizer, a PXI-7344 four axis motion controller, and a PXI-6221 DAQ module. The major advantage of a PXI system is the real time system integration that maintains a maximum of $250ps$ clock skew between its components. Shared backplane connections between modules allow for precise timing routines and dynamic signal routing, both required features to ensure the versatility of the system.

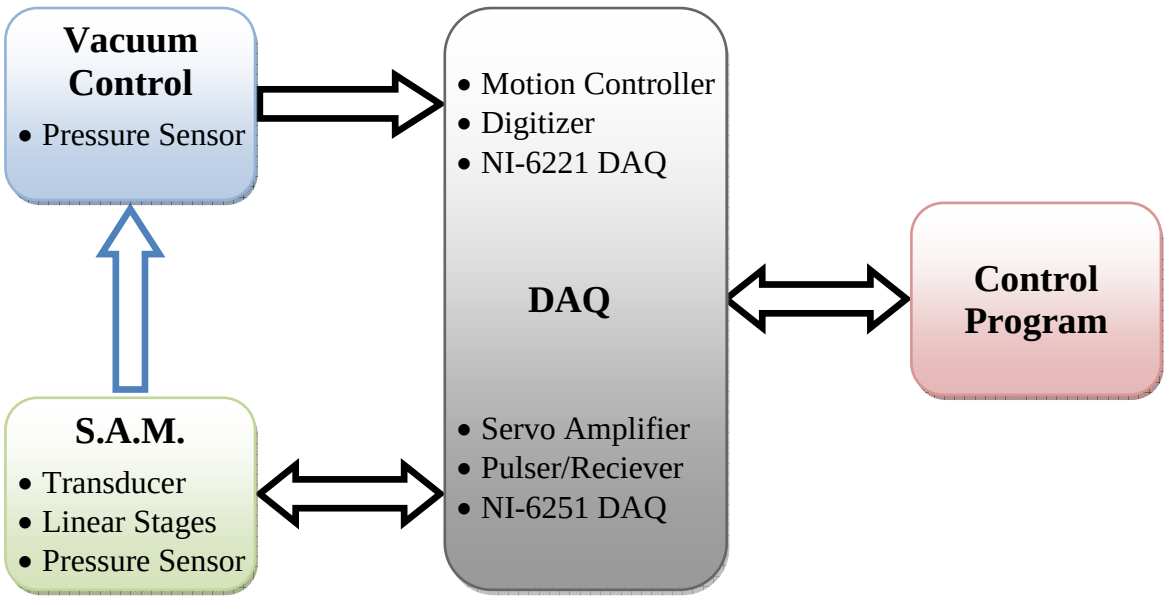

Figure 4.1-1: System diagram showing connectivity.

The PXI-5152 is a $300MHz$ bandwidth digitizer which is responsible for acquiring the amplified echo signals from the pulser/receiver. It is equipped with two channels capable

of sampling at $1GS/s$ but can achieve twice that rate if used in real time interlaced sampling mode. Acquired data are stored with 8 bits of vertical resolution in onboard memory, $64MB$ per channel allowing buffering of data to the computer. The bandwidth of the 5152 is more than adequate given the frequencies of interest for the experiments performed do not exceed $50MHz$. Additionally, the $64MB$ allows for $6.5mm^2$ worth of scan data before off loading to the computer is required, assuming standard scan parameters. This becomes useful when high scan rates are limited by time consuming data transfers. Transmitting blocks of data at specified periods increases overall data transfer and scanning rates.

For motion control, the PXI-7344 module was chosen. It is National Instrument's mid range motion controller with 4 axes of control, each configurable for stepper or DC motors. Some of the features include blended motion, electronic gearing, and 2D/3D interpolation. Motion commands from the user are interpreted by this module where PID control loops and signal conditioning circuits generate and route motor control signals to the servo amplifier. In addition, feedback from the linear stages like encoder pulses and limit switches are managed through the motion control module.

National Aperture was chosen to supply the linear stages used for transducer positioning. The selection process came down to three basic compromises, speed, accuracy, and cost. With multiple solutions from various companies the 3M series stages were chosen, specifically the MM-3M-EX stages. Two models were needed, one with an anti-backlash (AB) nut and one without. Without the AB nut the stage has an advertised positional accuracy of $\pm 3\mu m$, a resolution of $\pm 0.5\mu m$, a max speed of $6mm/s$, and a backlash of $50\mu m$. With the AB nut the positional accuracy becomes $\pm 1.5\mu m$, resolution to $\pm 0.124\mu m$, max speed to $1.65mm/s$, and the backlash is reduced to $3\mu m$. Increases in accuracy and resolution are seen with the AB nut but at the loss of max translation speed.

Encoder signals are used for positional feedback to the control software where synchronization between mechanical motion, pulse generation, and signal acquisition are managed. Trigger signals are generated and sent to the digitizer and pulser/receiver based on a set interval of encoder pulses. The mid range motion controllers are capable of this but the count has to be reset in software after each trigger generation, reducing the max loop rate to $100Hz$. Given that the selected linear stages have a half micron encoder resolution and a

translation speed of around $4mm/s$, the input encoder frequency will be approximately $8kHz$, exceeding the mid range motion controllers limit.

This has been resolved by assigning this task to the counter/timers on a PXI-6221 DAQ module, the third module of the PXI chassis. It provides 16 single ended or 8 differential analog inputs with 250KS/s sampling rate at 16 bit resolution, 2 analog outputs at $833KS/s$ with 16 bit resolution, 24 digital I/O at 1MHz, and 2 counter/timers with 32 bit resolution at $80MHz$. It is responsible for counting the encoder pulses and in some operational modes trigger generation.

Given the inability of the DAQ module to simultaneously acquire analog voltages and monitor encoder pulses and trigger generations a second DAQ module was needed to measure the pressure sensors. This second DAQ module is contained within the computer as a PCI card and posses similar specifications to the PXI-6221.

A local Rochester company, JSR Ultrasonics, supplied the pulser/receiver which manages the operation of the transducer. It generates the high voltage spike needed to induce an acoustic pulse from the transducer and also receives and amplifies the echo signals. The specific model is the DPR35E which has two operational modes, pulse/receive and through transmission. The latter requires two transducers, one for pulse generation and the other for reception while the pulse/receive mode use a single transducer for both functions. Various settings are configurable through serial communication with the PC. These include pulse energy, signal amplification, frequency filtering, and other operational parameters. Pulse generation can be triggered either externally or internally with adjustable repetition frequency.

Figure *4.1-1* also groups the components responsible for controlling the pressure differential across the sample. It consists of a vacuum pump, a bell jar, water/air separator, pressure adjusting needle valve, pressure sensor, a ball valve, and the necessary plumbing.

The vacuum pump used can generate up to $20inhg$ of vacuum but can produce significant oscillations in the output. These transient pressures are minimized through the use of a large vacuum reservoir, the bell jar. Besides smoothing the vacuum levels of the system the bell jar also helps maintain a constant pressure value when opening the valve to the waterbath vacuum chamber. Having a relatively large supply of low pressure air compared to the volume of the waterbath vacuum chamber sectioned off by the ball valve minimizes the

equalization effects. The importance of which stems from the method of dialing in the desired pressure differential across the sample.

With the waterbath vacuum chamber sealed the closed system is brought down to a specified pressure. The reservoir pressure is measured and recorded using a single calibrated silicon pressure sensor. While the pump maintains a constant flow rate, a series of needle valves relieving the system are used to control the internal pressure precisely. When the desired pressure is achieved the ball valve is opened, subjecting the waterbath vacuum chamber to the low pressure system. There is an initial equalization of pressure between the two volumes but the response is quick with a smooth settling to a steady state condition.

Figure *4.1-2* depicts typical pressure plots for the reservoir pressure and the differential pressure measured across the sample.

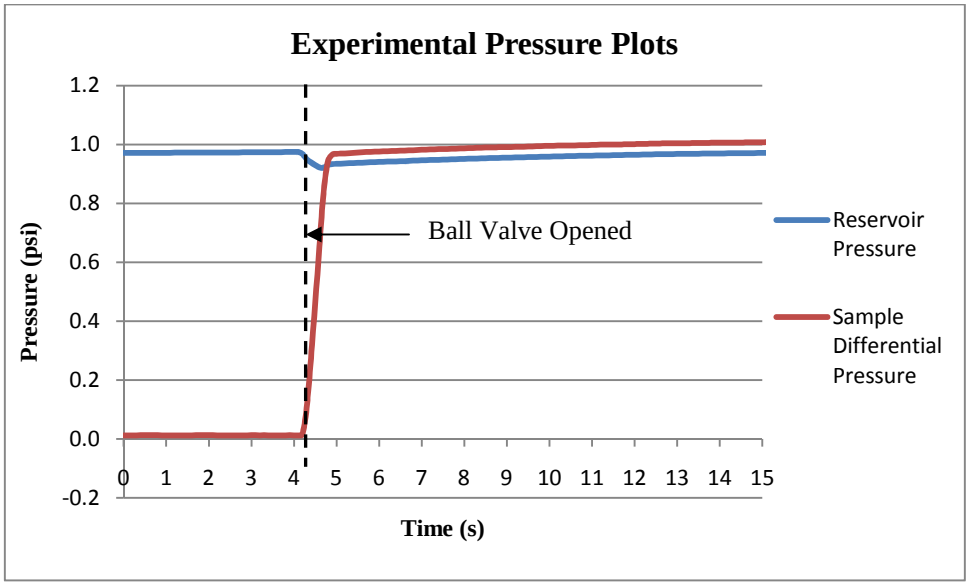

Figure 4.1-2: Example plots of typical pressure equalizations.

The plot shows a differential between the two steady state pressures. This is accredited to the hydraulic pressure of the water above the sample. This differential pressure is the numerical difference between the vacuum chamber pressure and the water pressure at the sample/water interface. A single differential pressure sensor is used to measure these two

pressures. For a given water level the pressure in the vacuum reservoir prior to a scan is adjusted accordingly to ensure the desired differential pressure across the sample is achieved.

The microscope itself is a uniquely designed piece of equipment. It is responsible for transducer positioning, diffusion media support, water management, and pressure application. The design consists of two separable sections, the upper stage and the lower base. Four half inch diameter case hardened carbon steel rods provide rigid rails for the two sections to orient themselves.

The upper stage consists of two motorized linear stages, a single manual micro linear positioner, and support structure made primarily out of quarter inch thick Aluminum 6061. Polytetrafluoroethylene (PTFE) sleeve bearings make a semi-elastic low friction connection between the four guide rods and the upper stage. The tolerances of all relevant part features where calculated to ensure a maximum positional error of $1\mu m$ at the transducer focal point over the full six inch slide path of the upper stage. The parallelism of the upper stage to the base is also of concern. Angled set screws in the upper plate bearing seats and relief slots on the middle plate provide a measure of adjustability to the relative angle of the upper stage. In order to maintain a relative 1% error in focal distance over the one inch translation of the transducer the upper stage must maintain a parallelism of $0.016in$ or 0.135°.

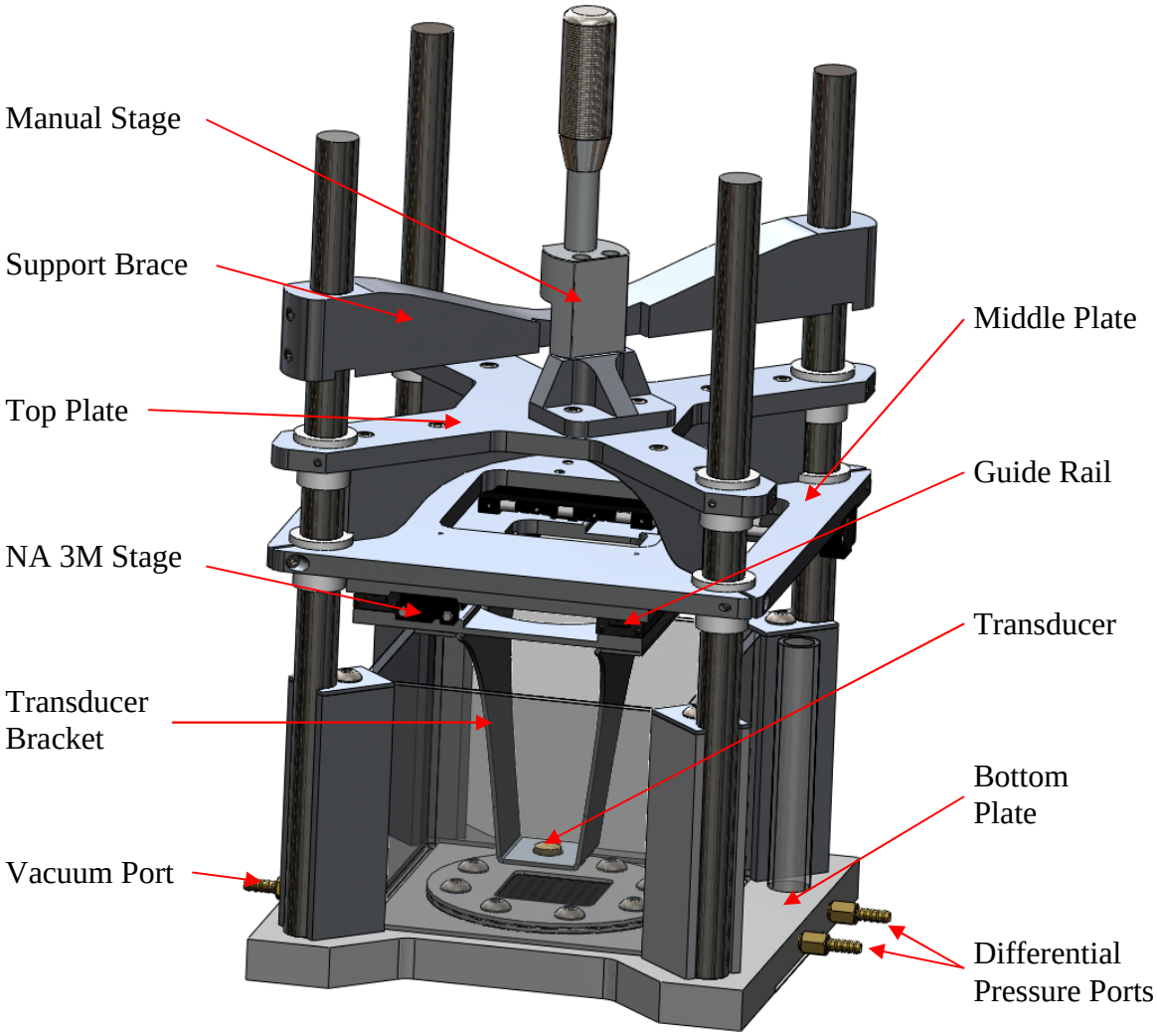

Figure 4.1-3: S.A.M. Part Label.

The motorized translation assembly is mounted to the bottom of the middle plate and consists of the two National Aperture 3M stages, four SMI XRS32-9 cross-roller guide rails, and the associated adapter plates; the design of which allows for multiple transducers to the utilized. The two stages are mounted perpendicular to each other and offset from the center. The cross-roller guides relieve the linear stages of any forces they might be subjected to other than those directly parallel with their translation axis. All four, two per axis, are pre-tensioned, providing near zero slack between the mounting rail and fixture points

The other half of the microscope provides the means for all other functions other than transducer positioning. The primary component of the base which all other parts are referenced is the bottom plate.

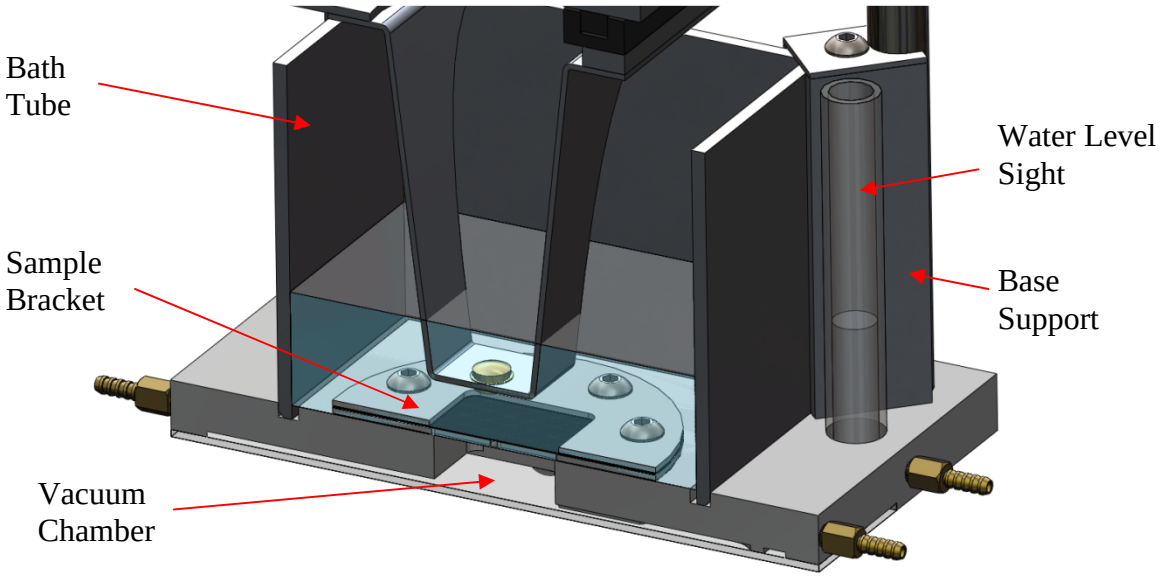

Figure 4.1-4: Cross-sectional image of microscope base.

This bottom plate is a $6x6x0.5in$ thick piece of Aluminum 6061 that houses the vacuum chamber, ports, and fastening holes for all connected parts. Sitting on top is an eight inch thick square Aluminum 6063 tube with 4 inch sides standing three inches tall. This bath tube holds the coupling water and provides the lateral support for the guide rods in conjunction with the base support bars.

The final primary components are the two sample brackets that hold the diffusion media in place. Both are $0.05in$ inch thick Aluminum 6061 $3in$ diameter plates with eight bolt holes for compression mating to the bottom plate. The bottom bracket has a $2x11$ grid of $1mm$ wide by $12.9mm$ long slots providing support of the sample while allowing water to pass through. The top bracket differs in that the grid area of the bottom bracket is replaced with a $1.12in$ square opening. Sealing is achieved with $0.005in$ thick PTFE gaskets on all contacting faces.

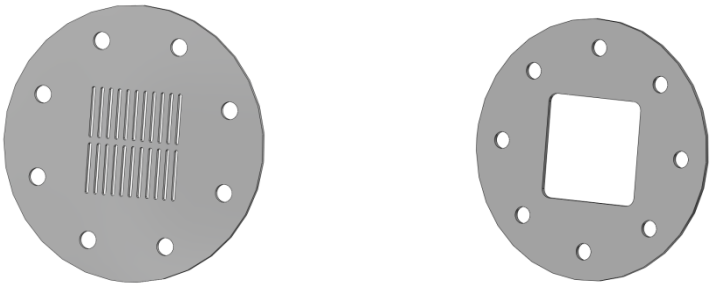

Figure 4.1-5: Sample Brackets. Bottom (Left) and Top (Right).

4.2-Control Logic

All the control software was programmed in LabVIEW (*Laboratory Virtual Instrument Engineering Workbench*), a visual programming environment which uses pictorial icons to represent blocks of code. These VI's form the basis of any program and are interconnected through lines or wires to form the desired program. The flowchart resemblance and intuitive assembly nature provides an advantage over text based coding. The program is ideally tailored to measurement, test, and control based experiments with preprogrammed VI libraries for mathematics, signal processing, analysis, visualization, etcetera. Being a product of National Instruments the connectivity and integration with all of their hardware is ensured along with many other third party providers. For all these reasons LabVIEW was the programming language of choice.

There are two primary programs written for the project, SAM-Scan and SAM-Data. As the names suggest the two differ in their primary objectives and have been separated to optimize the user interface functionality and program operation. The data collection program, SAM-Scan, is responsible for all motion control, DPR35E communication, trigger generation, and data logging. After a scan is complete and a review of the data is required the data processing program, SAM-Data, is used. This program reads the raw data collected and is capable of multiple processing schemes.

4.2.1-SAM-Scan

SAM-Scan provides the control for proceeding with a scan and logging the data. Its functions are all based on performing and supporting various types of scans. These include B-scans and C-scans using two types of motion control logic and three different beam profiling scans. The front panel is laid out with two sections, one side housing most of the controls and the other side contains all the feedback displays relevant to a scan.

To start a scan the settings for all the external hardware need to be set appropriately. This includes the digitizer, motion control module, and the pulser/receiver. The digitizer settings are all those pertaining to capturing the echo signals after amplification from the pulser/receiver. Settings for the transducer motion include everything from acceleration and deceleration values for the linear stages to PID loop iteration time. The pulser/receiver settings control is a little different in terms of programming since the communication to and from the computer are over a standard RS-232 com port. The other two devices are integrated into the PXI chassis so pre programmed VI's handle the communication protocol. Eighteen commands for the pulser/receiver were programmed into SAM-Scan which covers all functions of the device.

Scan path generation is also handled within the program. To define the desired operation the user can select the scan type and input the relevant parameters. After the scan area and pixel size are defined the program generates a list of coordinate points used to direct the linear stages. The resulting path is displayed to the user along with stats about the scan like the number of pixels and grid dimensions. Once the scan is initiated the program calls upon one of three different motion control loops which are responsible for transducer positioning and synchronization of motion with acoustic acquisition, details of which are described in section *4.3*. While motion of the transducer is defined and controlled by the program in B-scan and C-scan modes, the user has control when operating in M-scan mode. During the continual transmit and receive process the position of the transducer can be changed by either of two methods, keyboard arrow key inputs or direct coordinate input. All scanning modes are supported with real time axis feedback which includes stage position and a detailed cluster of its status.

During a scan the raw A-line signal is recorded and depending on the type of scan a number of operations are applied. For all scan types the envelope of the A-line signal is calculated and displayed. The frequency content of the signal is also calculated with an option for an additional short time Fourier transform which brackets the signal into time segments, displaying the frequency content as a function of time. Given its increased computational cost this feature is selectable. For M-scans, pulse measurements are available which identify envelope peaks subject to user defined parameters and their corresponding amplitude and location. Separation measurements are made between two cursors on the graph; one locates identified pulses while the other is positioned by the user. This provides a quick method for calculating the relative difference in both amplitude and depth for two A-line features.

Recorded data are saved in a LabVIEW specific file format referred to as TDMS *(Technical Data Management-Streaming)* which allows for storage of data on a binary level for fast write and read operations while a secondary header file is used to store file information and data descriptions. All settings and scan options are saved along with the captured data. Not only does this ensure all parameters of the scan are known but the data analysis program relies on this information to proceed with certain analyses without manual input from the user. The raw data recorded are the A-line signal, positional data, pressure sensor voltages, and time stamp data for synchronization.

During operation the program relies on correlations data for each sensor to convert the measured voltage values to the corresponding pressures. The user from within SAM-Scan can import correlations for each pressure sensor at which point a linear or polynomial fit of any order can be applied. The fit equation coefficients are then updated for use within the program. The same is true for SAM-Data where the sensor voltages are read from the data file and the correlations are used natively to obtain pressure values.

4.2.2-SAM-Data

The data processing program is responsible for all aspects of data processing, analysis, and management. With multiple processing modes and analysis options the program

provides a powerful tool for exploring scans and new hypotheses. To start, the program allows for analyses on a single file or for multiple file comparisons. Data can be represented in a number of ways, from 1D numerical displays to 3D plots of multi-dimensional results.

Like SAM-Scan, the user interface is split in a two segment screen lay out, the right side containing most of the controls while the left side has most of the graphical displays and plots. Each side has multi layered tab controls for space management, eliminating the need for scrolling to view the desired feature. This method, however, was not sufficient to accommodate the growing program in its development. To resolve this, control subVI's were used as popup menus which store the feature settings in global variables for access elsewhere in the program. Other than primary controls, most options and feature settings reside in these control subVI's.

The first programmed feature of SAM-Data was to use LabVIEW's own TDMS viewer. This allows the user to select any single TDMS file and view the contained information along with secondary header information. Additionally, the program has the ability to read in and edit any header data within the file without having to manually input details of the file before processing the data. The file header contains all the relevant information and settings from the acquired scan including a section for comments.

Before opening and processing a data file the user has the option to apply a number of operations to the raw data. These include A-line frequency domain filtering, nonlinear compensation, gain correction, and a few others. Settings for pulse detection, data decimation, and pressure data management are also adjustable by the user. After the appropriate options are set the program reads all the raw data into virtual memory and processes the A-line data. The corrected data are then stored in global variables where easy access is available to other operation in the program. Upon completion all A-lines are accessible for display. When an A-line is requested the envelope, frequency content, and unprocessed A-line are displayed. Pulse measurements can be preformed where amplitude and arrival time are calculated. With a secondary cursor on the graph the user can easily find the same information at any point in the acquired signal. The separations of the two points are automatically updated and displayed in both time and distance based on the specified pulse propagation speed. The spatial location of the selected A-line is also presented with

numerical indicators and on a scan path plot which shows the location of every acquired signal graphically.

Representative cross-sections of the scanned object are displayed on intensity plots for both C-scans and B-scans. While B-scan plots are rather straight forward, taking a single B-line data set and displaying the envelope intensity values versus time and location, C-scan image generation requires more definition. The four dimensional scan data are to be presented in a three dimensional fashion, representing a block of envelope values with a time-gate on the A-line signals effectively reduces the data dimensions to three. The program provides four different methods of quantify the selected A-line time-gates. It will either calculate the average envelope value within the time-gate, its maximum, or simple the value at an instantaneous time. The fourth option is to take the backscatter within the time-gate. This is simply the squared values of the envelope signal integrated over the defined time-gate.

The program features a number of secondary analyses which can be applied to the loaded scan. The available operations depend on the imported scan type. For all scans surface plots, peak trends, average spectrum, B-line backscatter, and backscatter ratios can be calculated. All of which provide different insight into the characteristics of the scan. For specialized scans like beam profiles and noise quantification scans more processes are available to the user which address their particular objectives. When interested in comparing the results of these secondary analyses with other scans the program provides a number of multi-file processes. Most of the available options simply perform one of the secondary single file analyses on a series of scans and store the results of each for review. The image difference and scan correlation processes, however, require a series of scans in order to proceed. Both use set files for references when operating on the others.

After the results are calculated the user can export the data for storage or further review. Numerical results are exported to tab delineated text files. Each is generated with a header containing pertinent information about the data. The user can choose to decimate the data and define the format of the exported numbers. Images can also be exported and saved in a number of formats. The user can define the color scale, normalization method, and image depth used. Image series are also managed nicely, exporting all in a single step and incrementing the file names.

For large scan files all these data can take up a lot of virtual memory. LabVIEW is designed to manage data in a conservative fashion, making copies of data arrays every time it is accessed or operated on. This ensures safe management of the information but it also means that the original data size is multiplied throughout the program, limiting the available memory. There are programming trick to limit this data multiplication but significant reductions are almost impossible. For large scan files virtual memory fills quickly. To counter this SAM-Data has two data management methods, Virtual Memory and Harddisk Hybrid. The first uses the standard method of storing data in virtual memory, providing fast read and write operation. The Hardisk Hybrid method reads and writes data to and from the hard disk is blocks. This limits the amount of total stored data in virtual memory, increasing the available virtual memory but decreasing the processing time. For most scans acquired in this research the Harddisk Hybrid method in not necessary.

4.3-Operational Modes

The operational modes describe the three programming techniques used to complete various types of scans. B-scans and C-scans can be performed using the continuous or iterative methods; both time and accuracy desired determine the method of choice. The beam profile scans, however are performed using the iterative method given the need for precise positioning and sub resolution pixel sizes. The third mode, M-scans, are a separate type of scan altogether and will be discussed along with the other modes in the following sections.

4.3.1-M-Mode

M-mode scans differ from the other two scanning modes in that there is no translation of the transducer. Repetitive transmit/receive operations are performed at regular intervals for a single location. Each capture A-line envelope is then plotted on a brightness display where echo intensity is plotted on a depth versus time grid. M-scans can be used to detect motion in the acoustic beam by tracking the changes in the A-line signals over time. An example being the measurement of heart valve motion, a common medical ultrasound procedure.

In this mode the pulser/receiver generates the trigger signals as these will be used to synchronize the digitizer to the acoustic pulses. With a set pulse repetition frequency (PRF) the captured A-line signals are averaged over a specified number and displayed in real time. Averaging of the signal helps reduce the unwanted noise and with a $5kHz$ max PRF a hundred A-lines can be averaged and displayed in just under $50Hz$, maintaining a real time refresh rate status. From the averaged A-line the envelope and frequency content are calculated. These three are then plotted along with a brightness image showing the acoustic energy as a function of depth and time.

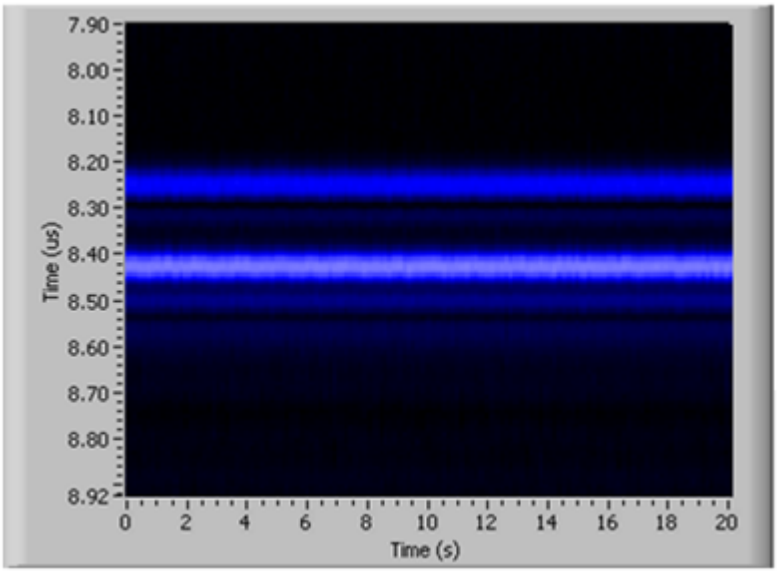

Figure 4.3-1: Example M-scan Brightness Plot.

Live pulse measurements can be performed that identify pulses and calculates their respective amplitudes and arrival times. An estimated pulse propagation speed can be specified allowing the program to estimate the depth of selected pulse features giving the user the ability to easily estimate length scales. This feature becomes very useful when focusing the transducer; verify the distance with echo depth measurements.

Another feature of the M-scan mode is the motion control flexibility. Transducer movement and location can be changed by either entering specific coordinates or by the keyboard arrow keys. Details of the motion control can be specified as well. Stage velocity

and acceleration limits are adjustable by the user and for keyboard inputs the step sizes are also configurable.

4.3.2-Continous

The continuous scanning method utilizes the encoder pulses of the linear stages to generate the trigger signals which synchronize the pulser/receiver and digitizer timing. The encoder signals are routed from the motion control module to the DAQ module where the counter/timer device tracks the pulses received. Using the final drive ratio of the scanning axis linear stage the program calculates the number of encoder pulses that represents the defined pixel size. Using this value the program generates a digital pulse at set length intervals of translation. This method allows for continuous motion of the transducer, reducing overall scan times by 88% on standard settings compared to the iterative method. Both B-scans and C-scans can be run using this motion control method.

The control logic used to seamlessly operate the linear stage motion with the acoustic side of the acquisition is relatively involved compared to the other two methods. Given the nature of the trigger generation the position of the first trigger signal for each scanned line shifts a number of encoder pulses. This phenomenon is due to the quotient remainder left when dividing pixel size by the length transversed per encoder phase pulses. To explain this, an understanding of encoder theory is required.

The linear stages used have a two phase encoder system. This means that two rotary disks are used that have a defined measurement pitch and are aligned 90° out of phase from each other. With one rotor used the distance traveled is calculated based on the number of digital state transitions. This gives a positional resolution of one half the rotor measurement pitch. When considering a two phase encoder system both rotor pulses are compared and all digital transitions are counted, this effectively reduces the positional resolution to one forth the measurement pitch used on the rotors. Since the counter/timer device on the DAQ system can only monitor one phase from the encoder and that only high to low or low to high transitions are considered the positional accuracy of this method is only one forth that of the motion control unit.

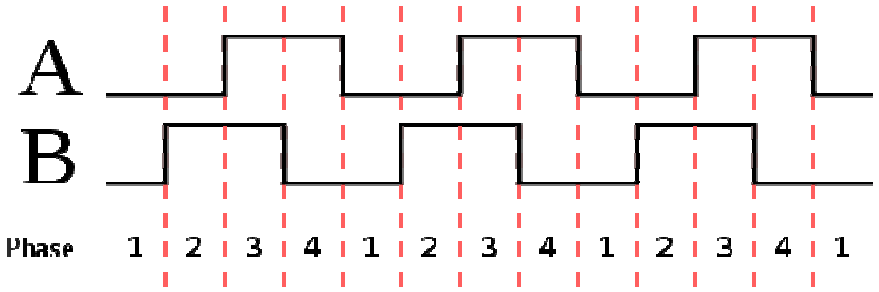

Figure 4.3-2: Encoder phases A and B offset by 90°.

To account for this the system uses a feature called High Speed Capture. This function allows the program to read the instantaneous position of the linear stages based on the more accurate motion controllers accounting of location. For each new line in the transducers scan path the program waits for the first generated trigger at which point the instantaneous location is recorded. These start positions are used with the know trigger separation distance to calculated all the pixel locations down to the two phase encoder accuracy.

The scanning axis used in this mode is the standard stage without the anti-backlash nut. It has an encoder resolution of on a motor gear with a ratio. The stage is connected to the motor through screw shaft with an threads per inch pitch. This results in a positional resolution of per count. This limits the continuous modes minimum pixel size to since the hardware requires at least two timing pulses for each high and low state of the generated trigger signal.

4.3.3-Iterative

For conditions where scan time is not an issue a third scanning mode was created, it is called the iterative mode. The name illustrates the method used for transducer motion. When a scan area is defined with a certain pixel size the program generates a series of coordinates that the transducer must go to. Unlike the continuous scanning mode where motion is uninterrupted this mode instructs the linear stages to stop at each pixel location. This allows

the system to acquire multiple A-line samples at each location where they are averaged before saving the data.

The pulser/receiver is capable of $5kHz$ pulse repetition frequency (PRF) so acquiring 100 A-line samples per location requires only $20ms$. Considering that the last echo signal typically measured is received $10us$ after the pulse is sent there is a remaining $190us$ before the next trigger; a conservative setting allowing any reverberations to dampen out before the next acquisition. Using this averaging scheme a typical scan of $4mm^2$ using a pixel size of $20\mu m$ requires a total scan time of approximately $800s$ or $80ms$ per pixel. So only 25% of the time spent scanning can be attributed to stationary repeated A-line records, the other 75% is spent moving the transducer from pixel to pixel. Comparing this to the previous scanning mode which would require $95s$ to complete the same scan but with no averaging consumes an effective $9.5ms$ per pixel; a significant reduction in scan time but sacrificing A-line signal to noise ratio and positional accuracy.

The velocity and accelerations used for these scans were set to $5{,}000\ counts/s$ and $100{,}000\ counts/s^2$ respectively on each axis. This translates to approximately $2.48\ mm/s$ and $49.6\ mm/s^2$ on the scanning axis and $0.62\ mm/s$ and $12.41\ mm/s^2$ on the perpendicular axis.

Chapter 5: Results

5.1-System Performance Quantification

After the system was assembled a series of tests where necessary to quantify its performance and gain an understanding as to its characteristics. The following sections outline the tests performed and the results collected.

5.1.1-Pulse Characteristics

The temporal resolution and frequency content of the transmitted pulse are important characteristic of the system. Having knowledge of the wave propagating through the target assist in both setup and interpreting the received data. Ideally a hydrophone with a known frequency response would be used to record the transmitted pulse. This would capture the acoustic wave transmitted from the transducer after propagating a set distance in water. The known response of the hydrophone could be corrected for and a pure reading of the wave would be captured.

For simplicity a polished steel plate was used as an acoustic mirror, reflecting the wave back to the transducer for reception. The wave recorded from this method would contain the effect of two transducer response functions including the water material response and the backscatter response from the steel plate. Fortunately steel has a very high acoustic impedance, approximately $Z = 45.4x10^6\ kg/m^2s$ compared to water $Z = 1.48x10^6\ kg/m^2s$. This provides an acoustic impedance mismatch boundary with a 93.7% reflection coefficient. Even though this method does not provide a direct measure of the transmitted pulse it does produce an excellent reference for evaluating the effect of a material placed in the propagation path.

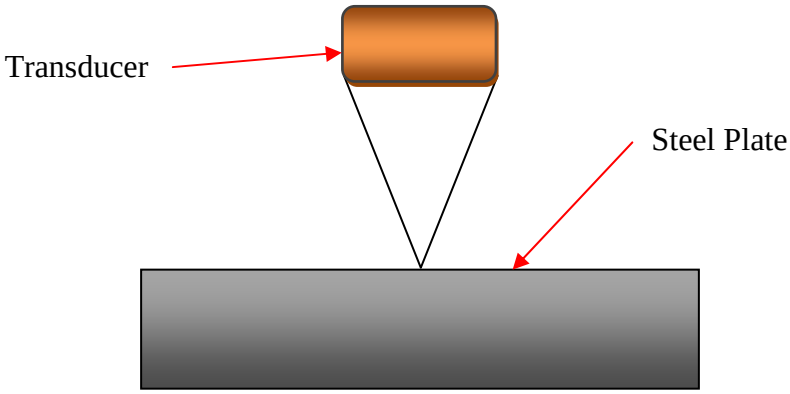

Figure 5.1-1: Pulse Reference Setup.

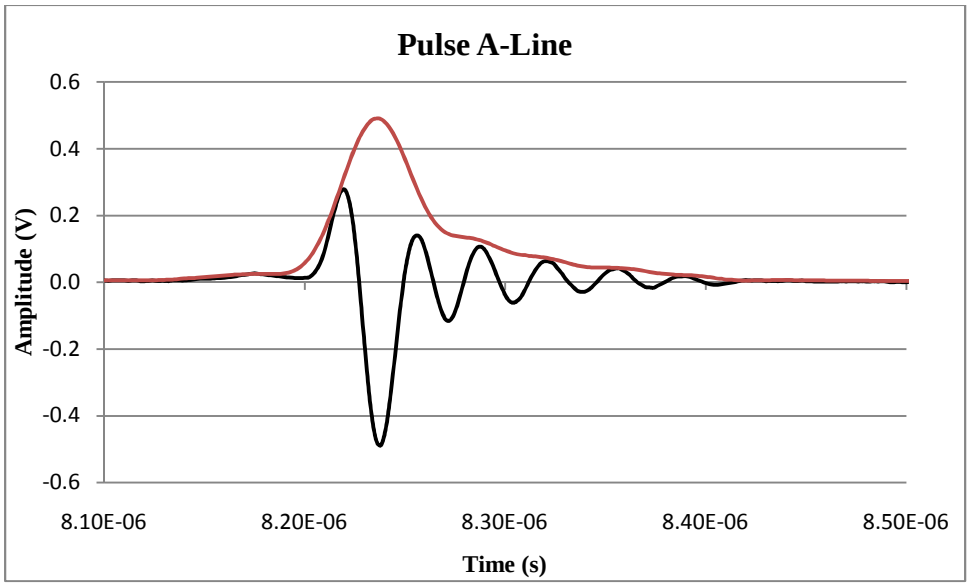

Figure 5.1-2: Received pulse from steel plate reflection.

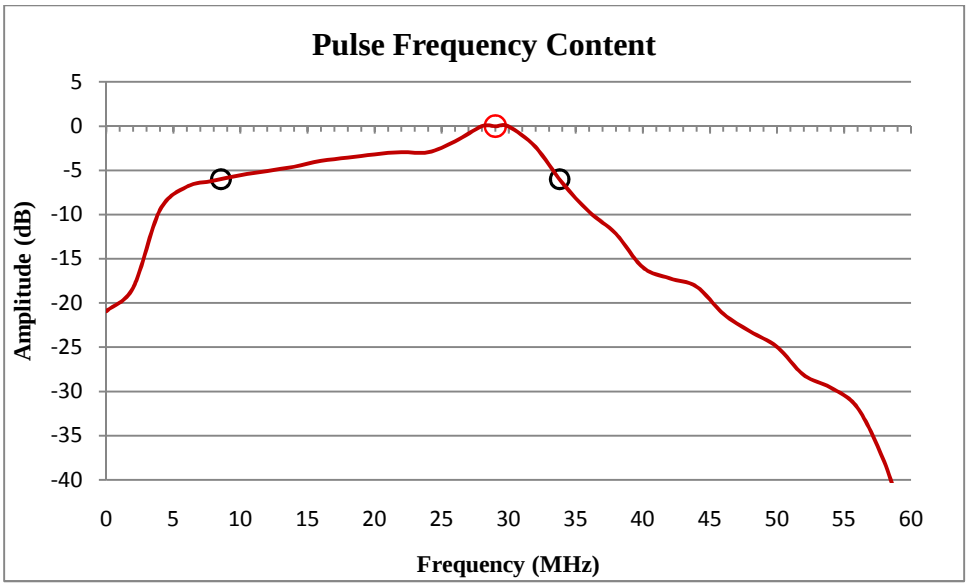

Figure 5.1-3: Pulse frequency response from steel plate reflection.

The data collected from this test revealed a temporal FWHM pulse width of $0.037\mu s$ which translates to a propagation distance of approximately $25\mu m$ in water. The pulse is very damped given its FWHM duration only lasts just over one cycle. Since the pulse duration and frequency bandwidths are inversely related it is expect to have a large frequency range. A Fourier analysis of the received pulse is shown in figure *5.1-3*. The calculated bandwidth of the transducer is $25.25MHz$ with a center frequency of $28MHz$. This gives the transducer a quality factor of 1.109. Quality factor is a measure of the transducers resonant damping where lower values are better for pulse echo imaging, typical medical transducer have values ranging from 2 to 4 [1].

5.1.2- Beam Profile

5.1.2.1- Intensity Map

With the transmitted pulse quantified in both the frequency and time domain the beam intensity map was quantified. This map defines the acoustic intensity as a function of distance from the transducer and radial distance from the beam axis. To capture the relative

acoustic intensity at various coordinate points a $12.5\mu m$ diameter tungsten wire was used as a point source. Like the previous tests the results will not represent the actual pulse amplitude but the backscatter amplitude. It is, however, relevant when considering the spatial relative change.

The test was performed with the tungsten wire suspended in the waterbath with its axis perpendicular to the scanning direction. At varying distances from the transducer a series of B-scans record the pulse echo as a function of radial distance from the wire. A dedicated scan procedure was programmed into the data collection program to facilitate its unique requirements. First, the iterative scanning method is used to allow linear step sizes down to $0.5\mu m$ and A-line averaging. Second, the digitizer time-gate is automatically updated from B-scan to B-scan as the focal distance is adjusted. Since the transducer depth must be adjusted manually the program prompts the user with the required adjustment before the next B-scan is started.

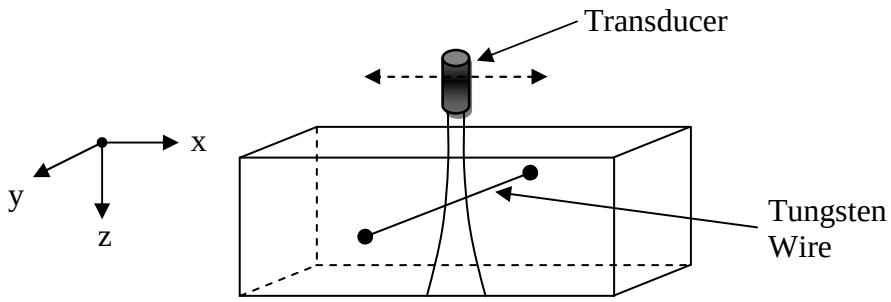

Figure 5.1-4: Beam profile scan setup.

The results of this test define the approximate beam intensity as a function of depth and radial offset from the beam centerline. The first key parameter calculated from the acquired data was the focal point of the beam and its width. It was found to be $6.016mm$ from the transducer face with a FWHM beam width of $89.98\mu m$. The second parameter extracted was the focal zone of the transducer. It is defined by the two half amplitude points fore and aft of the focal point. The transducer in question was measured to have a $0.6mm$ long focal zone, 6.7 times the focal beam width. This characterization of the acoustic beam

ensures proper focusing of the transducer and provides required knowledge for interpretation of resulting images.

It is worth noting the absence of defined side lobes in the measured beam profiles. Given that the presence of side lobes reduce image contrast, lower amplitudes relative to the main lobe is desirable. At the near end of the focal zone this transducer shows a side lobe fractional amplitude of 63% at a radial distance of $60.03\mu m$ from the main lobe peak. In comparison, the side lobe fractional amplitude at the focal point is only 9.7% at a radial distance of $110\mu m$. The results as described above are listed in table *5.1-1*.

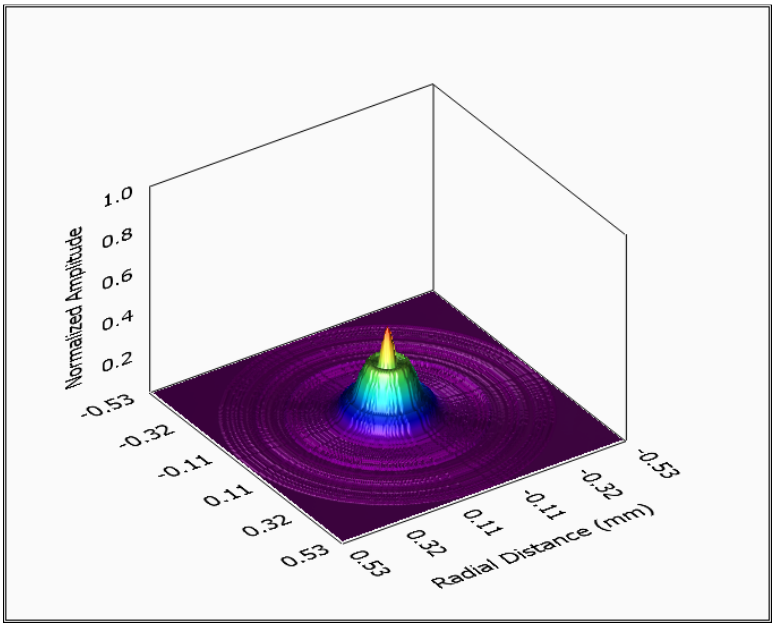

Figure 5.1-5: Near field half amplitude beam profile.

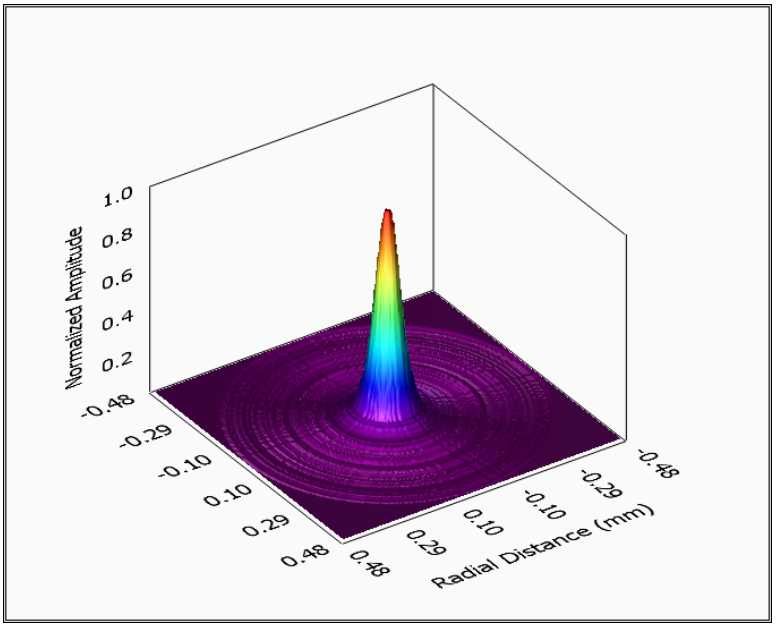

Figure 5.1-6: Peak Amplitude beam profile.

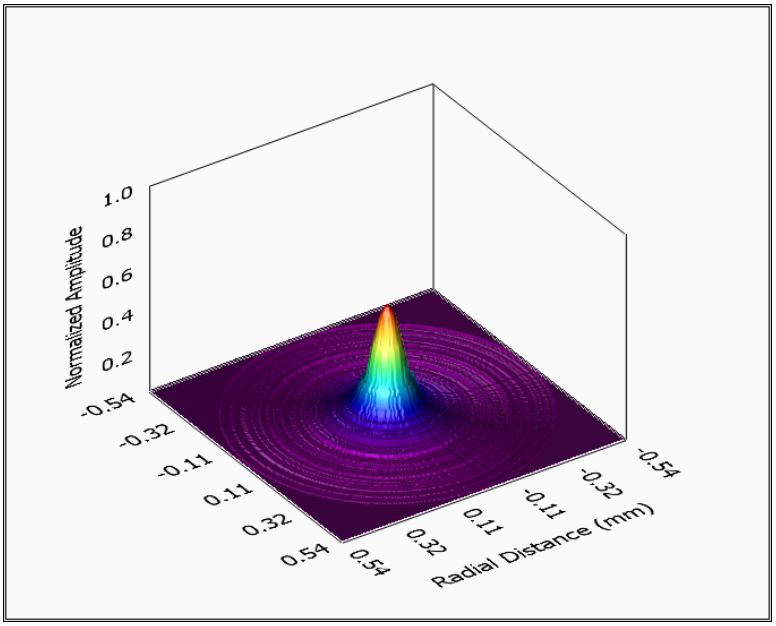

Figure 5.1-7: Far field half amplitude beam profile.

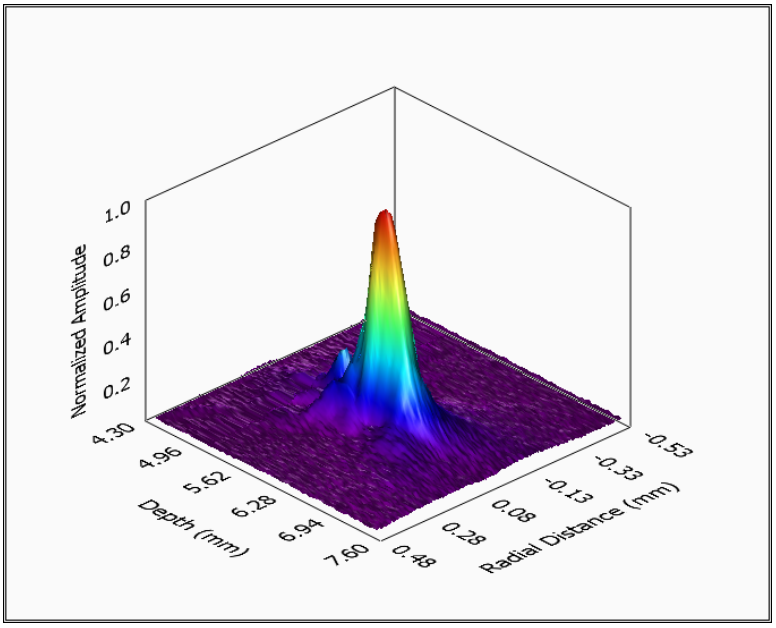

Figure 5.1-8: Beam Intensity Map.

Beam Profile Results			
Scan Depth (mm)	***5.740***	***6.016***	***6.340***
Normalized Amplitude (%)	*50.0*	*100.0*	*50.0*
Normalized FWHM (%)	*146.4*	*100*	*126.5*
FWHM (µm)	*131.72*	*89.98*	*113.86*
Side Lobe Fractional Amplitude (%)	*67.0*	*9.7*	*16.7*
Side Lobe Radial Distance (µm)	*60.03*	*110.01*	*139.77*

Table 5.1-1: Tabulated results of beam profile characterization.

The entire beam intensity plot is also plotted in figure *5.1-8*, showing the large peak in acoustic energy at the focal point. The effects of diffraction are clearly seen especially in the near field where large variations in the acoustic pattern are seen. This figure also illustrates the localized benefit of focusing with the sharp decrease in amplitude and divergence of the beam after the focal point but with significant increase in acoustic energy within the working zone.

The effects of frequency domain filter the A-line signals was also investigated. A characteristic of diffraction is the dependence of the beam pattern on pulse frequency. Higher frequency waves exhibit greater natural focusing so by considering only the higher frequency portions of the received pulse a decrease in the beam width is expected. By applying a high-pass filter with a cutoff frequency of $20MHz$ to the raw A-line data the measured beam diameter at the focal depth was $73.78\mu m$, a reduction of 18%. This method of increasing the effective resolution of the transducer can be applied to all recorded scans but the trade off is a large reduction signal amplitude. In this case the 18% decrease in beam diameter was accompanied by a 62% reduction in received amplitude. Given the large dampening effect of the GDL samples the small increase in resolution is not worth the reduction in pulse penetration.

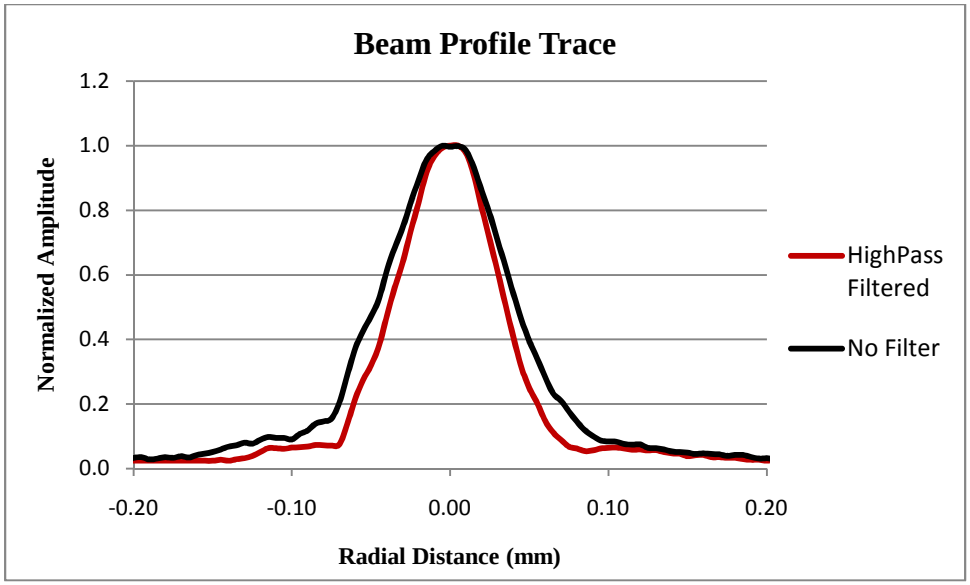

Figure 5.1-9: Beam profiles at the focal depth for filtered and un-filtered A-line data. The applied filter used a hamming window with a low cutoff frequency of 20MHz.

5.1.2.2- Amplitude Trace

Another method commonly used to define the resolution of a transducer is by scanning a sharp edge and examining the resulting echo amplitude decay. The theory states that as the full beam area remains over the top surface of the reflector the maximum acoustic energy will be reflected. As the beam moves across the edge of the reflector the fractional area of intercepted beam reduces, consequently decreasing the peak echo amplitude; the result being a blurred representation of the scanned edge. Considering a transducer whose resolution or beam width approaches zero the expected edge profile captured would converge to the actual shape of the edge.

To confirm the measured resolution from the tungsten wire scans, an amplitude trace was acquired. To ensure that the scan axis was perpendicular to the edge a $2x2mm$ C-scan was taken which revealed a $90.57°$ angle between the egde and the scan axis. This slight offset from $90°$ will result in an estimated 0.005% error in the measured beam diameter, far below any other source of error. At least $8.1°$ off $90°$ would be required for a 1% error due to non perpendicularity.

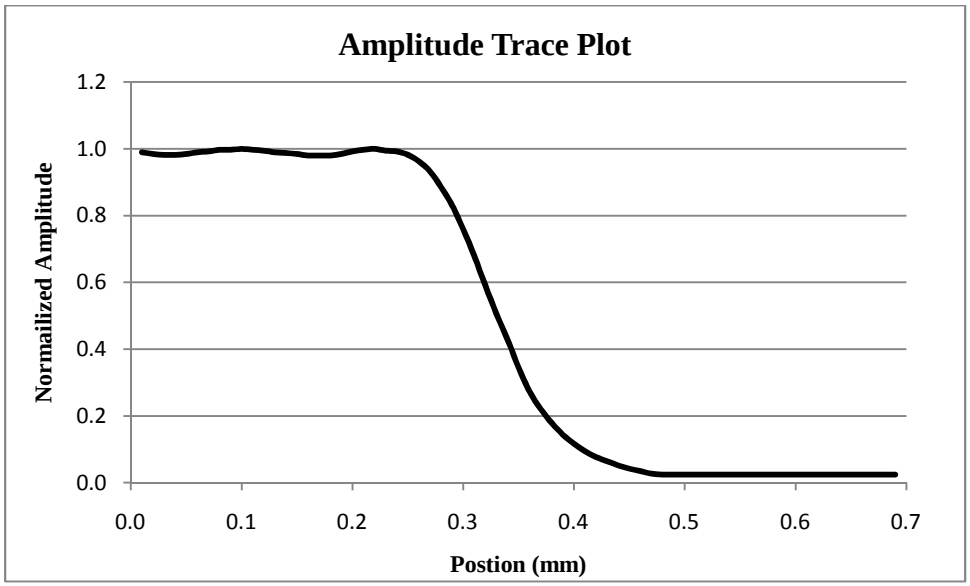

Figure 5.1-10: Trace of echo amplitude scanned over sharp edge.

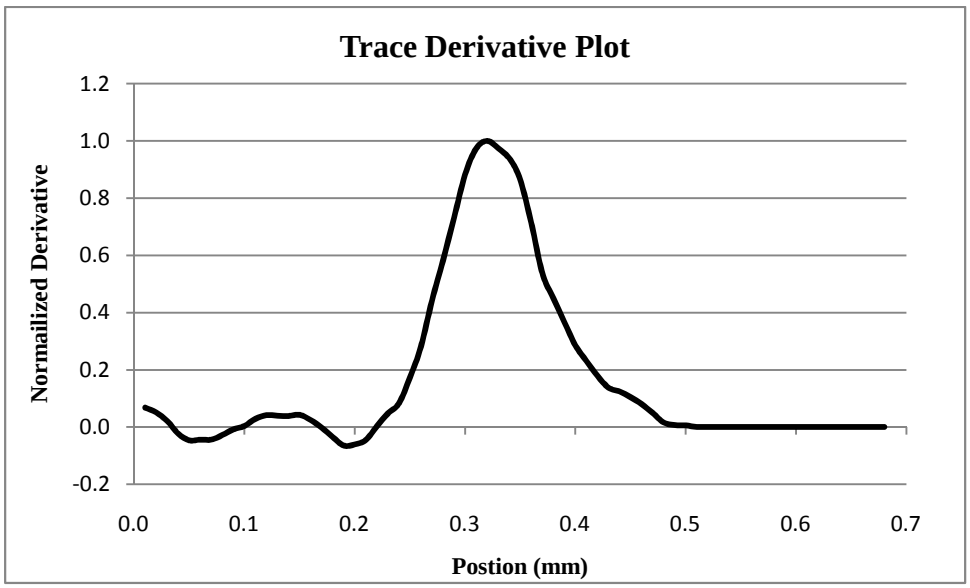

Figure 5.1-11: Derivative plot of echo amplitude trace.

The results showed the transducer's FWHM at the focal depth of $6.016mm$ to be $89.4\mu m$, this compares to the tungsten wire target scans $90.0\mu m$ FWHM measurement. Given that the calculated uncertainty in the measured results was $\pm 1.77\mu m$ the two values are in accord.

5.1.2.3- Dime Scans

During the development of the data analysis program an object with a known geometry was needed to help ensure the proper operation of some of its features. The objective was to recreate the three dimensional shape or surface of an object from the acquired data. A dime was chosen for these scans given its large acoustic impedance difference with water and its anti-symmetric stamped surface features. These two characteristics make the dime ideal for acoustic surface reconstruction.

Two example images are shown in figures *5.1-12* and *5.1-13*, illustrating the system's ability to reconstruct the dimes surface in two different locations. Figure *5.1-12* showing the liberty text and FDR's face was acquired using a pixel separation of $100\mu m$ over a

$10x10mm$ area. The scan area for figure *5.1-13* was $4x7mm$ using a pixel separation of $40\mu m$, both providing adequate resolution for capturing the desired surface features of the dime.

Figure 5.1-12: Reconstructed dime surface.

Figure 5.1-13: Backscatter plot of dime scan.

5.2-Investigative Section

The next section will discuss the first acquired scans after the acoustic microscope system was fully operational.

5.2.1- Initial Scans

To get a feel for the acoustic response from GDL samples the M-scan mode was first used, allowing the freedom to acquire acoustic samples from different locations while tuning the systems settings for optimal transmission and reception. These initial investigations provided a good understanding as to the typical response and how it can vary from one location to another. An example of this is depicted in the two plots below, showing the samples high degree of acoustic response variability.

The echo signal from location A illustrates the effect of phase sensitive interference as discussed in section *3.2.1*. When considering the source pulse, figure *5.1-2*, it's clear the response is the product of individual reflections within the GDL interfering with each other, distorting the physical media relation. For signals that resemble the response from location B, it stands to reason that the large initial echo is due to air pockets on the order of the beam diameter, reflecting most of the acoustic energy from the first water/air boundary.

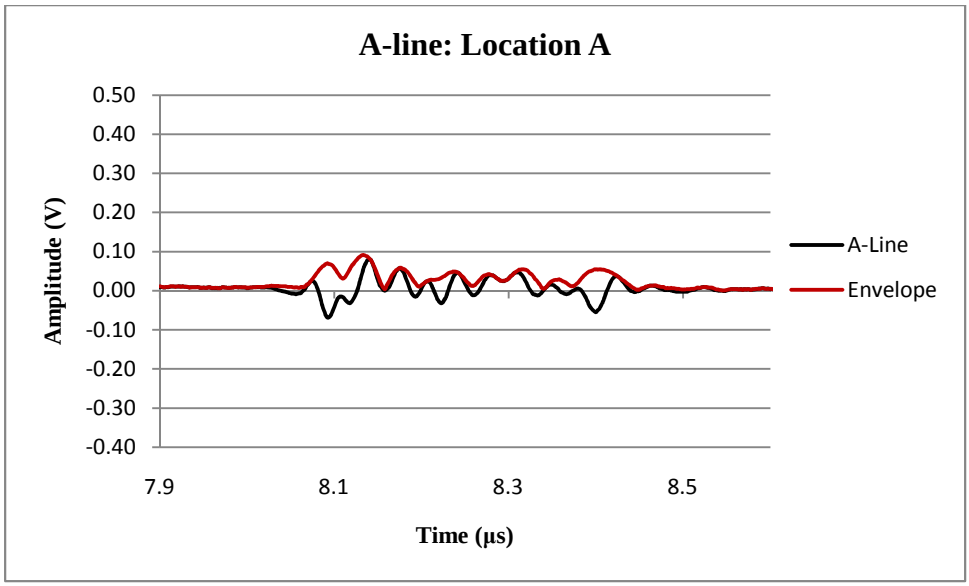

Figure 5.2-1: A-line samples from Toray -120 Plain. GDL C-scan_144.

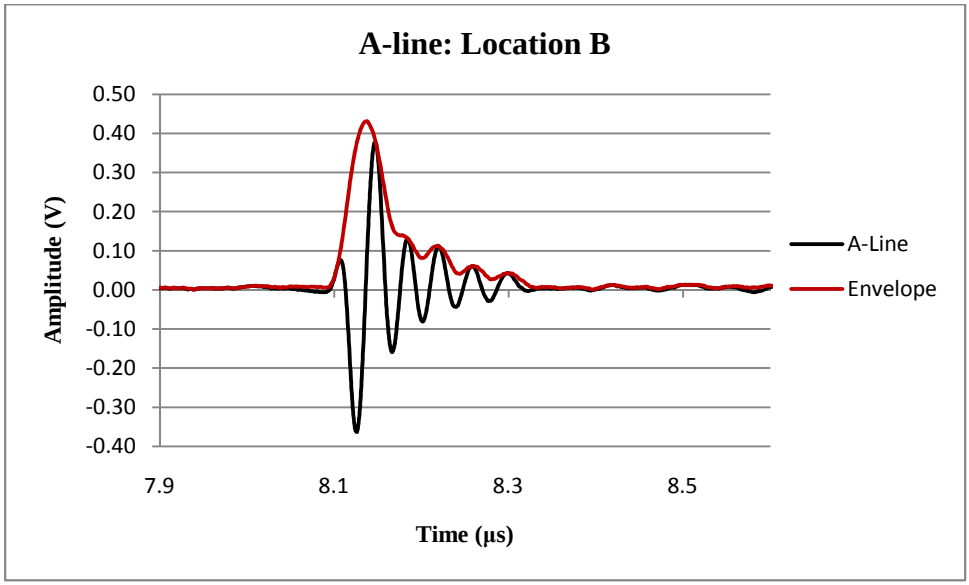

Figure 5.2-2: A-line samples from Toray -120 Plain. GDL C-scan_144.

Having observed the characteristics of the received echo signals the next step was to visualize its spatial variation and to identify any patterns that might present themselves. Figure *5.2-4* shows a B-scan taken with set pixel separation of $40\mu m$ over a $15mm$ scan line.

The sample was placed in the waterbath at which point water was manually pulled through the sample to introduce water into the microstructure matrix. The resulting B-line image showed a clear region of acoustic reflectivity within the GDL. Its structure was grainy and seemed random in nature making interpretation as to the physical structure difficult. Given the knowledge that the acoustic resolution is about nine times that of the individual fibers and their clustering ensures multiple scatterers within the resolution cell, constructive and destructive interference between individual reflections is expected. The result is speckle instead of clear reflections defining the microstructure. An optical image of a Toray-120 GDL is displayed in figure *5.2-3* with a $90\mu m$ red dot illustrating the relation between the sytem resolution and the feature sizes of the GDL microstructure.

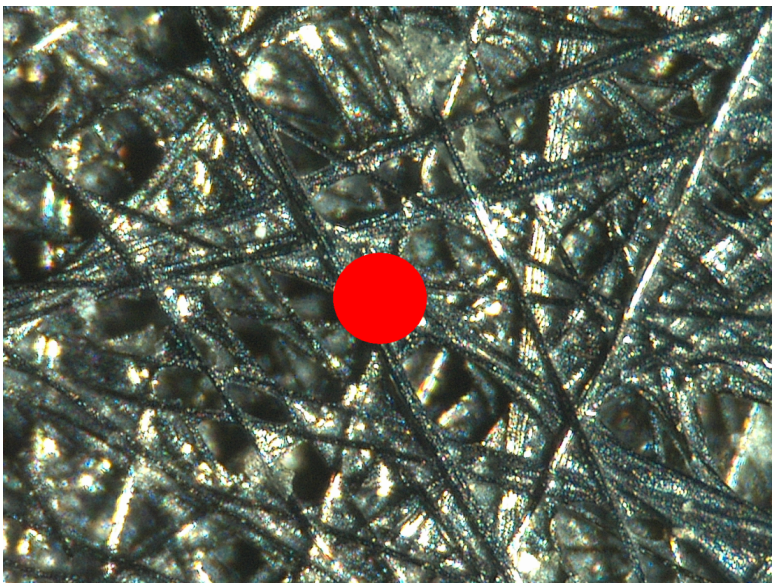

Figure 5.2-3: Optical image of Toray-120 GDL with 90 micron diameter dot (0.8x0.8mm).

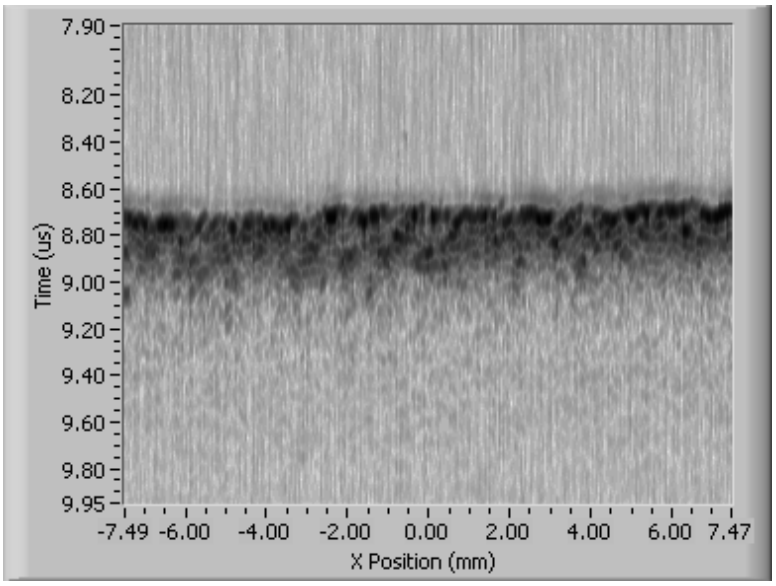

Figure 5.2-4: B-scan of Toray-120. GDL-B-scan_16.

Another observation was that the apparent penetration, defined by the maximum depth of significant echo signals, was highly dependent on the saturation of the GDL. The first sets of tests were performed on GDL samples that were considered either dry or wet based on whether they were vacuum saturated or not. The exact pressure drops across the samples were not recorded for these preliminary investigations; the objective was to observe any changes in the acoustic character as the saturation changed.

5.2.2- Saturation Imaging

5.2.2.1- B-scan Videos

From the first investigative scans of dry and wet GDL's it was observed that two characteristics of the B-scan images change. The first was that the amplitude of the first echo reduces in most locations along the scan line and the second was that the apparent penetration of the acoustic wave was increased. Intuitively this suggests that the air trapped within the pores of the GDL is being displaced by the water. Given that water/air boundaries

reflect ~99.9% of the incident energy, reducing the ratio of air within the insonified area will reduce the total reflected energy leaving more to be transmitted into the GDL.

In an attempt to capture the changes in the acoustic reflectivity a series of rapid consecutive B-scans were performed while water was being pulled through the GDL. For each test, which consisted of Toray GDL's with 20% PTFE loading, the samples started relatively dry. That is, the only pressure drop applied across the GDL thickness before scanning was due to the water head, approximately $2 in H_2O$. The acoustic microscope was set to acquire 30 B-lines of a single $2mm$ line segment of the GDL, each requiring $400ms$ to complete providing a refresh rate of $2.5fps$. During the scan, an increasing pressure differential reaching approximately $2psi$ was applied across the GDL thickness.

The results showed the progression of the acoustic backscatter, reducing with increased pressure. It was observed that coherent regions of high acoustic backscatter where present in the B-line images. As pressure was applied some of these regions reduced in size and some appeared to have shifted depth, moving toward the vacuum chamber. Intuitively, these regions of high acoustic reflectivity are pockets of air within the GDL and the changes seen are due to the forced displacement of air by the incoming water. The problem with this statement is the uncertainty in the signal interpretation. Given that the microstructure features are not resolvable with the current system resolution and that multiple scatterers are present in the acoustic resolution cell, the signal in subject to phase sensitive interference, rendering traditional ultrasonic object detection unreliable. However, the large difference in acoustic reflectivity between water/air boundaries and interfaces involving the samples microstructure provide large echo signals from air pockets, possibly overshadowing the random speckle amplitudes.

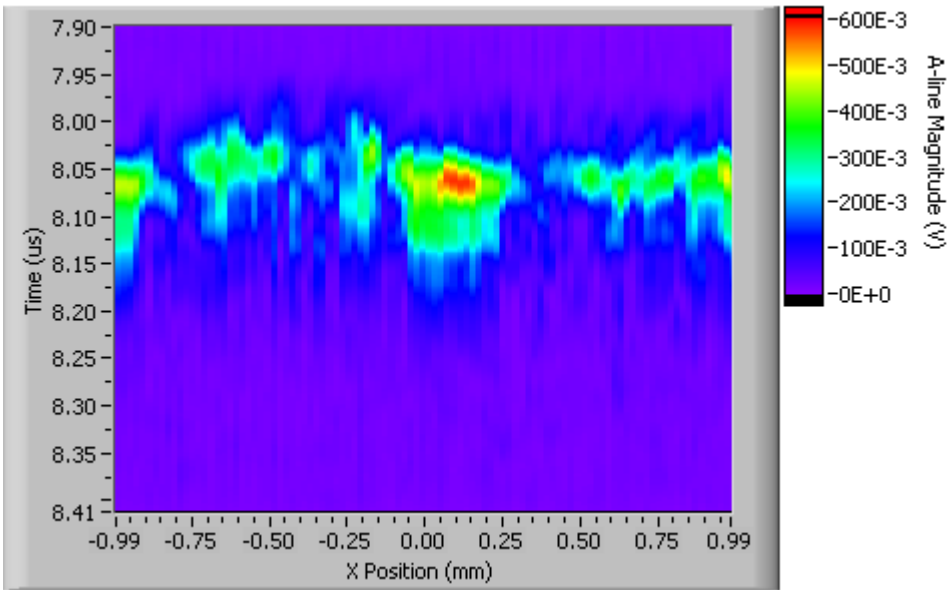

Figure 5.2-5: Video image results for frame 1 of Toray-060 with 20% PTFE. GDL-B-scan_48.

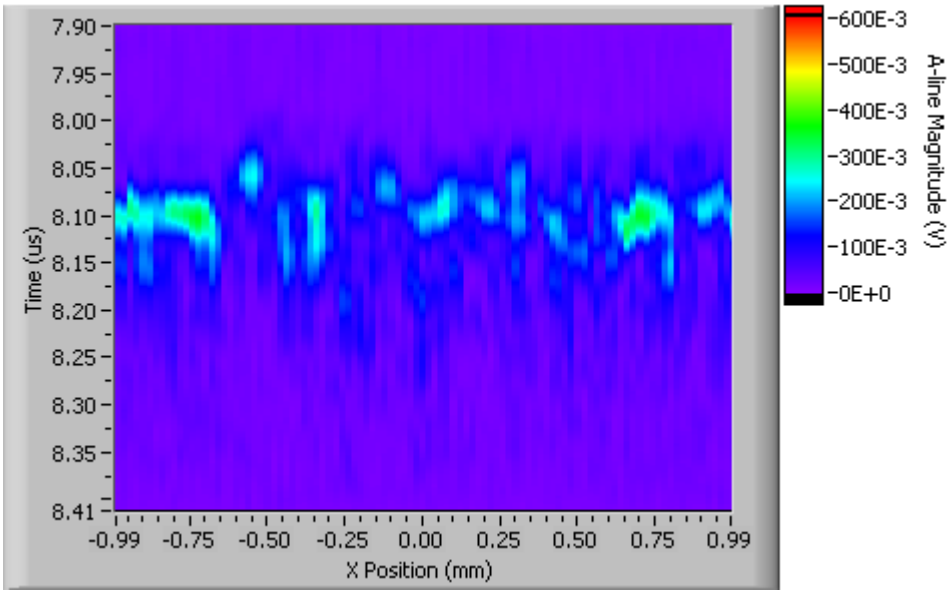

Figure 5.2-6: Video image results for frame 30 of Toray-060 with 20% PTFE. GDL-B-scan_48.

5.2.2.2- C-scans

Having investigated the variations and characteristics of B-scan images for different saturation conditions the same was completed for C-scan images which present an in-plane cross-sectional view of the GDL versus the B-scans through-plane perspective. Since the process of acquiring C-scans takes much longer than B-scans the progress of saturation under pressure application could not be captured, instead the before and after images were compared.

After acquiring the before and after C-scans the images were produced using a number of methods which represent the A-line envelope over a specified time-gate. The first observations made of the resulting images were the distinct regions of high acoustic energy clustered about the scanned area. If the signal was completely random the resulting image would be expected to have a more noise or speckle like appearance, this was clearly not the case. Secondly, a large decrease in average reflected acoustic energy was observed, this was also accompanied by a shift in average acoustic reflections into the GDL.

The images in figures *5.2-7* thru *5.2-10* are the result of two scans taken before and after the application of a differential pressure across the GDL, Toary-120 with 20% PTFE loading. The top image, the "dry" case, is derived from the initial scan where the GDL sample was subjected only to the pressure head of the coupling water, approximately $0.07psi$. The bottom image, the "wet" case, is derived from a scan after the same sample was subjected to a $2psi$ differential pressure. Both are of the same scan area and represent the average envelope value over a $0.2\mu s$ time-gate starting at $7.87\mu s$ arrival time. The images in figures *5.2-9* and *5.2-10* below are for a time-gate deeper in the GDL, starting at $8.17\mu s$. Both sets of images are scaled relative to each other, so those in figures *5.2-7* and *5.2-8* have a color scale range of 0 to $12e^{-9}V^2$ whereas figures *5.2-9* and *5.2-10* have a smaller range of 0 to $140e^{-12}V^2$.

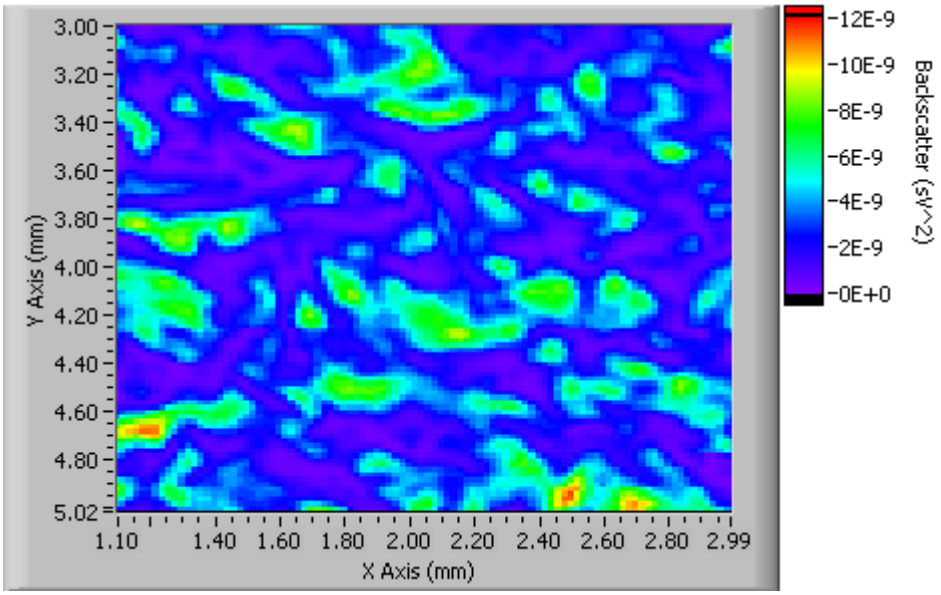

Figure 5.2-7: C-scan images depicting A-line backscatter over time-gate 7.87-8.07μs arrival time. C-scan-285 Δp=0.07psi.

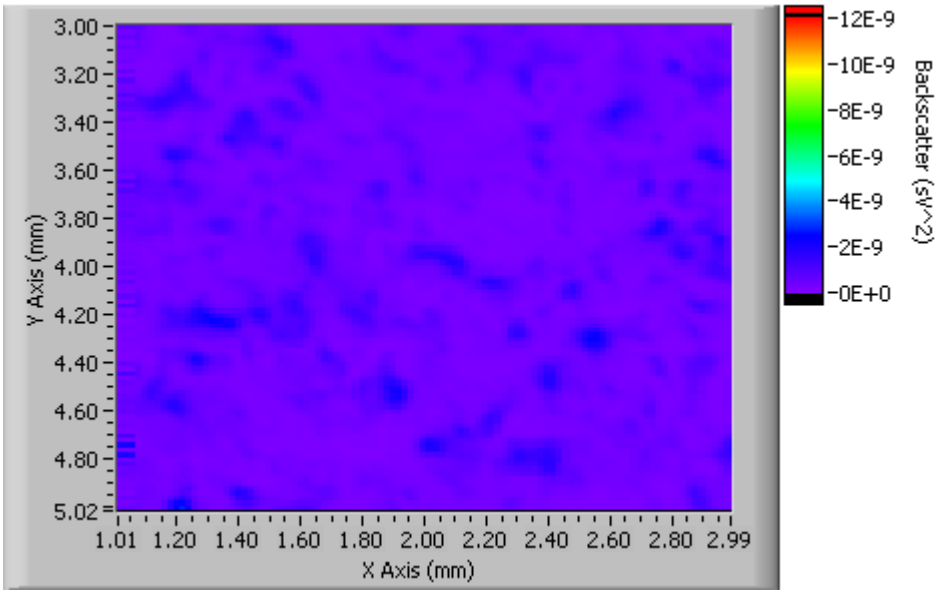

Figure 5.2-8: C-scan images depicting A-line backscatter over time-gate 7.87-8.07μs arrival time. C-scan-292 Δp=2psi (Bottom).

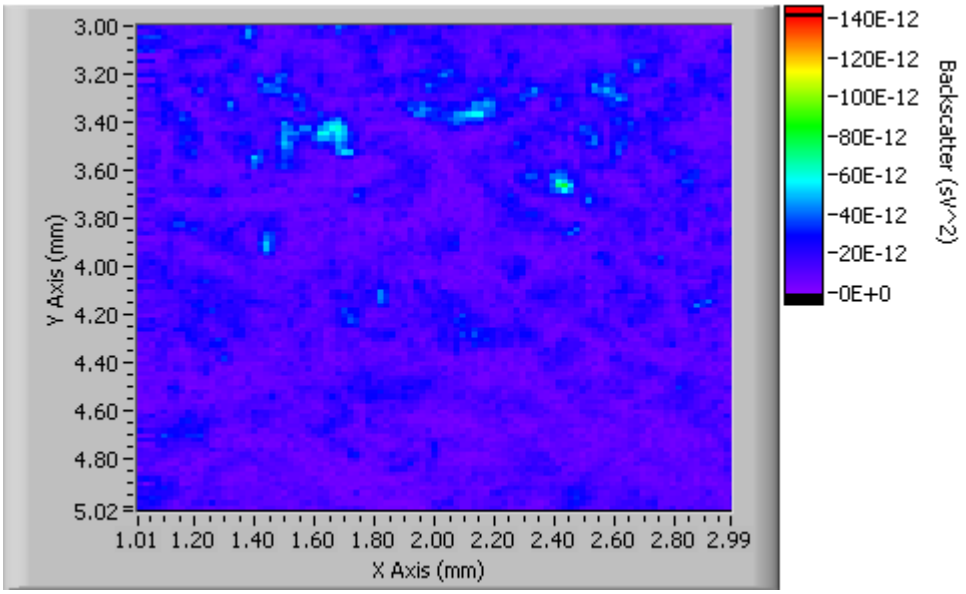

Figure 5.2-9: C-scan images depicting A-line backscatter over time-gate 8.17-8.37μs arrival time. C-scan-285 Δp=0.07psi.

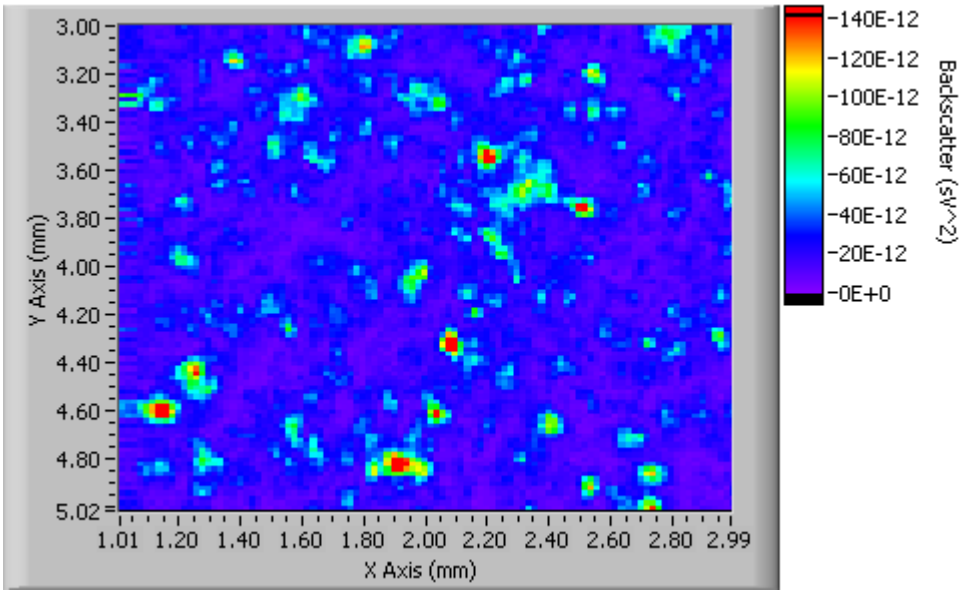

Figure 5.2-10: C-scan images depicting A-line backscatter over time-gate 8.17-8.37μs arrival time. C-scan-292 Δp=2psi.

Figure	*5.2-6 (Top)*	*5.2-6 (Bottom)*	*5.2-7 (Top)*	*5.2-7 (Bottom)*
Scan	*GDL-C-Scan_285*	*GDL-C-Scan_292*	*GDL-C-Scan_285*	*GDL-C-Scan_292*
Applied Δp	*0.07psi*	*2psi*	*0.07psi*	*2psi*
Time Gate Duration	$0.20\mu s$	$0.20\mu s$	$0.20\mu s$	$0.20\mu s$
Time Gate Start	$7.87\mu s$	$7.87\mu s$	$8.17\mu s$	$8.17\mu s$
Image Color Scale	$12E^{-9}sV^2$	$12E^{-9}sV^2$	$140E^{-12}sV^2$	$140E^{-12}sV^2$

Table 5.2-1: Tabular description for example C-scan images.

The two common observations noted for all C-scan saturation studies can be seen in the two sets of images above. The first being the large reduction in acoustic backscatter between the dry and wet cases, for this example a reduction of approximately 81.5% was observed. To quantify this, the average A-line backscatter for the entire scan was averaged and compared between the two saturation conditions. Figure *5.2-11* plots the average A-line backscatter per B-line for the dry and wet scans. Besides the obvious reduction in magnitude the dry case shows significantly greater variation from one B-line to the next. As the sample becomes more saturated these variations settle and converge on a more uniform value. The standard deviation in average backscatter between B-lines for the dry case was calculated to be 16.54% of the maximum recorded value where as the wet case showed only a 1.46% variation, exceeding a tenfold reduction.

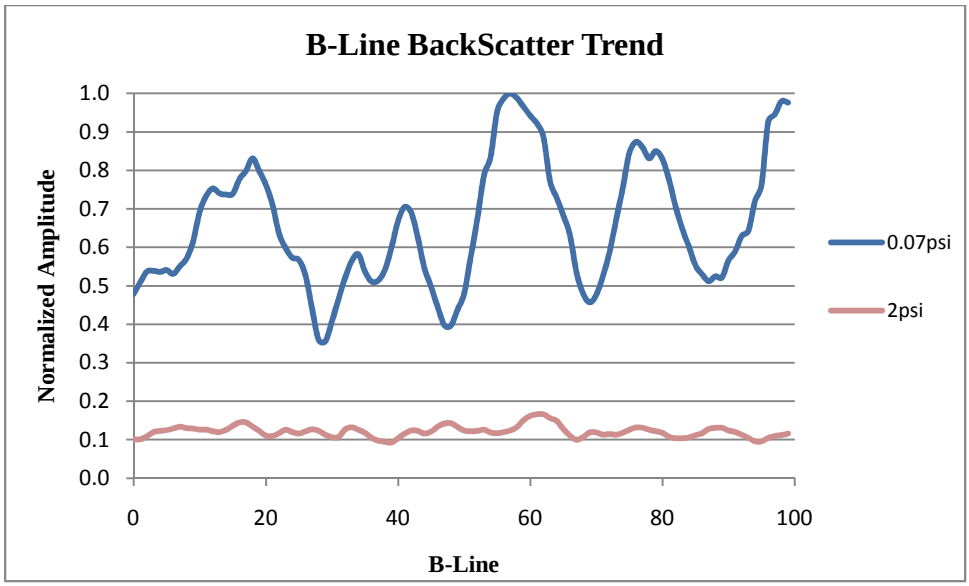

Figure 5.2-11: B-line backscatter trends for both the dry (0.07psi Δp, C-scans-285) and the wet (2psi Δp, C-scan-292) scans.

Scan	*GDL-C-Scan_285 (Dry)*	*GDL-C-Scan_292 (Wet)*
Applied Δp	*0.07psi*	*2psi*
Average Normalized B-line Backscatter	*65.7%*	*12.1%*
Std. Dev. In B-line Backscatter	*16.54%*	*1.46%*

Table 5.2-2: Tabular results for B-line backscatter plots from example C-scan saturation study.

The second observation noted was the increased acoustic backscatter deeper in the sample for the wet case. To quantify this observation all detected peaks in the A-line envelopes were plotted along with a trend line of the average echo amplitude for incremental time-gates, an exponential decay was then fit to the data. Figures *5.2-12*, *13*, and *14* show the results of this quantification for the given example.

It was found from the echo amplitude trends that the reduction in the initial acoustic reflections dropped by as much as 73.5% at an arrival time of $7.97\mu s$ or 62.7% comparing

peck average echo amplitudes where as the increase seen later in the sample reached 7.5% $0.155\mu s$ later, or assuming a propagation speed of $1473m/s$, $114\mu m$ into the sample. Intuitively this makes sense, with reduced initial reflected energy more is transmitted into the sample, increasing the amount deeper in the sample. From the way the test is set up the only difference between the two scans would be the amount of air present in the sample. Given that water/air boundaries are the primary acoustic reflector, increased saturation should reduce the average backscatter intensity.

The apparent attenuation for the two samples was also calculated. Most materials exhibit exponential decays in pulse amplitude where the rate is dependent on the dampening constant. Using a custom algorithm that identifies and isolates the logarithmic section of the echo amplitude trend an exponential decay equation is fit, equation *3.2-1*.

The two example cases exhibited dampening constants of $27.95\mu s^{-1}$ and $8.30\mu s^{-1}$ for the dry and wet cases respectively. This translates to an attenuation of the pulse amplitude per depth propagated of $-329.6db/cm$ for the dry case and $-97.9db/cm$ for the dry wet case. Given the 40 decibel range of the digitizer the average measurable penetrations expected of the two samples are $121.9\mu m$ and $410.6\mu m$ for the dry and wet cases respectively.

Given the extreme inhomogeneous nature of the GDL and the resulting acoustic response these calculated attenuation values come with large variances in the trends. The dry case trend had an average standard deviation of 46.2% over the identified time segments with a range of 25.5% to 73.1% having a standard deviation itself of 15.6%. Just as the B-line backscatter trends described the acoustic response becoming more uniform as the saturation increased so does the echo amplitude trends. The wet case showed an average standard deviation from the mean echo amplitude of 33.9% with a range of 26.6% to 44.4% and an associated standard deviation of the trends variations of 4.9%, showing a move toward uniformity.

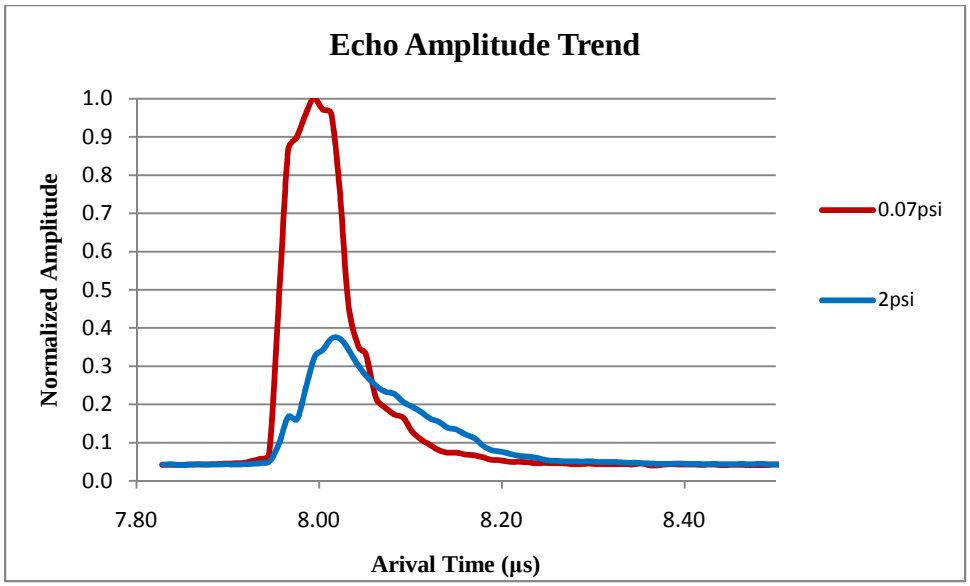

Figure 5.2-12: Echo amplitude trend for both the dry (0.07psi Δp, C-scans-285) and the wet (2psi Δp, C-scan-292) scans.

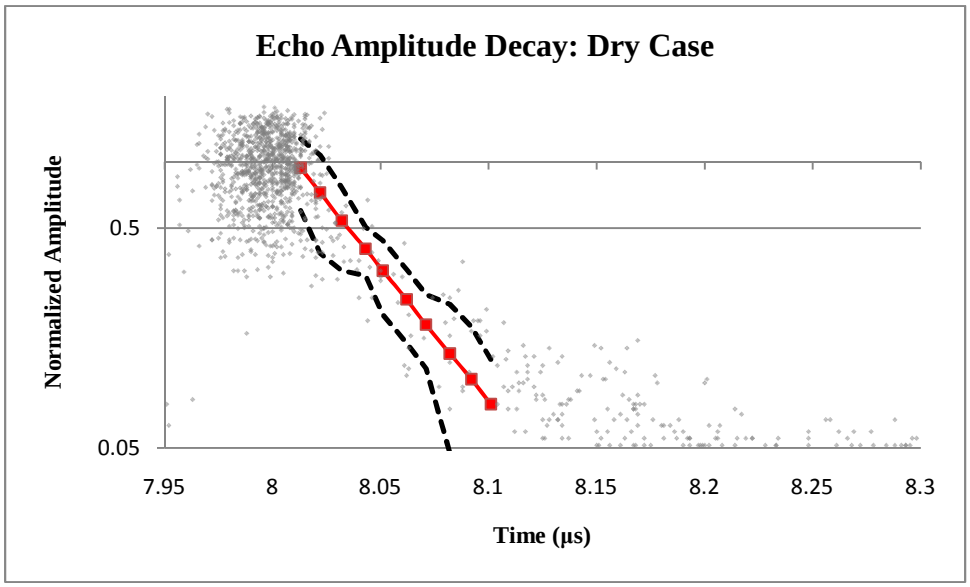

Figure 5.2-13: Individual echo amplitude fit exponential decay trends with one standard deviation bounds and 10% echo points plotted. Dry (0.07psi Δp, C-scans-285) case.

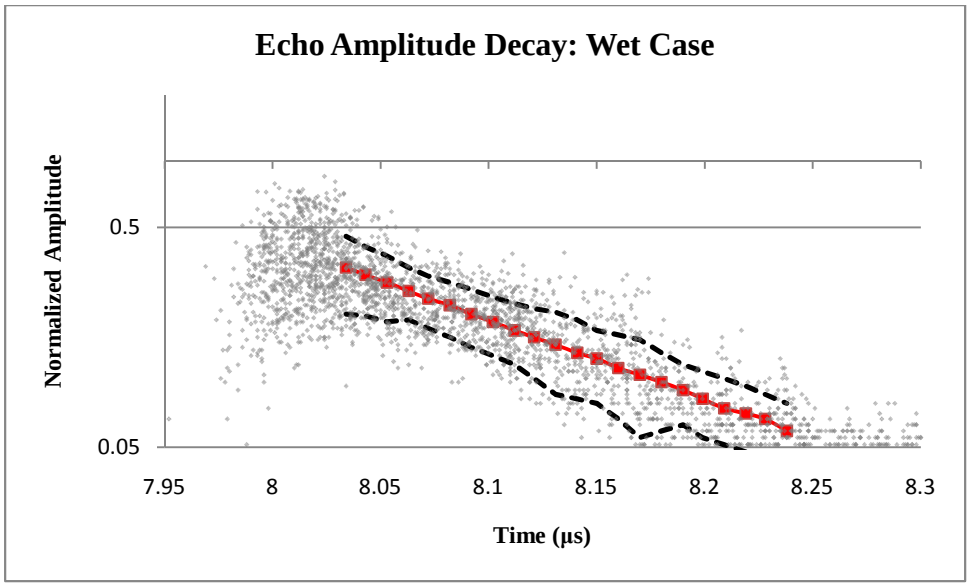

Figure 5.2-14: Individual echo amplitude fit exponential decay trends with one standard deviation bounds and 10% echo points plotted. Wet (2psi Δp, C-scan-292) case.

Scan	*GDL-C-Scan_285 (Dry)*	*GDL-C-Scan_292 (Wet)*
Applied Δp	*0.07psi*	*2psi*
Normalized Peak Amplitude	*1*	*37.31%*
Attenuation	$-329.6db/cm$	$-97.9db/cm$
Ave. Std. Dev. for Attenuation Trend	*46.2%*	*33.9%*
Std. Dev. Range For Attenuation Trend	*25.5-73.1%*	*26.6-44.4%*
Std. Dev. for Attenuation Trend Std. Dev.	*15.6%*	*4.9%*

Table 5.2-3: Tabular results for echo amplitude trends from example C-scan saturation study.

5.2.2.3- 3D ImageJ

One of the primary objectives at the start of this research was to investigate the spatial location of water within the GDL or simply to reconstruct the microstructure in three dimensions. The nature of ultrasonic imaging lends itself to this and has found applications in both medical and non-destructive evaluation. Given the results from this section which suggests that pockets of air within the GDL sample are identifiable by large acoustic reflections, a three dimensional map of these pockets might be possible.

While SAM-Data is capable of plotting the identified echo pulses in a three dimensional space, volume rendering was not programmed. To accomplish this, a public domain Java program called ImageJ was used which is capable of generating three dimensional maps based on a series of imported 2D images. The series used were C-scans created with thin time-gates incremented through the thickness of the sample. The example displayed below shows the volume renderings of two $2x2mm$ scans over a time duration of $0.6\mu s$ or an estimated $440\mu m$. The first is a dry reference and the other was taken after a $1psi$ differential pressure application. In both images distinct volumes were created, the major difference is in the quantity and average size of these volumes. Since the images used to create these volumes were of the average acoustic backscatter over a time-gate of $0.05\mu s$ they are most likely air pockets within the GDL. However, for reasons discussed in the following sections the probability that this is an accurate representation of air within the GDL is quite low.

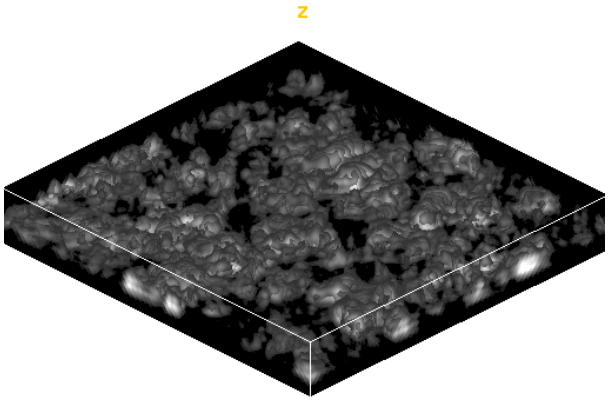

Figure 5.2-15: ImageJ volume rendering of C-scan-34 Toray-120 plain dry reference, Δp=0.07psi.

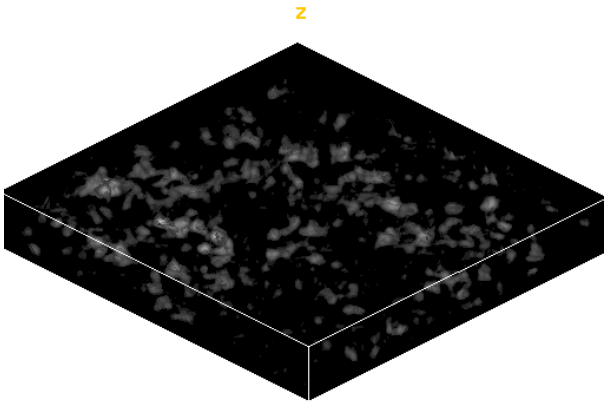

Figure 5.2-16: ImageJ volume rendering of C-scan-34 Toray-120 plain dry reference, Δp=0.07psi C-scan-36 Toray-120 plain wet, Δp=1.0psi).

5.2.3- Time-gate Investigation

Given the large acoustic attenuation of the GDL samples and the 40 decibel measurable range of the digitizer, echo signals deeper in the sample are missed. To address this, a stepless gate was used to block a specified portion of the signal so increased pulser/receiver amplification can be used without clipping the digitizer. The objective was to capture the deeper acoustic reflections and possibly identify the back reflections from the sample support.

Three GDL samples were used for these tests, Toray -120, -060, and -030 with 20% PTFE loading. Four scans were performed on each sample, two for a relatively dry sample and another two after being subjected to $2psi$ differential pressure across the GDL. Each saturation condition was then scanned and rescanned using the stepless gate to block the first half of the acquired A-line signals with an increased gain of $20db$ on the pulser/receiver.

Figures *5.2-17* and *5.2-18* presents the scans acquired before the sample, Toray-060 GDL with 20% PTFE loading, was saturated under a $2psi$ differential pressure which are shown in figures *5.2-19* and *5.2-20*. The two images per figure represent the A-line backscatter over a $0.10\mu s$ time-gate but at different depth within the GDL. The top images approximate a $75\mu m$ thick slice from the leading face of the GDL where the bottom images represent the last $75\mu m$ of the GDL. Given the $220\mu m$ thickness of the -060 sample, the $7.95\mu s$ initial echoes, and the assumed $1473m/s$ propagation speed, the two time-gates where 7.95 to $8.05\mu s$ and 8.15 to $8.25\mu s$.

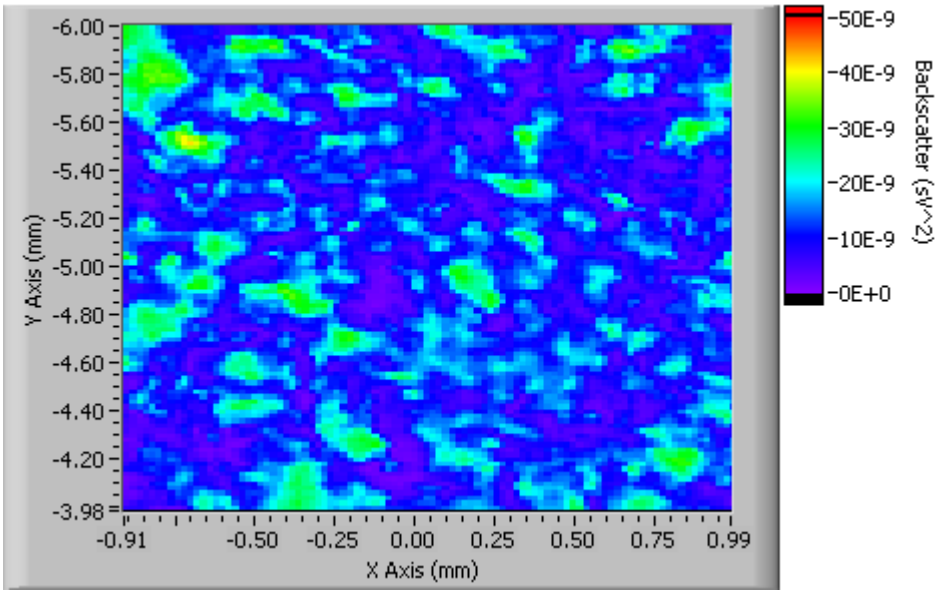

Figure 5.2-17: C-scan images of Toray-060 after 0.07psi Δp depicting A-line backscatter over 0.10μs time-gate. C-scan-30 with time-gate 7.95-8.05μs and pulser gain of 0dB.

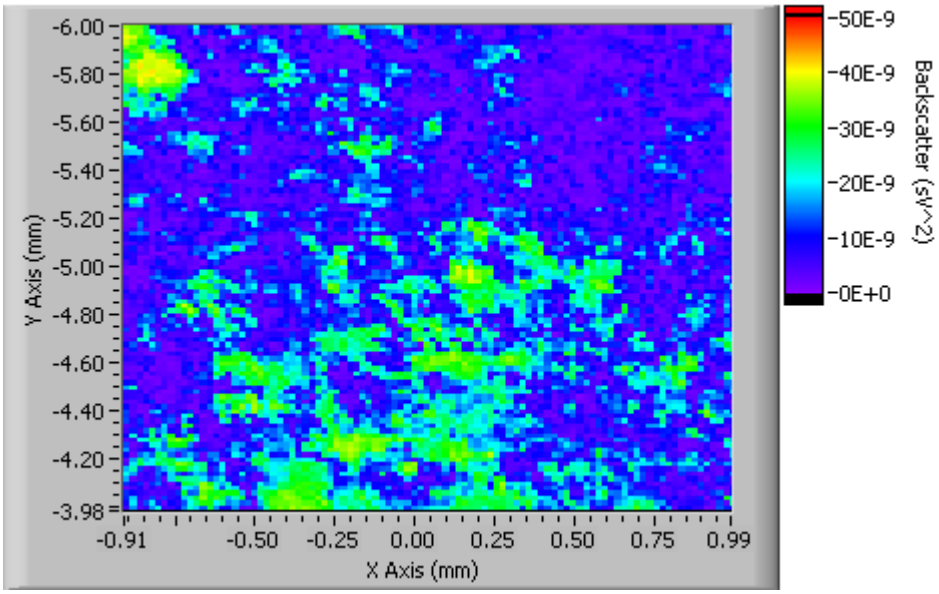

Figure 5.2-18: C-scan images of Toray-060 after 0.07psi Δp depicting A-line backscatter over 0.10μs time-gate. C-scan-31 with time-gate 8.15-8.25μs and pulser gain of 20dB.

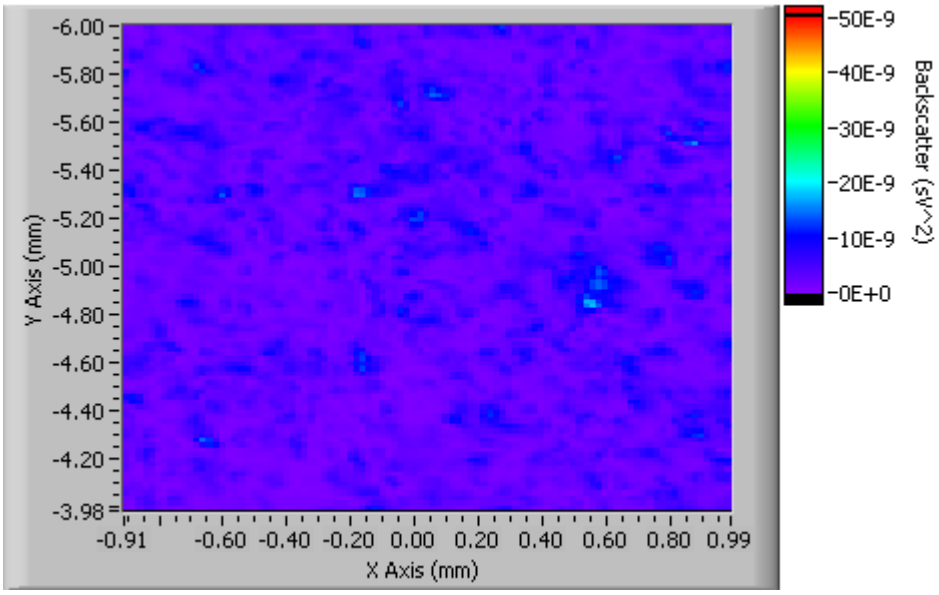

Figure 5.2-19: C-scan images of Toray-060 after 2psi Δp depicting A-line backscatter over 0.10μs time-gate. C-scan-32 with time-gate 7.95-8.05μs and pulser gain of 0dB.

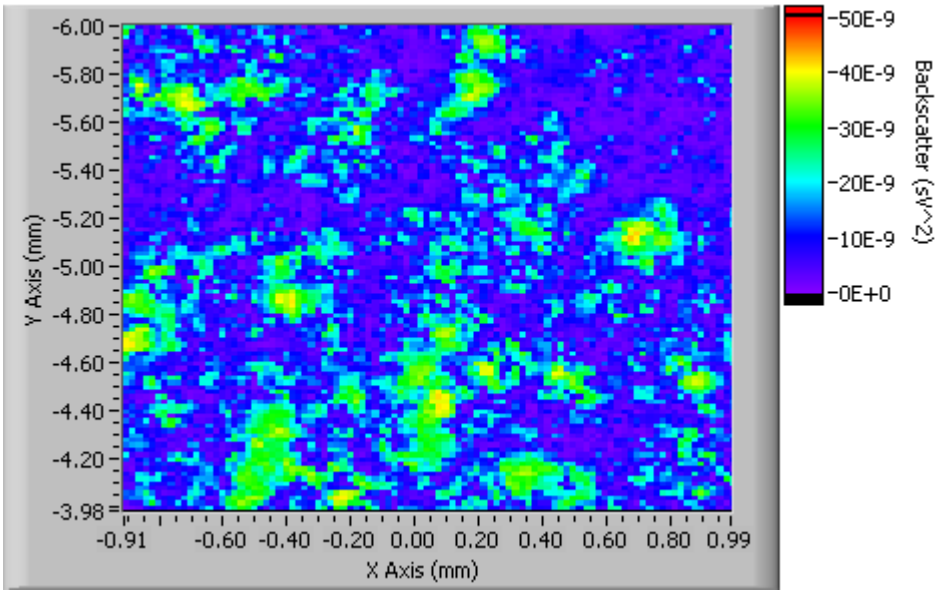

Figure 5.2-20: C-scan images of Toray-060 after 2psi Δp depicting A-line backscatter over 0.10μs time-gate. C-scan-33 with time-gate 8.15-8.25μs and pulser gain of 20dB.

A few notes are taken from theses scans. One, the clear evidence of higher acoustic attenuation for the dryer sample. Given the dry scans relatively consistent backscatter intensity between the different depth images compared to the wet scans apparent increase with depth, illustrates the difference in acoustic attenuation. This is assured given the consistent pulser gain increase of $20dB$ for both saturation conditions. The second note deals with the image patterns relative to the two time-gates. For the dry case the regions of high acoustic reflectivity are consistent between the two time-gates where as the wet case shows a large deviation in the pattern. This would suggest that the causes of the large reflections in the dry case are persistent throughout the thickness where as the deeper signals in the wet case are independent of those from shallower regions of the GDL.

The last note, and probably the most significant, is the lack of any clear back reflection or an end to the echoes. From the -060 scans the theoretical back surface of the sample based on the initial reflections, the thickness, and the assumed propagation speed, should come in around $8.25\mu s$, leaving $0.21\mu s$ until the last sample acquired in the A-lines. An error in the assumed propagation speed could account for this so the thinner, $127\mu m$ thick, Toray-030 GDL scans were reviewed.

Given the $127\mu m$ thick sample with a pulse propagation speed that of water the separation between the front and back reflections should be $0.173\mu s$. The observed signals, however, persisted for much longer. The following plot shows two A-lines acquired at identical locations but one was clipped before $8.214\mu s$ and amplified by $20dB$. Based on the arrival of the first pulse the last received echo from this sample should be acquired before $8.214\mu s$, the point at which the signal was amplified. It's clear that acoustic energy remain after this point in time. This can be due to an over estimate of the pulse propagation speed by as much as 50% or significant reverberations within the GDL are present. The following section aims to answer this question.

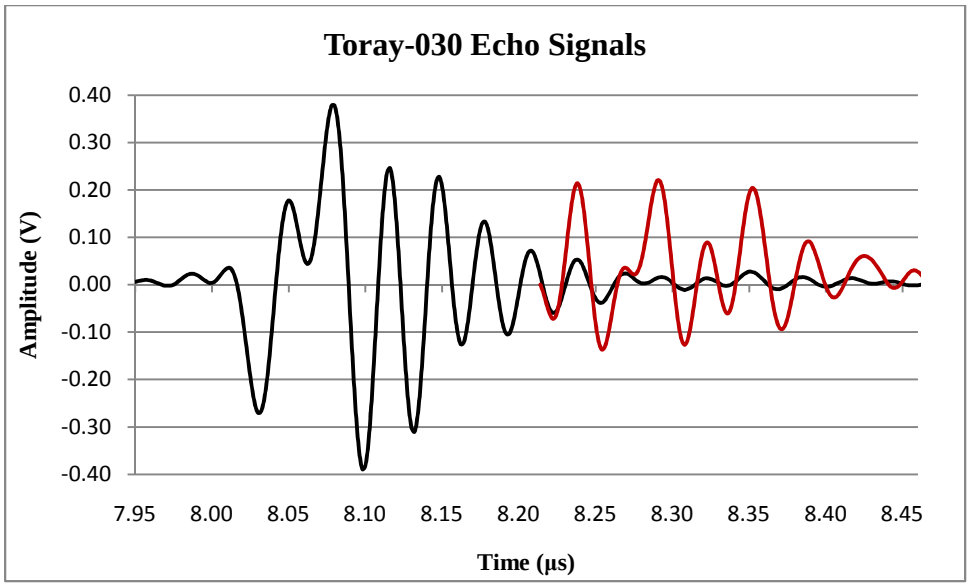

Figure 5.2-21: A-line of Toray-030 GDL with a 20dB amplified region.

5.2.4- Pulse Propagation Speed

In order to measure the phase velocity through the GDL a reference point with known distance is needed. Since the previous tests failed to provide a back reflection from the GDL support plate a new experimental setup was derived and is illustrated in figure *5.2-22*. As the figure depicts the GDL sample was supported off the surface of a steel plate with a $0.005in$ thick doughnut shaped Teflon gasket. The objective was to ensure a gap of at least one pulse width between the back face of the GDL and the steel plate so a clear reflection from the latter was received. One of the reasons why back reflections from previous tests were not detected was the interference from the GDL's microstructure flush with the support face, separating the GDL from the steel plate solves this problem.

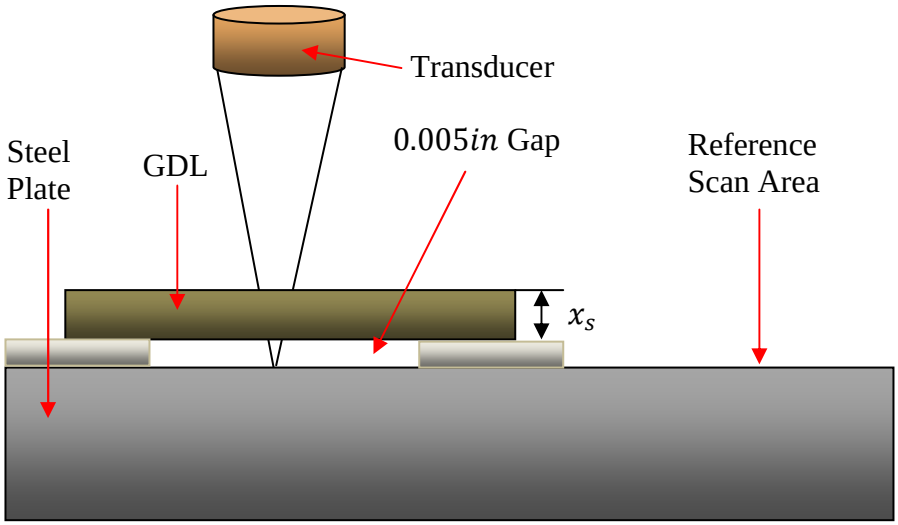

Figure 5.2-22: Propagation speed scan setup.

The sample used to estimate its pulse propagation speed was a $380\mu m$ thick Toray-120 with no PTFE treatment. To saturate the GDL it placed in a vacuum chamber where it was submerged in water. A vacuum of $20inHg$ was applied for ten minutes to extract as much air as possible. The actual saturation level was not confirmed but the objective of the test was to obtain an approximate propagation speed for a saturated GDL and the variation in the calculated values.

In order to calculate the propagation speed through the sample, c_s, its thickness, x_s, the speed of sound in water, c_w, and the steel plate depth are required. To ensure an accurate measurement of the steel plate depth a reference scan was taken over an area where only water separates the transducer from the plate. The plates echo pulse time-of-flight (TOF) was recorded and converted to depth assuming a speed of sound of $1473m/s$ in the water. In addition to the plate depth over this scanned area the surface normal vector was also calculated. It was found to have an angle of $0.569°$ in relation to the microscopes scan plane normal. With a reference depth and surface normal the distance between the transducer and steel plate at any location is known.

$$\hat{n} = \begin{bmatrix} 0.0035 \\ -0.0093 \\ 1 \end{bmatrix} \qquad (5.2\text{-}1)$$

The propagation speed through the sample is then defined by the following equation where Δt is the time difference between the measured TOF and that expected for a continuous water path at that depth.

$$C_s = \frac{2x_s C_w}{2x_s + \Delta t C_s} \qquad (5.2\text{-}2)$$

An example A-line acquired during the $2x2mm$ scan over the GDL is plotted in figure *5.2-23*. The acoustic signals from the GDL are clearly present up to approximately $8.1\mu s$ where small reverberations exist until the dominate echo off the steel plate is received around $8.3\mu s$. Figure *5.2-24* illustrates the spatial relation between the echo signals from within the GDL and those reflected off the steel plate. This also helps confirm the interpretation of the A-line signals.

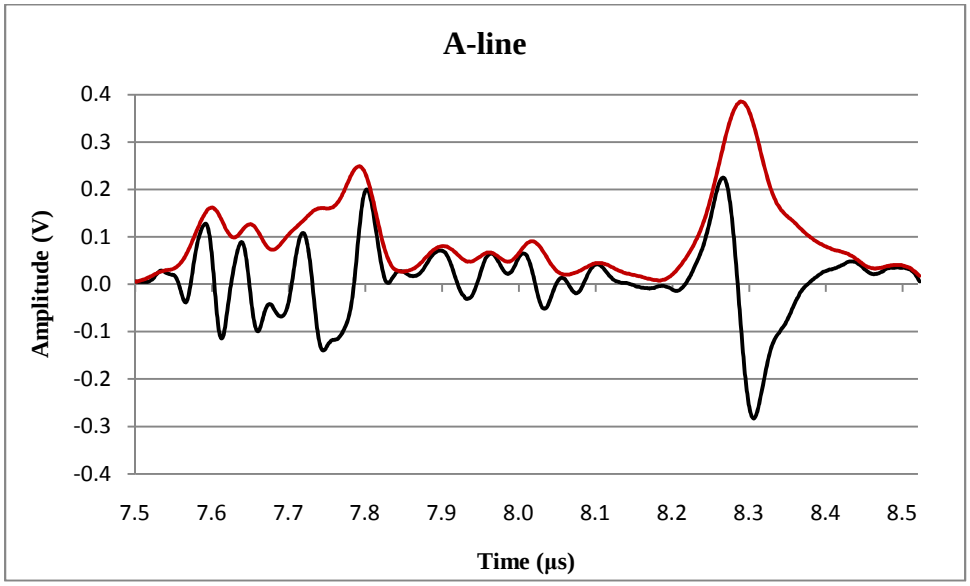

Figure 5.2-23: A-line of Toray-120 GDL with a 0.005" gap between support plate. C-scan-60.

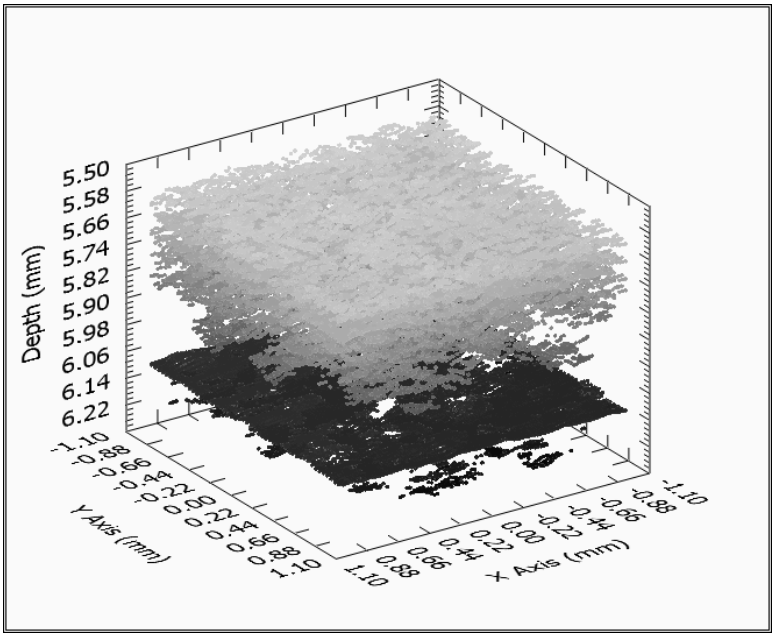

Figure 5.2-24: Identified echoes from C-scan-60 plotted.

The TOF for the steel plate echo is taken to be the instantaneous time associated with the envelope maximum between a specified time bracket of 8.2 to 8.4μs. Having acquired all the arrival times it was found that the average propagation speed through the sample was $1527.1 m/s$ with a standard deviation of $25.8 m/s$. The $54 m/s$ difference in propagation speed between water and the sample can be described as statistically significant based on the two sigma shift. Secondly, the instantaneous derivative of the estimated speed of sound in the sample with respect to the assumed sample thickness was $0.1365\ ms^{-1}/\mu m$ at the data mean, stating that a standard deviation in actual thickness of $189 \mu m$ would result in the $25.8 m/s$ standard deviation in the estimated material speed of sound. This simply insures that the variation in the estimated speed of sound is not entirely due to varying thickness in the scanned sample.

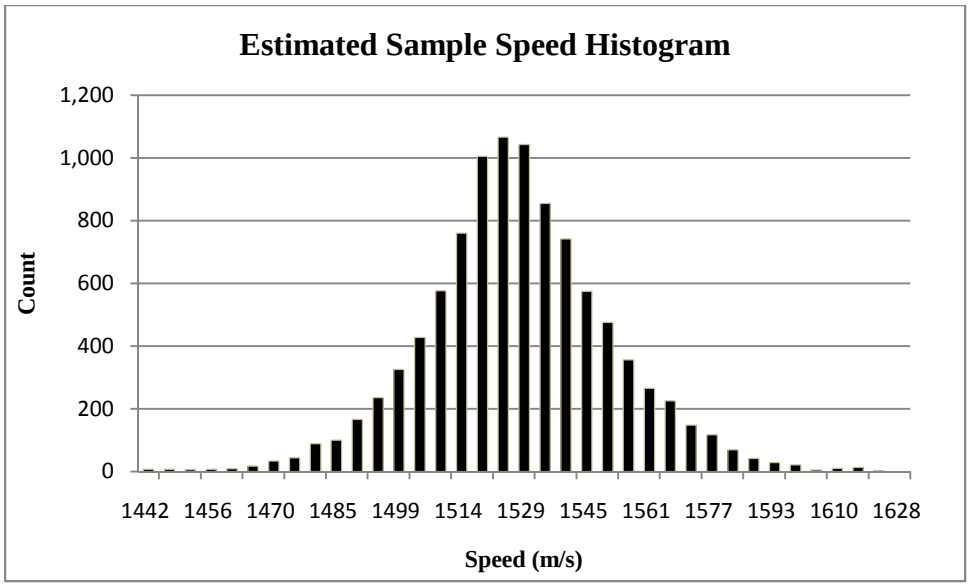

Figure 5.2-25: Histogram of calculated speed of sound through GDL sample.

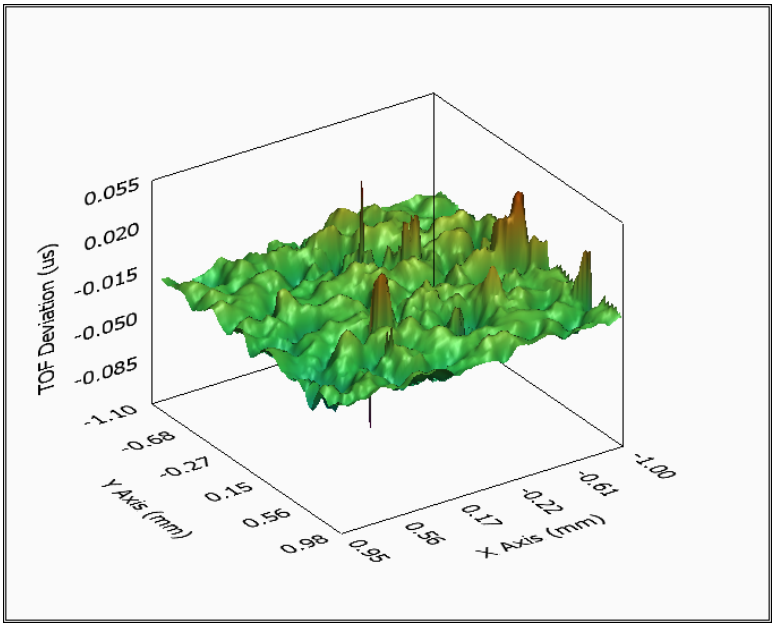

Figure 5.2-26: Deviation in time-of-flight between known water path duration and measured plotted over scanned area.

Interestingly there was no relation between the steel plate reflection amplitude and the propagation speed; the sample correlation coefficient was only 0.0159. This was an

unexpected result given the large variation of properties between the individual materials making up the sample. The pulse attenuation can be attributed to both absorption in the individual materials and backscatter from impedance boundaries along its path, both of which are functions of the material concentrations and geometric layout. It should also be noted that no relation between the measured backscatter from within the GDL and the pulse arrival time or amplitude was apparent, measuring a correlation coefficient of -0.109 and 0.028 respectivly. The separation between the steel plate and the GDL ensures little interference with the plates echo signal while the geometric properties of the GDL ensure interference between its echo signals. This with the last two correlations suggest that the received A-lines from within the GDL are semi-random, having little correlation to the physical media.

As observed previously the average backscatter from the GDL is reduced with increased saturation, which supports the hypothesis that air pockets within the GDL will generally provide a larger acoustic reflection than that of the carbon microstructure. As the saturation approaches unity the correlation between the physical media and the backscatter pattern will be reduced, leaving only what is referred to as a speckle pattern. Given the method of saturation and the estimated attenuation through the GDL it was clear that this sample had a higher than average saturation compared to those subjected to a $2psi$ differential pressure for saturation. This leads to the conclusion that any acoustic signals from the time region associated with the GDL's position present no relation in terms of acoustic energy, peak locations, or amplitude to the actual insonified material.

As for the steel plate reflections, its amplitude variation shows clear spatial transitions and has no correlation to GDL backscatter or estimated speed of sound. The standard deviation of its measured time-of-flight was found to be $0.0115\mu s$, approximately 20% of the transmitted pulse duration, based on the FWHM. From review of the individual A-line signals it was apparent that reverberations in the GDL were distorting the steel plate reflections and effectively shifting the peaks location. For areas of higher attenuation where the reflection amplitude approaches the reverberation noise magnitude this shift in peak location becomes more prominent. This phenomenon was illustrated in a plot of pulse TOF versus amplitude which shows a clear reduction in deviation from the mean as pulse amplitude increases.

From these tests it was clear that the acoustic signals from the sample are not a reliable indicator of the current state of the GDL, leaving only random speckle as saturation increases. The tests were however able to show a statistically significant increase in pulse propagation speed in the GDL compared to water, showing a relatively low standard deviation from the mean. The limitation to the tests was that a very high level of saturation was needed to receive a clear reflection from the steel plate, making any quantification of pulse speed for dryer samples difficult and unreliable.

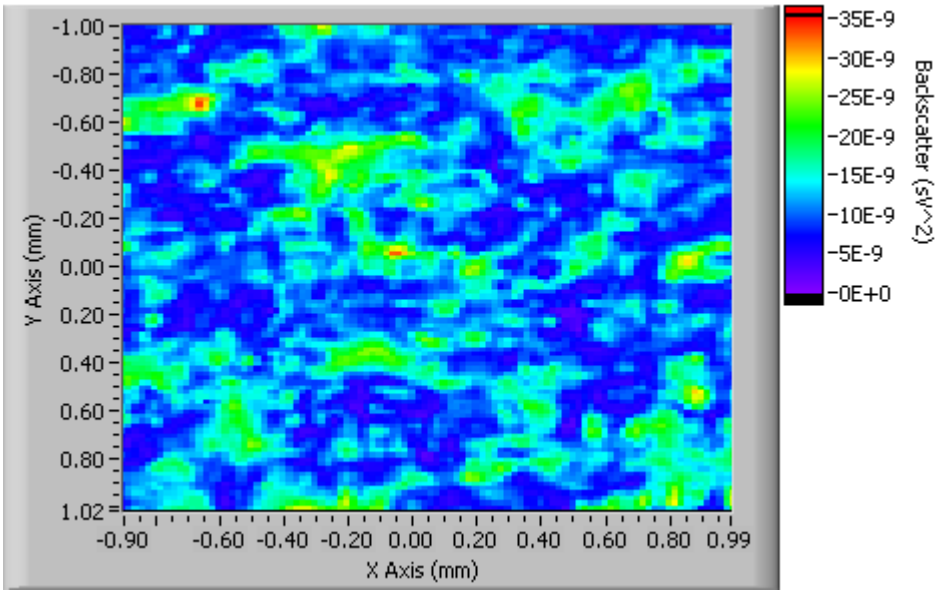

Figure 5.2-27: Acoustic backscatter from GDL sample, Time-gate 7.5-8.0μs.

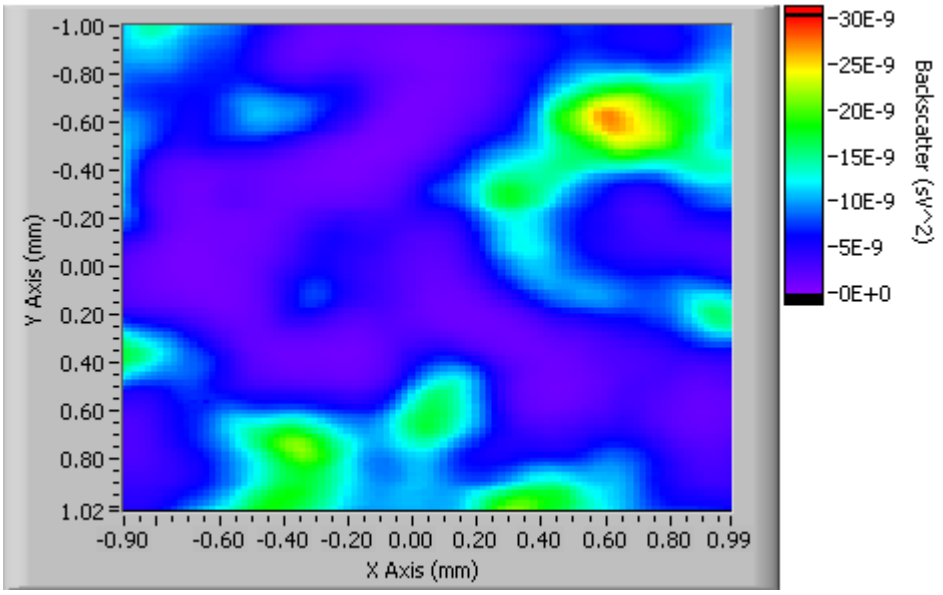

Figure 5.2-28: Acoustic backscatter from steel plate, time-gate 8.2-8.5μs.

5.3-GDL Saturation Distribution

5.3.1-Theory

Variations in the acoustic response from GDL samples were observed as a function of saturation but traditional ultrasonic imaging techniques failed to quantify the localized state. A new method for identifying regions of altered water concentration within a GDL sample is proposed and validated. The basis for this new method is its lack of dependency on a strong correlation between the acoustic signals and the physical media. Typical acoustic imaging techniques rely on sub feature size resolutions where clear echoes are identifiable and/or pulse characteristics like amplitude, spectral content, and time-of-flight are used to reconstruct and characterize the target material. This method, given the sub resolution feature size target structure and incoherent acoustic signals, relies on A-line variations from a dry reference scan.

In order to identify water within the GDL a dry reference scan is acquired. This provides a base line where all subsequent scans are compared. After saturating the GDL the reference scan is repeated, holding all settings and parameters constant. Assuming the GDL

was completely dry during the reference scan any changes in the acoustic signal must be due to the displacement of air by water within the insonifed column. This also assumes that the microstructure of the GDL was held fixed between scans as any variation in its position, though less significant, would also result in a change in the acoustic signal.

The A-line change at each pixel location is quantified by the peak value of the signals cross-correlation envelope over the auto-correlation envelope at zero delay. The exact formulation is listed equation *3.2-3* thru *3.2-6* where $X(k)_{ij}$ and $Y(k)_{ij}$ are the A-line signals for the reference and saturated scans respectively at location ij. The result is a measure of the relative change in the A-line signals.

The following plot compares two A-line signals, the first from a dry reference scan and the second the corresponding A-line after a $0.5psi$ differential pressure application. Figure *5.3-1* shows a location where there was relatively no variation in the acoustic response after the application of pressure suggesting no change occurred in the GDL between scans. Figure *5.3-2* on the other hand shows the before and after A-lines at a different location. Given the significant shape difference between the two A-lines clearly a change in the GDL occurred at this location. Based on the original assumption that no water was present in the GDL during the initial reference scan and that the GDL itself has not moved this change in acoustic response must be due to the entrance of water in the insonified column.

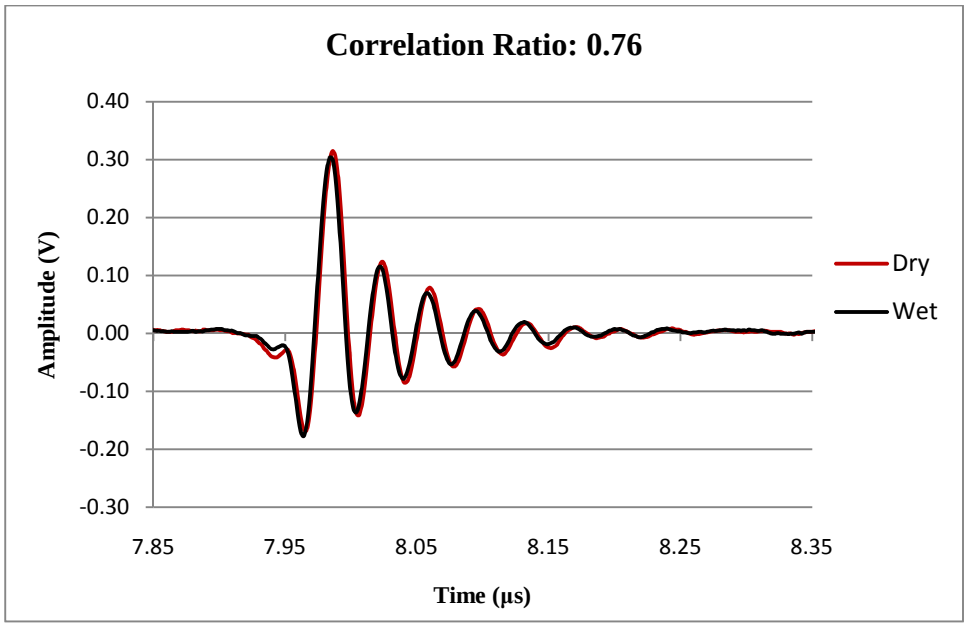

Figure 5.3-1: Example dry and wet A-lines after 0.5psi differential pressure application. Resulting correlation ration of 0.76. C-scans 296-300.

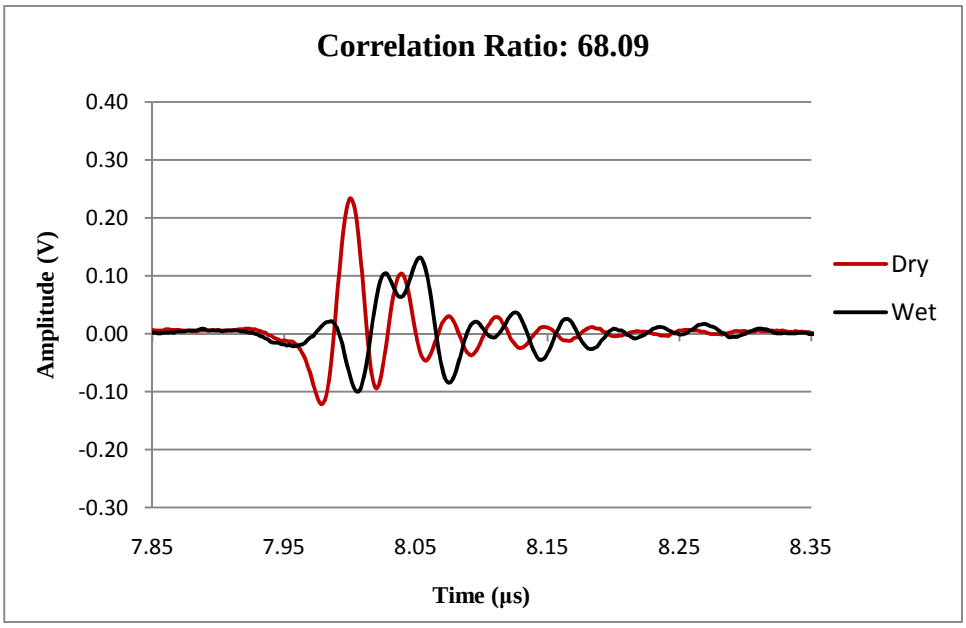

Figure 5.3-2: Example dry and wet A-lines after 0.5psi differential pressure application. Resulting correlation ration of 68.09. C-scans 296-300.

5.3.2-Validation

5.3.2.1- Image Difference vs. Correlation Ratio

The first set of validations were to compare results formulated with standard image difference and that of the correlation ratio. The examples below use scan data collected from a dry reference scan and from a saturated sample subjected to a $0.5psi$ pressure differential. Figure *5.3-3* show the resulting images from the two scans where the A-line backscatter defines the images intensity values at each pixel location. A clear reduction in the average backscatter was observed, starting at $4.05 \times 10^{-9} sV^2$ and dropping 21.6% to $3.17 \times 10^{-9} sV^2$. It was also noted that the variation between the two images where primarily of

reduced intensity and size of the dry reference scans higher acoustic regions but maintaining the overall pattern.

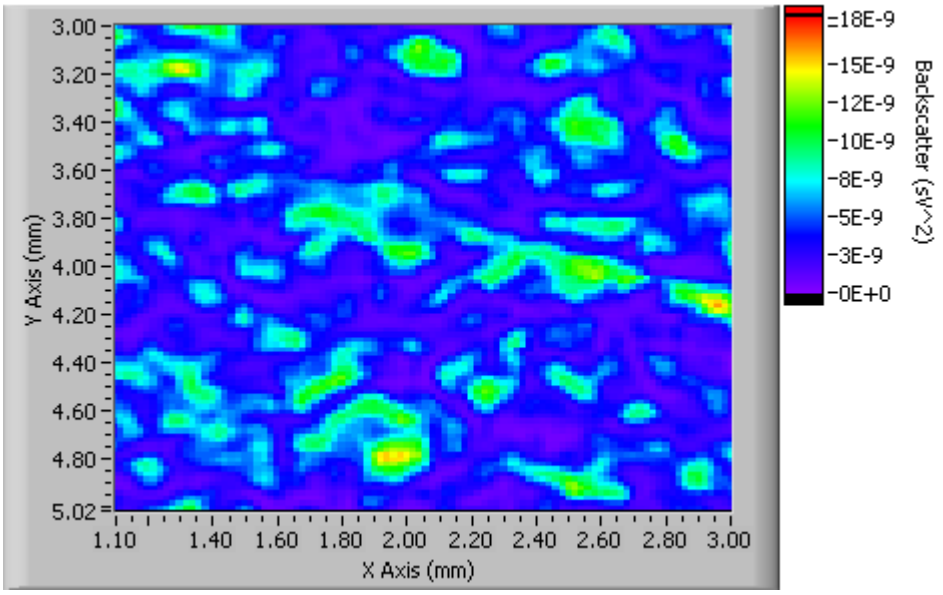

Figure 5.3-3: C-scan-317 dry reference scans backscatter, 0.07psi Δp.

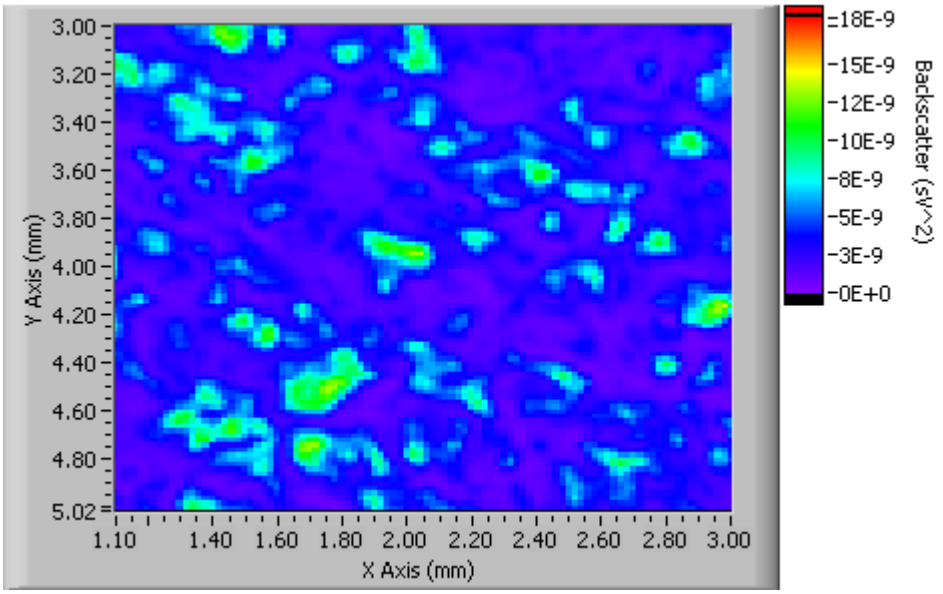

Figure 5.3-4: C-scan-317 dry reference scans backscatter, C-scan-321 saturated scans backscatter, 0.5psi Δp.

To quantify the change between the scans two methods where used, whose results are displayed in figure *5.3-5* and *5.3-6*. The first simply plots the percent change in the image backscatter while the second uses the correlation ratio method as defined in the previous section. It is apparent that the correlation ratio method highlights the lower intensity regions of the image difference method. Since the image difference values are derived from the A-line backscatter, which scales with the square of the envelope value, this characteristic is expected. The significant difference between the two methods is demonstrated by areas not defined by image difference but captured by the correlation ratio.

To better illustrate this point a new pair of scans are used were the difference between them significantly less. Figures *5.3-7* and *5.3-8* show the image difference and correlation ratio results for dry reference scans taken twenty minutes apart. The disparity between the two methods is quite apparent in this example. The image difference method identified a single location of significant change where as the correlation method identified several others. Two locations are specified in the results images of figures *5.3-7* and *5.3-8*. Location one is an example of a saturation point identified by the correlation ratio and not the image difference method while location two is the single point of change defined by the image difference method.

A comparison of the A-lines recorded for both scans at location one reveals a significant deviation at approximately $8.10\mu s$. For the time zero plot there are two significant peaks in the A-line, the first associated with the front surface reflection and the second from an impedance boundary within the GDL. The front surface reflection follows the transmitted pulse orientation, suggesting that the reflection coefficient is positive. The opposite is true for the second reflection where the coefficient appears to be negative. The significance is that positive coefficients result from a high to low acoustic impedance boundaries, like water to carbon, and negative coefficients result from low to high orientations, like water to air. With this it appears that an air pocket was present in the first scan and has been displaced or shifted some time before the second scan.

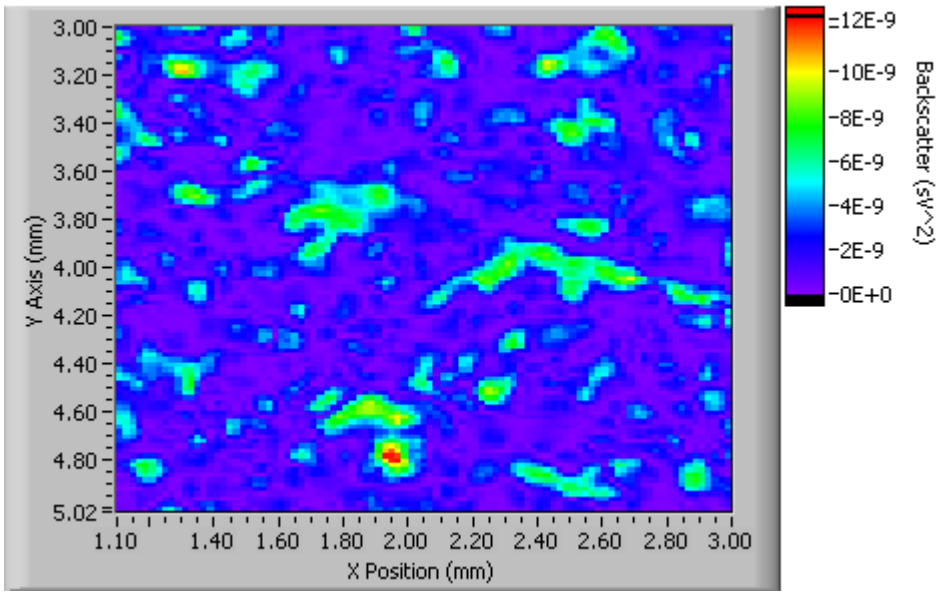

Figure 5.3-5: Relative amplitude image difference between C-scan-317 & 321, 0.5psi Δp.

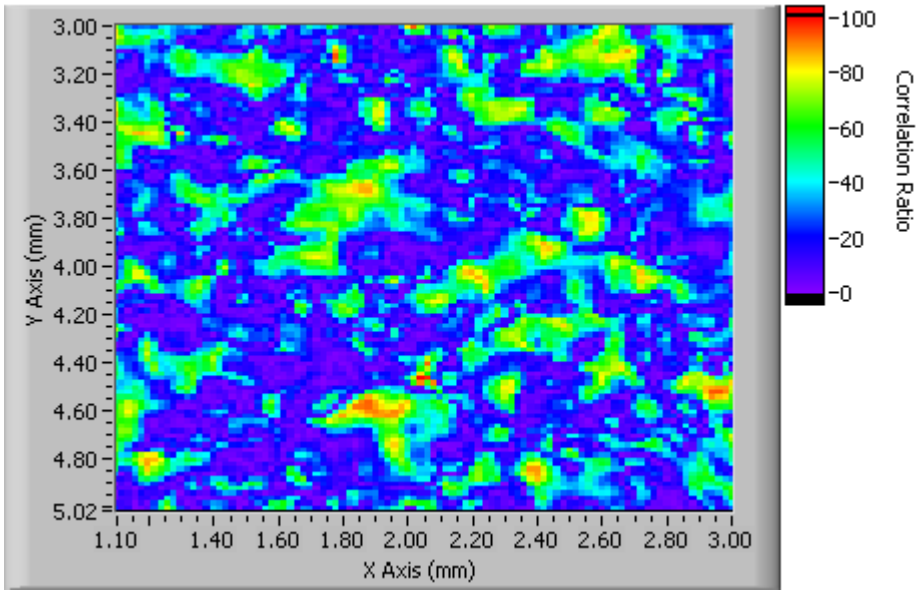

Figure 5.3-6: Relative amplitude correlation ratio between C-scan-317 & 321, 0.5psi Δp.

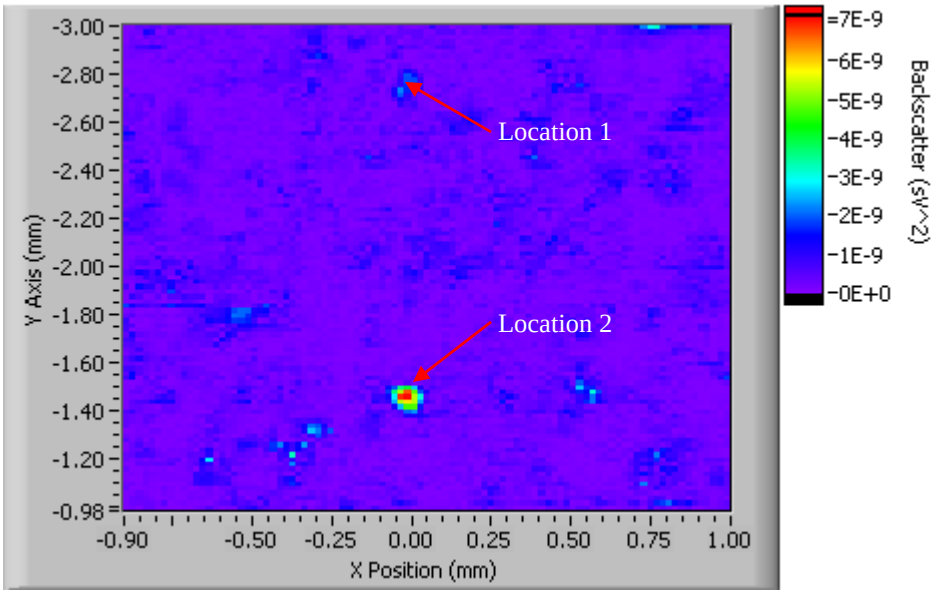

Figure 5.3-7: Relative amplitude image difference between C-scan-128 & 131, 0.07psi Δp.

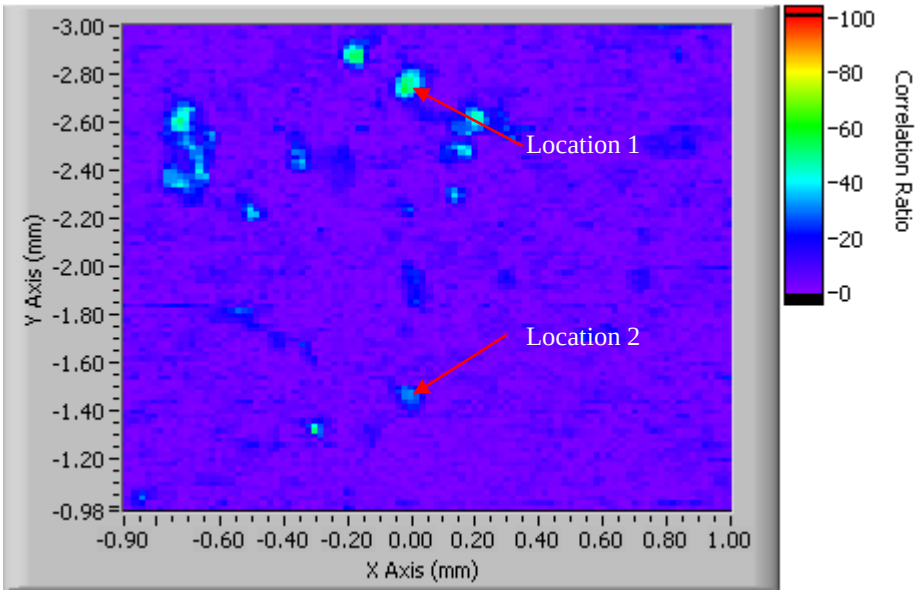

Figure 5.3-8: Correlation ratio between C-scan-128 & 131, 0.07psi Δp.

The correlation ratio method clearly identified this variation in the received signal but it barely registered on the image difference results. Since the image difference method defines change as a difference in the total sum of the squared envelope values this deviation was not very significant in that regard. The correlation method, however, defines the difference by quantifying the similarity between the two A-lines using the auto and cross-correlation formulas. This point can be seen in the two A-line comparison plots for both locations. This point is made in the A-line comparison at location 2. While the shape of the A-lines is consistent between scans the amplitude was reduced, hence the large emphasis in the image difference method compared to the correlation ratio result.

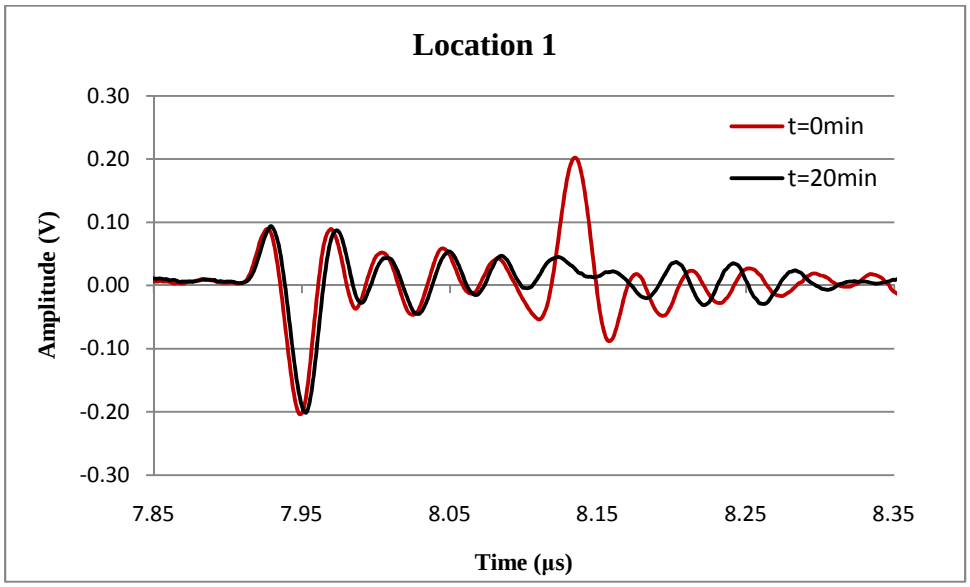

Figure 5.3-9: A-line comparison location 1 for C-scan-128 & 131.

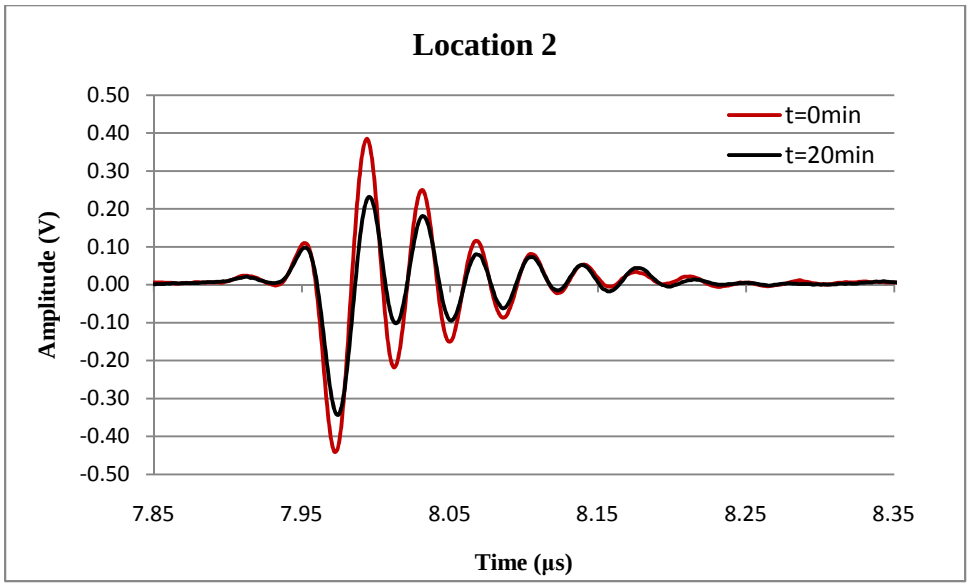

Figure 5.3-10: A-line comparison location 2 for C-scan-128 & 131.

5.3.2.2- Silicon Pin Hole Tests

Based on the assumption made the areas identified by the correlation method are areas where water has entered the GDL. The problem is that no secondary validation to confirm that water has indeed penetrated these regions was available. To address this, a series of tests were performed which attempt to control where water enters the GDL. To accomplish this, a Toray-120 sample had an approximately $80\mu m$ thick silicon layer applied to one side. After curing, a $400\mu m$ diameter hole was cut in the silicon layer. This was to control the location of water passage for one side of the GDL. A series of $2x2mm$ scans proceeded, capturing the acoustic response before and after a pressure application of $1psi$ for two different orientations of the sample in the microscope.

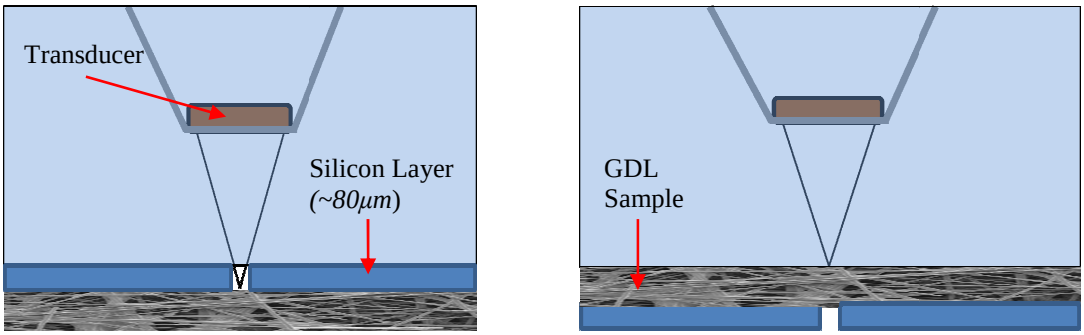

Orientation 1 Orientation 2

Figure 5.3-11: Silicon covered pin hole scan orientations.

The first orientation places the silicon layer facing the transducer, ensuring that water will only penetrate the GDL through the hole in the silicon layer during the application of a pressure differential. The images in figure *5.3-12* and *5.3-13* show the acoustic backscatter from the dry and wet scans taken for this orientation. To capture only the echo signals from the GDL a time-gate was chosen to exclude the front and back reflections of the silicon. Given the pulse attenuation through this layer, increased amplification was needed to visualize the GDL's acoustic response, producing the images granular texture. However, this also causes the scale clip for the corresponding region under the hole in silicon as no additional attenuation is in effect. After comparing the two images this clipped region is the only area where any significant change has occurred after the application of a pressure differential.

The results also provide an acoustic response image from a completely dry sample given the cover of silicon. This reinforces the observation of large variations in acoustic reflectivity for dry samples as it was speculated that this could be due to the saturation of various locations under the water head in standard tests.

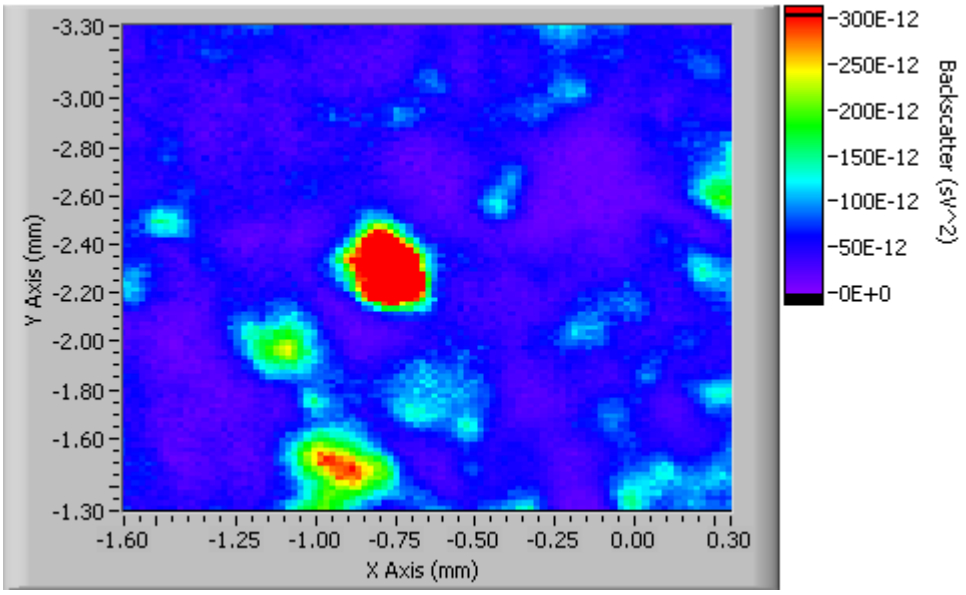

Figure 5.3-12: Dry scans backscatter over time-gate 8.4-8.65μs. 0.07psi Δp C-scan-108 orientation 1.

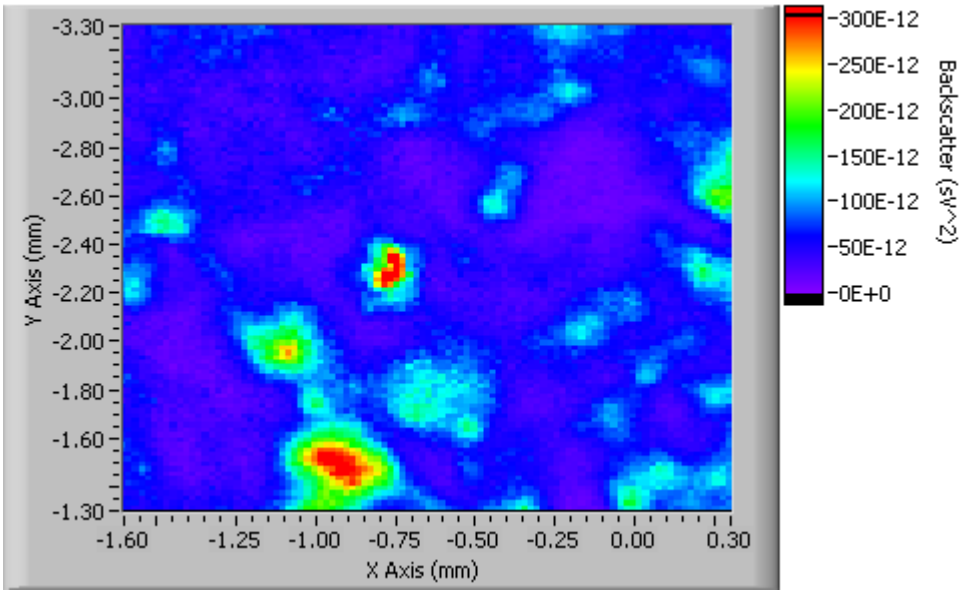

Figure 5.3-13: Wet scans backscatter over time-gate 8.4-8.65μs. 1.0psi Δp C-scan-110 orientation 1.

Review of the correlation ratio images reveals a single column of water penetrating the GDL through the hole in the silicon layer. It also shows very little spread in the saturated column as the estimated diameter of identified change was $350\mu m$.

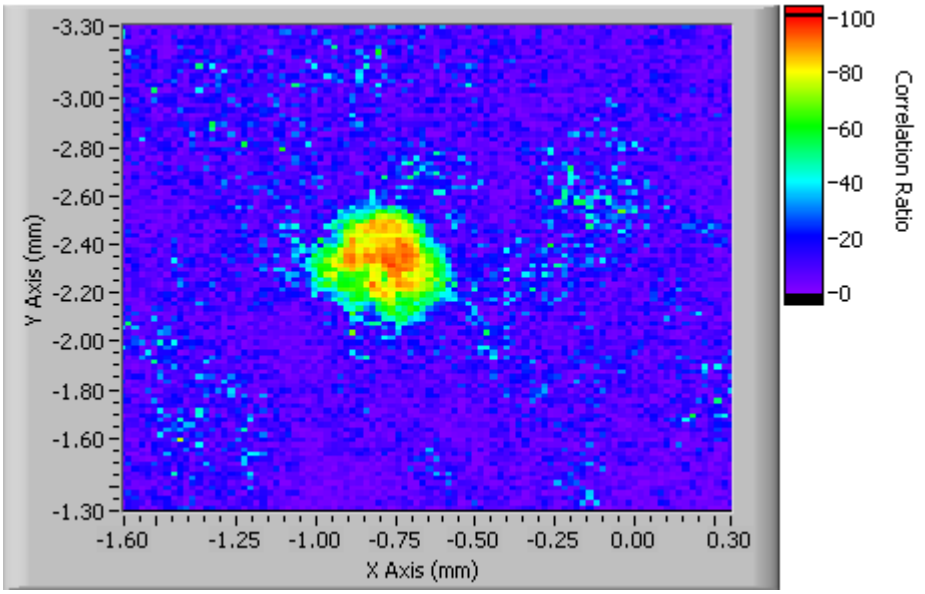

Figure 5.3-14: Correlation ratio between C-scan-108 & 110, orientation 1.

The scans performed using the second orientation provided the saturation pattern for a GDL were water is available to penetrate anywhere on its surface but exit through a single port as opposed to the previous test were the reverse was facilitated. The results revealed no apparent effect of the silicon covered bottom face. Just by inspection of the two dry/wet images no evidence of an isolated change corresponding to the hole in the silicon layer was visible.

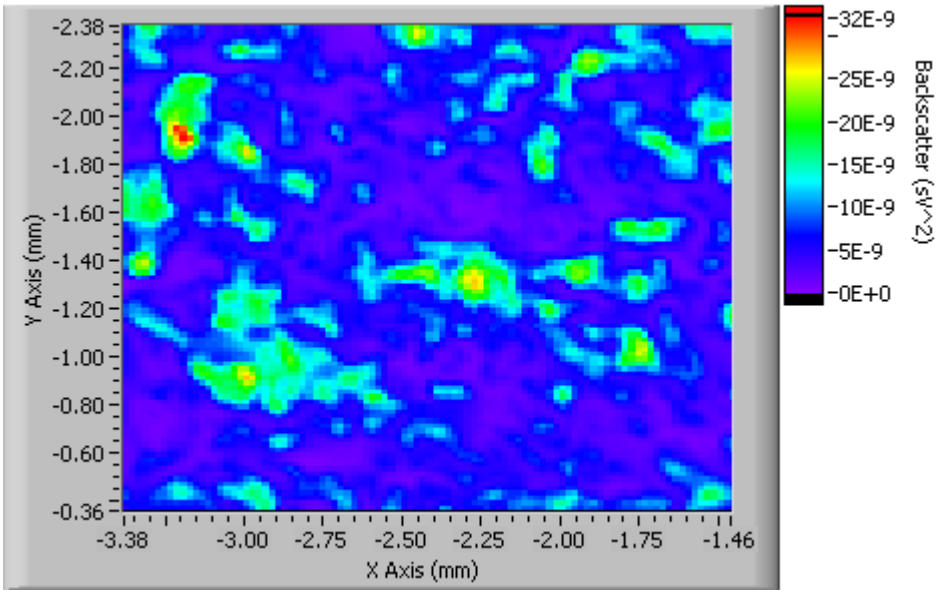

Figure 5.3-15: Dry scans backscatter over time-gate 8.0-8.4μs. 0.07psi Δp. C-scan-116 orientation 2.

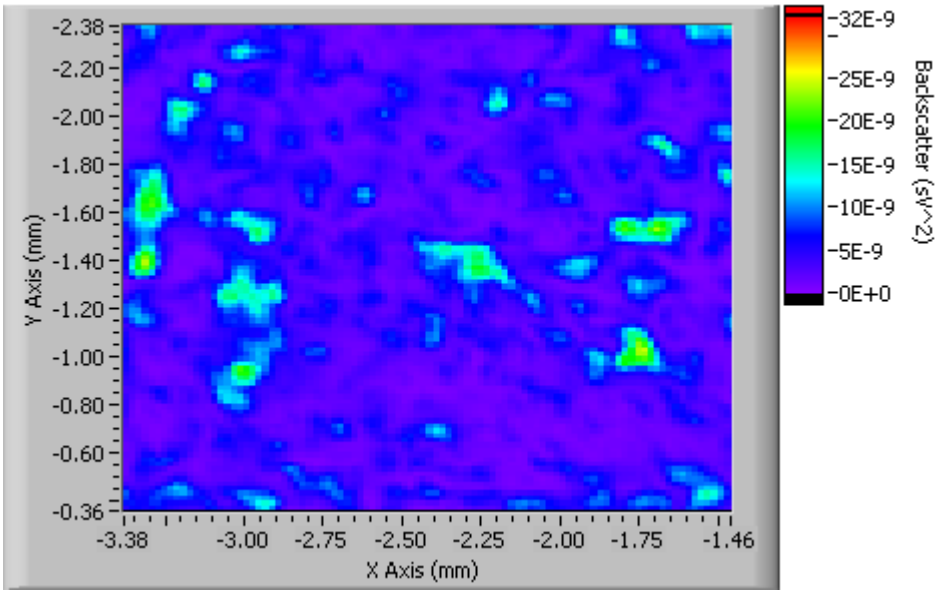

Figure 5.3-16: Wet scans backscatter over time-gate 8.0-8.4μs. 1.0psi Δp.C-scan 122 orientation 2.

The correlation ratio results showed an unbiased distribution of preferential saturation points. Again, no evidence of the single exit point was apparent in the generated image. What this suggests is as the pressure is reduced in the vacuum chamber all the connected pores of the GDL follow suit while the water/GDL interface provides the pressure boundary given the hydrophobic nature of the microstructure. This provides a uniform pressure distribution over the boundary surface and as the local capillary forces are overcome water saturates the GDL in the locations depicted in figure *5.3-17*.

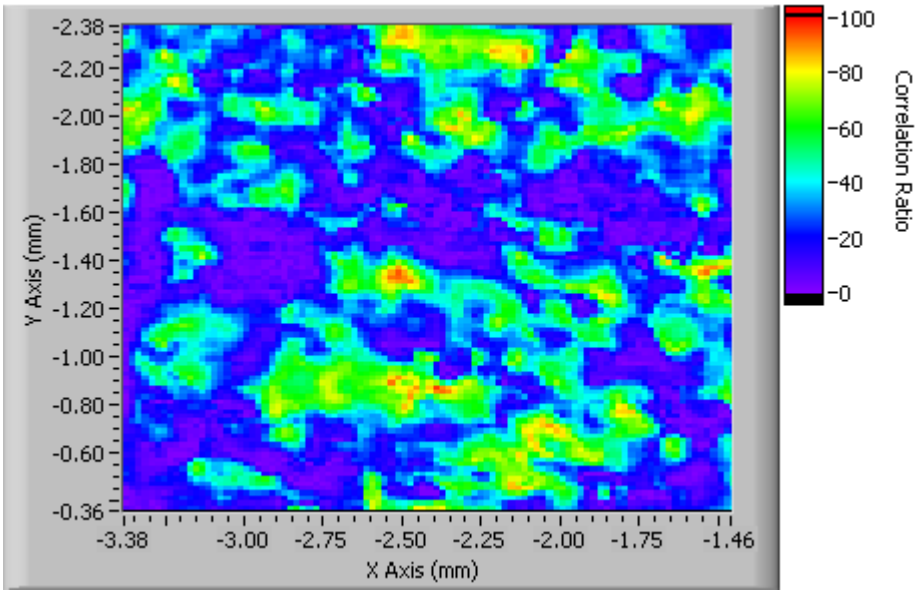

Figure 5.3-17: Correlation ratio between C-scan-116 & 122, orientation 2.

5.3.3-Saturation Distributions

5.3.3.1- PTFE Variation

After validating the new correlation method of identifying regions of water penetration a study was performed to compare the results collected for Toary-120 with varying levels of PTFE content. It was speculated that a clear distinction would be made between the GDL's spatial distribution of saturation regions. In order to capture this, a tests methodology was developed that would record the saturation state of the test sample before, during, and after the application of set pressure differentials.

For a given GDL sample the tests were set to acquire three dry reference scans separated by twenty minutes. After these three scans were completed a series of pressure applications and scans would commence. For each pressure level, as listed in table *5.3-1*, a repetitive B-scan series would capture the center line saturation progression during the application of a pressure differential in terms of acoustic backscatter. The selected area was then rescanned, mimicking the dry reference C-scans.

Each test was performed with identical settings. The B-scans were performed using the continuous scanning mode to ensure a reasonable refresh rate of 0.918 seconds over the $2mm$ center scan line. The trigger generation for these scans were set to acquire A-lines every $20\mu m$. All C-scans were taken over a $2x2mm$ area with the same pixel separation, creating a 10,000 pixel image. Since acquisition time for the C-scans was not of concern but accuracy and signal-to-noise ratio was, the iterative scanning mode was used, set to average ten A-lines at each pixel location. This resulted in a total scan time of 802 seconds.

Scan #	*Pressure kPa (psi)*	
Dry Reference	*0.483*	*(0.07)**
Sat. Stability (20min)	*0.483*	*(0.07)**
Sat. Stability (40min)	*0.483*	*(0.07)**
Sat. Level 1	*1.034*	*(0.15)*
Sat. Level 2	*1.724*	*(0.25)*
Sat. Level 3	*2.413*	*(0.35)*
Sat. Level 4	*3.447*	*(0.50)*
Sat. Level 5	*5.171*	*(0.75)*
Sat. Level 6	*6.895*	*(1.0)*
Sat. Level 7	*13.790*	*(2.0)*
Sat. Level 8	*20.684*	*(3.0)*

**Water head pressure*

Table 5.3-1: Pressure application series for all saturation distribution tests.

The results were then processed using the correlation ratio method, taking the first scan as the dry reference. To quantify the saturation image an in-house developed particle analysis algorithm converts the image to binary and counts the isolated "saturated" regions or "cells," outputting the fractional coverage area, cell count, average cell size, and the standard deviation of the cell size distribution.

Using this methodology, four Toray-120 samples were tested differing by their percent by weight PTFE loadings, 0%, 10%, 20%, and 40%. Figures *5.3-18* through *20* show the resulting particle analysis results.

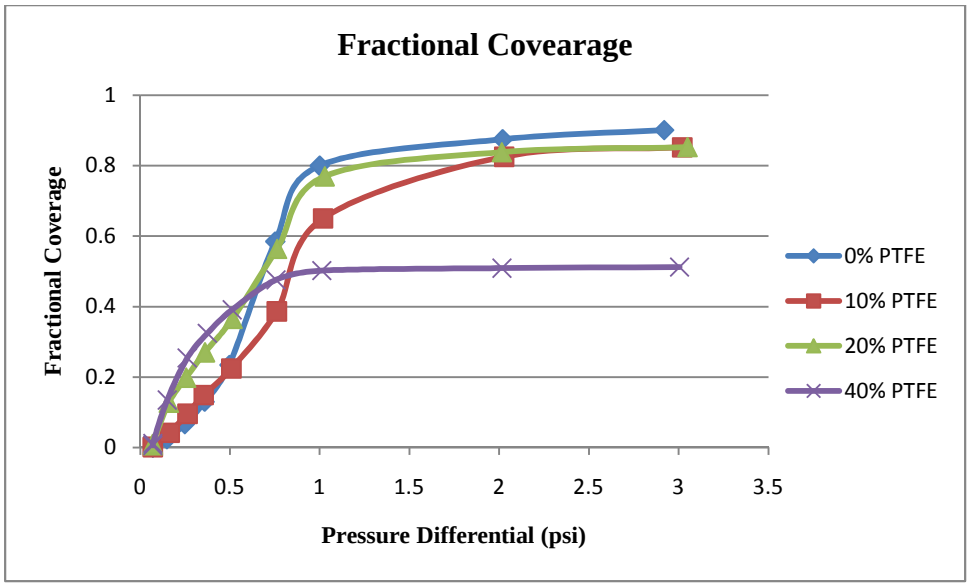

Figure 5.3-18: Fractional coverage as a function of Δp for Toray PTFE comparison series.

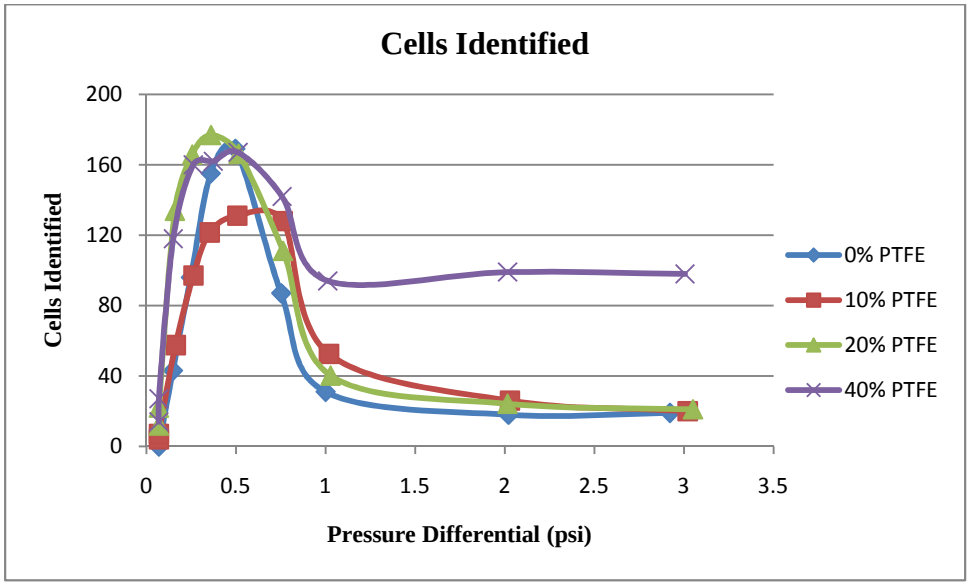

Figure 5.3-19: Total cells identified as a function of Δp for Toray PTFE comparison series.

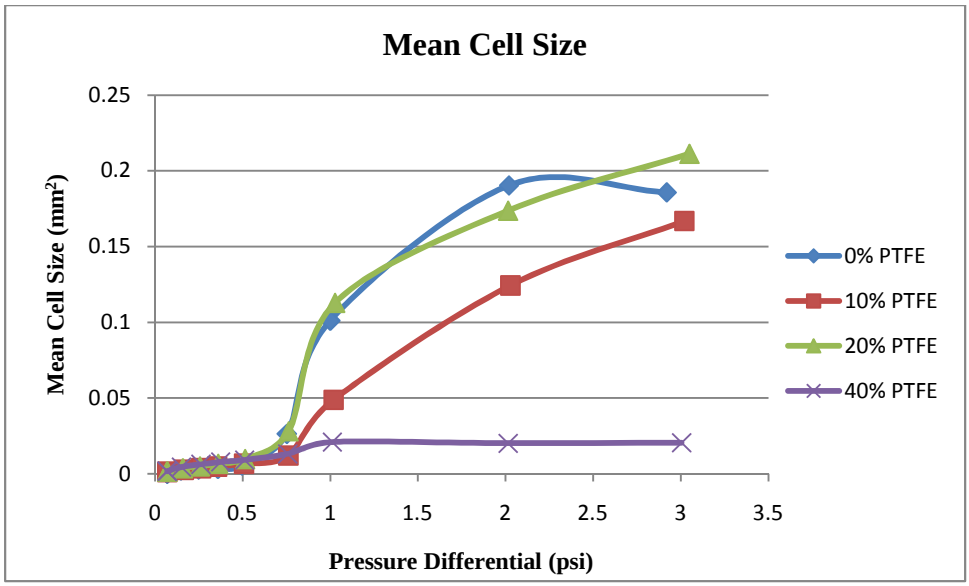

Figure 5.3-20: Average cell size as a function of Δp for Toray PTFE comparison series.

The results show a general trend in the parameters for all PTFE loadings with the exception of the 40% appearing to be significantly different after the application of $1psi$. All the samples follow a steep increase in fractional coverage which levels off at an apparent maximum value. The number of cells identified and mean cell size plots in figures *5.3-19* and *20* describe a saturation pattern where the number of cells increases steadily along with the average cell size. A critical point is reached when cells connect with each other, reducing the number of individual saturation points and drastically increasing the mean cell size. This point of transition can be seen in the fractional coverage plots as the inflection point where the expansion rate goes from positive to negative.

The acoustic backscatter for each C-scan of the PTFE series of tests was also investigated. The backscatter energies for all recorded echo signals in a scan line were averaged for each of the 100 B-lines making up the scan. An example case is shown in figure *5.3-21* where the normalized dry reference, $0.5psi$, $1.0psi$, and $3.0psi$ scan results are plotted. Not only does the average B-line backscatter go down but the deviation between B-lines does as well. Intuitively this can be explained by the decreasing presence of the dominant acoustic reflector, air. While the GDL is assumed to be relatively dry the amplitude of the echo pulses depends greatly on the localized microstructure, leaving interference and

fiber clusters to govern the echo amplitude. As the saturation of the GDL increases the size and number of air pockets along with the acoustic coupling to the microstructure reduce the probability of a pure water/air boundary reflection, ultimately leveling off to the baseline speckle amplitude generated by a fully saturated GDL.

Figure *5.3-22* plots the average C-scan backscatter trends, normalized to the maximum B-line backscatter acquired in a single sample series at the various saturation pressure levels. The calculated standard deviations between the scans B-line backscatters have also been plotted for each data point. While the trends show a distinction between the PTFE levels for the scans acquired before the $0.75psi$ pressure differential application, after this point the pattern breaks down. However, these data does illustrate the general acoustic behavior of Toray-120 GDL samples subjected to increasing levels of saturating differential pressures.

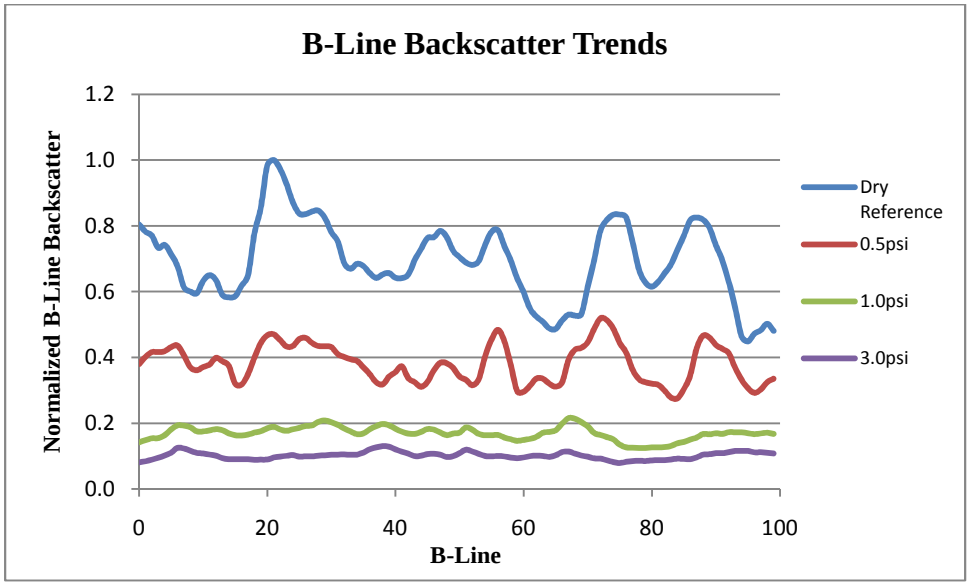

Figure 5.3-21: Average normalized B-line backscatter Toray-120 20% PTFE Loading. C-scan-229 series.

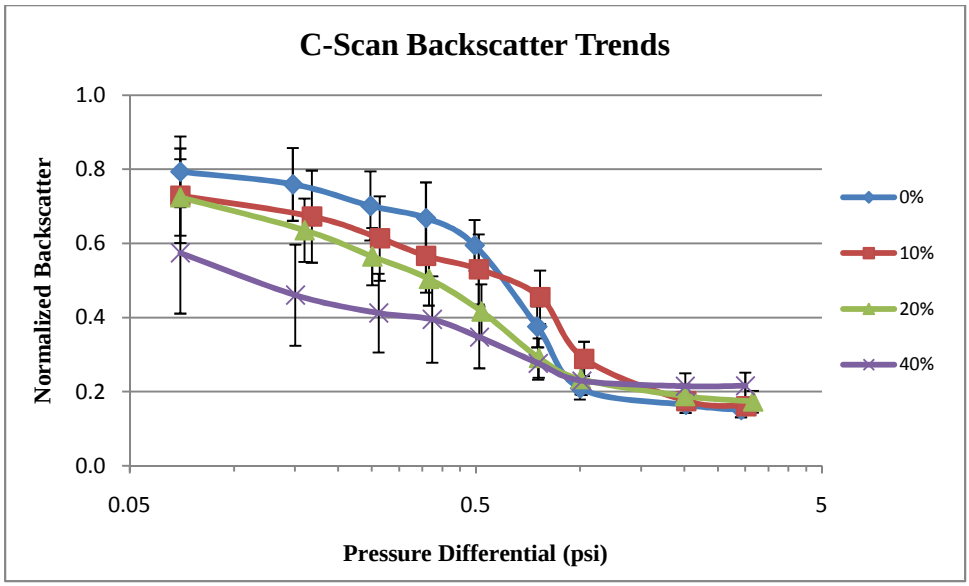

Figure 5.3-22: C-scan backscatter with B-line std. dev. bars as a function of Δp for Toray PTFE series.

Since the particle analysis and backscatter results for a single scan have relatively low errors associated with them, listed in table *A.5*, the differences between individual test series is clear. The problem arises when trying to draw conclusions about the effect PTFE has on the acoustic response. The inhomogeneous nature of the samples microstructure and the large variations in the echo signals ensure significant variations in the measured results. To gather some idea as to the repeatability of these results for the same test sample, Toray-120 with 20% PTFE loading was retested six times. The average values for the calculated particle analysis results are presented in figures *5.3-23* thru *25* along with the standard deviation error bars associated with each data point.

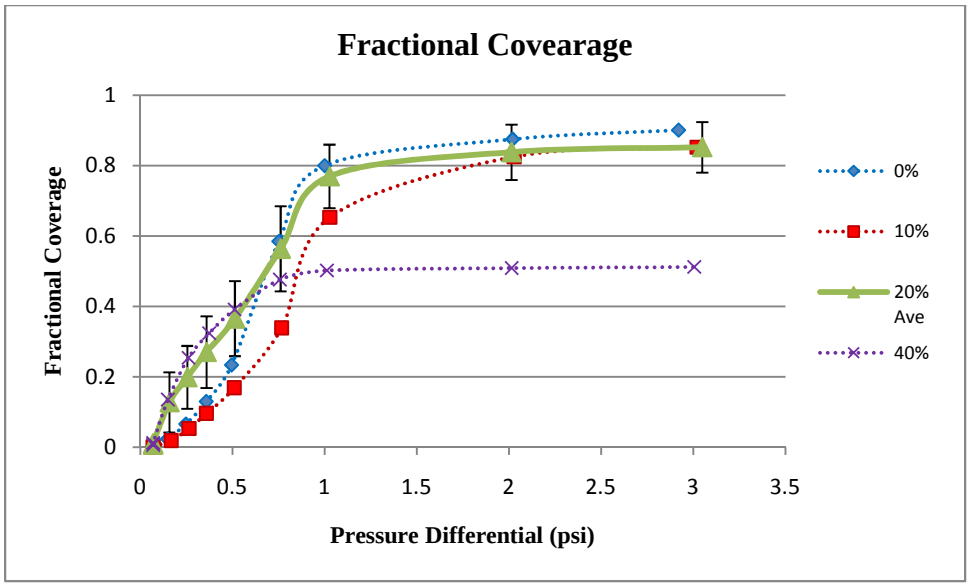

Figure 5.3-23: Average fractional coverage for Toray-120 20%PTFE loading.

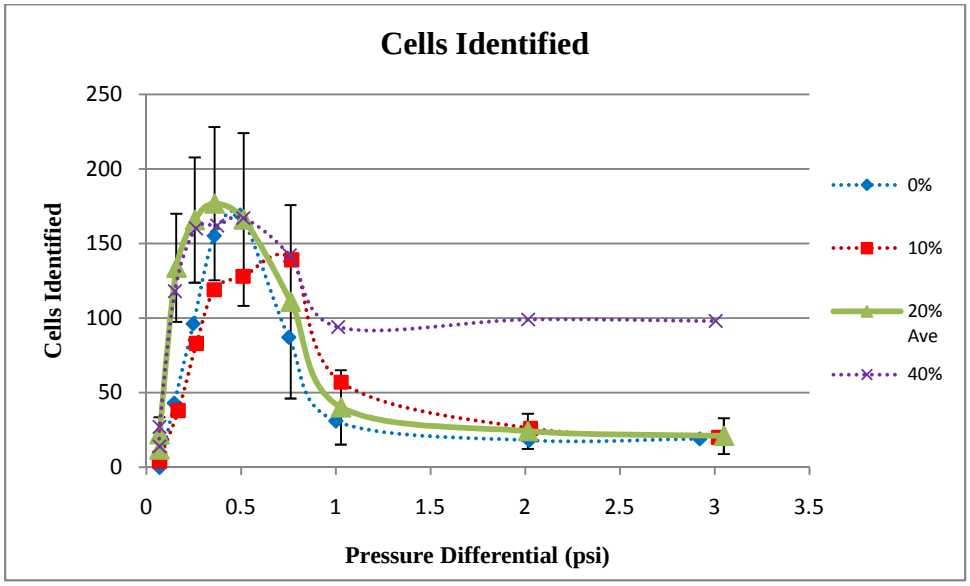

Figure 5.3-24: Average total cells identified for Toray-120 20% PTFE loading.

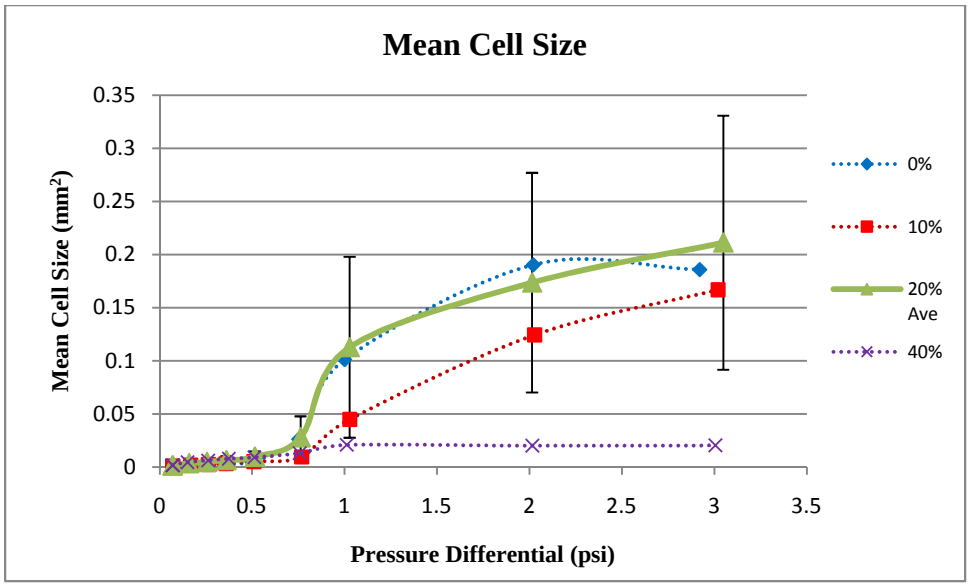

Figure 5.3-25: Average cell size for Toray-120 20% PTFE loading.

With the 0%, 10%, and 40% results plotted alongside the average 20% PTFE values it's clear that only the 40% test results appear significantly different. To test the hypothesis that the two mean values are different a t-distribution with 5 degrees of freedom is assumed.

Null Hypothesis $$H_0: \mu_1 - \mu_2 = 0 \qquad (5.3\text{-}1)$$

Test Statistic $$T_0 = \frac{\bar{X}_1 - \bar{X}_2}{S_p\sqrt{\frac{1}{n_1} + \frac{1}{n_2}}} \qquad (5.3\text{-}2)$$

Acceptance Criterion $$-t_{\alpha/2,n_1+n_{2-2}} < T_0 < t_{\alpha/2,n_1+n_{2-2}} \qquad (5.3\text{-}3)$$

It was found that the only statistically significant differences found between the data sets were in the fractional coverage and cell count results. With a 95% confidence the 40% sample proved to deviate from the 20% sample for the 1, 2, and 3psi pressure levels. The cell counts were found to deviate after 2psi.

5.3.3.2- GDL MPL/Cloth Comparison

Since the results of the PTFE study were inconclusive given the limited data set, scans of two different types of diffusion media were performed. The first GDL to be scanned in the types comparison series was the Toray-090 coated on one side with a microporous layer (MPL). This layer is a highly hydrophobic coating which possesses pores sizes between that of the diffusion media and the catalyst layers [38]. Its purpose is to assist in water transport and management near the catalyst layer, limiting the formation of liquid water in this critical region. Typical thicknesses are around $20\mu m$ and it is positioned between the aforementioned diffusion media and catalyst layer. Optical images of both sides, with and without MPL, are shown in figures *5.3-26* and *27*.

The second type of diffusion media to be compared to the Toray-120 GDL is the woven carbon cloth diffusion media. This material is manufactured with woven bands of carbon fibers as seen in figure *5.3-28* as opposed to the carbon papers were fibers are laid in-plane and oriented semi-random. The cloth tested had a thickness of $\sim 430um$ as opposed to the $\sim 380um$ and $\sim 290um$ thick Toary-120 and Toary-090 samples.

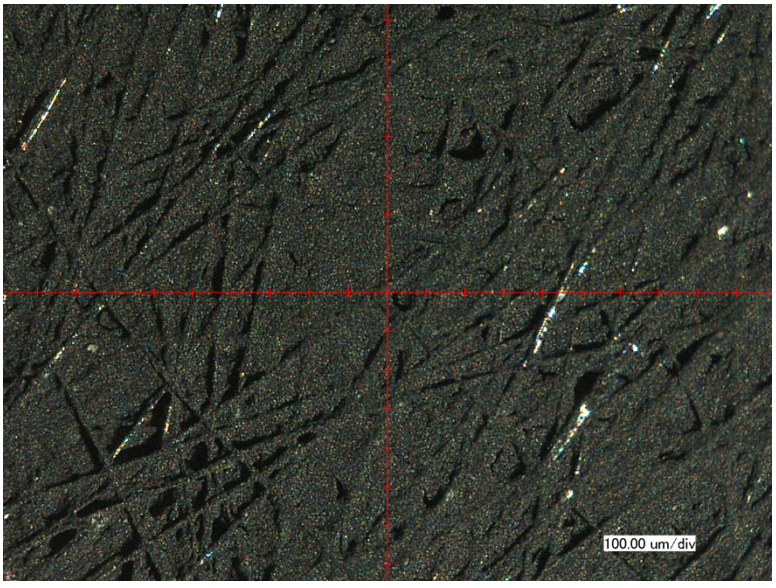

Figure 5.3-26: 2x2mm optical image of Toray-090, MPL side.

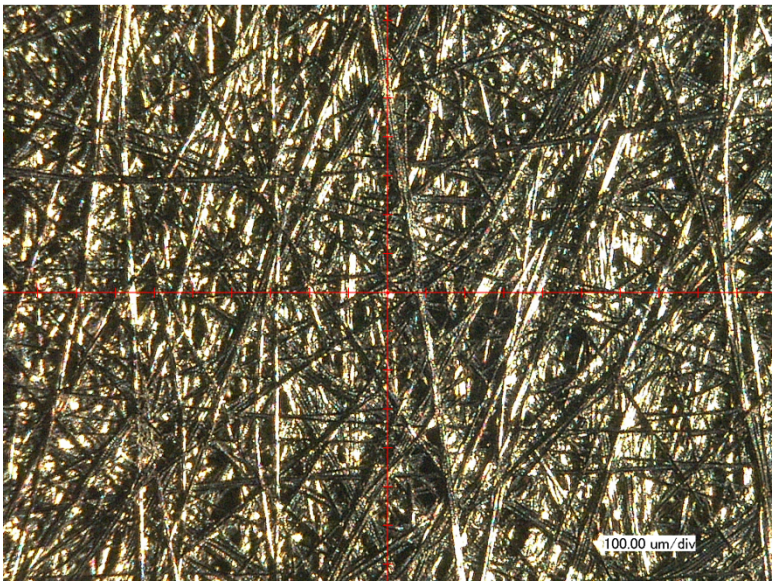

Figure 5.3-27: 2x2mm optical image of Toray-090, non-MPL side.

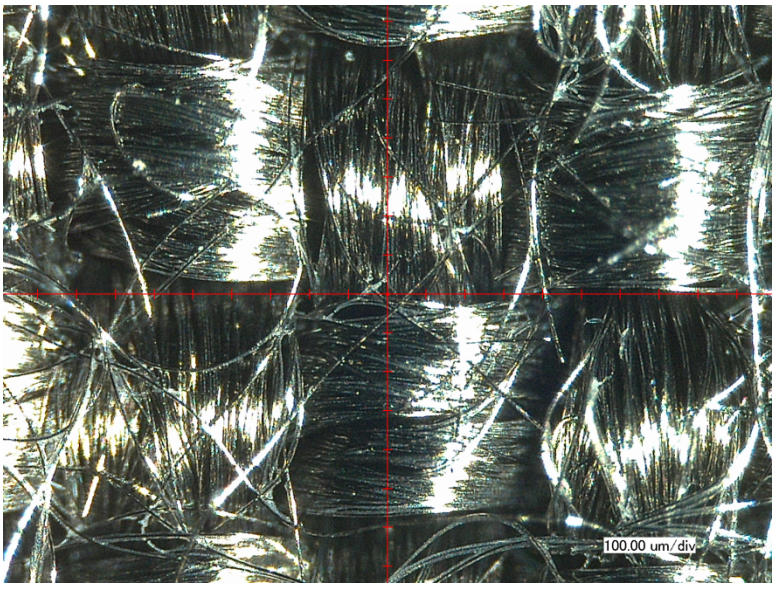

Figure 5.3-28: 2x2mm optical image of carbon cloth A with 10% PTFE.

The type comparison series of tests were performed in an identical fashion as the PTFE comparison series and processed using the same criterion. For each sample two tests were completed to obtain some idea of the expected deviations in the collected data. For the Toray-090 sample with MPL, two different orientations were scanned twice, one with the MPL facing the transducer, orientation 1, and another with the MPL facing down, orientation 2.

After processing the data and generating the correlation ratio images at the different saturation pressures it was very clear that the different GDL types produce significantly different saturation patterns. Figures *5.3-29* thru *44* present the correlation ratio images of both Toray-090 MPL orientation scans, a Toray-120 20% PTFE scan, and a carbon cloth scan after the, $0.15psi$, $0.5psi$, $1.0psi$, and $3.0psi$ saturation pressure applications. By basic inspection it is clear that the Toray-090 orientation 1 and carbon cloth GDL scans fall on opposite sides of the results spectrum while the Toray-120 and Toray-090 orientation 2 scans produce results similar to each other but between the other two.

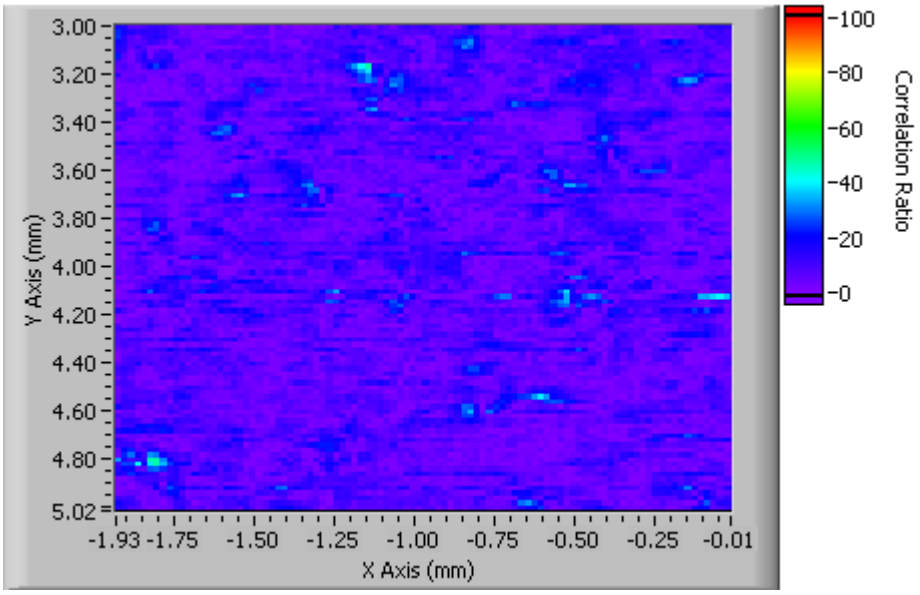

Figure 5.3-29: Correlation ratio image results for Toray-090 sample with MPL facing up after 0.15psi saturation pull. C-scan-359 series.

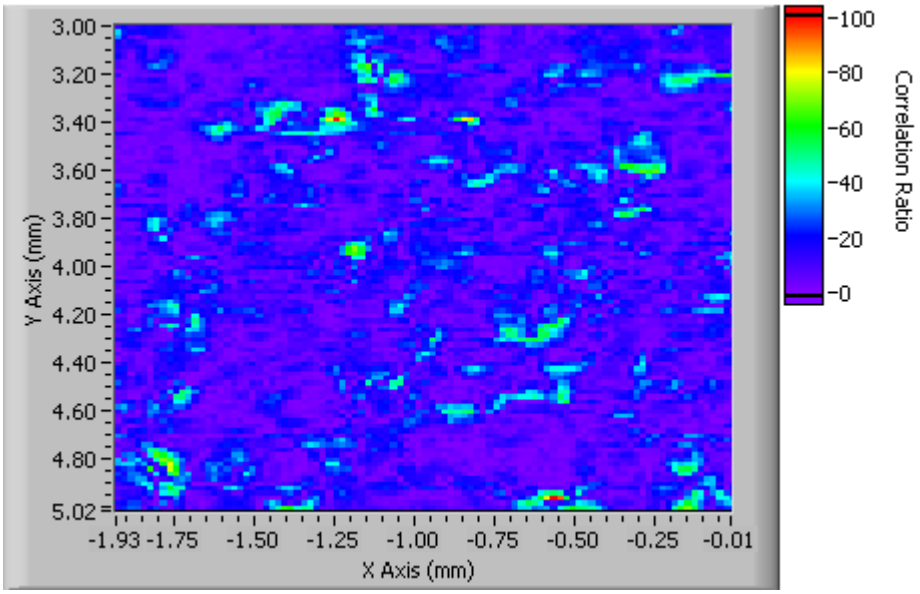

Figure 5.3-30: Correlation ratio image results for Toray-090 sample with MPL facing up after 0.5psi saturation pull. C-scan-359 series.

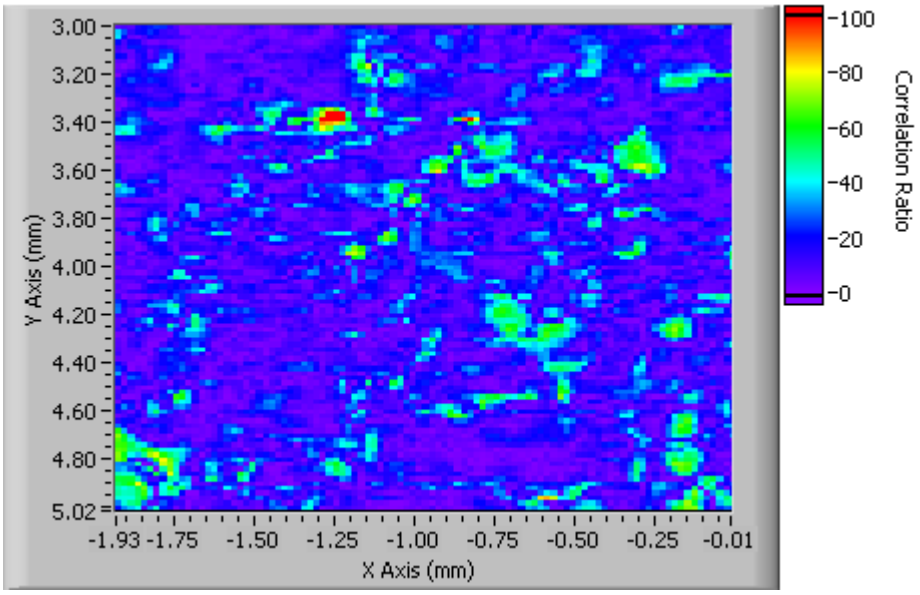

Figure 5.3-31: Correlation ratio image results for Toray-090 sample with MPL facing up after 1.0psi saturation pull. C-scan-359 series.

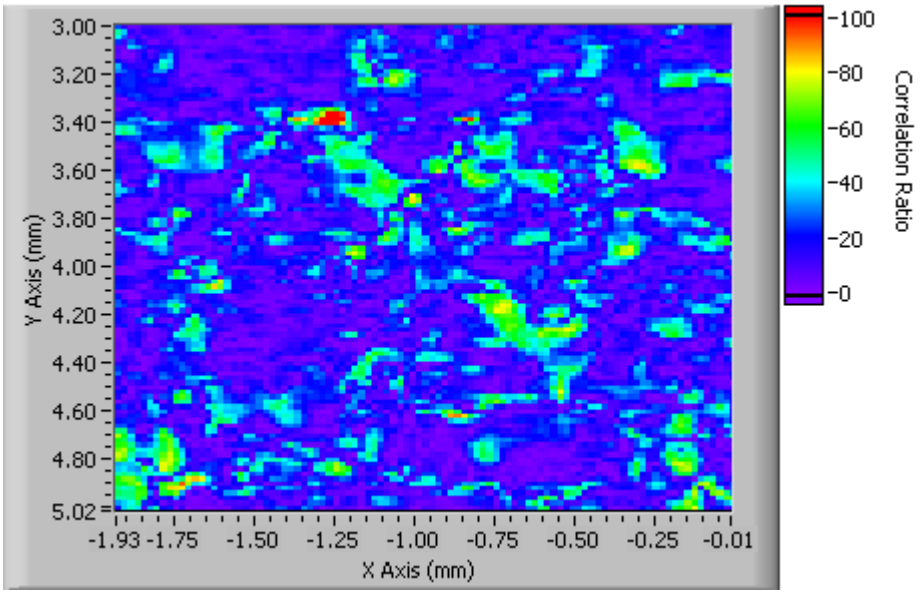

Figure 5.3-32: Correlation ratio image results for Toray-090 sample with MPL facing up after 3.0psi saturation pull. C-scan-359 series.

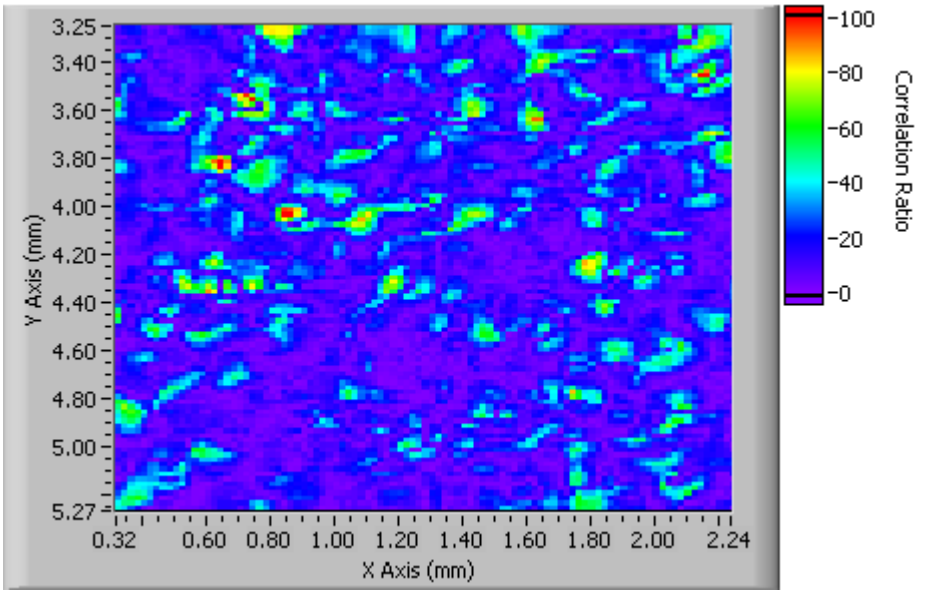

Figure 5.3-33: Correlation ratio image results for Toray-090 sample with MPL facing down after 0.15psi saturation pull. C-scan-369 series.

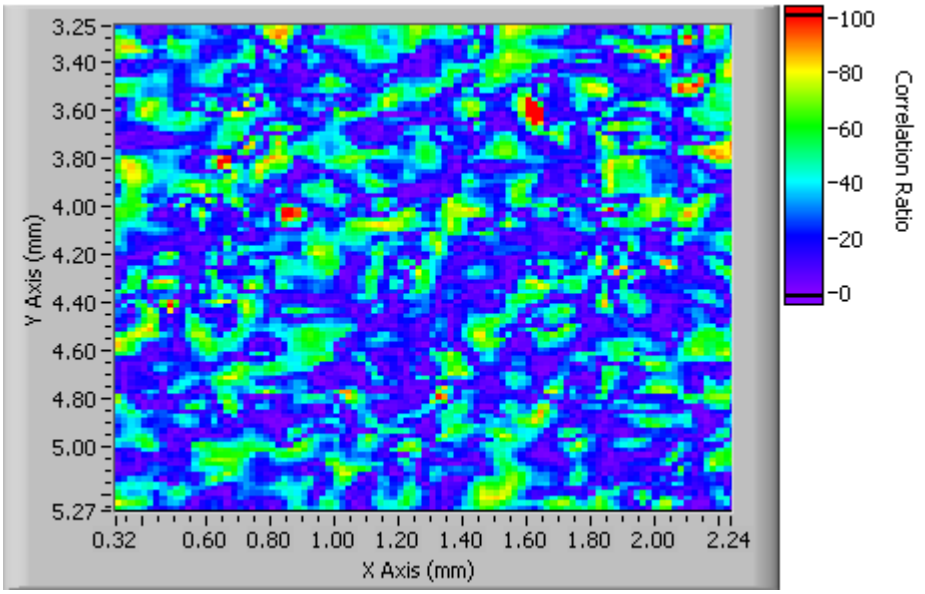

Figure 5.3-34: Correlation ratio image results for Toray-090 sample with MPL facing down after 0.5psi saturation pull. C-scan-369 series.

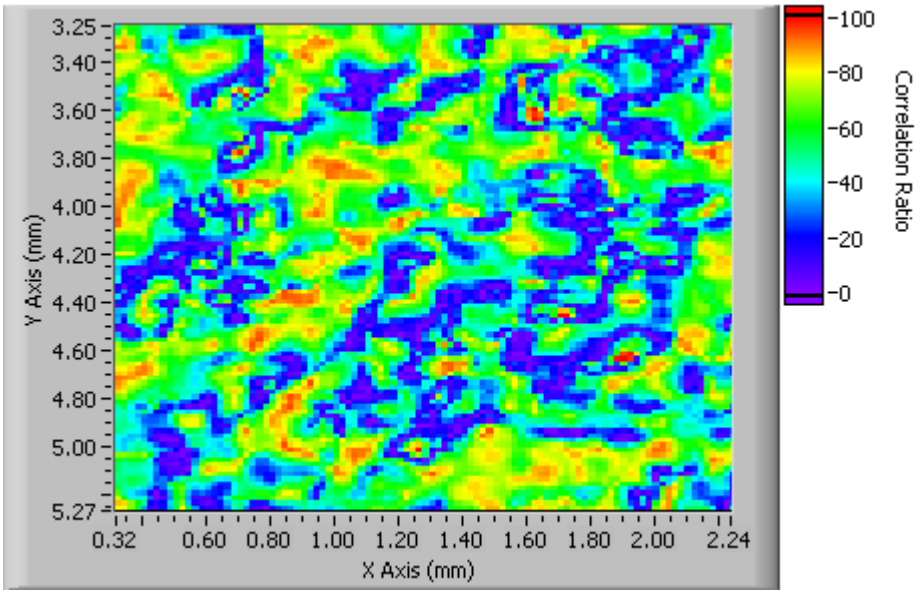

Figure 5.3-35: Correlation ratio image results for Toray-090 sample with MPL facing down after 1.0psi saturation pull. C-scan-369 series.

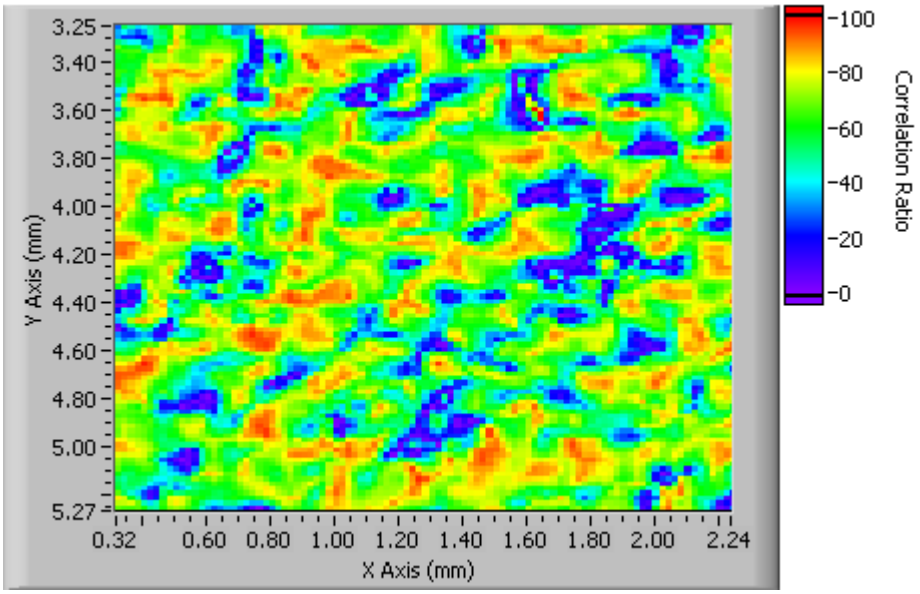

Figure 5.3-36: Correlation ratio image results for Toray-090 sample with MPL facing down after 3.0psi saturation pull. C-scan-369 series.

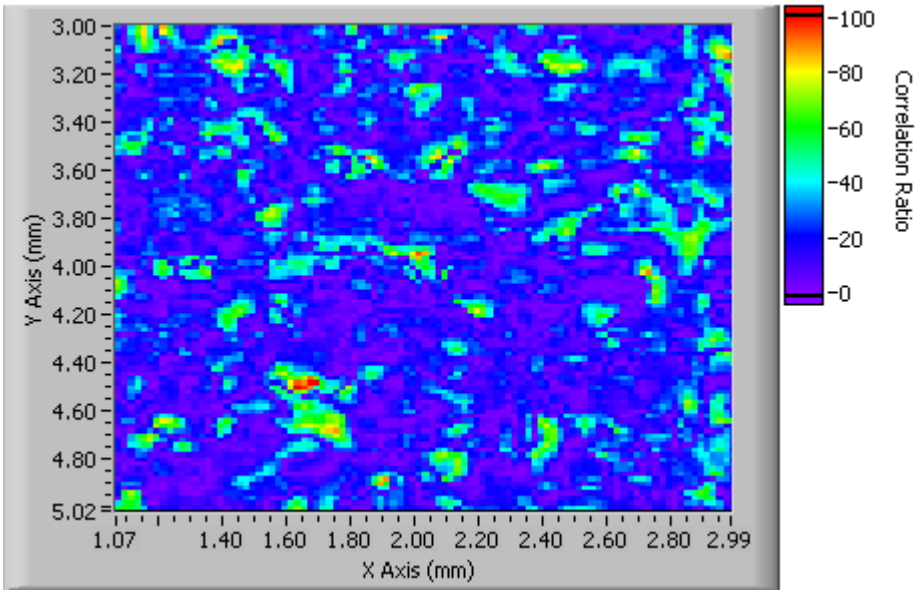

Figure 5.3-37: Correlation ratio image results for Toray-120 sample with 20% PTFE loading after 0.15psi saturation pull. C-scan-307 series.

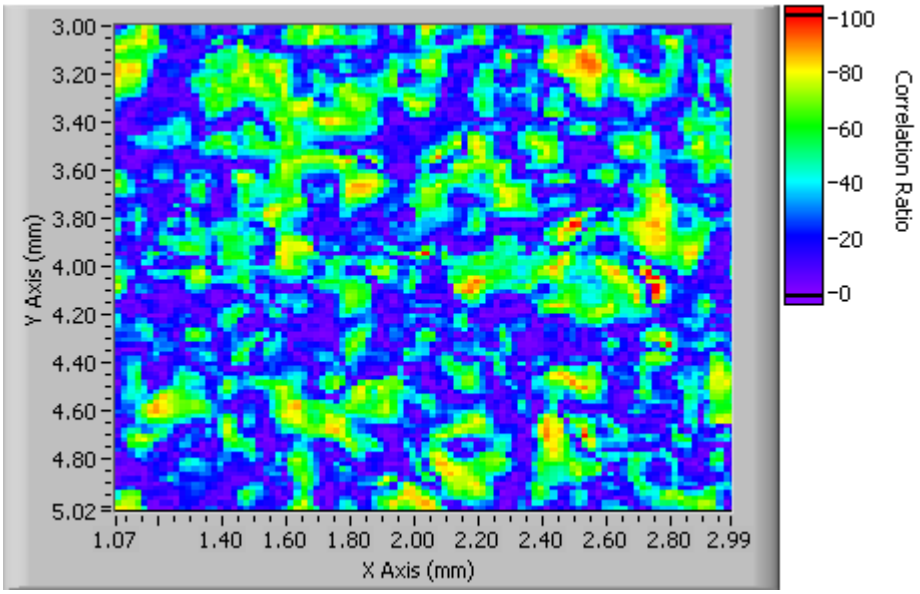

Figure 5.3-38: Correlation ratio image results for Toray-120 sample with 20% PTFE loading after 0.5psi saturation pull. C-scan-307 series.

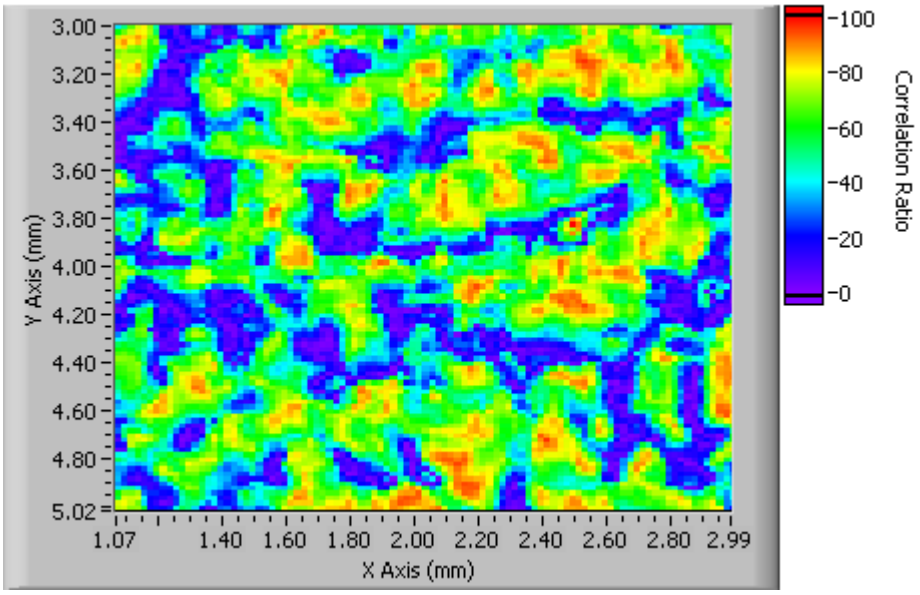

Figure 5.3-39: Correlation ratio image results for Toray-120 sample with 20% PTFE loading after 1.0psi saturation pull. C-scan-307 series.

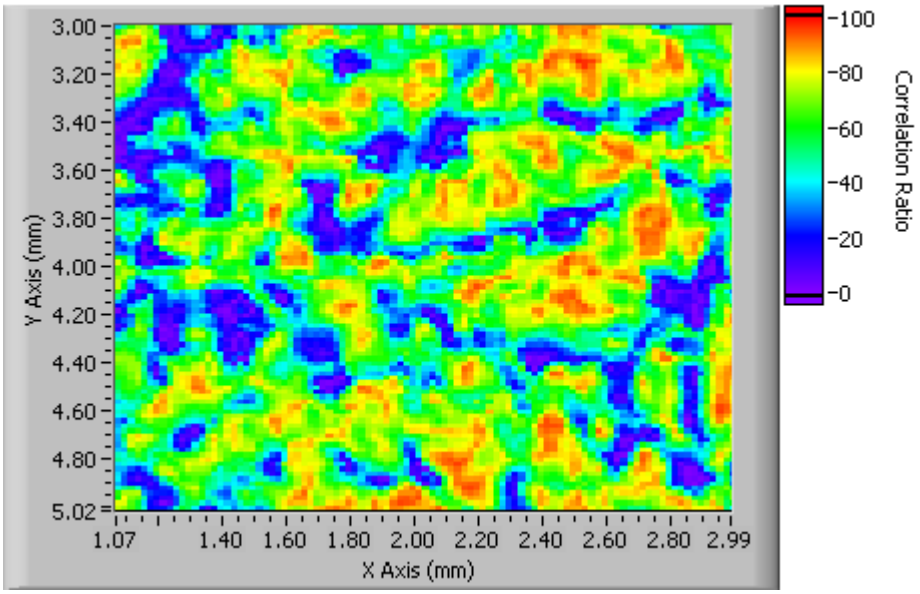

Figure 5.3-40: Correlation ratio image results for Toray-120 sample with 20% PTFE loading after 3.0psi saturation pull. C-scan-307 series.

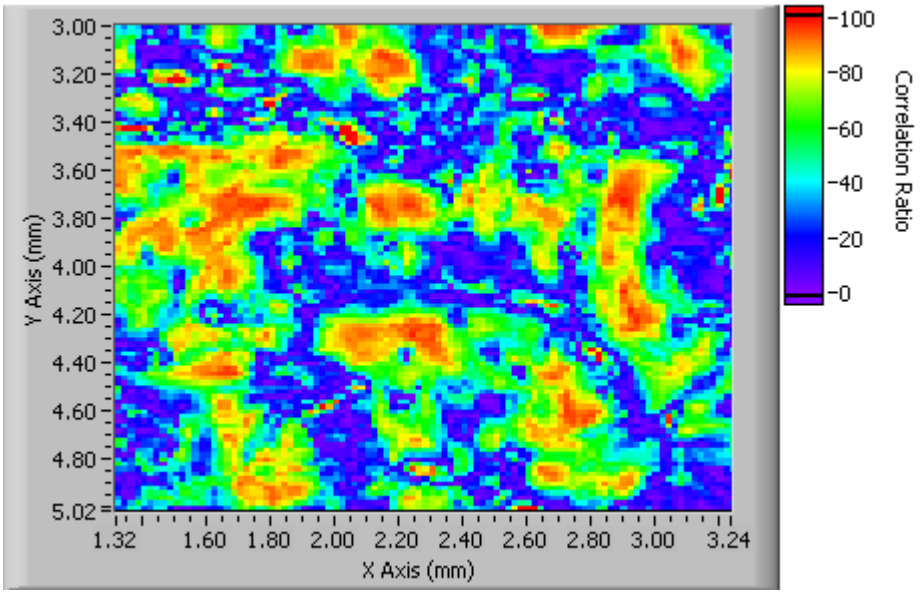

Figure 5.3-41: Correlation ratio image results for carbon cloth sample after 0.15psi saturation pull. C-scan-274 series.

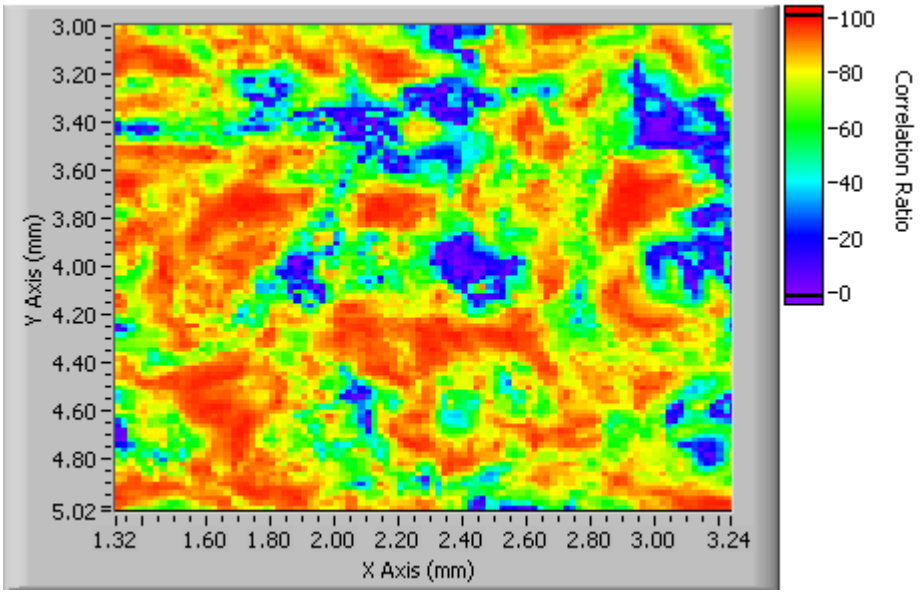

Figure 5.3-42: Correlation ratio image results for carbon cloth sample after 0.5psi saturation pull. C-scan-274 series.

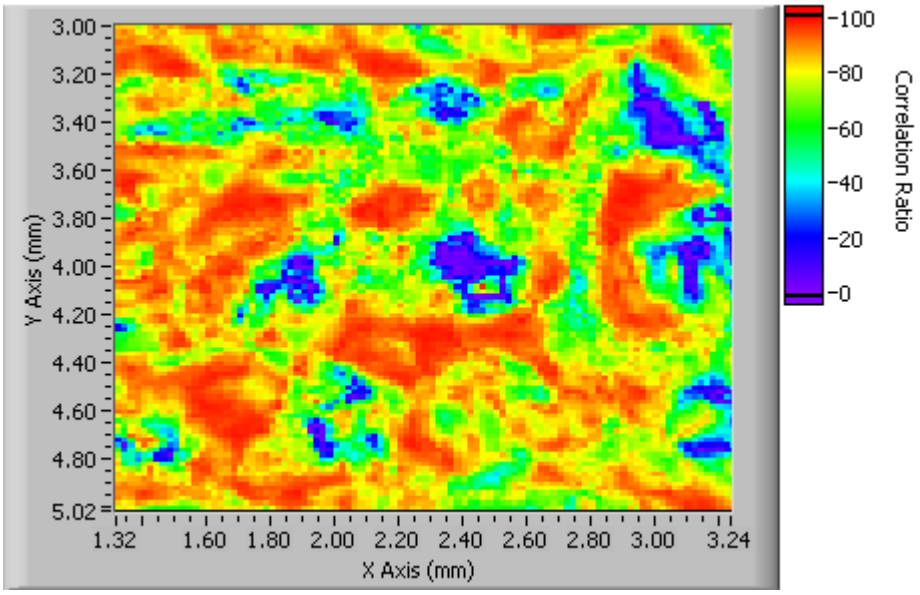

Figure 5.3-43: Correlation ratio image results for carbon cloth sample after 1.0psi saturation pull. C-scan-274 series.

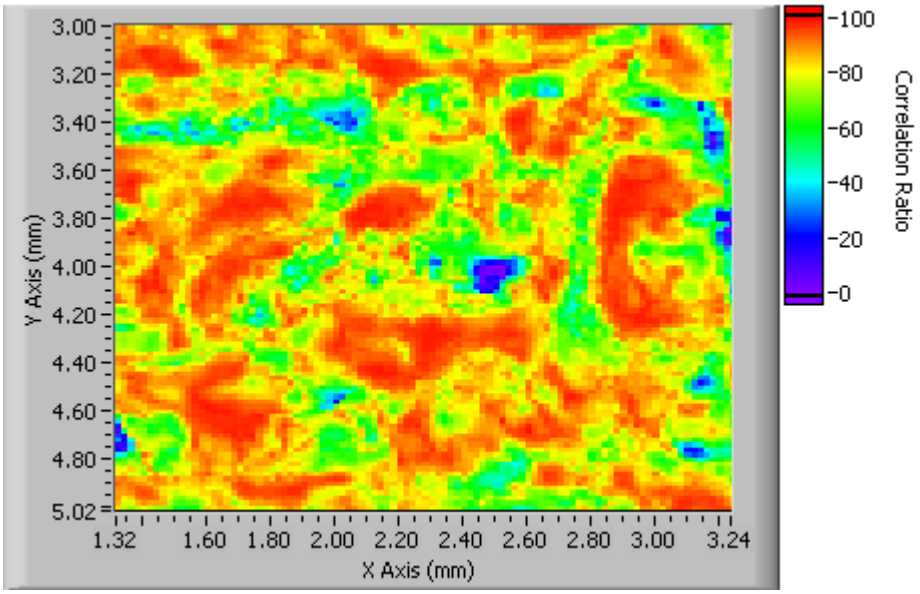

Figure 5.3-44: Correlation ratio image results for carbon cloth sample after 3.0psi saturation pull. C-scan-274 series.

This visual inspection is confirmed quantitatively with the particle analysis results and C-scan backscatter values presented in figures *5.3-45* thru *49*. It should be noted that only one of the two carbon cloth scans was able to capture saturation results above $0.75psi$. The first test resulted in a complete drain of the waterbath during the $1.0psi$ pressure application. The Toray-090 orientation 1 scans also ran into high water flow rates in the upper pressure regions. A maximum of $2.7psi$ was achievable in these scans.

The fractional coverage plots show three distinct trends diverging with increasing saturation pressures. As the correlation images show the carbon cloth exhibited the steepest increase in saturation with a maximum fractional coverage area of 91.0% & 99.3% at the $3.0psi$ data point. The Toray-090 with the MPL providing the water/sample interface showed the opposite trend and possessed the lowest coverage area of 12.9% & 24.9%. The Toray-120 and Toray-090 orientation 2 scans resulted in similar trends, not surprising given the similarity in their microstructure. Toary-090 orientation 2 scan results, 79.0% & 93.8%, and Toray-120 results of $85 \pm 7.2\%$ maximum fractional coverage area.

Observations made about the relative cell size and quantity in the correlation ratio images are verified in the mean cell size and cell quantity plots in figures *5.3-46* and *47*. The Toray-120 scans produced a maximum average cell size of $0.211mm^2$ between the 21 identified cells. The Toray-090 orientation 1 produced the smallest maximum cell size of $0.0041mm^2$ between 177 cells while the scan of its opposite side with no MPL resulted in almost identical values to the Toray-120, $0.210mm^2$ between 34 cells. The carbon cloth results showed the greatest difference in results with a maximum average cell size of $1.0623mm^2$ between 11 cells. Comparing the relative difference to the Toray-120 results the Toray-090 orientation 1, 2, and cloth results were 19.7%, 99.4% and 502.8% respectively.

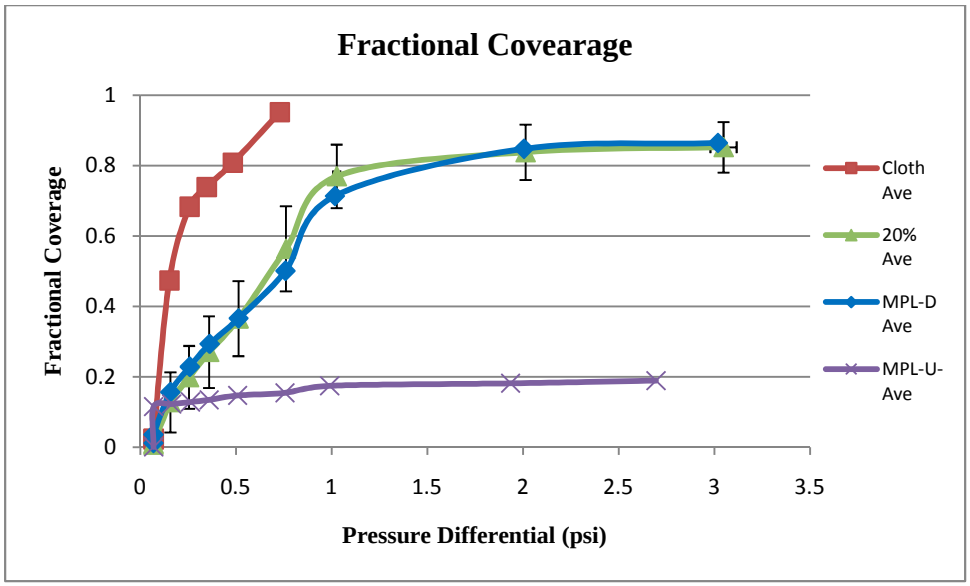

Figure 5.3-45: Fractional coverage as a function of Δp for Toray type comparison series.

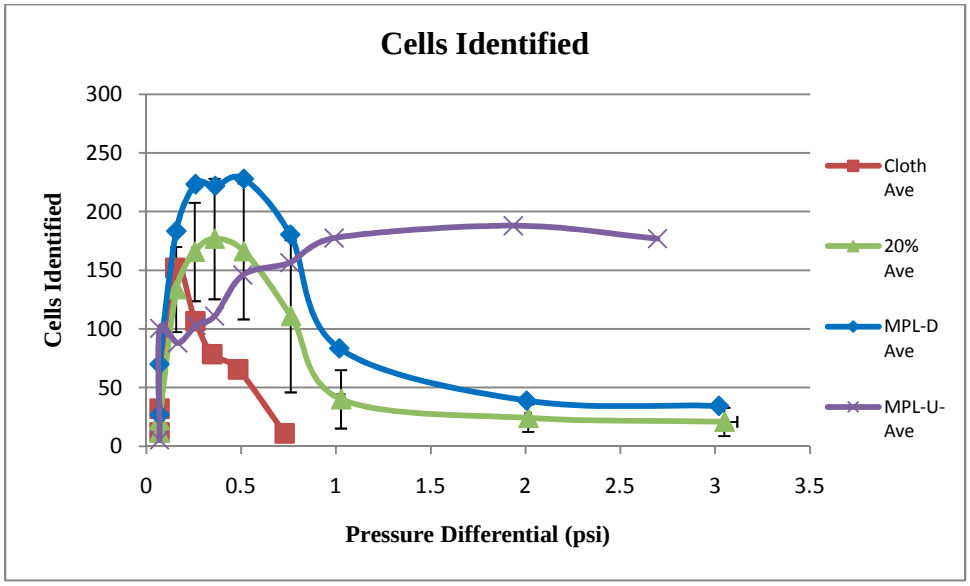

Figure 5.3-46: Total cells identified as a function of Δp for Toray type comparison series.

The final quantification used to distinguish the different scans is the C-scan backscatter displayed in figure *5.3-48*. The plots tell the same story, Toray-120 and Toray-090 orientation 2 are almost identical statistically while the carbon cloth and Toray-090 orientation 1 show vastly different trends. It is interesting to note that the Toray-090 with the

MPL facing up shows the most resistant to saturation. While the average backscatter is reduced with increasing saturation pressure the spread between individual A-line backscatter values increases as opposed to all other scans where the deviation reduces with increased saturation.

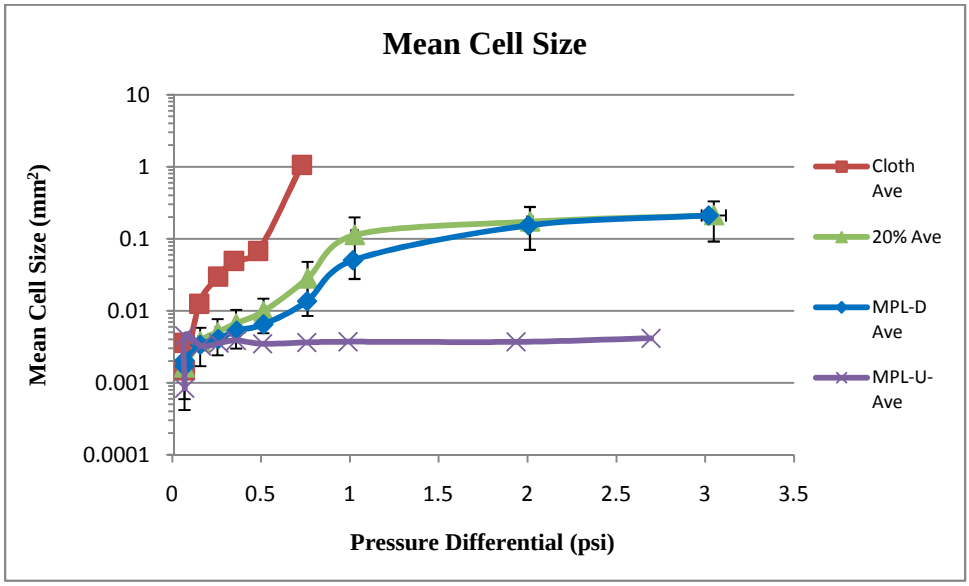

Figure 5.3-47: Average cell size as a function of Δp for Toray type comparison series.

To explain this figure *5.3-30* shows the B-line backscatter trends for different saturation pressures. It's apparent that the dry reference scan has the largest average backscatter but is more uniform between scan lines. From the optical image of figure *5.3-26* its clear that the surface is smoother and more homogenous compared to the raw fibrous face of the other samples. This assists in the uniformity of the acoustic response. The phenomenon of increasing backscatter variation can be attributed to the extreme hydrophobicity of the MPL. As seen in the correlation images the Toray-090 orientation 1 scans describe a saturation pattern of many relatively small penetration points. While the acoustic echo amplitudes reduce over these areas where water has entered the GDL there are a significant number of locations where no water has penetrated, maintain the large acoustic reflection and contributing to the increased spread in backscatter.

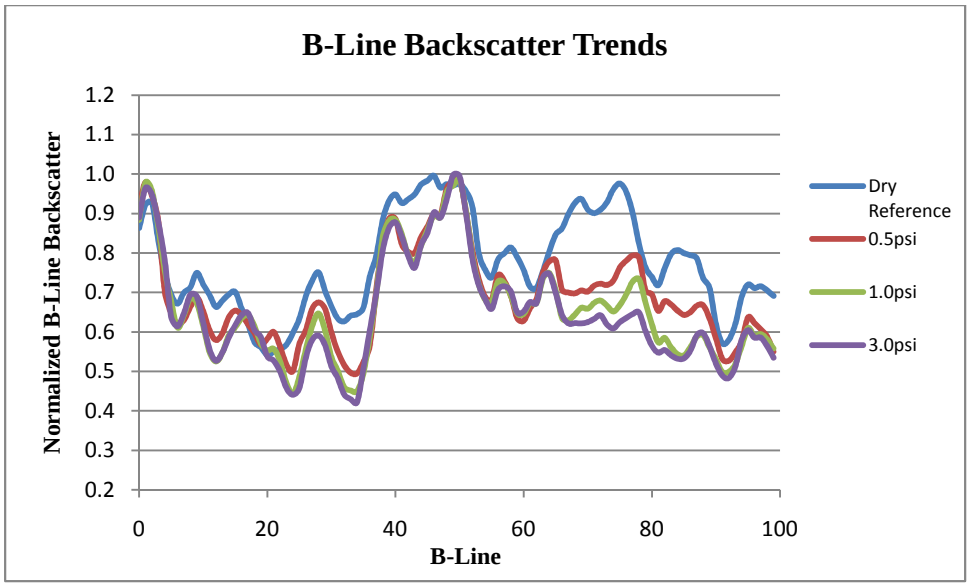

Figure 5.3-48: Average normalized B-line backscatter Toray-090 with MPL facing up. C-scan-350 series.

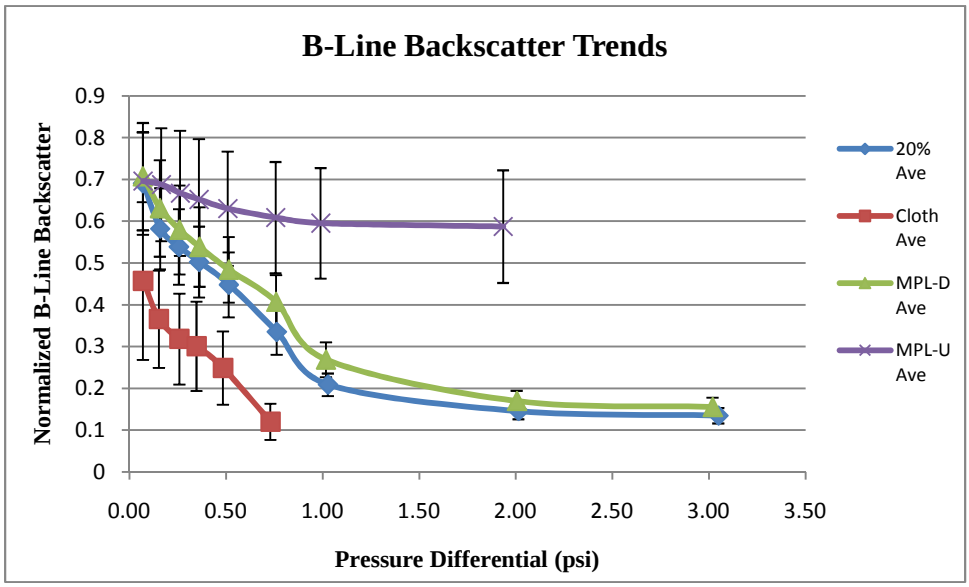

Figure 5.3-49: C-scan backscatter with B-line std. dev. bars as a function of Δp for Toray type comparison series.

Chapter 6: Conclusion

6.1-Results Summary

The objective of this research was to characterize the acoustic response of typical gas diffusion materials and investigate possible techniques for microstructure reconstruction and water transport characterization.

The process of reaching these goals started with the design and construction of a fully functional scanning acoustic microscope. Its requirements included positional accuracy around one micron, support structure for the diffusion media which allows for precise pressure saturation, and an acoustic source with resolutions approaching the feature size of the scanned sample. With the design and hardware selection the positional accuracy requirement was meet, achieving $\pm 3\mu m$ and $\pm 1.5\mu m$ for axes 1 and 2. The design also provided accurate pressure application with an average error of $0.02psi$ from the desired value. The system resolution fell short of the final requirement with a transducer possessing a beam width of $90\mu m$ and a temporal resolution of $25\mu m$, not able to resolve individual fibers of GDL samples. It was however, able to identify variations in the sample saturation and generate statistically meaningful echo signals.

With a fully developed acoustic microscope and data analysis software, the beam characteristics, initial GDL imaging, and two saturation studies were performed. The first steps in this process provide the knowledge required to develop a functional methodology for identifying the locations of water penetration and to quantify its spatial distribution for comparative studies. The first study was to identify any effect PTFE loading has on the saturation characteristic of Toray-120 GDL while the second study demonstrated the differences between types of diffusion media.

The results from the PTFE study showed that only the highest loading of hydrophobic material, 40%, produced significantly different results, the other three test samples, 0%, 10%, and 20%, could not be statistically differentiated. The inconclusive results were in part due to the inhomogeneous nature of the diffusion media. Large variations in material

properties over the typical scan area resulted in poor repeatability for a single test sample. The other contribution to the statistical uncertainty was the limited data set collected. The final conclusion was that the Toray-120 with 40% PTFE loading generated penetration cells an order of magnitude smaller than those of the lower PTFE content samples and exhibited a peak fractional coverage area of approximately 50% where the other samples where between 80% and 90% coverage after a $3.0psi$ saturation pressure application.

The second study which compared the various types of diffusion materials was more conclusive. The same set of characterizations were made of carbon cloth and Toray-090 with a microporous layer scanned in two different orientations, one with the MPL acting as the water/sample boundary and the other having the uncoated surface as the boundary. The results of these three were compared to that of the Toray-120 with a PTFE loading of 20%. It was found that after a $3.0psi$ saturation pressure application the cloth samples exhibited the highest peak fractional coverage area of 91.0% & 99.3% were as the Toray-090 with the MPL providing the water/sample interface possessed the lowest, 12.9% & 24.9%. This is compared to the Toray-120 results of $85 \pm 7.2\%$. The same relation was found in the other saturation characteristics quantified.

The overall contribution this work provided was insight into the acoustic response of a material like the GDL. Having no prior work to base this research on it offers the foundation of future work having described the effect of saturation on the overall pulse attenuation, backscatter, and the propagation speeds spatial dependence. It has also demonstrated the ability of a new imaging technique which identifies locations of altered saturation. Having put this new method to use a comparative study was presented, describing the basic characteristics of water penetration for various GDL samples.

6.2-Future Work

The continuation of this work can move in many directions. One option is to expand on the proposed saturation imaging technique and use it to study the different characteristics of commercially available diffusion medias or the second option is more fundamental work into the acoustic response of this material. Both options show promise and the details of which are laid out in the following.

The most straight forward path ahead is to expand on the current data set. Currently, the Toary-120 with 20% PTFE loading has the largest data set, having been saturation tested six separate times. Repeating some of the other test series would greatly improve the statistical confidence in the conclusions outlined in the results section. In addition, comparison of different material properties and their affect on the spatial distribution of water saturation could prove useful in identifying the most significant characteristics of GDL water management. A useful addition to the saturation studies would be to record the water flow rate through the sample during the pressure applications. This would provide a measure of permeability and break through pressures for the samples. In conjunction with visual recordings of the water emergence and acoustic backscatter more insight into the transport properties would be possible.

The final expansion to the correlation ratio imaging method would be a refinement of the technique where depth of first change is extracted, providing the first step towards a three dimensional mapping of water penetration. If the insonifed region of the sample remains unchanged between scans the acoustic signal will also remain unchanged. However, if some alteration has occurred in the material, like water entrance, the echo signal will change from the point of first variation onward. This would also assist in capturing in-plane water transport.

For the fundamental work option were A-line interpretation is used to extract information about the insonifed object, the pulse/echo format used in this research can be paired with anther transducer positioned behind the sample. This would provide direct measurement of the transmitted pulse after propagating through the sample, not just the backscattered energy. Direct measurements of attenuation and pulse propagation speed would be possible but the most intriguing application would be the measurement of acoustic

energy division. A comparison between the source pulse, backscatter, and transmitted energies could provide more insight into the materials acoustic energy loss and material properties.

The final suggestion for future work would be to use optical images of the scanned area and overlay them with the generated acoustic images. This would provide a way to correlate the acoustic response patterns with the actual material. Use of reference objects like cut slots or some form of surface feature that is resolvable in both imaging modalities will be needed to orient the two pictures.

References

[1] Rao, N. A. H. K., 2002, "Ultrasound Imaging," Wiley & Son.
[2] Szabo, T. L., 2004, Diagnostic Ultrasound Imaging: Inside Out, Elsevier Academic, Boston, MA, Chap. 2.
[3] Foster, F. S., Pavlin, C. J., Harasiewicz, K. A., Christopher, D. A., and Turnbull, D. H., 2000, "Advances in Ultrasound Biomicroscopy," Ultrasound in Medicine & Biology, 26(1), pp. 1-27.
[4] Rao, N. A. H. K., 2008, "Ultrasound Imaging Lecture 8," Rochester, NY.
[5] Szabo, T. L., 2004, Diagnostic Ultrasound Imaging: Inside Out, Elsevier Academic, Boston, MA, Chap. 8.
[6] Szabo, T. L., 2004, Diagnostic Ultrasound Imaging: Inside Out, Elsevier Academic, Boston, MA, Chap. 6.
[7] Szabo, T. L., 2004, Diagnostic Ultrasound Imaging: Inside Out, Elsevier Academic, Boston, MA, Chap. 4.
[8] 2008, Panametrics_Ndt Transducer Pdf Brochure, Oct. 27, 2008, www.olympus-ims.com/data/File/Panametrics-UT.en.pdf
[9] Kossoff, G., 1979, "Analysis of Focusing Action of Spherically Curved Transducers [Medical Application]," Ultrasound in Medicine & Biology, 5(Copyright 1980, IEE), pp. 359-65.
[10] Lai, D., 2008, "Independent Component Analysis (Ica) Applied to Ultrasound Speckle Texture Analysis and Tissue Characterization," Rochester, NY.
[11] Szabo, T. L., 2004, Diagnostic Ultrasound Imaging: Inside Out, Elsevier Academic, Boston, Chap. 5.
[12] Wang, T. T., Herbert, J. M., and Glass, A. M., 1988, The Applications of Ferroelectric Polymers, Chapman & Hall.
[13] Krammer, P., and Hassler, D., 1987, "Measurement of Spatial Time-of-Flight Fluctuations of Ultrasound Pulses Passing through Inhomogeneous Layers," Proc. IEEE 1987 Ultrasonics Symposium, pp. 939-942.
[14] Silverman, R. H., Cannata, J., Shung, K. K., Gal, O., Patel, M., Lloyd, H. O., Feleppa, E. J., and Coleman, D. J., 2006, "75 Mhz Ultrasound Biomicroscopy of Anterior Segment of Eye," Ultrasonic Imaging, 28(3), pp. 179-188.
[15] Knspik, D. A., Starkoski, B., Pavlin, C. J., and Foster, F. S., 2000, "A 100-200 Mhz Ultrasound Biomicroscope," Ultrasonics, Ferroelectrics and Frequency Control, IEEE Transactions on, 47(6), pp. 1540-1549.
[16] Yokosawa, K., Shinomura, R., Sano, S., Ito, Y., Ishikawa, S., and Sato, Y., 1996, "A 120-Mhz Ultrasound Probe for Tissue Imaging," Ultrasonic Imaging, 18(4), pp. 231-239.
[17] Christopher, T., 1997, "Finite Amplitude Distortion-Based Inhomogeneous Pulse Echo Ultrasonic Imaging," IEEE Transactions on Ultrasonics, Ferroelectrics, and Frequency Control, 44(1), pp. 125-139.

[18] Hyungsuk, K., Zagzebski, J. A., and Varghese, T., 2008, "Estimation of Ultrasound Attenuation from Broadband Echo-Signals Using Bandpass Filtering," Ultrasonics, Ferroelectrics and Frequency Control, IEEE Transactions on, 55(5), pp. 1153-1159.
[19] Adams, T., 2007, "Acoustic Images Reveal Flaws," Advanced Materials & Processes, 165(12), pp. 45-47.
[20] Thomas, R., 2005, "Acoustic Micro Imaging of Cracks," Advanced Materials & Processes, 163(6), pp. 49-51.
[21] Cheitov, A. M., Maev, R. G., and Severin, F. M., 2007, "Acoustic Microscopy of Internal Structure of Resistance Spot Welds," Ultrasonics, Ferroelectrics and Frequency Control, IEEE Transactions on, 54(8), pp. 1521-1529.
[22] Liu, S., Guo, E., Levin, V. M., Liu, F., Petronyuk, Y. S., and Zhang, Q., 2006, "Application of Pulse Acoustic Microscopy Technique for 3d Imaging Bulk Microstructure of Carbon Fiber-Reinforced Composites," Ultrasonics, 44(Supplement 1), pp. e1037-e1044.
[23] Zinin, P. V., Berezina, S., Fei, D., Rebinsky, D. A., Lemor, R. M., Weiss, E. C., Arnoud, C., Arnold, W., and Koehler, B., 2003, "Detection and Localization of Subsurface Defects in Dlc Films by Acoustic Microscopy," Proc. Ultrasonics, 2003 IEEE Symposium on, 1, pp. 881-884 Vol.1.
[24] Lobkis, O. I., Kundu, T., and Zinin, P. V., 1995, "A Theoretical Analysis of Acoustic Microscopy of Spherical Cavities," Wave Motion, 21(2), pp. 183-201.
[25] Stor-Pellinen, J., Haeggstrom, E., and Luukkala, M., 2000, "Measurement of Paper-Wetting Processes by Ultrasound Transmission," Measurement Science and Technology, 11(4), pp. 406-411.
[26] Mcintyre, C. S., Hutchins, D. A., Billson, D. R., and Stor-Pellinen, J., 2001, "The Use of Air-Coupled Ultrasound to Test Paper," Ultrasonics, Ferroelectrics and Frequency Control, IEEE Transactions on, 48(3), pp. 717-727.
[27] Habeger, C. C., Mann, R. W., and Baum, G. A., 1979, "Ultrasonic Plate Waves in Paper," Ultrasonics, 17(2), pp. 57-62.
[28] Turhan, A., Heller, K., Brenizer, J. S., and Mench, M. M., 2006, "Quantification of Liquid Water Accumulation and Distribution in a Polymer Electrolyte Fuel Cell Using Neutron Imaging," Journal of Power Sources, 160(2), pp. 1195-1203.
[29] Boillat, P., Kramer, D., Seyfang, B. C., Frei, G., Lehmann, E., Scherer, G. G., Wokaun, A., Ichikawa, Y., Tasaki, Y., and Shinohara, K., 2008, "In Situ Observation of the Water Distribution across a Pefc Using High Resolution Neutron Radiography," Electrochemistry Communications, 10(4), pp. 546-550.
[30] Hartnig, C., Manke, I., Kuhn, R., Kleinau, S., Goebbels, J., and Banhart, J., 2009, "High-Resolution in-Plane Investigation of the Water Evolution and Transport in Pem Fuel Cells," Journal of Power Sources, 188(2), pp. 468-474.
[31] Manke, I., Hartnig, C., Grunerbel, M., Lehnert, W., Kardjilov, N., Haibel, A., Hilger, A., Banhart, J., and Riesemeier, H., 2007, "Investigation of Water Evolution and Transport in Fuel Cells with High Resolution Synchrotron X-Ray Radiography," Applied Physics Letters, 90(17), pp. 174105-3.
[32] Sinha, P. K., Halleck, P., and Wang, C.-Y., 2006, "Quantification of Liquid Water Saturation in a Pem Fuel Cell Diffusion Medium Using X-Ray Microtomography," Electrochemical and Solid-State Letters, 9(7), pp. A344-A348.

[33] Larminie, J., and Dicks, A., 2003, Fuel Cell Systems Explained, SAE International and John Wiley & Sons, Ltd., West Sussex, Chap. 4.
[34] Mench, M. M., 2007, Fuel Cell Engines, John Wiley & Sons, Hoboken, New Jersey, Chap. 6.
[35] Mench, M. M., 2007, Fuel Cell Engines, John Wiley & Sons, Hoboken, New Jersey, Chap. 3.
[36] Larminie, J., and Dicks, A., 2003, Fuel Cells Systems Explained, John Wiley & Sons, West Sussex, England, Chap. 3.
[37] Mench, M. M., 2007, Fuel Cell Engines, John Wiley & Sons, Hoboken, New Jersey, Chap. 4.
[38] Mench, M. M., 2007, Fuel Cell Engines, John Wiley & Sons, Hoboken, New Jersey, Chap. 5.
[39] Lim, C., and Wang, C. Y., 2004, "Effects of Hydrophobic Polymer Content in Gdl on Power Performance of a Pem Fuel Cell," Electrochimica Acta, 49(24), pp. 4149-4156.
[40] Zhou, P., and Wu, C. W., 2010, "Liquid Water Transport Mechanism in the Gas Diffusion Layer," Journal of Power Sources, 195(Compendex), pp. 1408-1415.
[41] Ju, H., 2008, "Analyzing the Effects of Immobile Liquid Saturation and Spatial Wettability Variation on Liquid Water Transport in Diffusion Media of Polymer Electrolyte Fuel Cells (Pefcs)," Journal of Power Sources, 185(1), pp. 55-62.
[42] Zhou, T., and Liu, H., 2006, "Effects of the Electrical Resistances of the Gdl in a Pem Fuel Cell," Journal of Power Sources, 161(1), pp. 444-453.

Appendix A: Error Analyses

A.1-Hardware Error

A.1.1-NI-5152 Digitizer

Purpose: A-line echo signal digitization.

Accuracy: $1.26\%\ of\ input\ +\ 1.0\%\ of\ FS\ + 500\mu V$

$\pm 1V\ FS\ \&\ 0.5V\ input$

$\sigma_v = 16.8mV$

Average of ten samples $\sigma = \frac{16.8mV}{\sqrt{10}}$

$\sigma_v = 5.31mV$

Resolution (V): $Range/_{bits}$

$2V/_{(2^8)} = 3.906mV$

Resolution (t): $5ps = 5 * 10^{-12}s$

Range: $Clip = \pm 0.5457V$

$dB = 20log\left(\frac{0.00531}{0.5457}\right) = -40.2dB$

Measured Std Dev.:

Measured standard deviation as a function of pulser/receiver gain

$$\sigma_{27dB} = 5.63mV$$

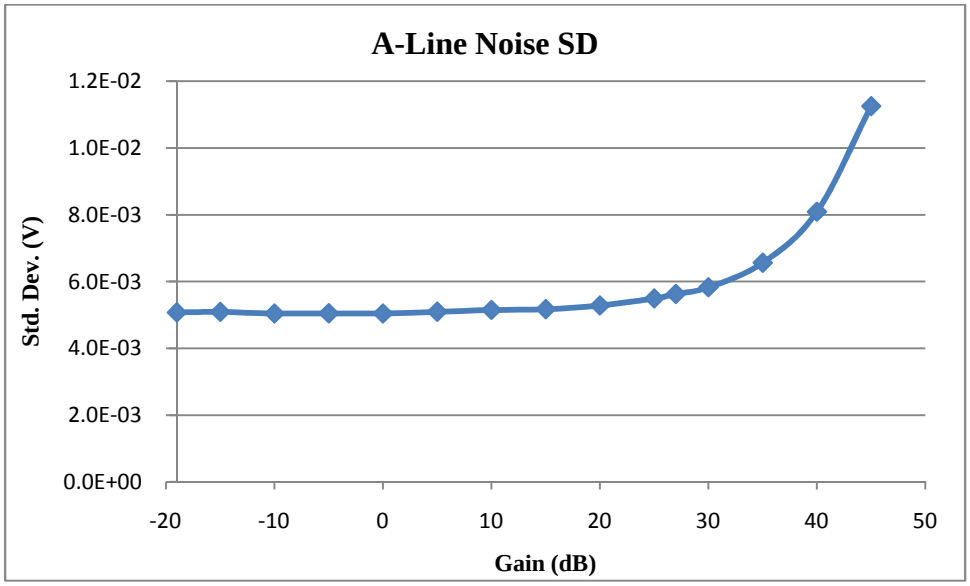

Figure A.1-1: Observed A-line noise standard deviation as a function of pulser/receiver gain. (Log base ten gain scale)

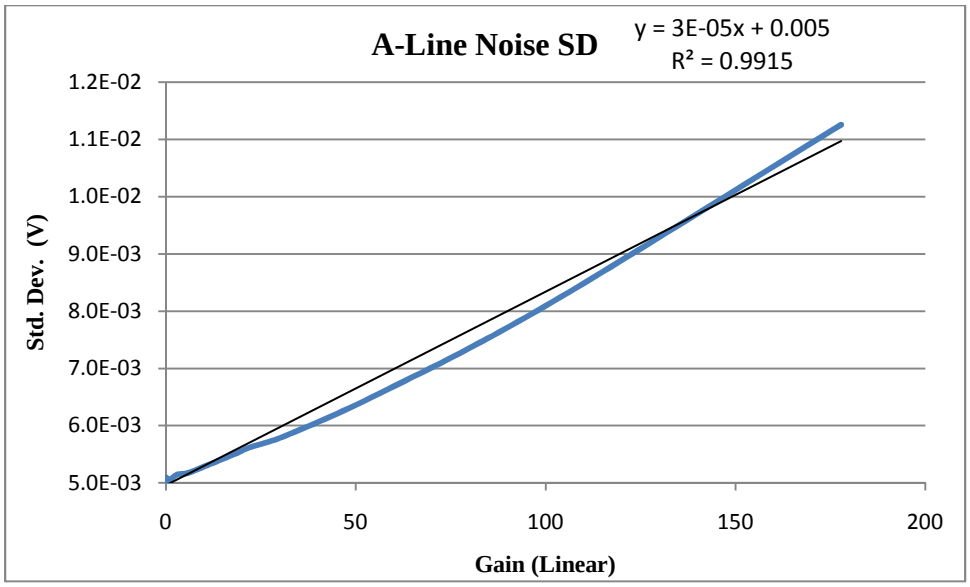

Figure A.1-2: Observed A-line noise standard deviation as a function of pulser/receiver gain. (Linear gain scale)

A.1.2-NI-6030E DAQ:

Purpose: Pressure sensor voltage measurements.

Accuracy: $\sigma_v = 0.061mV$

Resolution (V): $Range/_{bits}$

$0.2V/_{(2^{16})} = 3.05\mu V$

Resolution (t): $5ps = 5 * 10^{-12}s$

A.1.3-PX26-005DV: *Pressure sensor measurments*

Accuracy: $1\%\ FS$

Excitation Accuracy: $10mV$

Output Skew: $5mV_{Out}/_{V_{Ex}}$

$\sigma_v = 0.05mV$

A.2-Pressure Sensor Calibration and Errors

A.2.1-Water Column Pressure Error

A water column was used in the pressure senor calibration. The following outlines the uncertainty analysis for the applied pressures as calculated with equation A.2-1.

$$P(psi) = \rho\left[H_0 + \frac{50 - V}{H_s}\right] \tag{A.2-1}$$

The height scale to convert water volume from the cylinder indicators to the height of water is defined in equation A.2.1-2.

$$H_s = \left[\frac{V}{L}\right] = \left[\frac{29.25ml \pm 0.25\ ml}{12in \pm 0.015\ in}\right] \tag{A.2-2}$$

$$H_s = 2.44\ in$$

The corresponding variance of the height scale is calculated with equation A.2.1-3.

$$V(H_s) = \sigma_{H_s}^2 = \left(\frac{\partial H_s}{\partial L}\right)^2 (\sigma_L)^2 + \left(\frac{\partial H_s}{\partial V}\right)^2 (\sigma_V)^2 \tag{A.2-3}$$

$$V(H_s) = \left(\frac{1}{12}\right)^2 (0.25)^2 + \left(\frac{29.25}{12^2}\right)^2 (0.015)^2 \tag{A.2-4}$$

$$\sigma_{H_s} = 0.021\ \frac{ml}{in}$$

With this the total estimated pressure variance is described by equation A.2.1-5.

$$\begin{aligned} V(P) = \quad & \left(\frac{\partial P}{\partial \rho}\right)^2 (\sigma_\rho)^2 + \left(\frac{\partial P}{\partial H_0}\right)^2 (\sigma_{H_0})^2 \\ & + \left(\frac{\partial P}{\partial V}\right)^2 (\sigma_V)^2 + \left(\frac{\partial P}{\partial H_s}\right)^2 (\sigma_{H_s})^2 \end{aligned} \tag{A.2-5}$$

$$\frac{\partial P}{\partial \rho} = \left[H_0 + \frac{50 - V}{H_s}\right] \qquad (A.2\text{-}6)$$

$$\frac{\partial P}{\partial H_0} = \rho \qquad (A.2\text{-}7)$$

$$\frac{\partial P}{\partial V} = \frac{\rho}{H_s} \qquad (A.2\text{-}8)$$

$$\frac{\partial P}{\partial H_s} = \frac{\rho}{(H_s)^2}[50 - V] \qquad (A.2\text{-}9)$$

The results of the water column pressure estimates are presented in the following tables and figures. Table *A.2-1* lists the variable values used while table *A.2-2* and figure *A.2-1* display the resulting calibration points used for calibrating both sensors along with the estimated confidence intervals as defined by equation *A.2-10*.

$$-\sigma_{P_C} * t_{\alpha/2,n-2} < P_C < \sigma_{P_C} * t_{\alpha/2,n-2} \qquad (A.2\text{-}10)$$

$$\alpha_{(95\%,two\ sided)} = 0.025$$
$$n = 11$$

Calibration Pressure Variables			
Variable	***Units***	***Value***	***Std. Dev.***
Density	*lbm/ft^3*	*62.621*	*0.008*
Height Offset	*in*	*4.125*	*0.015*
Height Scale	*ml/in*	*2.44*	*0.021*
Volume Measurement	*ml*	*--*	*0.25*

Table A.2-1: Pressure column variable values.

Calibration Pressure Error			
Measured Volume (ml)	***Calculated Pressure (psi)***	***Std. Dev. (psi)***	***95% CI (psi)***
0	*0.89209*	*5.241E-03*	*2.255E-02*
5	*0.81783*	*4.856E-03*	*2.090E-02*
10	*0.74357*	*4.485E-03*	*1.930E-02*
15	*0.66931*	*4.129E-03*	*1.777E-02*
20	*0.59505*	*3.794E-03*	*1.633E-02*
25	*0.52079*	*3.485E-03*	*1.500E-02*
30	*0.44653*	*3.211E-03*	*1.382E-02*
35	*0.37227*	*2.980E-03*	*1.282E-02*
40	*0.29801*	*2.803E-03*	*1.206E-02*
45	*0.22375*	*2.692E-03*	*1.158E-02*
50	*0.14949*	*2.653E-03*	*1.142E-02*
	Ave	***3.666E-03***	***1.578E-02***
	Max	***5.241E-03***	***2.255E-02***

Table A.2-2: Pressure estimates with 95% confidence interval.

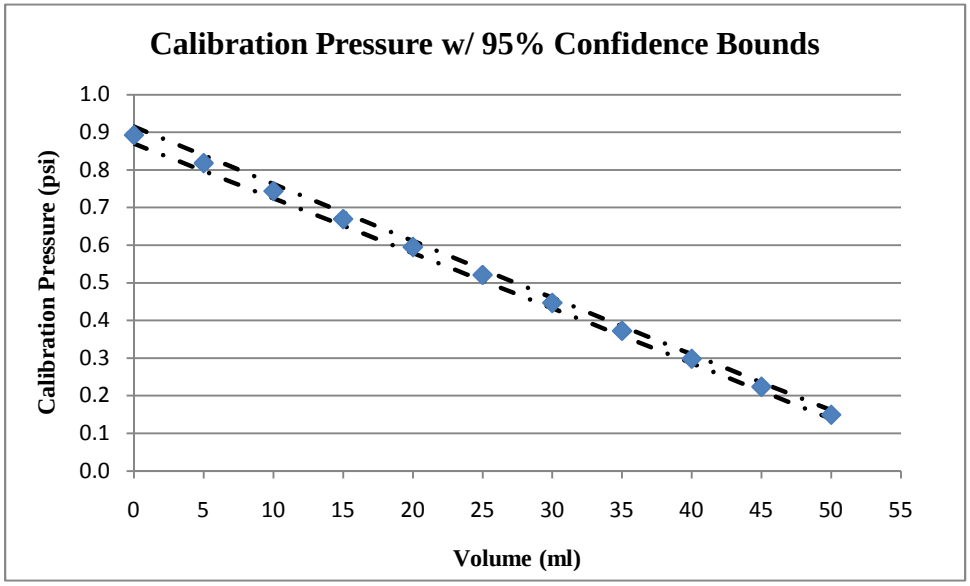

Figure A.2-1: Water column data points with 95% confidence interval.

A.2.2-Pressure Sensor Calibration Linear Slope/Intercept Error:

The following outlines the error analysis associated with the pressure sensors linear calibration fit as defined by equation *A.2-11*.

$$\hat{y} = \hat{\beta}_0 + \hat{\beta}_1 x \tag{A.2-11}$$

$$\hat{\beta}_0 = \bar{y} - \hat{\beta}_1 \bar{x} \tag{A.2-12}$$

$$\hat{\beta}_1 = \frac{\sum_{i=1}^{n}(x_i - \bar{x})(y_i - \bar{y})}{\sum_{i=1}^{n}(x_i - \bar{x})^2} = \frac{S_{xy}}{S_{xx}} \tag{A.2-13}$$

$$\bar{x} = \frac{1}{n}\sum_{i=1}^{n} x_i \tag{A.2-14}$$

$$\bar{y} = \frac{1}{n}\sum_{i=1}^{n} y_i \tag{A.2-15}$$

Equations *A.2-16* thru *A.2-18* defines the variance associated with the linear fit constants of equations *A.2-12* and *A.2-13*.

$$\hat{\sigma}^2 = \frac{\sum_{i=1}^{n}(y_i - \hat{y}_i)^2}{n-2} \tag{A.2-16}$$

$$V(\hat{\beta}_0) = \sigma^2\left(\frac{1}{n} + \frac{\bar{x}^2}{S_{xx}}\right) \tag{A.2-17}$$

$$V(\hat{\beta}_1) = \frac{\sigma^2}{S_{xx}} \tag{A.2-18}$$

Total error on estimated pressure is based on the variance of the linear fit slope and offset and are combined with the error associated with the measured voltage. Normal

probability distributions assumed for the voltage error and t-distributions with 9 degrees-of-freedom for the 95% confidence interval on the linear fit, equation *A.2-24*.

$$\hat{y} = \hat{\beta}_0 + \hat{\beta}_1 x \tag{A.2-19}$$

$$V(P) = \left(\frac{\partial P}{\partial \hat{\beta}_0}\right)^2 \left(\sigma_{\hat{\beta}_0}\right)^2 + \left(\frac{\partial P}{\partial \hat{\beta}_1}\right)^2 \left(\sigma_{\hat{\beta}_1}\right)^2 + \left(\frac{\partial P}{\partial x}\right)^2 (\sigma_x)^2 \tag{A.2-20}$$

$$\frac{\partial P}{\partial \hat{\beta}_0} = -1 \tag{A.2-21}$$

$$\frac{\partial P}{\partial \hat{\beta}_1} = x \tag{A.2-22}$$

$$\frac{\partial P}{\partial x} = \hat{\beta}_0 \tag{A.2-23}$$

$$-\sigma_{P_E} * t\alpha_{/2,n-2} < P_E < \sigma_{P_E} * t\alpha_{/2,n-2} \tag{A.2-24}$$

$$\alpha_{(95\%,\text{two sided})} = 0.025$$

$$\text{n} = 11$$

$$\boldsymbol{t_{0.025,9}} = 2.262$$

Tables *A.2-3* thru *A.2-6* list the resulting pressure sensor calibration data points and their corresponding confidence intervals on the estimated pressures. In addition figure *A.2-1* plots the measured calibration data points against the calculated linear fit.

Pressure Sensor 1 Calibration					
Data Point	***Voltage (mV)***	***Estimated Pressure (psi)***	***Calculated Pressure (psi)***	***Se (psi)***	***95% CI (psi)***
1	*15.447*	*0.89846*	*0.89037*	*1.299E-03*	*2.938E-03*
2	*14.297*	*0.82356*	*0.81799*	*1.233E-03*	*2.789E-03*
3	*13.115*	*0.74866*	*0.74360*	*1.167E-03*	*2.640E-03*
4	*11.948*	*0.67377*	*0.67016*	*1.104E-03*	*2.498E-03*
5	*10.771*	*0.59887*	*0.59608*	*1.044E-03*	*2.361E-03*
6	*9.573*	*0.52397*	*0.52068*	*9.850E-04*	*2.228E-03*
7	*8.405*	*0.44907*	*0.44717*	*9.316E-04*	*2.107E-03*
8	*7.222*	*0.37418*	*0.37272*	*8.818E-04*	*1.995E-03*
9	*6.034*	*0.29928*	*0.29795*	*8.371E-04*	*1.894E-03*
10	*4.852*	*0.22438*	*0.22356*	*7.988E-04*	*1.807E-03*
11	*3.657*	*0.14948*	*0.14835*	*7.671E-04*	*1.735E-03*
			Ave	***1.004E-03***	***2.005E-03***
			Max	***1.299E-03***	***2.938E-03***

Table A.2-3: Pressure sensor 1 calibration data points with pressure errors.

Sensor 1 Fit Equation $\hat{y} = \hat{\beta}_0 + \hat{\beta}_1 x$	
$\hat{\beta}_1$ ***(slope)***	*6.294E-02*
$\hat{\beta}_0$ ***(offset)***	*-8.180E-02*
$V(\hat{\beta}_1)$	*4.879E-09*
$V(\hat{\beta}_0)$	*5.152E-07*
$V(x)$*	*2.000E-06*
$95\%\ CI_{max}$	*2.938E-03*

* *N=2000:* $\sigma = 0.06324mV$

Table A.2-4: Pressure sensor 1 calibration data linear fit results.

Pressure Sensor 2 Calibration					
Data Point	**Voltage (mV)**	**Estimated Pressure (psi)**	**Calculated Pressure (psi)**	**Se (psi)**	**95% CI (psi)**
1	8.322	0.89846	0.89090	1.101E-03	2.492E-03
2	7.584	0.82356	0.81740	1.033E-03	2.337E-03
3	6.852	0.74866	0.74450	9.675E-04	2.188E-03
4	6.097	0.67377	0.66931	9.025E-04	2.041E-03
5	5.359	0.59887	0.59581	8.423E-04	1.905E-03
6	4.621	0.52397	0.52231	7.861E-04	1.778E-03
7	3.861	0.44907	0.44662	7.334E-04	1.659E-03
8	3.107	0.37418	0.37153	6.874E-04	1.555E-03
9	2.36	0.29928	0.29713	6.494E-04	1.469E-03
10	1.62	0.22438	0.22343	6.206E-04	1.404E-03
11	0.88	0.14948	0.14973	6.018E-04	1.361E-03
			Ave	**8.114E-04**	**1.835E-03**
			Max	**1.101E-03**	**2.492E-03**

Table A.2-5: Pressure sensor 2 calibration data points with pressure errors.

Sensor 2 Fit Equation $\hat{y} = \hat{\beta}_0 + \hat{\beta}_1 x$	
$\hat{\beta}_1$ **(slope)**	9.959E-02
$\hat{\beta}_0$ **(offset)**	6.209E-02
$V(\hat{\beta}_1)$	1.243E-08
$V(\hat{\beta}_0)$	3.327E-07
$V(x)$*	2.000E-06
95% CI_{max}	2.492E-03

* *N=2000:* $\sigma = 0.06324mV$

Table A.2-6: Pressure sensor 2 calibration data linear fit results.

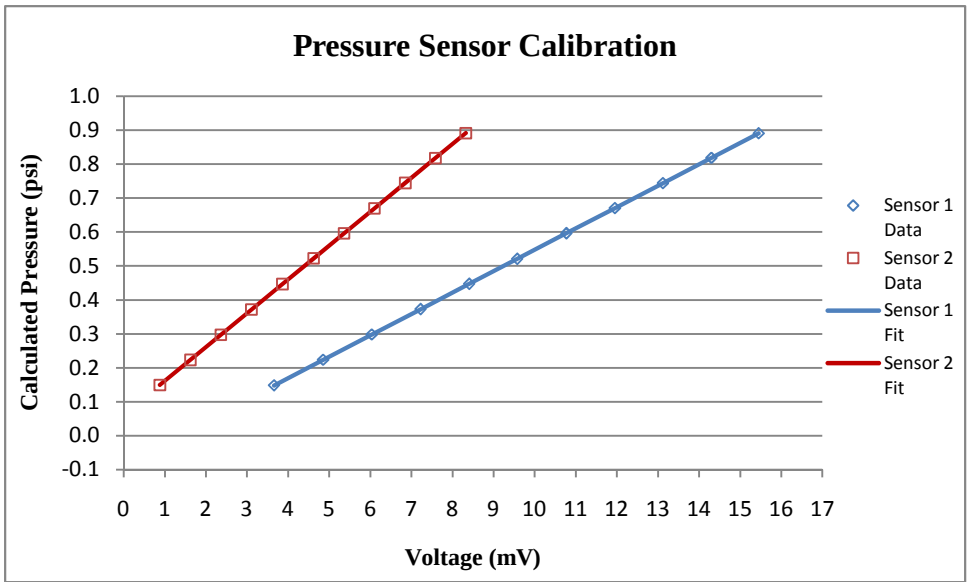

Figure A.2-2: Pressure sensor calibration data points with corresponding linear fit lines.

A.3-A-line Attribute Calculations and Errors

A.3.1-Analytic Signal Calculation

The following defines the method used to calculate the imaginary portion of the complex analytic signal from the measured real part of the signal refered to as the A-line. The Hilbert transform, equation *A.3-1*, provides the imaginary part of the analytic signal as described in equation *A.3-3*.

$$H(t) = \frac{1}{\pi}\int_{-\infty}^{\infty}\frac{A(\tau)}{t-\tau}d\tau \qquad (A.3\text{-}1)$$

Or in discrete form.

$$H_m = \begin{cases} \frac{2}{\pi}\sum_{n-odd}\frac{A_n}{m-n}, & m-even \\ \frac{2}{\pi}\sum_{n-even}\frac{A_n}{m-n}, & m-odd \end{cases} \qquad (A.3\text{-}2)$$

$$A(t) = X(t) + jH(t) \tag{A.3-3}$$

The magnitude of the Analytic signal is commonly refered to as the signal envelope.

$$E(t) = \sqrt{X(t)^2 + H(t)^2} \tag{A.3-4}$$

The uncertainty associated with the envelope is based on the measurement error of the real portion and its propagation through the Hilbert. Since the Hilbert is just a transform with the same units the error remains the same. This is confirmed by the following definition of the Hilbert variance.

$$V(H_m) = \sum \left(\frac{\partial H_m}{\partial A_n}\right)^2 (\sigma_{A_n})^2 \tag{A.3-5}$$

$$V(H_m) = \begin{cases} \left(\frac{2\sigma_A}{\pi}\right)^2 \sum_{n-odd} \left(\frac{1}{m-n}\right)^2, & m - even \\ \left(\frac{2\sigma_A}{\pi}\right)^2 \sum_{n-even} \left(\frac{1}{m-n}\right)^2, & m - odd \end{cases} \tag{A.3-6}$$

$$V(H_m) = (\sigma_A)^2 \tag{A.3-7}$$

The envelope of the A-line is defined by equation *A.3-8* as the magnitude of the complex signal.

$$V(E_m) = \sqrt{Re(A)^2 + Im(A)^2} \tag{A.3-8}$$

$$V(E_m) = \sqrt{2(\sigma_A)^2} \tag{A.3-9}$$

$$V(E_m) = \sqrt{2(5.63mV)^2}$$

$$\sigma_E = 7.962mV$$

A.3.2-Fourier Transform

The Fourier transform was used to define the frequency content of the acquired A-line signals. The following defines this transform and the associated error with the estimated power spectrum.

The Fourier transform is defined by equation *A.3-10*.

$$A(f) = \int_{-\infty}^{\infty} A(t) e^{-i2\pi t f} dt \qquad \textit{(A.3-10)}$$

Or in discrete form.

$$f_m = \sum_{n=1}^{N} A_n e^{\frac{-i2\pi mn}{N}} \qquad \textit{(A.3-11)}$$

$$Re(f_m) = \sum_{n=1}^{N} A_n \, Cos\left(\frac{2\pi mn}{N}\right) \qquad \textit{(A.3-12)}$$

$$Im(f_m) = \sum_{n=1}^{N} A_n \, Sin\left(\frac{2\pi mn}{N}\right) \qquad \textit{(A.3-13)}$$

The uncertainty associated with the frequency spectrum defined by equation *A.3-14* and is outlined below.

$$V(f_m) = \sum \left(\frac{\partial f_m}{\partial A_n}\right)^2 \left(\sigma_{A_n}\right)^2 \qquad \textit{(A.3-14)}$$

$$V(f_m) = \sum_{n=1}^{N} \left(e^{\frac{-i2\pi mn}{N}}\right)^2 \left(\sigma_{A_n}\right)^2 \qquad \textit{(A.3-15)}$$

$$V\left(Re(f_m)\right) = \sum_{n=1}^{N} \left(Cos\left(\frac{2\pi mn}{N}\right)\right)^2 \left(\sigma_{A_n}\right)^2 \qquad \textit{(A.3-16)}$$

$$V\left(Im(f_m)\right) = \sum_{n=1}^{N}\left(Sin\left(\frac{2\pi mn}{N}\right)\right)^2 \left(\sigma_{A_n}\right)^2 \qquad (A.3\text{-}17)$$

$$\sigma_f = 90.08mV$$

A.3.3-Acoustic Backscatter

Acoustic backscatter, equation *A.3-18*, defines the amount of energy contained in the received A-line signal.

$$B = \int_{-\infty}^{\infty} A(t)^2 dt \qquad (A.3\text{-}18)$$

Or in discrete form.

$$B = \frac{\Delta t}{2}\sum_{n=1}^{N-1}[A_i^2 + A_{i+1}^2] \qquad (A.3\text{-}19)$$

The uncertainty associated with the A-line backscatter is dependent on the signal itself, as described in equation *A.3-21*, so two examples are presented which illustrate the scale of the backscatter error.

$$V(B) = \sum_{n=1}^{N}\left(\frac{\partial B}{\partial A_n}\right)^2 \left(\sigma_{A_n}\right)^2 + \left(\frac{\partial B}{\partial \Delta t}\right)^2 (\sigma_{\Delta t})^2 \qquad (A.3\text{-}20)$$

$$\begin{aligned} V(B) = {} & (\Delta t A_1)^2\left(\sigma_{A_1}\right)^2 + 2\sum_{n=2}^{N-2}(\Delta t A_n)^2\left(\sigma_{A_n}\right)^2 \\ & +(\Delta t A_n)^2\left(\sigma_{A_n}\right)^2 + \left[\frac{1}{2}\sum_{n=1}^{N-1}[A_i^2 + A_{i+1}^2]\right]^2 (\sigma_{\Delta t})^2 \end{aligned} \qquad (A.3\text{-}21)$$

Figure *A.3-1* plots the two A-line examples used to illustrate the typical range expected for the A-line backscatter and its estimated confidence interval as listed in table *A.3-1*.

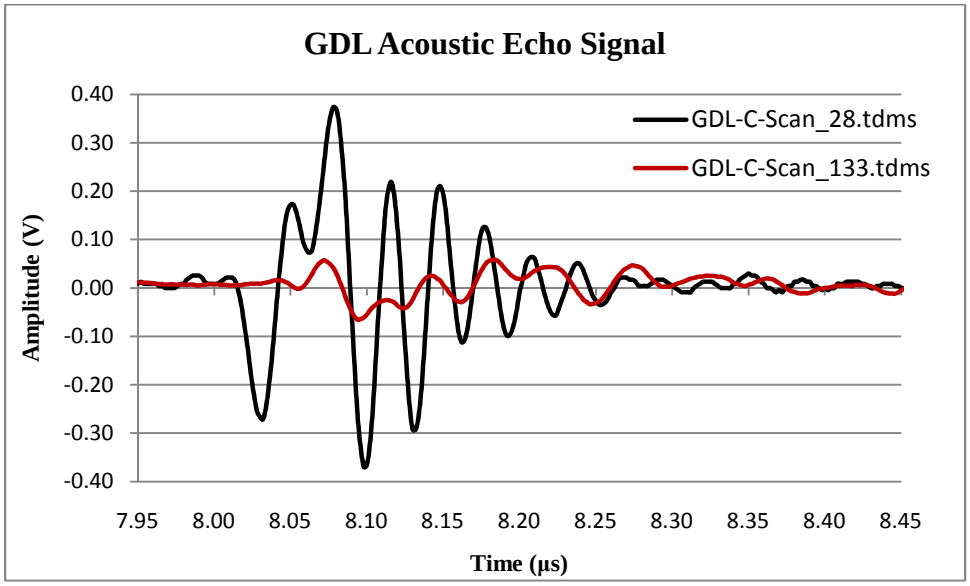

Figure A.3-1: Two A-line examples used to illustrate the backscatter attributes.

A-line	*C-Scan_28*	*C-Scan_133*
Voltage Std. Dev.	*5.63mV*	
Time Std. Dev.	*5ps*	
Backscatter	*6.14E-9 sV^2*	*3.03E-10 sV^2*
BS Std. Dev.	*3.18E-11 sV^2*	*1.66E-11 sV^2*
Percent Std. Dev.	*0.52%*	*5.46%*

Table A.3-1: A-line backscatter and estimated error values as propagated from A-line voltages.

A.4-Beam Diameter Error

The scan of a sharp edge provides an amplitude trace whose derivative approximates the beam profile. The acoustic beam diameter as measured from the full width half maximum (FWHM) points on the amplitude trace and derivative plots, figure *A.4-1* and *A.4-2*, are presented along with an error estimate for the final FWHM value. Details of the acquisition process are outlined in section *5.1.2.2*.

Given the discrete data set an interpolation was needed to define the left and right half maximum lateral coordinates, y_R & y_L, and their corresponding derivative amplitudes, A.

$$FWHM = y_R - y_L \tag{A.4-1}$$

$$y_R = y_{R0} + (A - A_{R0})\left[\frac{y_{R1} - y_{R0}}{A_{R1} - A_{R0}}\right] \tag{A.4-2}$$

$$y_L = y_{L0} + (A - A_{L0})\left[\frac{y_{L1} - y_{L0}}{A_{L1} - A_{L0}}\right] \tag{A.4-3}$$

Since the amplitudes, equation *A.4-4*, used for the FWHM measurements are from the derivative plots the error associated with them must be calculated as the voltage measurement error propagates through. The variances of these values are calculated with equation *A.4-5*.

$$A_{ij} = \frac{dV}{dy} = \frac{V_{i0} - V_{i1}}{y_{i0} - y_{i1}} \tag{A.4-4}$$

$$V(A_i) = \left(\frac{dA}{dV_{i0}}\right)^2 (\sigma_V)^2 + \left(\frac{dA}{dV_{i1}}\right)^2 (\sigma_V)^2 \left(\frac{dA}{dy_{i0}}\right)^2 (\sigma_y)^2 + \left(\frac{dA}{dy_{i1}}\right)^2 (\sigma_y)^2 \tag{A.4-5}$$

$$\frac{dA}{dV_{i0}} = \frac{1}{y_{i0} - y_{i1}} \tag{A.4-6}$$

$$\frac{dA}{dV_{i1}} = -\frac{dA}{dV_{i0}} \tag{A.4-7}$$

$$\frac{dA}{dy_{i0}} = \frac{V_{i0} - V_{i1}}{(y_{i0} - y_{i1})^2} \tag{A.4-8}$$

$$\frac{dA}{dy_{i1}} = -\frac{dA}{dy_{i0}} \tag{A.4-9}$$

The error propagation of the derivative amplitude and position variables to define the variance of the left and right FWHM values are as follows.

$$V(y_i) = \left(\frac{dy_i}{dy_{i0}}\right)^2 (\sigma_y)^2 + \left(\frac{dy_i}{dy_{i1}}\right)^2 (\sigma_y)^2 \left(\frac{dy_i}{A}\right)^2 (\sigma_A)^2 + \left(\frac{dy_i}{dA_{i0}}\right)^2 (\sigma_{A_{i0}})^2 + \left(\frac{dy_i}{dA_{i1}}\right)^2 (\sigma_{A_{i1}})^2 \tag{A.4-10}$$

$$\frac{dy_i}{dy_{i0}} = 1 - \left[\frac{A - A_{i0}}{A_{i1} - A_{i0}}\right] \tag{A.4-11}$$

$$\frac{dy_i}{dy_{i1}} = \frac{A - A_{i0}}{A_{i1} - A_{i0}} \tag{A.4-12}$$

$$\frac{dy_i}{A} = \frac{y_{i1} - y_{i0}}{A_{i1} - A_{i0}} \tag{A.4-13}$$

$$\frac{dy_i}{dA_{i0}} = \frac{(A - A_{i1})(y_{i1} - y_{i0})}{(A_{i0} - A_{i1})^2} \tag{A.4-3}$$

$$\frac{dy_i}{dA_{i1}} = \frac{(A_{i0} - A)(y_{i1} - y_{i0})}{(A_{i0} - A_{i1})^2} \tag{A.4-14}$$

$$V(FWHM) = V(y_R) + V(y_L) \tag{A.4-15}$$

LSF Beam Profile Results						
Variable	**Value**	$\sqrt{V(x)}$	**Units**	**Variable**	**Value**	$\sqrt{V(x)}$
y_{L0}	2.9946	0.0005	mm	y_{R0}	3.0846	0.0005
y_{RL1}	3.0046	0.0005	mm	y_{R1}	3.0946	0.0005
A_{L0}	-2.0230	0.0603	V/mm	A_{R0}	-2.2025	0.0268
A_{L1}	-3.5100	0.0644	V/mm	A_{R1}	-1.6887	0.0141
A	-2.1811	0.0744	V/mm	A	-2.1811	0.0744
y_L	2.9956	0.000767	V/mm	y_R	3.0850	0.001598
FWHM	89.4	1.77	μm			

Table A.4-1: Beam profile amplitude trace values of interest for FWHM calculation.

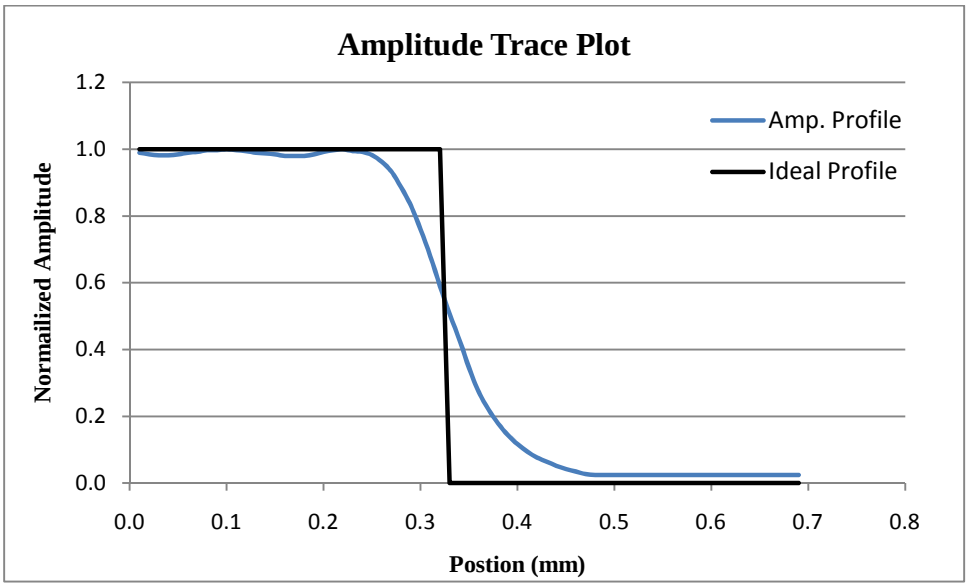

Figure A.4-1: Amplitude trace plot of scanned sharp edge with theoretical ideal trace.

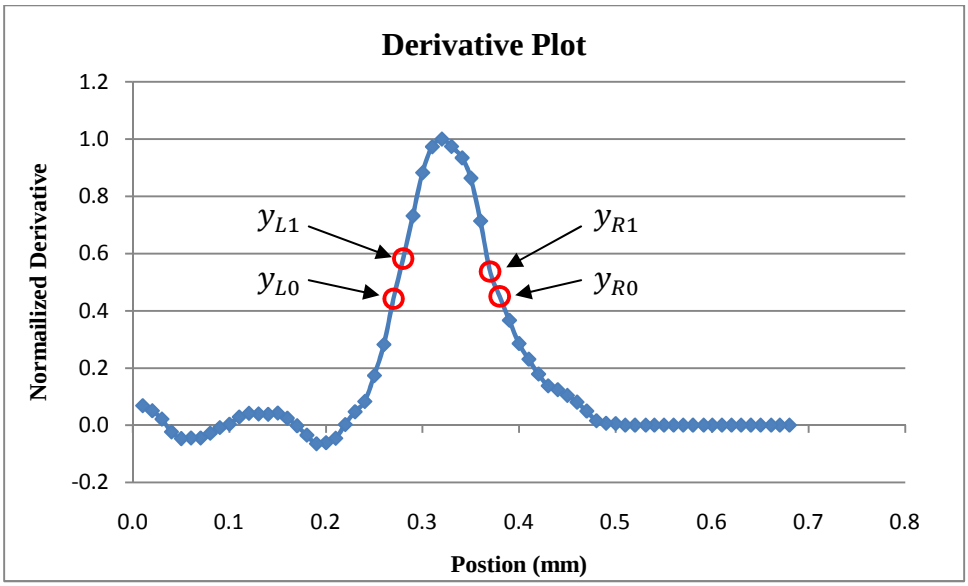

Figure A.4-2: Derivative plot of amplitude trace with identified interpolation points for FWHM calculation.

A.5-Error Summation

Table E presents the measurement and calculation errors for common values used throughout the thesis. All confidence interval are two-sided bounds for $\boldsymbol{\alpha} = 0.025$. All but the pressure values are calculated based on known variances and an assumed normal distribution. The pressure estimation values are calculated based on unknown variances with a t probability distribution with 9 degrees of freedom.

Quantity	*Units*	*CI Criterion*	$\sqrt{V(x)}$	*Error (95%)*
A-line Voltage	*mV*	$z_{0.025} = 1.96$	*5.63*	*±11.03*
Envelope	*mV*	$z_{0.025} = 1.96$	*7.96*	*±15.61*
Frequency Amp.	*mV*	$z_{0.025} = 1.96$	*90.08*	*±176.56*
Backscatter	sV^2	$z_{0.025} = 1.96$	*~2.42E-11*	*~ ±4.74E-11*
FWHM	*μm*	$z_{0.025} = 1.96$	*1.77*	*±3.47*
Pressure	*psi*	$t_{0.025,9} = 2.262$	*1.299E-03*	*±2.938E-03*

Table A.5-1: Summary of common measurements and calculations.

Appendix B: System Connectivity

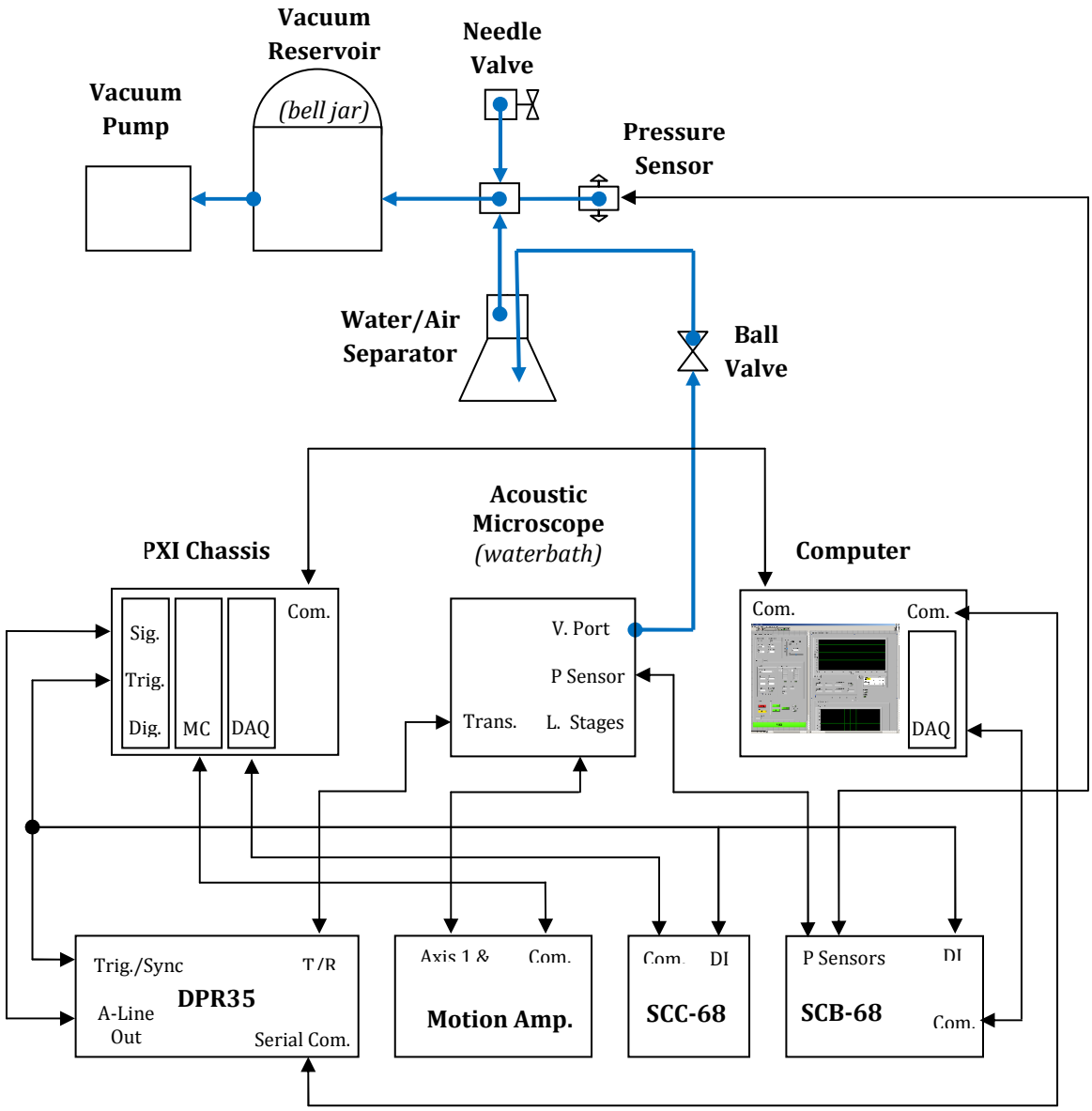

Figure B-1: System connectivity diagram.